



Theses and Dissertations

---

2018-11-01

## 3D Printing for Microfluidics

Hua Gong  
*Brigham Young University*

Follow this and additional works at: <https://scholarsarchive.byu.edu/etd>



Part of the [Engineering Commons](#)

---

### BYU ScholarsArchive Citation

Gong, Hua, "3D Printing for Microfluidics" (2018). *Theses and Dissertations*. 7690.  
<https://scholarsarchive.byu.edu/etd/7690>

This Dissertation is brought to you for free and open access by BYU ScholarsArchive. It has been accepted for inclusion in Theses and Dissertations by an authorized administrator of BYU ScholarsArchive. For more information, please contact [ellen\\_amatangelo@byu.edu](mailto:ellen_amatangelo@byu.edu).

# 3D Printing for Microfluidics

Hua Gong

A dissertation submitted to the faculty of  
Brigham Young University  
in partial fulfillment of the requirements for the degree of

Doctor of Philosophy

Gregory P. Nordin, Chair  
Adam T. Woolley  
Brian A. Mazzeo  
Karl F. Warnick  
Shiuh-hua Wood Chiang

Department of Electrical and Computer Engineering  
Brigham Young University

Copyright © 2018 Hua Gong

All Rights Reserved

## ABSTRACT

### 3D Printing for Microfluidics

Hua Gong

Department of Electrical and Computer Engineering, BYU

Doctor of Philosophy

This dissertation focuses on developing 3D printing as a fabrication method for microfluidic devices. Specifically, I concentrate on the 3D printing approach known as Digital Light Processing stereolithography (DLP-SLA) in which serially projected images are used to sequentially photopolymerize layers to build a microfluidic device. The motivation for this work is to explore a much faster alternative to cleanroom-based microfabrication that additionally offers the opportunity to densely integrate microfluidic elements in compact 3D layouts for dramatic device volume reduction. In the course of my research, an optical approach was used to guide custom resin formulation to help create the interconnected hollow regions that form a microfluidic device. This was based on a new mathematical model to calculate the optical dose delivered throughout a 3D printed part, which also explains the effect of voids. The model was verified by a series of 3D printed chips fabricated with a commercial 3D printer and a custom resin. Channels as small as  $108\text{ }\mu\text{m} \times 60\text{ }\mu\text{m}$  were repeatably fabricated. Next, highly compact active fluidic components, including valves, pumps, and multiplexers, were fabricated with the same 3D printer and resin. The valves achieved a  $10\times$  size reduction compared with previous results, and were the smallest 3D printed valves at the time. Moreover, by adding thermal initiator to thermally cure devices after 3D printing, the durability of 3D printed valves was improved and up to 1 million actuations were demonstrated.

To further decrease the 3D printed feature size, I built a custom 3D printer with a 385 nm LED light source and a  $7.56\text{ }\mu\text{m}$  pixel pitch in the plane of the projected image. A custom resin was also developed to take advantage of the new 3D printer's features, which necessitated developing a UV absorber screening process which I applied to 20 candidate absorbers. In addition, a new mathematical model was developed to use only the absorber's molar absorptivity measurement to predict the resin optical penetration depth, which is important for determining the z-resolution that can be achieved with a given resin. The final resin formulation uses 2-nitrophenyl phenyl sulfide (NPS) as the UV absorber. With this resin, along with a new channel narrowing technique, I successfully created flow channel cross sections as small as  $18\text{ }\mu\text{m} \times 20\text{ }\mu\text{m}$ .

With the custom 3D printer, smaller valves and pumps become possible, which led to the invention of a new method of creating large numbers of high density chip-to-chip microfluidic interconnects based on either simple integrated microgaskets (SIMs) or controlled-compression integrated microgaskets (CCIMs). Since these structures are directly 3D printed as part of a device, they require no additional materials or fabrication steps. As a demonstration of the efficacy of this approach, 121 chip-to-chip interconnects in an  $11 \times 11$  array for both SIMs and CCIMs with an areal density of 53 interconnects per  $\text{mm}^2$  were demonstrated, and tested up to 50 psi without leaking. Finally, these interconnects were used in the development of 3D printed chips with valves having  $30\times$  smaller volume than the valves we previously demonstrated. These valves served as a building block for demonstrating the miniaturization potential of an active fluid mixer using our 3D

printing tools, materials, and methods. The mixer provided a set of selectable mixing ratios, and was designed in 2 configurations, a linear dilution mixer-pump (LDMP) and a parallelized dilution mixer-pump (PDMP), which occupy volumes of only 1.5 mm<sup>3</sup> and 2.6 mm<sup>3</sup>, respectively.

Keywords: 3D printing, microfluidics, digital light processing, stereolithography, lab on a chip, resin formulation, valve, pump, mixer, interconnect



## ACKNOWLEDGMENTS

To start with, I would like to thank my advisor, Dr. Gregory P. Nordin, who brought me to Brigham Young University. I have learned so much from you, both in school and in life. We make a good team, and I would forever miss all the late-night discussions and brainstorm sessions we had. I am also grateful for our collaborator, Dr. Adam T. Woolley. The meetings with you and suggestions from you have been inspiring. To my other committee members, Dr. Brian A. Mazzeo, Dr. Karl F. Warnick, and Dr. Shih-hua Wood Chiang, I thank you for your help. Your inputs on this dissertation are truly appreciated.

To my fellow students and researchers, it has been a pleasure to work with you and learn from you. Thanks go to Dr. Vishal Sahore, Dr. Radim Knob, Dr. Long-Fang Tsai, Michael Beauchamp, Anna Nielsen, Haifa Almughamsi, Matthew Viglione, Mawla Boaks, Ellen Parker, Clayton Ramstedt, José Sánchez, Bryce Bickham, and Kent Hooper. Special shoutout for Ph.D. students, Matthew and Mawla. I hope your research will be smooth and fruitful.

At last, I would like to offer my deepest gratitude to my wife, Holly, who has supported me along this journey. Without you I can never become what I am. Also, I could not thank you enough for giving me Max and Evie. You help me become a better person, a better husband and a better father.

## TABLE OF CONTENTS

<b>List of Tables</b> . . . . .	<b>viii</b>
<b>List of Figures</b> . . . . .	<b>ix</b>
<b>Nomenclature</b> . . . . .	<b>xv</b>
<b>Chapter 1 Introduction</b> . . . . .	<b>1</b>
1.1 Overview . . . . .	3
1.2 List of Publications . . . . .	4
<b>Chapter 2 Background</b> . . . . .	<b>5</b>
2.1 Fused Deposition Modeling (FDM) . . . . .	5
2.2 Polyjet (PJ) . . . . .	7
2.3 Stereolithography (SLA) . . . . .	10
<b>Chapter 3 Optical Approach to Resin Formulation for 3D Printed Microfluidics</b> . . .	<b>12</b>
3.1 Experimental . . . . .	12
3.1.1 3D Printer . . . . .	12
3.1.2 Materials . . . . .	13
3.1.3 Resin Optical Absorbance . . . . .	14
3.1.4 Flow Channel Flushing . . . . .	15
3.2 Resin Optical Analysis . . . . .	15
3.2.1 Mathematical Model . . . . .	16
3.2.2 Measurement of $h_a$ and $T_c$ . . . . .	19
3.3 Resin Optical Properties and Flow Channel Formation . . . . .	22
3.3.1 Mathematical Model - Multiple Exposures . . . . .	23
3.3.2 Total Dose with an Embedded Channel . . . . .	25
3.3.3 Effect of Build Layer Thickness . . . . .	28
3.4 Experimental Results and Discussion . . . . .	29
3.5 Conclusions . . . . .	36
<b>Chapter 4 High Density 3D Printed Microfluidic Valves, Pumps, and Multiplexers</b> .	<b>38</b>
4.1 Experimental . . . . .	38
4.1.1 Materials . . . . .	38
4.1.2 3D Printer . . . . .	39
4.1.3 Device Fabrication . . . . .	40
4.2 Results and Discussion . . . . .	43
4.2.1 3D Printed Valves . . . . .	43
4.2.2 3D Printed Pumps . . . . .	46
4.2.3 3D Printed Multiplexers and Mixers . . . . .	49
4.3 Conclusions . . . . .	54

<b>Chapter 5</b>	<b>Custom 3D Printer and Resin for <math>18\ \mu\text{m} \times 20\ \mu\text{m}</math> Microfluidic Flow Channels</b>	<b>55</b>
5.1	Materials and Methods	55
5.1.1	Custom 3D Printer	55
5.1.2	Materials	58
5.1.3	Molar Absorptivity Measurement	59
5.1.4	Dose Calibration	61
5.1.5	3D Printing	61
5.1.6	Material Mechanical Properties	61
5.1.7	Post-Print Curing	62
5.2	Results and Discussion	63
5.2.1	Absorber Selection	63
5.2.2	Material Properties and Layer Dose	71
5.2.3	Small Cross Section Channels	72
5.2.4	Long Channels	78
5.2.5	Tall High Aspect Ratio Channel	79
5.3	Conclusions	80
<b>Chapter 6</b>	<b>3D Printed High Density, Reversible, Chip-to-chip Microfluidic Interconnects</b>	<b>81</b>
6.1	Materials and Methods	82
6.1.1	3D Printer and Materials	82
6.1.2	3D Printing	83
6.1.3	Surface Roughness Measurement	83
6.1.4	Pressure and Reusability Measurements	83
6.2	Results and Discussion	85
6.2.1	Concept	85
6.2.2	Simple Integrated Microgasket (SIM) Approach	87
6.2.3	Controlled-Compression Integrated Microgasket (CCIM) Approach	90
6.2.4	Scaling	92
6.3	Demonstration: Valve Testing	93
6.4	Conclusions	96
<b>Chapter 7</b>	<b>3D Printed Selectable Dilution Mixer Pumps</b>	<b>98</b>
7.1	Materials and Methods	99
7.1.1	3D Printer and Materials	99
7.1.2	3D Printing and Sample Preparation	99
7.1.3	Concentration Measurement	100
7.2	Results and Discussion	102
7.2.1	Pumps	102
7.2.2	Linear Dilution Mixer Pump (LDMP)	107
7.2.3	4-to-1 Valve	117
7.2.4	Parallelized Dilution Mixer Pump (PDMP)	118
7.3	Conclusions	122

<b>Chapter 8</b>	<b>Conclusions</b>	<b>124</b>
8.1	Summary	124
8.1.1	Optical Approach to Resin Formulation for 3D Printed Microfluidics	124
8.1.2	High Density 3D Printed Microfluidic Valves, Pumps, and Multiplexers	124
8.1.3	Custom 3D Printer and Resin for $18\ \mu\text{m} \times 20\ \mu\text{m}$ Microfluidic Flow Channels	125
8.1.4	3D Printed High Density, Reversible, Chip-to-chip Microfluidic Interconnects	125
8.1.5	3D Printed Selectable Dilution Mixer Pumps	126
8.2	Future Research	127
8.2.1	3D Printer	127
8.2.2	Resin	127
8.2.3	Other Possibilities	128
<b>References</b>		<b>129</b>

## LIST OF TABLES

2.1	Microscope photographs of channels fabricated with commercial 3D printing service bureaus. PJ = Polyjet, SL-SLA = scanned laser stereolithography. . . . .	9
3.1	Resin viscosities. . . . .	14
3.2	$h_a$ and $T_c$ from membrane measurements. . . . .	21
3.3	Results for different channel heights and layer thicknesses for PEGDA resins with varying concentrations of Sudan I. See text for details. . . . .	31
3.4	Normalized layer thicknesses, $\zeta_l$ , and exposure times, $t_l$ , for the results in Table 3.3. . .	32
3.5	Channels in 0.4% Sudan I resin as a function of width and height for $t_l = 0.8$ s and $z_l = 10$ $\mu\text{m}$ ( $\zeta_l = 0.57$ ). . . . .	33
3.6	Channels in 0.6% Sudan I resin as a function of width and height for $t_l = 1.55$ s and $z_l = 10$ $\mu\text{m}$ ( $\zeta_l = 0.91$ ). . . . .	34
4.1	Pump timing logic. Red: actuated (pressure applied; valves closed); green: not actuated (valves open). . . . .	47
4.2	Mixer timing logic. Red: actuated (pressure applied; valves closed); green: not actuated (valves open). Valves not listed in the table are closed. . . . .	53
5.1	UV absorbers . . . . .	60
5.2	Solubility in PEGDA and fluorescence with 385 nm excitation. Dash indicates insolubility. . . . .	64
5.3	Comparison of monochromatic and polychromatic resin exposures. . . . .	66
5.4	Summary of fit parameters based on measured spectra and on measured thickness vs. exposure time data. All resins are formulated with 1% Irgacure 819 in addition to the specified absorber. . . . .	70
5.5	Comparison of Young's modulus and durometer measurements for NPS and Martius Yellow resins. Durometer measurements are unitless and Young's Modulus, $E$ , is in MPa. . . . .	71
6.1	Experimentally tested interconnect array sizes and periods. . . . .	88
7.1	Details on the thickness and exposure of different fluidic component membranes. . . .	104
7.2	Comparison of LDMP and PDMPs with different DIP count. Here, we assume the pump DC dimensions are the same for LDMP and PDMPs, and that $V_{\text{mixer}} = N \times V_{\text{pump}}$ . . .	120
7.3	Available serial dilution ratios with various dilution factors for the fabricated PDMP design. A dilution factor of 4 is a subset of a dilution factor of 2. . . . .	120

## LIST OF FIGURES

2.1	Illustration of FDM. [1] (Copyright © 2008 CustomPartNet) . . . . .	6
2.2	Illustration of PJ. [1] (Copyright © 2008 CustomPartNet) . . . . .	8
2.3	Test design for 3D printing service bureaus. The base is 12 mm $\times$ 4 mm and the height is 3.8 mm at the back wall. . . . .	8
2.4	Illustration of SL-SLA. [1] (Copyright © 2008 CustomPartNet) . . . . .	10
2.5	Illustration of DLP-SLA. Reproduced with permission [2]. . . . .	11
3.1	Schematic illustration of device orientation and imaged DLP pixels on 3D printer build platform. . . . .	13
3.2	Measured resin absorbance compared with Asiga 3D printer LED emission spectrum for several commercial and custom PEGDA resins. The 1% Irgacure curve is the absorbance of PEGDA mixed with 1% (w/w) Irgacure 819 photoinitiator. The Sudan I resins contain both Sudan I and 1% (w/w) Irgacure 819. . . . .	14
3.3	Schematic illustration of Beers Law and definition of $h_a$ . See text for details. . . . .	16
3.4	(a) Polymerization depth, $z_p$ , of resins with different $h_a$ as a function of the normalized layer exposure time, $\tau_p$ (Eq. 3.5). (b) Normalized dose as a function of depth, $z$ , for different values of $h_a$ and the normalized exposure time, $\tau$ . . . . .	18
3.5	(a) CAD design and (b) photo of 3D printed sample for determining $h_a$ and $T_c$ . . . . .	19
3.6	Microscope photograph of membrane for 0.2% Sudan I resin with 2 s layer exposure time and 50 $\mu\text{m}$ build layer thickness. The posts on which the membrane layer is fabricated are 5 layers tall. . . . .	20
3.7	(a) Measured membrane thicknesses for different resins along with curve fits of Eq. 3.5. Corresponding values of $h_a$ and $T_c$ are in Table 3.2. Error bars are present for individual measurements but are generally too small to see. (b) $h_a$ of Sudan I resins as a function of Sudan I concentration. . . . .	20
3.8	Microscope photograph of membrane of 0.2% Sudan I resin with 0.45 s exposure time and 10 $\mu\text{m}$ build layer thickness. The measured membrane thickness is 10 $\mu\text{m}$ . . . . .	21
3.9	Layer-by-layer fabrication process for a simplified device. The device is rotated 180 degrees in (d) relative to (a-c). See text for details. . . . .	22
3.10	Normalized dose as a function of depth, $z$ , for five 3D printed layers. Each layer receives a single exposure. Solid line indicates total dose. See text for details. . . . .	25
3.11	Normalized dose as a function of normalized depth, $\gamma$ , for a 12-layer case with a flow channel in Layers 5 and 6 (red and black layer index numbers along the top indicate exposure or no exposure in that layer, respectively). . . . .	27
3.12	Effect of layer thickness on total normalized dose. The first 200 $\mu\text{m}$ represents a flow channel such that layers in this region are not exposed. . . . .	28
3.13	Flow channels 200 $\mu\text{m}$ high by 5 pixels (135 $\mu\text{m}$ ) wide with 0.2% Sudan I resin for build layer thicknesses of (a) 50 $\mu\text{m}$ , (b) 25 $\mu\text{m}$ , and (c) 10 $\mu\text{m}$ . Layer exposure times, $t_l$ , are 1.5 s, 0.71 s, and 0.45 s, respectively. . . . .	30
3.14	(a) Minimum flow channel height with 100% yield for PEGDA resins with different Sudan I concentrations. (b) Experimental results of yield (green: 100%, yellow: partial, red: none) for normalized channel height and normalized layer thickness. . . . .	35

3.15	Smallest consistently open channels printed with commercial and open source resins. Microscope photos (a), (c), and (d) are taken with a $5\times$ objective while (b) uses a $10\times$ objective. The build layer thickness for (a) and (b) is $50\text{ }\mu\text{m}$ , and $100\text{ }\mu\text{m}$ for (c) and (d).	36
4.1	CAD design of (a) for a 3D printed membrane valve. Schematic illustration and microscope photos of (b), (d) open and (c), (e) closed valves. The microscope photos show the bottom of the valve. See text for details.	41
4.2	Complete 3D printed valve CAD design includes cylindrical holes in which to connect PTFE tubing.	42
4.3	(a) Typical valve pressure measurement and (inset) schematic illustration of test setup. The fluid and control pressures are measured with pressure sensors G1 and G2. (b) $\Delta P$ as a function of fluid chamber height and (c) membrane thickness. Each data point in (b) and (c) consists of an average of at least 10 valves, with most being an average of over 20 valves. Error bars indicate $\pm 1$ standard deviation. $h_{ctrl}$ : control chamber height; $D$ : diameter; $t_{memb}$ : membrane thickness; $h_{fluid}$ : fluid chamber height.	44
4.4	Valve maximum fluid pressure as a function of control pressure for different baking times. The number of valves tested for each baking time are 0 min: 3, 20 min: 8, 30 min: 9, 60 min: 8, 90 min: 7.	45
4.5	(a) CAD design of 3D printed pump. C1-C3 connect to external pressure sources. The partially transparent channels are flushing channels for the valve control chambers, which are later sealed with epoxy. (c) Side view of a 3D printed pump. See text for details. (c) Bottom view photograph of 3D printed pump in (b).	46
4.6	(a) Maximum flow rate (zero back pressure) as a function of the phase interval, $\Delta t$ . (b) Fluid volume expelled by pump for a single pump cycle calculated from the data in (a). 9 pumps were tested with vacuum and 5 without. The large error bars for vacuum at 20 ms are due to 2 pumps having significantly smaller flow rates than the others.	48
4.7	(a) Typical maximum back pressure measurement and (inset) experimental setup. (b) Maximum back pressure as a function of control pressure (average and standard deviation for 7 pumps).	49
4.8	Flow rate as a function of the outlet height for a control pressure of 9 psi (average and standard deviation for 6 pumps). Different pumps were used in all tests.	50
4.9	(a) Multiplexer schematic diagram. (b) CAD design taking advantage of stacked layout flexibility enabled by 3D printing. Valve labeling is the same as (a) with corresponding control lines labeled C1, C2, etc. (c) Bottom view of multiplexer fabricated according to the CAD design in (b). (d)-(i) Demonstration of arbitrary 3-to-2 multiplexing. See text for details. Arrows indicate active flow direction.	51
4.10	(a) Flow generated only by gravity. Note lack of Red/Black mixing. (b, c) Bottom view of DC channel layout in (b) Mixer 1 and (c) Mixer 2. Red channels, R1 in (b) and R1 and R2 in (c), connect the Red inlet valve (V2 in Fig. 4.9a) to the DC, while the black channels, B1 in (b) and B1 and B2 in (c), connect the Black inlet valve (V3) to the DC. Buffer is the channel that connects the Buffer inlet to the DC through valve V1. O1 and O2 connect the DC to Outlets 1 and 2, respectively, through valves V4 and V5. (d) and (e) compare the mixing performance of the designs in (b) and (c). See text for details.	52

5.1	3D CAD model of our custom 3D printer. . . . .	56
5.2	Schematic illustration of 3D printer. . . . .	56
5.3	UV absorber evaluation criteria and process flow. 20 absorbers are initially considered. Rejected absorbers are indicated at each step in the process where they do not pass the evaluation criterion. . . . .	58
5.4	Molecular structures for monomer, photoinitiator, and UV absorbers used in this study (except for UV386A, which is proprietary). . . . .	59
5.5	Measured molar absorptivity and LED source spectrum. . . . .	62
5.6	(a) $D_n(z)$ calculated from molar absorptivity for 1% Irgacure 819 resin. (b) Same as (a) except for 1% Avobenzone and 2% NPS resins. . . . .	67
5.7	Measured polymerization thickness as a function of exposure time for 13 resins. Each resin contains 1% Irgacure 819 in addition to the specified UV absorber. Dashed lines indicate fit to Model 3. Inset shows that Model 4 (solid lines) is a better fit for some resins. . . . .	69
5.8	SEM images of flow channel cross sections for 2% NPS. See text for details. All channels are designed to be 4 pixels wide. Larger layer thickness results in larger vertical wall surface relief. $t_{\text{layer}}$ is layer thickness, $N_{\text{minlayer}}$ is the minimum number of layers for open channel, and $h_{\text{channel}}$ is channel height. . . . .	73
5.9	Normalized dose as a function of normalized depth. . . . .	74
5.10	Calculated dose as a function of depth for the cases in Fig. 5.8. . . . .	74
5.11	Same as Fig. 5.8 except for 3% NPS. $t_{\text{layer}}$ is layer thickness, $N_{\text{layer}}$ is number of layers, and $h_{\text{design}}$ is the designed channel height. . . . .	75
5.12	Calculated normalized dose as a function of depth for the 3 layer cases in Fig. 5.11 . . .	75
5.13	(a) Primary and additional edge exposure patterns for a single layer containing a flow channel. (b) Channel narrowing for 2% NPS resin for additional edge exposure. The build layer size is $8.3 \mu\text{m}$ layers and the designed flow channel height is $25 \mu\text{m}$ . (c) Same as (b) except for 3% NPS resin with $6 \mu\text{m}$ layers and a designed flow channel height of $18 \mu\text{m}$ . (d), (e) Measured channel width and height, respectively, as a function of edge exposure time. . . . .	77
5.14	(a) Microscope photograph of single layer serpentine channel. (b) Schematic illustration of 3D stacked serpentine channel design. Each layer is shown as a different color. (c) Photograph of 3D printed device with 24 3D serpentine channels. The photo is taken through the glass slide on which the device is 3D printed. (d) SEM image of 3D serpentine channel cross section. . . . .	78
5.15	Photograph and SEM images of 3D printed high aspect ratio flow channel. . . . .	79
6.1	(a) Clamping mechanism for interface and test chips. (b) Photo of clamped interface and test chips ready for pressure testing. (c) Schematic illustration of pressure test set up. Syringe pump is connected sequentially to individual tubes to pressure test each associated interconnection port microgasket (see text for details). . . . .	84



6.2	(a) Schematic illustration of a $3.4\text{ mm} \times 3.4\text{ mm} \times 1\text{ mm}$ device chip connected to an interface chip (clamping mechanism not shown). The interface chip supplies a world-to-chip interface with an array of cylindrical recesses into which PTFE tubing is epoxied. (b) Schematic illustration of the interior of the interface chip showing how channels are routed from the cylindrical recesses to an array of interconnects on the device chip. Alignment blocks on the top of the device chip are also visible. (c) Underside of interface chip. Close-up shows that interconnects consist of an array of flow channels that terminate on the flat bottom surface of the chip, and that the device chip alignment blocks fit into recesses on the interface chip. . . . .	85
6.3	Measured average surface roughness as a function of layer exposure time. The error bars indicate the standard deviation of the three measurements for each exposure time that are described in Sect. 6.1.3. Inset: microscope photo of device with adjacent regions having 600 and 800 ms layer exposure times. Faint pixelation is more observable for the former than the latter. . . . .	86
6.4	SIM design. (a) Integrated square microgaskets printed around each vertical channel on the top surface of a device chip. The top surface is in the XY plane with the Z direction being out of the plane. (b) Schematic illustration of the cross section of the vertical plane indicated in (a). The microgaskets have height $D$ above the surrounding planar surface of the chip. . . . .	87
6.5	Using the device and interface chips in Fig. 6.2 for each of the 9 SIM in Fig. 6.4. . . .	88
6.6	(a) $11 \times 11$ interconnect array test set up. (b) Composite image from four Zeta-20 microscope images of fabricated $11 \times 11$ array of SIMs. Close up shows details of SIMs, including slight pixelation of the sealing surface. . . . .	89
6.7	Pressure as a function of time for the test set up in Fig. 6.6a repeated 100 times. . . .	90
6.8	CCIM design. (a) Integrated microgaskets printed around each vertical channel in a square recess. (b) Schematic illustration of the cross section of the vertical plane in (a). The microgaskets have height $D$ above the surrounding planar surface of the chip. (c) Composite image from four Zeta-20 microscope images of fabricated $11 \times 11$ array of CCIMs. Close up shows details of CCIMs. (d) Pressure as a function of time for the test set up in Fig. 6.6a repeated 100 times. . . . .	91
6.9	(a) Schematic illustration of geometry to test 400 CCIM interconnects in a $20 \times 20$ array using two independent sets of flow channels (red and blue) that cross up and down between the chips. The plane shows the separation between device (upper) and interface (lower) chips. (b) Photograph of assembled device and interface chips. The two separate flow channels are filled with water containing red and blue food coloring. (Close-up) Microscope image of flow channels. . . . .	92
6.10	Schematic diagrams of 3D printed pneumatically actuated membrane valve in (a) open and (b) closed states. (c) Single $300\text{ }\mu\text{m}$ diameter valve with fluid and control channels connected to individual CCIMs. (d) (upper) Microscope image of 45-valve array chip assembled with corresponding interface chip in clamping fixture as shown in (e). (d) (lower) Close-up of 45-valve array with each row of valves having their control ports connected in series to a pair of CCIMs, and each column of valves having their fluid ports connected in series to a pair of CCIMs. Each valve is $300\text{ }\mu\text{m}$ in diameter. . . . .	94
7.1	Microfluidic 3D printing fabrication process flow. . . . .	99

7.2	(a) Functional illustration of a 3D printed pump. (b) and (c) 3D printed valve in open and closed states. See text for details. . . . .	103
7.3	CAD drawing of a pump with a serpentine outlet channel. . . . .	105
7.4	(a)-(d) Microscope photos of a pump at various stages in its operation. The DC has the same diameter as the valves, which is 40 pixels. (a)→(b): Outlet valve opens, and the meniscus moves back by the volume of the valve upward membrane displacement, $V_{valve}$ ; (b)→(c): DC is actuated, and the meniscus moves forward by the volume of the DC downward membrane displacement, $V_{DC}$ ; (c)→(d): outlet valve is actuated, and the meniscus moves further forward by the volume of the valve downward membrane displacement, which is the same as its upward membrane displacement, $V_{valve}$ . . . . .	106
7.5	Measured pumping volume for DCs with different diameters and 50 $\mu\text{m}$ height for both the fluid and control chambers. The unit of the x-axis dimension, pixel, is the DLP image plane pixel pitch, 7.56 $\mu\text{m}$ . . . . .	107
7.6	(a) Schematic of LDMP. It contains 2 pumps which are connected to a fluid reservoir. They can selectively pump fluid to the mixer which performs mixing. (b) 3D layout of (a). Pumps are stacked on top of the mixer, and the mixer has 2 large DCs connected to each other via cone-shaped channels. (c) Photograph of a 3D printed device designed for characterization of 4 LDMPs on a single chip. (d) Microscope photo of an LDMP which uses microgaskets developed in Chapter 6. . . . .	108
7.7	A complete mixer-pump cycle, denoted as $\tau_{MP}$ . At the beginning, the outlet valve is closed. Then, both mixer DCs are released to be prepared for the fluid injected by pumps during the subsequent $N_{pump}$ pumping periods, $N_{pump}\tau_{pump}$ . After the mixer is filled, it mixes fluid for $N_{mix}$ mixing periods for a time of $N_{mix}\tau_{mix}$ . Finally, the outlet valve opens, and both mixer DCs are actuated to expel the mixture. . . . .	110
7.8	(a) LDMP flushing chip. (b) LDMP operation chip. (c) LDMP device chip assembled with flushing chip. (d) LDMP device chip assembled with operation chip. . . . .	111
7.9	(a) Chip-to-chip interconnect surface of the LDMP flushing chip. Each channel matches to a microgasket interconnect on the LDMP device chip. (b) Chip-to-chip interconnect surface of the LDMP operation chip. The channels in black dashed boxes in (a) are removed, leaving a blank surface to seal the corresponding device chip microgasket channel. Because these chips are used for numerous designs, there is an extra channel which is not used in the LDMP, shown in the white dashed box. . . . .	111
7.10	(a) Water and Red flow induced only by gravity. The fluid in the ROI encompassed by the dashed box is segregated, as expected. (b) Standard deviation, $\sigma$ , of relative concentration, $C_{rel}(x,y)$ , in the ROI as a function of frames in recorded video. . . . .	112
7.11	The mean and standard deviation of relative concentration $C_{rel}(x,y)$ in the ROI as a function of the frame number. The state (open/closed) of the outlet valve is plotted as the red curve where a pulse corresponds to open. The outlet is initially filled with Water. Near Frame 26,000 ( $\sim 108$ s) the outlet channel is flushed with Red. (a) $N_{mix} = 1$ . (b) $N_{mix} = 2$ . (c) $N_{mix} = 6$ . (d) $N_{mix} = 8$ . See text for mixing details. . . . .	114
7.12	Microscope photos of the outlet valve in a mixer-pump in closed state (a) and open state (c). We average the pixel gray level inside the dashed box, and compare the results between closed and open state. (b) Direct comparison of the boxed region in closed and open state. The boxed region is darker in closed state. . . . .	115

7.13	Experimental data for $\bar{C}_{rel}$ and $\sigma$ for different Red concentrations using $N_{mix} = 6$ mixing periods. The Red concentration for (a)-(e) are $i/6$ where $i \in [1, 2, 3, 4, 5]$ . . . . .	116
7.14	Plot of measured relative concentration vs. ideal relative concentration with 6, 8, and 10 mixing periods. The measured relative concentration is averaged over frames in 3 full consecutive mixer pump cycles starting from frame 20,000. . . . .	117
7.15	(a) CAD design of a 3D printed 4-to-1 valve that contains 4 inlet channels and 1 outlet channel. (b) Microscope photo of a fabricated 4-to-1 valve under pressure. The membrane is deflected such that it is in contact with the central area of the bottom of the valve, covering all 4 inlet channels and therefore closing the valve. . . . .	118
7.16	(a)-(c) Schematic of PDMPs with 1, 2, and 4 DIPs, respectively. A DIP has 2 inlet valves to enable pumping from either fluid source. The 1-to-1 valve is a normal valve, but a n-to-1 valve controls connecting n inlets to 1 outlet. (d, e) Different perspectives of a PDMP CAD design with 4 pumps and a 4-to-1 valve. The green vertical channels are fluidic channels, and the rest are control (pneumatic) channels. The outlet channel consists of two sections with heights of $50 \mu\text{m}$ (ROI1) and $100 \mu\text{m}$ (ROI2), respectively. (f) Microscope photo of a 3D printed device based on (d, e). Inside the white dashed box are 2 inlet valves and a DC. . . . .	119
7.17	Measured relative concentration vs ideal for different dilution factors using PDMPs. Three PDMPs are tested for a dilution factor of 2 to obtain the error bars. . . . .	122

## NOMENCLATURE

AIBN	Azobisisobutyronitrile
CCIM	Controlled-Compression Integrated Microgasket
DIP	Dual Inlet Pump
DLP	Digital Light Processing
DLP-SLA	Digital Light Processing Stereolithography
FDM	Fused Deposition Modeling
Irgacure 819	Phenylbis (2,4,6-trimethylbenzoyl) phosphine oxide
LDMP	Linear Dilution Mixer Pump
NPS	2-nitrophenyl phenyl sulfide
PDMP	Parallelized Dilution Mixer Pump
PEGDA	Poly(ethylene glycol) diacrylate
PJ	Polyjet
SIM	Simple Integrated Microgasket
SLA	Stereolithography
SL-SLA	Scanned Laser Stereolithography

## CHAPTER 1. INTRODUCTION

Microfluidic lab-on-a-chip technology [3] has been widely touted as a flexible tool for diagnostic assays in a range of biomedical applications, such as drug discovery [4]; tissue engineering [5], [6]; pathogen diagnostics [7]–[10]; cancer screening based on rare cell detection [11] and the presence of relevant biomarkers such as protein [12]–[15], DNA [16], and micro-RNA [17], [18] analytes, among a myriad of other potential uses. Notably, the small size and self-contained assay components provided by microfluidic devices make this technology highly attractive for point-of-care applications. However, despite numerous proof of concept publications with biological relevance, and two and a half decades of microfluidics research [19], the high potential of this technology for biomedical sciences has not yet been realized. This achievement gap largely results from the difficulty of microfluidic device fabrication. Traditionally, microfluidic devices have been constructed of glass or silicon [20], embossed or injection molded plastics [3], [21], or polydimethylsiloxane (PDMS) [22], [23]. While largely effective, the fabrication methods are cumbersome and time consuming; fabrication typically requires access to cleanroom equipment and includes photolithographic microfabrication of molds for each individual layer, molding and release of each layer, and then careful layer alignment and bonding of the individual layers to form a completed device. Not surprisingly, these fabrication methods place practical limits on the number of layers ( $\sim 2$ -5) that can be incorporated into a traditional microfluidic device, which effectively constrains microfluidic device geometry to two dimensions and correspondingly increases device footprint and limits its effectiveness.

As an alternative to existing technologies, we here focus on development of 3D printing technology which has the potential to overcome the key limitations of conventional microfluidics fabrication that have hindered its broad adoption in biology. To elaborate, as we observed in Ref. 24, 3D printing offers a true rapid-prototyping capability for microfluidics in which a “fail fast and often” strategy can be employed to positively disrupt the microfluidic device development process

by using early and rapid empirical feedback to iteratively guide and accelerate device development. A key enabler of rapid iteration is fast 3D printing and post-processing such that one or more iterations of *fabrication*  $\rightarrow$  *test*  $\rightarrow$  *adjust design* can be performed in a single day. In addition to a vastly streamlined fabrication process, 3D printing avoids the significant startup and operational costs of a cleanroom, thereby making microfluidic device development available to a much broader audience. Moreover, use of standardized elements and functional blocks in the design and layout of a device can permit non-specialists to apply microfluidics to research, prototyping, and product development in many fields. For these reasons, the advantages of 3D printing for microfluidic device fabrication are increasingly being recognized [25]–[35]. A particularly promising 3D printing method for fluidics, thus the focus of this dissertation, is stereolithography (SLA) based on Digital Light Processing (DLP). In this approach a micromirror array is used to optically define the pattern for an individual layer by selective photopolymerization of a photo-sensitive resin. Successive layers of resin are exposed with appropriate optical patterns to fabricate an entire device [32], [34], [36], [37].

For successful 3D printing, the critical aspect of fluidic devices is that they consist primarily of a series of small (micro) voids inside the polymerized material. These voids form a variety of structures including passive components [38]–[40] such as flow channels, splitters, mixers, reaction chambers, and droplet generators, and active components such as valves [24], [41] and pumps [41]. Note that this emphasis on small voids is in direct contrast to many typical 3D printing applications in which external features [42], [43] or sparse structures [37] are important. During DLP-SLA fabrication, such voids are regions of unpolymerized resin that must be flushed after 3D printing, which is an easier process than trying to remove a solid sacrificial support as required by other 3D printer technologies such as polyjet [44], [45]. Unfortunately, as shown in Ref. 46, current commercial 3D printing tools and materials are unable to fabricate truly microfluidic voids ( $< 100\ \mu\text{m}$ ), and hence 3D printed devices are at best in the large microfluidic regime ( $100\text{--}500\ \mu\text{m}$ ), [24], [39], [45], [47]–[50] but more often in the millifluidic ( $> 1\ \text{mm}$ ) [44], [51]–[53] or sub-millifluidic ( $0.5\text{--}1.0\ \text{mm}$ ) [38], [54]–[59] regimes (see Ref. 60 for a review of 3D printed microfluidics in terms of these size categories). Therefore, a critical need exists to advance 3D printing such that it becomes suitable for microfluidics.

## 1.1 Overview

This dissertation focuses on developing materials, tooling, and methods to enable 3D printing to successfully fabricate microfluidic devices with features in the truly microfluidic, as opposed to millifluidic, regime [60] for both passive and active components [46], [61], [62].

Chapter 2 introduces the background of 3D printing. We discuss three types of 3D printing techniques commonly used to fabricate fluidic systems, which are fused deposition modeling (FDM), polyjet (PJ), and stereolithography (SLA).

Chapter 3 details an optical approach used to guide custom formulation of resins to minimize the cross sectional size of fabricated flow channels. We focus on SLA 3D printing with Digital Light Processing (DLP) based on a micromirror array and use a commercially available 3D printer. We develop a mathematical model for the optical dose delivered through the thickness of a 3D printed part, including the effect of voids.

Chapter 4 demonstrates that DLP-SLA 3D printer can be used to create highly compact microfluidic devices with active components such as valves and pumps. Leveraging the work on optical formulation of inexpensive resins in Chapter 3, the smallest 3D printed valves to date are demonstrated.

Chapter 5 shows that a custom DLP-SLA 3D printer and a specifically-designed, low cost, custom resin can readily achieve flow channel cross sections as small as  $18\text{ }\mu\text{m} \times 20\text{ }\mu\text{m}$ . We demonstrate the evaluation criteria and process flow required to develop a high-resolution resin. In doing so, a new mathematical model is introduced for characterizing the resin optical penetration depth based only on measurement of the absorber’s molar absorptivity. We also develop a novel channel narrowing technique that, together with the new resin and 3D printer resolution, enables small flow channel fabrication.

Chapter 6 introduces 3D printed simple integrated microgaskets (SIMs) and controlled-compression integrated microgaskets (CCIMs) to connect a small device chip to a larger interface chip that implements world-to-chip connections.

Chapter 7 explores the miniaturization potential of a common class of microfluidic component, an active fluid mixer, but with the additional ability of directly selecting the desired mixing ratio. The motivation is to illustrate how the flexibility of 3D printing in combination with

unrestricted 3D layout of individual device elements and routing of fluid channels enables the realization of extremely small, complex microfluidic components.

## 1.2 List of Publications

1. Hua Gong, Michael J. Beauchamp, Steven Perry, Adam T. Woolley, and Gregory P. Nordin, "Optical approach to resin formulation for 3D printed microfluidics," *RSC advances*, vol. 5, no. 8, pp. 106621-106632, 2015
2. Hua Gong, Adam T. Woolley, and Gregory P. Nordin, "High density 3D printed microfluidic valves, pumps, and multiplexers," *Lab on a Chip*, vol. 16, no. 13, pp. 2450-2458, 2016
3. Hua Gong, Adam T. Woolley, and Gregory P. Nordin, "Custom 3D printer and resin for  $18\ \mu\text{m} \times 20\ \mu\text{m}$  microfluidic flow channels," *Lab on a Chip*, vol. 17, no. 17, pp. 2899-2909, 2017
4. Hua Gong, Adam T. Woolley, and Gregory P. Nordin, "3D printed high density, reversible, chip-to-chip microfluidic interconnects," *Lab on a Chip*, vol. 18, no. 4, pp. 639-647, 2018
5. Hua Gong, Adam T. Woolley, and Gregory P. Nordin, "3D printed selectable dilution mixer pumps," *Biomicrofluidics*, 2018 (submitted)
6. Long-Fang Tsai, Hua Gong, Kathryn L. Dallon, Brian A. Mazzeo, and Gregory P. Nordin, "Light emission from electrodes under dielectrophoresis conditions," *Journal of Micro/Nanolithography, MEMS, and MOEMS*, vol. 15, no. 2, p. 025001, 2016
7. Michael J. Beauchamp, Hua Gong, Adam T. Woolley, and Gregory P. Nordin, "3D printed microfluidic features using dose control in X, Y, and Z dimensions," *Micromachines*, vol. 9, no. 7, p. 326, 2018
8. Ellen K. Parker, Anna V. Nielsen, Michael J. Beauchamp, Haifa M. Almughamsi, Jacob B. Nielsen, Mukul Sonker, Hua Gong, Gregory P. Nordin, and Adam T. Woolley, "3D printed microfluidic devices with immunoaffinity monoliths for extraction of preterm birth biomarkers," *Analytical & Bioanalytical Chemistry*, pp. 1-9, 10 2018



## **CHAPTER 2. BACKGROUND**

The invention of 3D printing, also known as additive manufacturing, dates back to the early 1980s when Charles Hull filed his patent for a stereolithography (SLA) fabrication system. Since then many other types of 3D printing techniques have been developed as well, such as laser sintering, laminated object manufacturing (LOM), fused deposition modeling (FDM), Polyjet (PJ, also known as inkjet), etc. Also, these 3D printing techniques have been applied to a wide variety of areas. In aerospace industry 3D printing is used to fabricate light weight and energy efficient structures. In space exploration there are rocket engines that are entirely 3D printed. Automotive manufacturers are attempting to adopt 3D printing for making replacement parts as needed. People in architecture and construction use 3D printing as a modeling tool. In education, now students can easily create a custom designed product. 3D printing has also found its applications in food and fashion industry.

Even though all 3D printing techniques have their own unique way to fabricate a 3D object, the general principle is basically the same. It starts with computer-aided design (CAD) where a 3D structure is created in a computer program. The computer program exports an STL file which describes the 3D structure and is widely accepted as the standard format via which 3D printer communicates with computer. After a 3D printer receives the STL file, it begins printing accordingly. When the print is finished, normally some post processing is required.

In microfluidics, 3D printed devices are usually fabricated with FDM, PJ, or SLA, so here I only focus on them instead of the entire 3D printing field, therefore allowing me to discuss them in greater depth.

### **2.1 Fused Deposition Modeling (FDM)**

FDM printers (Fig. 2.1) are the most commonly seen 3D printers. It uses a heated nozzle to melt the thermoplastic filament that is fed to it. The molten plastic is forced through the small

tip on the nozzle and deposits on the build platform or the already built part. Immediately after deposition, the plastic cools down and solidifies. Since this is a layer-by-layer process, once a layer is printed, the build platform moves down for the next layer.

The advantages of FDM are that it is safe and simple, and requires no chemical post-processing; there is no liquid resin to cure in the process, making it nice and clean; both the 3D printing machine and consumable materials are very affordable [63]–[65]; also, it can process a wide range of materials including almost any thermoplastic, which enables flexible multi-material printing [66], [67]. These benefits have inspired researchers to apply it to microfluidics. Symes *et al.* created a 3D printed bespoke, low-cost reactionware with reagents directly printed into 3D matrix [68]. Moore *et al.* investigated the behavior of 3D printed capillary valves in centrifugal microfluidic disc [69]. He *et al.* converted a desktop 3D printer to a sugar printer to build water soluble sugar cast for making PDMS devices [70]. Because the nature of FDM, Yuen were able to insert integrated glass cover slips or polystyrene films with and without an embedded porous membrane, and optical devices with embedded Corning® Fibrance™ Light-Diffusing Fiber into

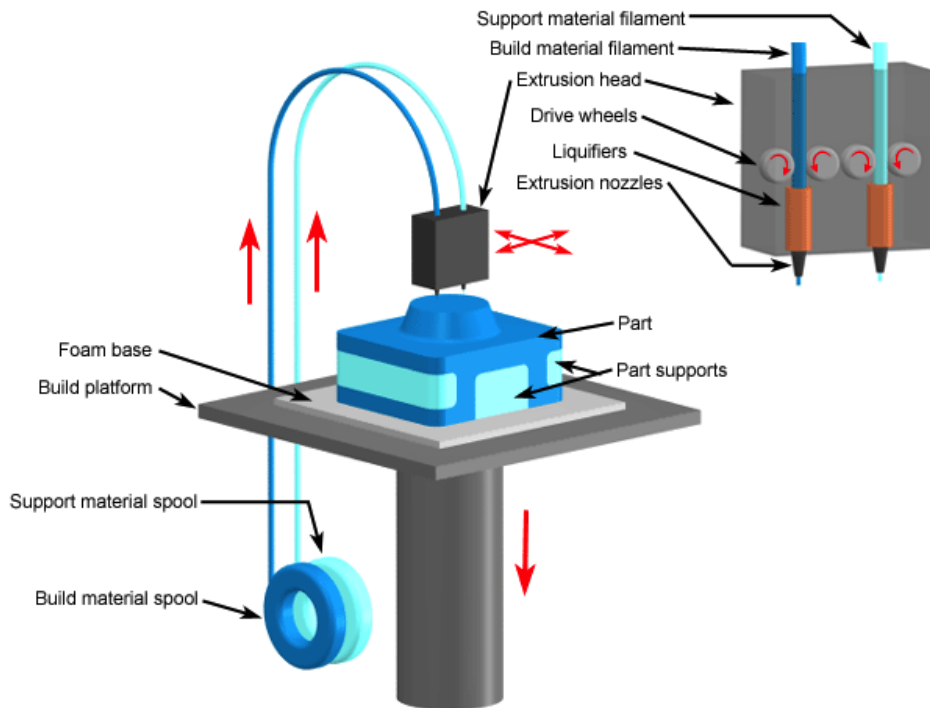


Figure 2.1: Illustration of FDM. [1] (Copyright © 2008 CustomPartNet)

various 3D printed fluidic devices [71]. Li *et al.* even took advantage of the extruded filament orientation to assist fluid mixing [72]. Furthermore, FDM is used to print hydrogels and other biocompatible structure [73], [74].

Despite numerous advantages, FDM suffers from several weaknesses, such as low resolution, [75] poor surface finish, and slow fabrication, among which the low resolution is most problematic. It is determined by the translation mechanism, physical geometry of the nozzle, and 3D printing material properties. The translation mechanism can be upgraded to obtain more precise positioning of the nozzle, but the other two factors are difficult to control. As a result, FDM is only capable of fabricating features that are at least hundreds of microns [60].

## 2.2 Polyjet (PJ)

PJ is very similar to the 2D inkjet printing, and it can be categorized into 2 categories, photopolymer-based or powder-based [29]. Here, I mainly discuss the former, because despite the fact that both of them share the problem of rough surface that would scatter light, making microscopy unable to perform, the latter forms an object by using a binding material to glue particles together, which leads to a weaker print than photopolymer.

In photopolymer-based PJ illustrated in Fig. 2.2, small droplets of UV curable resin are dispensed by an inkjet nozzle and cured on the fly as each layer is printed. Voids are defined by jetting a second, wax-like support material that must be removed after fabrication. PJ usually has a large print area, typically 30 cm  $\times$  30 cm, which allows a very large part to be built. It can also build multiple devices in one job, 20-1000 in 1-2 hours depending on device size [29]. Using PJ, printing with multiple material is easy to achieve. It has been reported that there are PJ 3D printers capable of printing 14 different materials simultaneously, including colors [29], [76], [77]. Unlike FDM, PJ mostly targets the high-end market, and normally cost 10 (even 50) times more, for which reason it provides the most commercially ready 3D printing solution for microfluidics. Therefore in as early as 2002, PJ became the first 3D printing technique utilized to attempt to fabricate “microfluidic” devices by making templates for soft lithography [78]. Later, Bonyár *et al.* had 1 mm  $\times$  2 mm trenches built directly on the 3D printed devices which are later sealed to form channels [79]. Sochol *et al.* demonstrated 3D printed millifluidic capacitors,

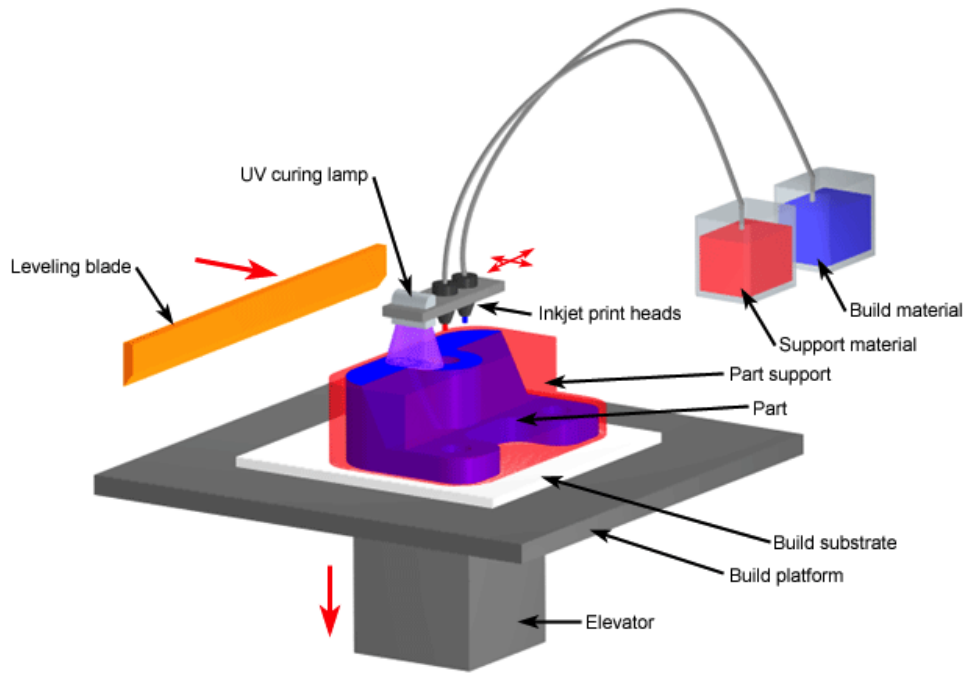


Figure 2.2: Illustration of PJ. [1] (Copyright © 2008 CustomPartNet)

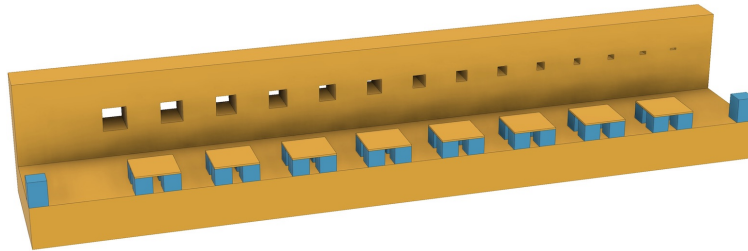


Figure 2.3: Test design for 3D printing service bureaus. The base is  $12\text{ mm} \times 4\text{ mm}$  and the height is  $3.8\text{ mm}$  at the back wall.

diodes, and transistors [44]. Fluidic components built with PJ were used to detect alpha-fetoprotein biomarker [51], and monitor drug transport with cells [52].

However, PJ still has not overcome the dimension barrier to enter truly microfluidic regime. To better describe the problem, in September 2015 we evaluated the minimum flow channel size that can be fabricated using PJ and SLA from four commercial 3D print service bureaus using state-of-the-art 3D printing tools. In every case the highest resolution resin and fabrication option were chosen ( $42\text{ }\mu\text{m}$  in x-y and  $16\text{ }\mu\text{m}$  in z for PJ and  $75\text{ }\mu\text{m}$  in x-y and  $25\text{ }\mu\text{m}$  in z for SLA).

Table 2.1: Microscope photographs of channels fabricated with commercial 3D printing service bureaus. PJ = Polyjet, SL-SLA = scanned laser stereolithography.

Channel size	3D Printing Service Bureaus				
	Invent-A-Part PJ \$33	Stratasys PJ \$75	Stratasys SL-SLA \$77	3D Systems SL-SLA \$66	Fineline SL-SLA \$186
700×700 $\mu\text{m}^2$					
650×650 $\mu\text{m}^2$					
600×600 $\mu\text{m}^2$					
550×550 $\mu\text{m}^2$					
500×500 $\mu\text{m}^2$					
450×450 $\mu\text{m}^2$					
400×400 $\mu\text{m}^2$					
350×350 $\mu\text{m}^2$					
300×300 $\mu\text{m}^2$					
250×250 $\mu\text{m}^2$					

The same test design was sent to each bureau (Fig. 2.3), which included a series of 1.08 mm long channels with varying cross sectional size. Channels were deliberately designed to be short to minimize problems with removal of uncured resin or support material so that void size limitations inherent to the fabrication processes could be unambiguously determined. Results are shown in Table 2.1, where PJ processes (Invent-A-Part and Stratasys) are far from successful.

## 2.3 Stereolithography (SLA)

In SLA a vector scanned laser (Fig. 2.4) or a stationary image pattern from a projector (Fig. 2.5) is used to photopolymerize an appropriate photosensitive resin layer-by-layer until a full device is completed.

Because scanned laser stereolithography (SL-SLA) is a linear process, the larger the print area, the longer it takes. Therefore, in most setups, such as Fig. 2.4, the laser remains immobile, and the laser beam rasters the region that needs to be polymerized by tuning the scanning mirror to achieve higher build speed. But lasers commonly generate a Gaussian beam, which makes the

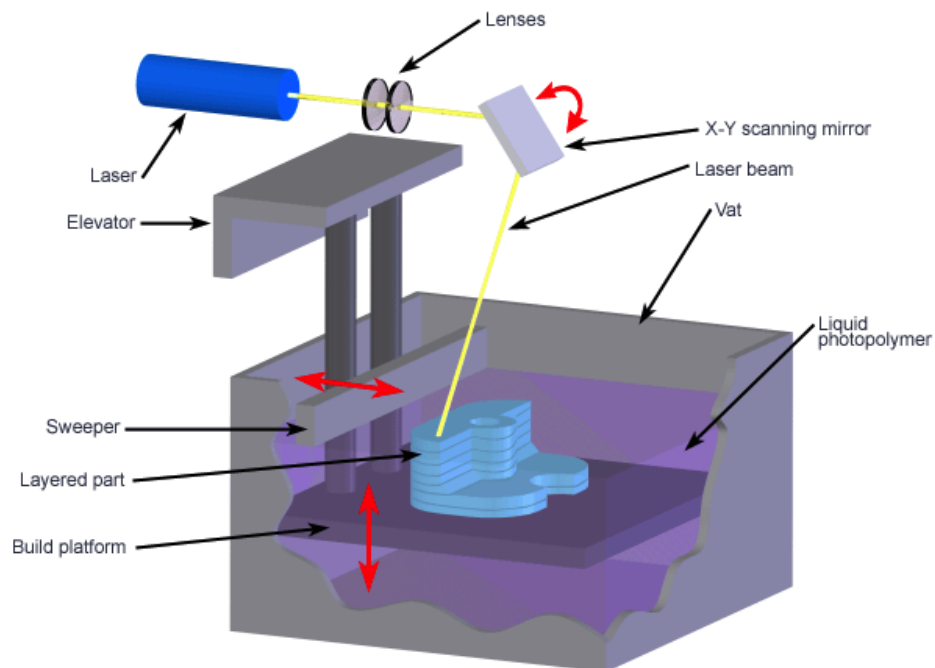


Figure 2.4: Illustration of SL-SLA. [1] (Copyright © 2008 CustomPartNet)



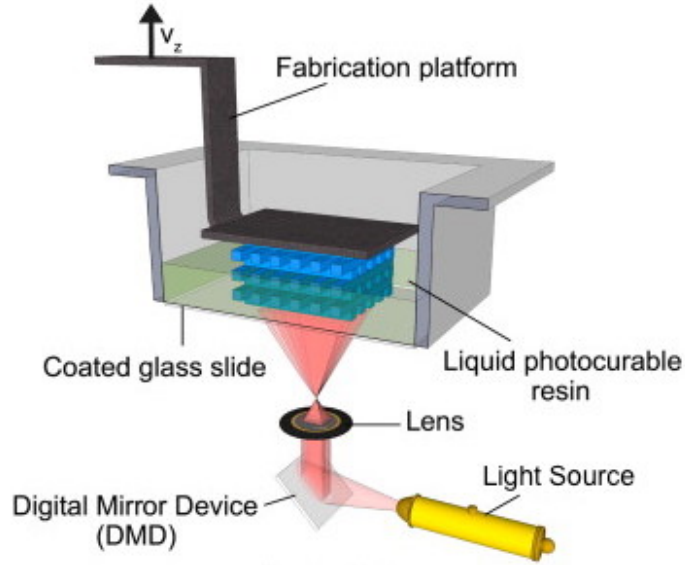


Figure 2.5: Illustration of DLP-SLA. Reproduced with permission [2].

spot size a function of working distance. Specifically, long working distance required to rapidly scan a large region would result in a large spot size, lowering the resolution. Since microfluidics is not the market pull on SL-SLA 3D printers, their resolution is compromised for speed. As we can see in Table 2.1, both 3D Systems and Fineline SL-SLA processes print channels down to  $350\ \mu\text{m} \times 350\ \mu\text{m}$ , which is approximately 5 and 14 times larger than the printer resolution specifications in width (x-y) and height (z), respectively. By far the sharpest, smoothest, and most optically clear part is the one from Fineline, which offers a  $500\ \mu\text{m} \times 500\ \mu\text{m}$  minimum interior dimension specification, but has pricing much higher than the rest. The bottom line is that at this time commercial 3D print service bureaus cannot generate truly microfluidic structures.

An alternate approach is based on SLA 3D printers with Digital Light Processing (DLP) micromirror arrays such as from Asiga, B9 Creations, Miicraft, or Full Spectrum Laser. With this method, each layer is exposed in one shot, so users do not need to make the trade-off between resolution and speed. Moreover, if the individual device size can be scaled down by both making them small and folding them in 3D, it opens the possibility of using 3D printing for scalable manufacturing as well as prototyping.

## **CHAPTER 3. OPTICAL APPROACH TO RESIN FORMULATION FOR 3D PRINTED MICROFLUIDICS**

Commercial resins tend to be formulated for general 3D printing applications rather than focused specifically on the needs of microfluidic devices, [3], [80] i.e., small voids. Hence the smallest flow channel cross sectional dimensions reported to date are  $250\text{ }\mu\text{m} \times 250\text{ }\mu\text{m}$ , [39]  $400\text{ }\mu\text{m} \times 400\text{ }\mu\text{m}$ , [40] and  $500\text{ }\mu\text{m} \times 500\text{ }\mu\text{m}$  [38]. In this chapter we focus on custom formulation of resins that enable much smaller flow channels to be realized. Specifically, I discuss our mathematical model for the total optical dose delivered as a function of depth through a 3D printed device, including void regions, and use it to guide the formulation of custom resins. I also discuss the guidelines we developed for minimum achievable flow channel size given a resin's optical properties, and demonstrate reliable fabrication of flow channels as small as  $60\text{ }\mu\text{m} \times 108\text{ }\mu\text{m}$ . This analysis indicates how to achieve even smaller dimensions. In addition, we apply our results to an open source and several commercial resins and find good agreement with our model's predictions. The work in this chapter is reported in Ref. 46.

### **3.1 Experimental**

#### **3.1.1 3D Printer**

We use an Asiga Pico Plus 27 3D printer to fabricate devices and test our resins. It has  $27\text{ }\mu\text{m}$  resolution in the X-Y plane and the Z-axis layer thickness can be set in  $1\text{ }\mu\text{m}$  increments (i.e.,  $9\text{ }\mu\text{m}$ ,  $10\text{ }\mu\text{m}$ ,  $11\text{ }\mu\text{m}$ , etc.). The optical engine appears to be based on a Texas Instruments (TI) DLP4500 module, which has a  $912 \times 1140$  micromirror array in a diamond pixel orientation. Each test part is rotated  $45^\circ$  on the build platform so that it aligns with the diamond orientation of the pixels (see Fig. 3.1). This ensures that flow channel widths can be sized as an integer number of pixels to unambiguously determine the minimum channel width that can be successfully fabricated.



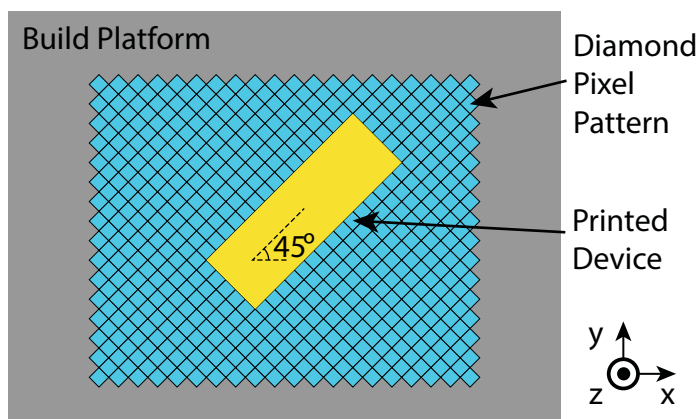


Figure 3.1: Schematic illustration of device orientation and imaged DLP pixels on 3D printer build platform.

### 3.1.2 Materials

Resins for DLP-SLA 3D printing generally consist of one or more monomer materials, a photoinitiator, and an absorber, where the latter is used to control the penetration depth of the incident light. For our resins, the monomer, photoinitiator, and absorber are, respectively, poly(ethylene glycol) diacrylate (PEGDA, MW 258), phenylbis (2,4,6-trimethylbenzoyl) phosphine oxide (Irgacure 819), and Sudan I. We have previously shown [81] that polymers formed from this molecular weight PEGDA result in a microfluidic material that is long-term stable in water. PEGDA and Sudan I were purchased from Sigma-Aldrich (St. Louis, MO), while Irgacure 819 was procured from BASF (Vandalia, Illinois). All materials were used as received. Resins were prepared by mixing 1% (w/w) Irgacure 819 in PEGDA along with a variable amount of Sudan I (0.05%, 0.1%, 0.15%, 0.2%, 0.4% or 0.6% w/w), and sonicating for 30 min. Resin containers were wrapped in aluminum foil to protect the resin from light.

For comparison, two commercial resins were acquired and tested: PlasClear (made by Asiga and sold by Proto Products, Fairview, TN) and FSL Clear (Full Spectrum Laser, Las Vegas, NV). We also mixed and tested an open source resin, PR48, from Autodesk's Ember 3D printing project [82]. For this resin, di(trimethylolpropane) tetraacrylate (DTPTA), trimethylolpropane ethoxylate triacrylate (TPET), 2-[(butylamino)carbonyl]oxyethyl acrylate (BACA), and 2,5-bis(5-tert-butyl-benzoxazol-2-yl)thiophene (TBT) were purchased from Sigma-Aldrich and ethyl (2,4,6-trimethylbenzoyl) phenylphosphinate (TPO), was purchased from Combi-Blocks (San

Table 3.1: Resin viscosities.

Resin	Viscosity (cP)	Reference
PEGDA	57	83
PlasClear	1262	82
FSL Clear	700	84
PR48	286	82

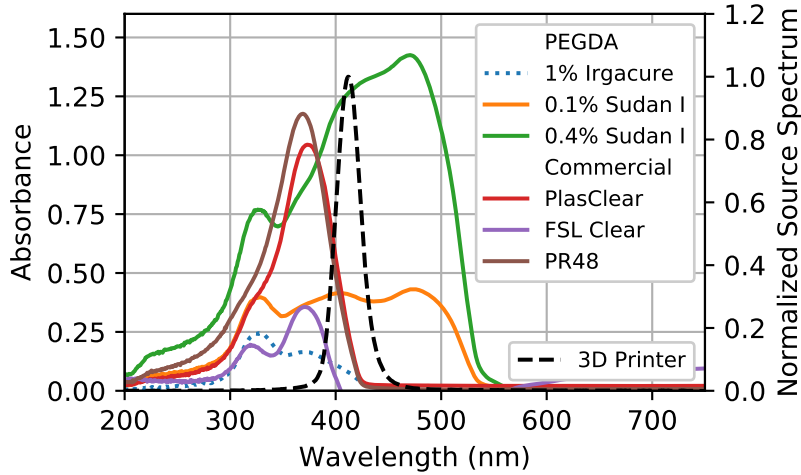


Figure 3.2: Measured resin absorbance compared with Asiga 3D printer LED emission spectrum for several commercial and custom PEGDA resins. The 1% Irgacure curve is the absorbance of PEGDA mixed with 1% (w/w) Irgacure 819 photoinitiator. The Sudan I resins contain both Sudan I and 1% (w/w) Irgacure 819.

Diego, CA). PR48 resin was prepared with 24g each of DTPTA and TPET and 12g of BACA along with 96mg (0.16% w/w) of the optical absorber, TBT, and 0.24g (0.4% w/w) of the photoinitiator, TPO. This mixture was sonicated in an amber glass container for at least 20 minutes to ensure thorough mixing, following which the container was wrapped in aluminum foil. Resin viscosities are given in Table 3.1.

### 3.1.3 Resin Optical Absorbance

Successful DLP-SLA 3D printing requires that the absorption spectrum of both the photoinitiator and absorber be matched with the emission spectrum of the 3D printer optical source. We used a QE65000 spectrometer from Ocean Optics (Dunedin, FL) to measure the absorbance of

each resin and the 3D printer optical source spectrum. Resin absorbance measurements were made with 80  $\mu\text{m}$  thick cells filled with liquid resin illuminated by attenuated light from an XCITE-120Q source (Lumen Dynamics, Ontario, Canada). The optical dose for each measurement was low enough that resin polymerization was not observed post-measurement.

Fig. 3.2 shows the emission spectrum of the 3D printer LED (dashed line). It has a peak at 412 nm and a FWHM of 25 nm. The figure also shows the absorbance of various resins. The dotted line is for PEGDA with 1% Irgacure 819 and no Sudan I, such that it is essentially the absorbance of Irgacure 819. Note that it has some overlap with the 3D printer source spectrum, which indicates that the LED light can activate the photoinitiator. The 0.1% and 0.4% Sudan I curves show the absorbance when different amounts of Sudan I are added to 1% Irgacure 819 in PEGDA. The Sudan I absorption dominates the resin absorbance in the wavelength range of the LED.

For the commercial resins, the PlasClear absorbance spectrum partially overlaps the 3D printer source spectrum. The PlasClear spectrum is likely dominated by the absorber in its resin formulation so it is not clear how much spectral overlap there is with its photoinitiator and the LED. The PR48 spectrum is very similar to the PlasClear spectrum, so it is likely that they use the same or closely related absorbers. The spectrum of the FSL Clear resin has the least overlap with the 3D printer source spectrum and would likely work better with a source that has a shorter wavelength.

### **3.1.4 Flow Channel Flushing**

Immediately after 3D printing, un-solidified resin must be flushed from flow channels in the fabricated part. The process we use is to first rinse the part with isopropyl alcohol (IPA), followed by a  $\sim 5$  min soak in IPA, and then blow dry with nitrogen. Care is taken to blow nitrogen through both sides of the flow channels.

## **3.2 Resin Optical Analysis**

In this section we develop a simple mathematical model for the optical dose delivered to a photopolymerizable resin during a single exposure to introduce the concepts, notation, and material

parameters that will be used in the more extensive model developed in Sect. 3.3. We discuss our experimental method to obtain material parameters for each of the resins introduced in Sect. 3.1 and our results.

### 3.2.1 Mathematical Model

As illustrated in Fig. 3.3, consider a photopolymerizable resin that occupies the half-space  $z \geq 0$  and has absorption coefficient  $\alpha$  with units of  $\mu\text{m}^{-1}$ . Assume light is incident from  $z < 0$  and propagates in the  $+z$  direction. Just inside the resin at  $z = 0$  the optical irradiance is  $I_0$ . The irradiance for  $z \geq 0$ ,  $I(z)$ , in units of  $\text{W}/\text{cm}^2$  is given by the well-known Beer's law [85] where we define the characteristic penetration depth as  $h_a = 1/\alpha$ :

$$\begin{aligned} I(z) &= I_0 e^{-\alpha z} \\ &= I_0 e^{-z/h_a}. \end{aligned} \tag{3.1}$$

The corresponding dose,  $D(z, t)$ , in units of  $\text{J}/\text{cm}^2$  for an exposure time of  $t$  is

$$\begin{aligned} D(z, t) &= tI(z) \\ &= tI_0 e^{-z/h_a}. \end{aligned} \tag{3.2}$$

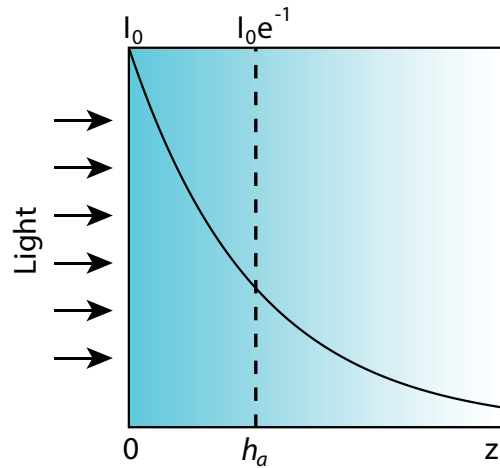


Figure 3.3: Schematic illustration of Beers Law and definition of  $h_a$ . See text for details.

For a photopolymerization process, we define the critical dose,  $D_c$ , as the dose at which polymerization of the resin has proceeded far enough to result in a solid or nearly solid material. Its particular value is specific to a given resin and the spectral properties of the optical source. We can express the critical dose at some distance  $z = z_p$  as

$$D_c = t_p I_0 e^{-z_p/h_a}, \quad (3.3)$$

where  $t_p$  is the time it takes to reach the critical dose at the depth  $z_p$ . Therefore  $z_p$  represents the polymerization depth for an exposure time of  $t_p$ . Note that in general  $t_p$  and  $z_p$  represent a family of paired values for which the above equation is true (i.e., picking the exposure time  $t_p$  sets the polymerization depth  $z_p$  and vice versa). We can define the critical time,  $T_c$ , as the time it takes to reach the critical dose for an optical irradiance of  $I_0$ , which can be expressed as

$$T_c = \frac{D_c}{I_0}. \quad (3.4)$$

Using this definition, we solve Eq. 3.3 for the polymerization depth,  $z_p$ , as

$$z_p = h_a \ln \frac{t_p}{T_c}, \quad (3.5)$$

or, in unitless parameters,  $\zeta = z/h_a$  and  $\tau = t/T_c$ ,

$$\zeta_p = \ln \tau_p. \quad (3.6)$$

The polymerization depth,  $z_p$ , is shown for a variety of  $h_a$  values in Fig. 3.4a. Note that when  $\tau_p = 1$ ,  $z_p = \zeta_p = 0$  regardless of  $h_a$ . In other words, when the exposure time is  $T_c$ , the resin at  $z = 0$  receives just enough dose to become solidified, but resin at  $z > 0$  does not. Moreover, when the resin is exposed for some  $\tau_p \geq 1$ , the resin at  $z = 0$  receives a dose that is  $\tau_p$  times larger than the critical dose,  $T_c$ . For example, if  $\tau_p = 5$ , then  $\zeta_p = \ln 5 = 1.6$  such that  $z_p = 1.6h_a$  and at  $z = 0$  the resin receives 5 times the critical dose.

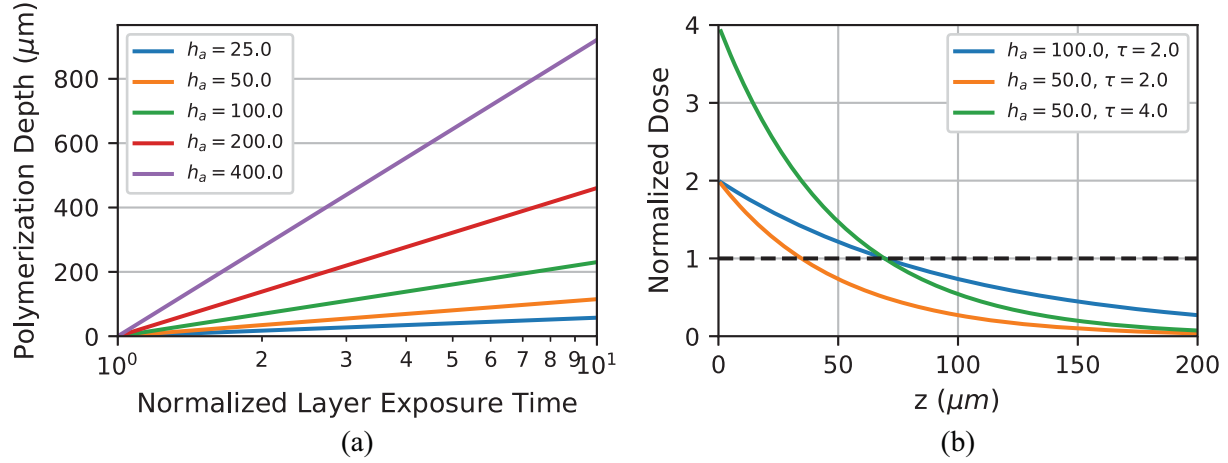


Figure 3.4: (a) Polymerization depth,  $z_p$ , of resins with different  $h_a$  as a function of the normalized layer exposure time,  $\tau_p$  (Eq. 3.5). (b) Normalized dose as a function of depth,  $z$ , for different values of  $h_a$  and the normalized exposure time,  $\tau$ .

From Eqs. 3.2 and 3.4 the normalized dose,  $\Omega(z, t)$ , can be expressed as

$$\Omega(z, t) = D(z, t)/D_c \quad (3.7)$$

$$= \frac{t}{T_c} e^{-z/h_a}, \quad (3.8)$$

or in unitless parameters

$$\Omega(\zeta, \tau) = \tau e^{-\zeta}. \quad (3.9)$$

When  $\Omega \gtrsim 1$ , the resin receives enough dose to be solidified. Again, when  $\zeta = 0$  the normalized dose is  $\tau$ .

In Fig. 3.4b we plot the normalized dose as a function of  $z$  for several values of  $h_a$  and  $\tau$ . For  $h_a = 100 \mu\text{m}$  and  $\tau = 2$ , the polymerization depth,  $z_p$ , (at which the normalized dose is 1) is  $68 \mu\text{m}$ . For  $h_a = 50 \mu\text{m}$  the normalized exposure time must be twice as long to obtain the same polymerization depth, and the corresponding dose at  $z = 0$  is of course twice as large. The obvious point is that a longer exposure time is required to reach a given polymerization depth as  $h_a$  is reduced, and the inhomogeneity of the dose in the polymerized layer is increased. On the other hand, while larger  $h_a$  values need shorter exposure times, the material beyond the polymerization depth receives a larger dose than for smaller values of  $h_a$ , even with the shorter exposure times.

This fundamental tradeoff has significant consequences for minimizing flow channel height in a 3D printed microfluidic device, which we explore in Sect. 3.3.

### 3.2.2 Measurement of $h_a$ and $T_c$

According to our model, the optical properties of a particular resin are determined by  $h_a$  and  $T_c$ . Fortunately, these are straightforward to obtain experimentally by simply measuring the thickness of a polymerized layer as a function of exposure time and fitting the results to Eq. 3.5. The device design we use to determine  $h_a$  and  $T_c$  is shown in Fig. 3.5a. There are 6 single layer membranes along the forward edge of the device, each supported by 4 pillars. A typical 3D printed device is shown in Fig. 3.5b, and a membrane in Fig. 3.6. As expected, the membrane is thicker than the build layers visible in the adjacent posts since the layer exposure time must be as long or longer than the time it takes the polymerization front to reach the previously built layer (so that the new layer attaches to the previous layer).

For each resin, a series of samples are 3D printed with different layer exposure times, and the thicknesses of the 6 membranes on each sample are measured and averaged. The average membrane thicknesses and associated curve fits are shown in Fig. 3.7a as a function of layer exposure time. Values of  $h_a$  and  $T_c$  are given in Table 3.2. Note that  $h_a$  is the slope of the fitted line whereas  $T_c$  is the line's intercept with the x-axis.

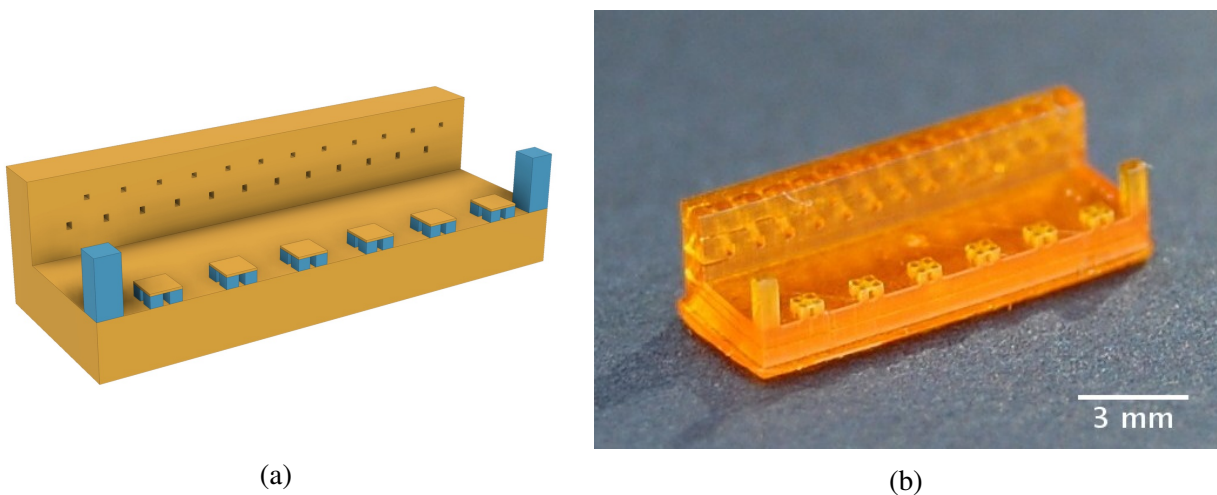


Figure 3.5: (a) CAD design and (b) photo of 3D printed sample for determining  $h_a$  and  $T_c$ .

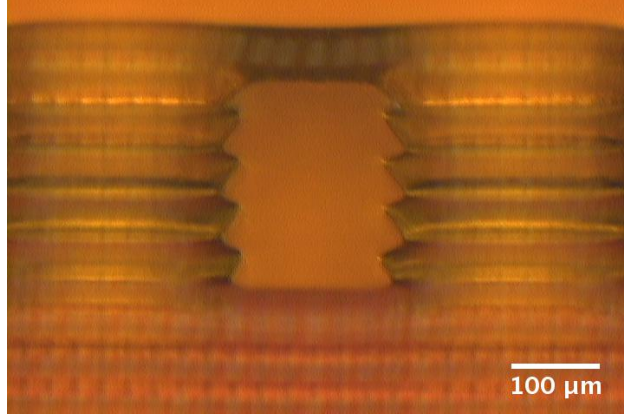


Figure 3.6: Microscope photograph of membrane for 0.2% Sudan I resin with 2 s layer exposure time and 50  $\mu\text{m}$  build layer thickness. The posts on which the membrane layer is fabricated are 5 layers tall.

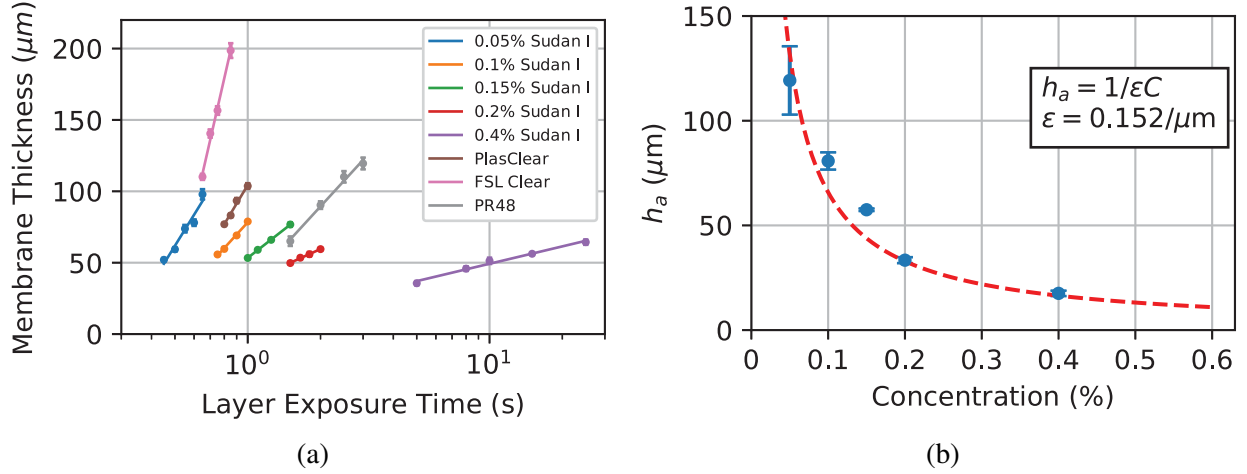


Figure 3.7: (a) Measured membrane thicknesses for different resins along with curve fits of Eq. 3.5. Corresponding values of  $h_a$  and  $T_c$  are in Table 3.2. Error bars are present for individual measurements but are generally too small to see. (b)  $h_a$  of Sudan I resins as a function of Sudan I concentration.

FSL Clear has by far the largest  $h_a$ , which is due to the small overlap of its absorbance spectrum with the 3D printer source spectrum (Fig. 3.2). The  $h_a$  for PlasClear and 0.05% Sudan I are comparable, as is  $h_a$  for PR48 and 0.1% Sudan I. Increasing the Sudan I concentration decreases the penetration depth,  $h_a$ . The functional relationship between the two is given by

$$h_a = \frac{1}{\epsilon C}, \quad (3.10)$$



Table 3.2:  $h_a$  and  $T_c$  from membrane measurements.

Resin	$h_a$ ( $\mu\text{m}$ )	$T_c$ (sec)
0.05% Sudan I	119.2	0.298
0.1% Sudan I	80.8	0.379
0.15% Sudan I	57.5	0.395
0.2% Sudan I	33.4	0.336
0.4% Sudan I	17.5	0.604
PlasClear	123.0	0.428
FSL Clear	322.1	0.459
PR48	80.2	0.656

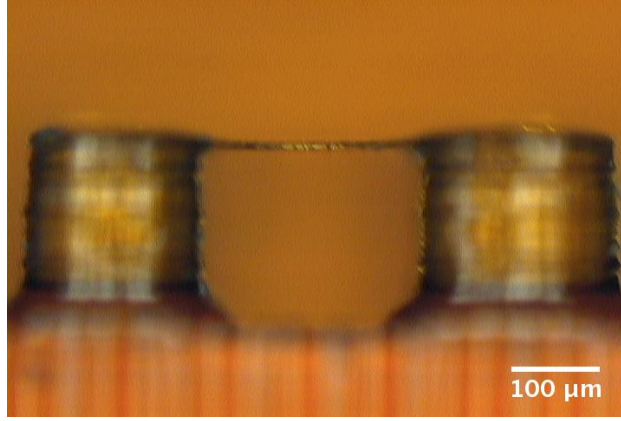


Figure 3.8: Microscope photograph of membrane of 0.2% Sudan I resin with 0.45 s exposure time and 10  $\mu\text{m}$  build layer thickness. The measured membrane thickness is 10  $\mu\text{m}$ .

where  $\varepsilon$  is absorptivity and  $C$  is concentration since, according to Beer's law,  $\alpha = \varepsilon C$ . Fig. 3.7b shows  $h_a$  as a function of Sudan I concentration along with a fit to Eq. 3.10.

Knowledge of  $h_a$  and  $T_c$  for a particular resin allows one to use the mathematical model to calculate a reasonable starting point for exposure parameters to create a specific structure. For example, to fabricate a 10  $\mu\text{m}$  thick membrane using 0.2% Sudan I resin the model predicts a 0.45 s exposure time. The fabricated result is shown in Fig. 3.8 in which the membrane thickness is indeed 10  $\mu\text{m}$ .

### 3.3 Resin Optical Properties and Flow Channel Formation

Consider the layer-by-layer fabrication of a simple 3D printed microfluidic device with a single flow channel as schematically illustrated in Fig. 3.9. In A-C the part is shown being built upside down with light incident from the bottom through a window in the resin tray to expose each layer. The final part is shown right side up in Fig. 3.9d. The interfaces between build layers are indicated by dashed lines, and the layer indices are shown to the left in each drawing. Note in Fig. 3.9b that when Layer 5 is formed, the flow channel region of the layer is unexposed, leaving the resin in that region in a liquid state. Likewise, exposure of Layer 6 leaves the same region unexposed. Exposure of Layer 7 creates the top of the flow channel, and also traps liquid resin in the flow channel (which must be flushed after fabrication). In general, the trapped resin receives some optical dose during Layer 7's exposure because Layer 7 does not absorb all of the incident light. Similarly, the trapped resin receives further optical doses as subsequent layers are exposed. If the sum of these doses is  $\gtrsim D_c$ , the trapped resin can solidify and block the channel. A flow channel must therefore be tall enough to avoid this situation, which sets the optical constraint for the minimum flow channel height that can be fabricated for a given resin.

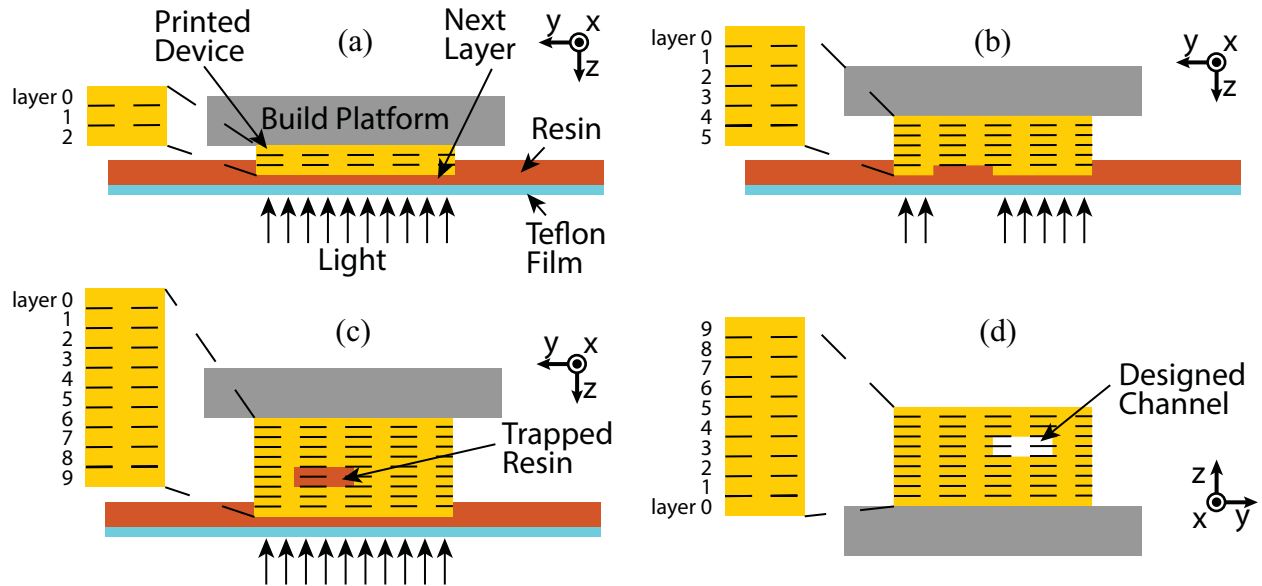


Figure 3.9: Layer-by-layer fabrication process for a simplified device. The device is rotated 180 degrees in (d) relative to (a-c). See text for details.

In this section we develop a mathematical model to determine the total optical dose delivered within each layer. We use the model to examine the dose when fabricating a flow channel, and analyze the effects of  $h_a$  and changing the build layer thickness.

### 3.3.1 Mathematical Model - Multiple Exposures

Let  $z = 0$  be the plane that defines the bottom of the device being printed (see Fig. 3.9d). Let  $z_l$  be the build layer thickness and  $I_n(z)$  the irradiance during exposure of layer  $n$ . We can write  $I_n(z)$  as

$$I_n(z) = I_0 e^{-[(n+1)z_l - z]/h_a}, \quad (3.11)$$

where  $(n+1)z_l$  is the position of the top of the  $n^{th}$  layer, and  $n \in [0, N-1]$  with  $N$  being the total number of layers in the device. The corresponding dose,  $D_n(z, t)$ , for a layer exposure time of  $t_l$  (assumed to be the same for all layers) is

$$\begin{aligned} D_n(z, t_l) &= t_l I_n(z) \\ &= t_l I_0 e^{-[(n+1)z_l - z]/h_a}. \end{aligned} \quad (3.12)$$

The normalized dose is

$$\begin{aligned} \Omega_n(z, t_l) &= \frac{t_l}{T_c} e^{-[(n+1)z_l - z]/h_a} \\ &= \tau_l e^{-[(n+1) - z/z_l]\zeta_l}, \end{aligned} \quad (3.13)$$

where  $\zeta_l$  is the normalized layer thickness,  $z_l/h_a$ . If we define  $\gamma = z/z_l$  (i.e., normalize  $z$  by the layer thickness) we can rewrite the normalized dose in layer  $n$  as

$$\Omega_n(\gamma, \tau_l) = \tau_l e^{-[(n+1) - \gamma]\zeta_l}. \quad (3.14)$$

Note that this is only valid for

$$\begin{aligned}(n+1) - \gamma &\geq 0 \\ \Rightarrow \gamma &\leq n+1\end{aligned}\tag{3.15}$$

(i.e.,  $z \leq$  top of current build layer), so we write the normalized dose for layer  $n$  as

$$\Omega_n(\gamma, \tau_l) = \begin{cases} \tau_l e^{-[(n+1)-\gamma]\zeta_l}, & \text{if } \gamma \leq n+1. \\ 0, & \text{otherwise.} \end{cases}\tag{3.16}$$

The dose for layer  $n$  only affects layer  $n$  and earlier layers, but not subsequent (as-yet unbuilt) layers.

Note that the normalized dose for a given layer at the back ( $\gamma = n$ ) and front ( $\gamma = n+1$ ) of a layer are

$$\Omega_{back} = \tau_l e^{-\zeta_l}\tag{3.17}$$

$$\begin{aligned}\Omega_{front} &= \tau_l \\ &= \Omega_{back} e^{\zeta_l},\end{aligned}\tag{3.18}$$

respectively. To have a successful 3D print, the entire layer must be polymerized, i.e.,  $\Omega_{back} \geq 1$ . The minimal requirement is

$$\Omega_{back} = 1,\tag{3.19}$$

in which case the normalized dose at the front of the layer is

$$\Omega_{front} = e^{\zeta_l}.\tag{3.20}$$

The total dose throughout the thickness of the 3D printed part,  $\Omega$ , is just the sum of the individual layer doses,

$$\Omega(\gamma, \tau_l) = \sum_{n=0}^{N-1} \Omega_n(\gamma, \tau_l),\tag{3.21}$$

where  $\Omega_n(\gamma, \tau_l)$  is given by Eq. 3.16.

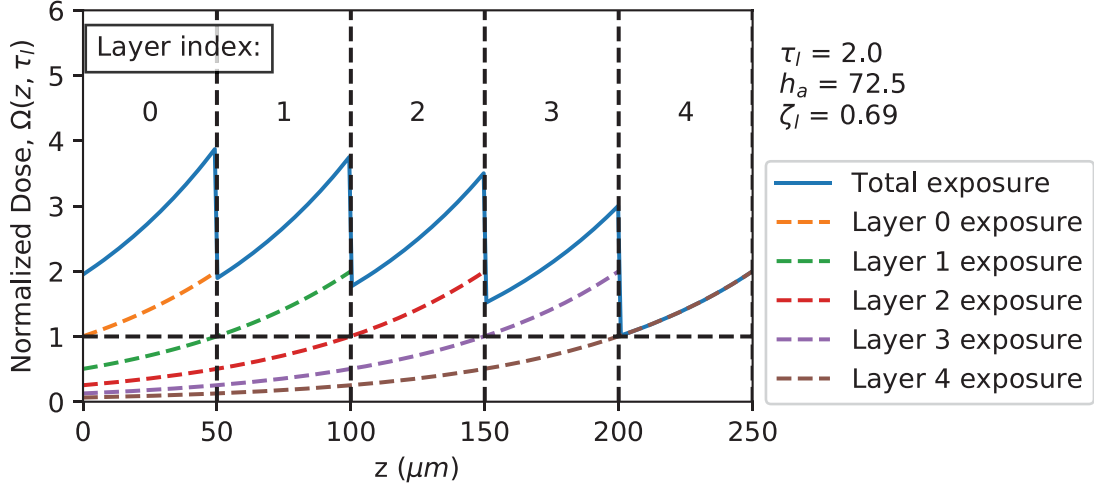


Figure 3.10: Normalized dose as a function of depth,  $z$ , for five 3D printed layers. Each layer receives a single exposure. Solid line indicates total dose. See text for details.

To illustrate the main features of Eq. 3.21, consider the 5-layer case shown in Fig. 3.10 in which  $\zeta_l = 0.69$  and the normalized layer exposure time,  $\tau_l$ , is 2.0 such that  $\Omega_{back} = 1.0$  (which satisfies the condition in Eq. 3.19) and  $\Omega_{front} = \tau_l = 2.0$ . Note that the total dose in Layers 0-3 is affected by the exposure of subsequent layers. For example, the normalized dose at the back ( $z = 0 \mu\text{m}$ ) and front ( $z = 50 \mu\text{m}$ ) of Layer 0 is 2.0 and 3.9, respectively, while the dose at the back ( $z = 200 \mu\text{m}$ ) and front ( $z = 250 \mu\text{m}$ ) of the last layer (Layer 4) is 1.0 and 2.0 since it receives only one exposure. Also note that in each of the layers there is significant dose inhomogeneity, which will likely affect the internal stress of an actual 3D printed part.

### 3.3.2 Total Dose with an Embedded Channel

The total normalized dose in Eq. 3.21 is a function of depth,  $\gamma$ , in the 3D printed part. So far we have assumed that every layer receives an exposure. However, when a flow channel is formed, there is no exposure in the region of each layer in which the flow channel is situated. We can account for this by defining a parameter for each layer,  $n$ ,

$$\delta_n = \begin{cases} 0, & \text{if } n \text{ is in a flow channel} \\ 1, & \text{otherwise,} \end{cases} \quad (3.22)$$

such that the total normalized dose,  $\Omega$ , becomes

$$\Omega(\gamma, \tau_l) = \sum_{n=0}^{N-1} \delta_n \Omega_n. \quad (3.23)$$

We can now substitute Eq. 3.16 for  $\Omega_n$  by recognizing that for a layer with index  $m$ , exposures of layers with index  $< m$  have no effect. This is equivalent to starting the sum at

$$m = \text{floor}(\gamma) = \lfloor \gamma \rfloor, \quad (3.24)$$

which is the largest integer value less than or equal to  $\gamma$ . The total normalized dose can therefore be written as

$$\begin{aligned} \Omega(\gamma, \tau_l) &= \sum_{n=\lfloor \gamma \rfloor}^{N-1} \delta_n \tau_l e^{-[(n+1)-\gamma]\zeta_l} \\ &= \tau_l e^{-\zeta_l} \sum_{n=\lfloor \gamma \rfloor}^{N-1} \delta_n e^{-(n-\gamma)\zeta_l} \\ &= \Omega_{back} \sum_{n=\lfloor \gamma \rfloor}^{N-1} \delta_n e^{-(n-\gamma)\zeta_l}. \end{aligned} \quad (3.25)$$

Equivalently, we can change the summation index to  $n' = n - \lfloor \gamma \rfloor$ , such that

$$\begin{aligned} \Omega(\gamma, \tau_l) &= \Omega_{back} \sum_{n'=0}^{(N-\lfloor \gamma \rfloor)-1} \delta_{(n'+\lfloor \gamma \rfloor)} e^{-(n'+\lfloor \gamma \rfloor-\gamma)\zeta_l} \\ &= \Omega_{back} e^{(\gamma-\lfloor \gamma \rfloor)\zeta_l} \sum_{n'=0}^{(N-\lfloor \gamma \rfloor)-1} \delta_{(n'+\lfloor \gamma \rfloor)} e^{-n'\zeta_l} \\ &= \Omega_l(\gamma - \lfloor \gamma \rfloor) \chi_{\lfloor \gamma \rfloor} \\ &= \Omega_l(\gamma') \chi_{\lfloor \gamma \rfloor} \end{aligned} \quad (3.26)$$

with

$$\gamma' = \gamma - \lfloor \gamma \rfloor, \quad (3.27)$$

$$\Omega_l(\gamma') = \Omega_l(\gamma - \lfloor \gamma \rfloor) = \Omega_{back} e^{(\gamma - \lfloor \gamma \rfloor) \zeta_l}, \quad (3.28)$$

$$\chi_{\lfloor \gamma \rfloor} = \sum_{n'=0}^{(N-\lfloor \gamma \rfloor)-1} \delta_{(n'+\lfloor \gamma \rfloor)} e^{-n' \zeta_l}. \quad (3.29)$$

Note that  $\gamma'$  is in the range  $[0,1)$  and is the normalized depth within a layer, with 0 being the back of a layer and 1 the front of a layer. This coordinate is the same for every layer.  $\Omega_l(\gamma')$  is the normalized dose as a function of depth in a layer for a single exposure of that layer, and is in the range  $[\Omega_{back}, \Omega_{front})$ . It is also the same for every layer.  $\chi_{\lfloor \gamma \rfloor}$  is the contribution to the dose of the layer with index  $\lfloor \gamma \rfloor$  from the current and all subsequent layer exposures. Note that  $\chi_{\lfloor \gamma \rfloor}$  is governed by  $\delta_n$  since  $\delta_n$  specifies which layers are actually exposed.

To illustrate the implications of Eq. 3.26 for flow channel fabrication, consider a 3D printed device that has 12 layers and  $\zeta_l = 0.69$ . We assume that all layers are exposed except Layers 5 and 6, which represent a flow channel. The exposure time is the same as for Fig. 3.10. The total normalized dose for the structure is shown in Fig. 3.11. The normalized dose in the first 5 layers is similar to what we observe in Fig. 3.10 (the differences are due to the additional dose from

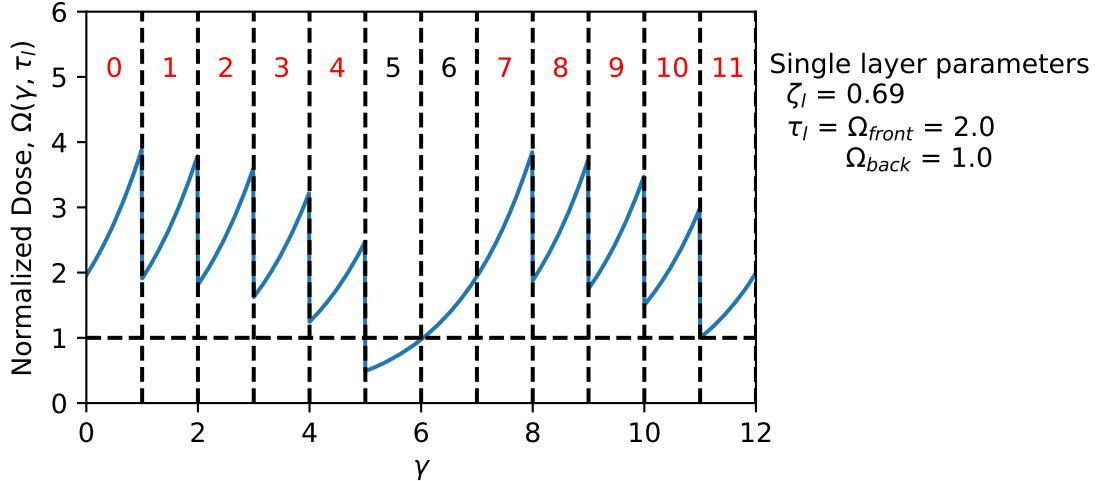


Figure 3.11: Normalized dose as a function of normalized depth,  $\gamma$ , for a 12-layer case with a flow channel in Layers 5 and 6 (red and black layer index numbers along the top indicate exposure or no exposure in that layer, respectively).

subsequent layer exposures). The normalized dose in the last 5 layers is identical to Fig. 3.10. The resin in the unexposed Layers 5 and 6 receives some dose from the exposures of the overlying Layers 6-11. The dose is high enough to polymerize the resin in Layer 6, and even in Layer 5 the normalized dose is a significant fraction of 1. According to the discussion of Fig. 3.4b, an obvious way to avoid this situation is to increase the absorbance of the resin, i.e., make  $h_a$  smaller, which increases  $\zeta_l$  and the layer exposure time,  $\tau_l$ . Once  $h_a$  is set, however, successful fabrication of flow channels requires that the flow channel height is large enough that exposure of the overlying layers does not overly polymerize resin in the flow channel region.

### 3.3.3 Effect of Build Layer Thickness

For a given resin which has a particular value for  $h_a$ , changing the build layer thickness,  $z_l$ , changes  $\zeta_l$ . Larger  $\zeta_l$  results in less light getting through the current build layer to further expose underlying layers. However, a larger  $\zeta_l$  has some negative consequences as illustrated below.

As an example, consider a 200  $\mu\text{m}$  tall flow channel in 0.2% Sudan I ( $h_a = 33.4 \mu\text{m}$ ) with build layer thicknesses of 10, 25, and 50  $\mu\text{m}$ . The corresponding number of build layers spanned by the flow channel is 20, 8, and 4, respectively. In all cases we set  $\Omega_{back} = 1$ . As shown in Fig. 3.12, the 50  $\mu\text{m}$  build layer case ( $\zeta_l = 1.5$ ) has minimal penetration of the critical dose

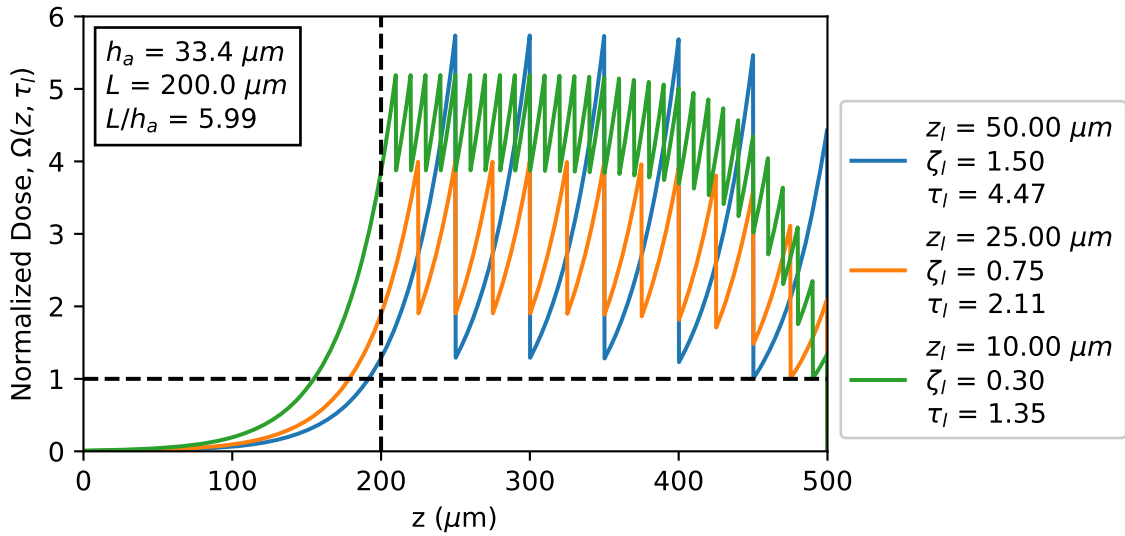


Figure 3.12: Effect of layer thickness on total normalized dose. The first 200  $\mu\text{m}$  represents a flow channel such that layers in this region are not exposed.



( $\Omega = 1$ ) into the flow channel region. However, the variation of dose within individual layers is large ( $> 400\%$ ), which can result in significant internal stress. Moreover, the front of each layer is so exposed ( $\Omega_{front} = 4.47$ ) that there are not as many available sites for polymer in the next layer to crosslink with, which reduces layer-to-layer adhesion. When the build layer thickness is decreased to  $25\text{ }\mu\text{m}$  ( $\zeta_l = 0.75$ ), the dose variation within individual layers is reduced to  $\sim 100\%$  at the cost of a little more penetration into the flow channel. A build layer thickness of  $10\text{ }\mu\text{m}$  ( $\zeta_l = 0.3$ ) results in greater penetration of the polymerization front into the flow channel ( $\sim 50\text{ }\mu\text{m}$ ) but with only  $\sim 25\%$  dose variation within each exposed layer. Moreover, the average dose in each layer is nearly twice as large as for the  $25$  and  $50\text{ }\mu\text{m}$  build layer cases, which results in a greater degree of crosslinking and likely greater internal strength.

As illustrated by this example, there is a trade-off between dose inhomogeneity within individual build layers and penetration of the polymerization front into the flow channel region. In the next section we experimentally evaluate different layer thicknesses with resins having a variety of  $h_a$  values to determine practical limits to flow channel miniaturization.

### 3.4 Experimental Results and Discussion

To evaluate the practical limits of flow channel size as a function of  $h_a$  and build layer thickness, we fabricate a series of channels through the  $1.08\text{ mm}$  thick rectangular block that comprises the back of the device in Fig. 3.5a. The length of the channels is deliberately kept short to minimize the effect of flushing un-solidified resin from the channels after fabrication. Any difficulty in flushing this resin would obscure limitations to flow channel size imposed by the optical properties of the resin, which is the focus of this chapter.

We first consider fabrication of flow channels for the  $200\text{ }\mu\text{m}$  high channel modeled in Fig. 3.12 in  $0.2\%$  Sudan I PEGDA resin. The results are shown in the microscope photos of Fig. 3.13. For the  $50\text{ }\mu\text{m}$  build layer case, the vertical edges of the flow channel are serrated with the top of each layer jutting into the channel more than the bottom. This is due to the top of a layer receiving a much larger dose than the back of the layer such that polymerization does not extend all the way to the back of the layer at the edge. Moreover, somewhat counter-intuitively, channels built with this layer thickness are sometimes clogged. The  $25\text{ }\mu\text{m}$  build layer case in Fig. 3.13b

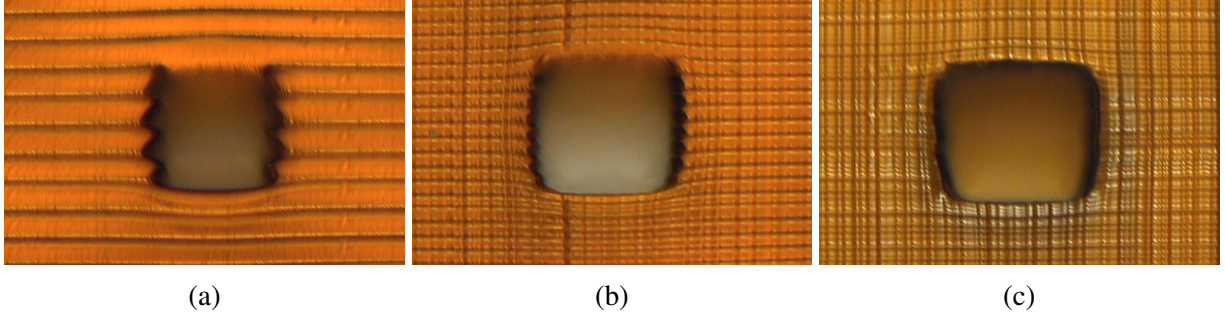


Figure 3.13: Flow channels 200  $\mu\text{m}$  high by 5 pixels (135  $\mu\text{m}$ ) wide with 0.2% Sudan I resin for build layer thicknesses of (a) 50  $\mu\text{m}$ , (b) 25  $\mu\text{m}$ , and (c) 10  $\mu\text{m}$ . Layer exposure times,  $t_l$ , are 1.5 s, 0.71 s, and 0.45 s, respectively.

shows much less edge serration and no channels showed signs of clogging. Likewise, 10  $\mu\text{m}$  build layers (Fig. 3.13c) improve the sidewall smoothness still further and all channels are open.

The top of each flow channel is the back surface of an exposed layer. In Fig. 3.13a and 3.13b these surfaces are visibly rough, whereas in Fig. 3.13c it is much smoother. Evidently, smaller  $\zeta_l$  results in smoother surfaces over the top of voids. In addition, in Fig. 3.13b and more so in Fig. 3.13c there are vertical lines on the face of the 3D printed surface. These are due to wear of the teflon film on the bottom of the resin tray that is induced by the 3D printer's slider. This wear is a major reason for periodically needing to use a fresh tray. Finally, in each photo the horizontal build layers above and below each channel are visibly bowed, as are the vertical channel boundaries. This bowing is due to stress in the 3D printed part being relieved as the channel terminates at the part's exterior surface.

Table 3.3 shows similar microscope photos for flow channels with 5 pixel (135  $\mu\text{m}$ ) widths and channel heights of 100, 150, 200, and 250  $\mu\text{m}$  and 10, 25, and 50  $\mu\text{m}$  build layers for PEGDA resins with Sudan I concentrations of 0.1%, 0.15%, 0.2%, and 0.4%. Multiple 3D printed parts were made, each with multiple flow channel sizes. The number of both unclogged and total attempted fabricated channels for each combination of geometry and resin are shown on the photos to give an informal measure of yield for each channel size. The exposure parameters and normalized layer thicknesses are given in Table 3.4. In each case the layer exposure time is initially set such that the calculated  $\Omega_{\text{back}}$  is 1, and then adjusted as needed until parts are successfully printed. In several cases larger channel heights were made, but the results are not included in Table 3.3.

Table 3.3: Results for different channel heights and layer thicknesses for PEGDA resins with varying concentrations of Sudan I. See text for details.

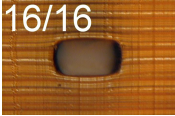
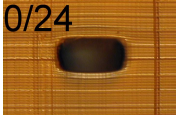
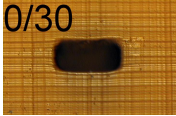
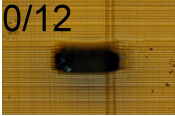


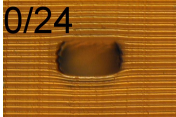
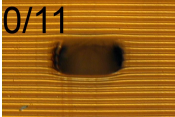
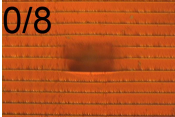
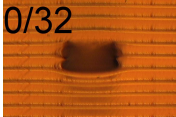
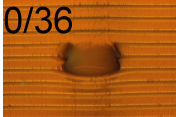
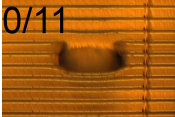
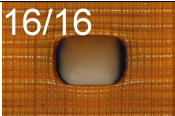
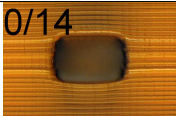
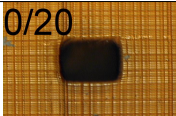
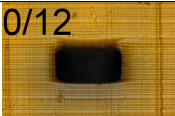
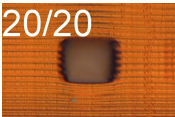
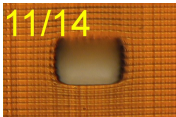
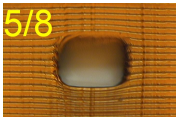
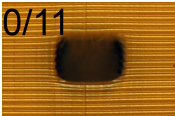
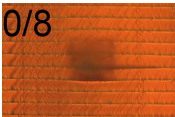
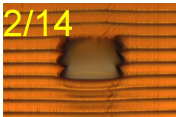
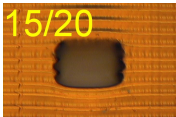
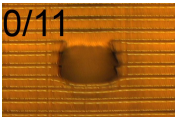
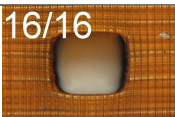

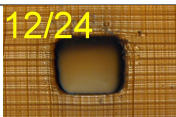
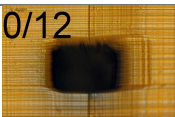



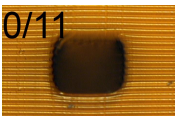


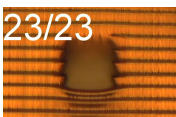
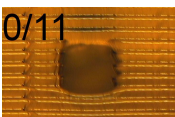


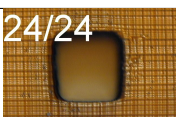
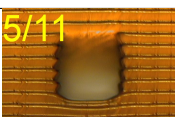
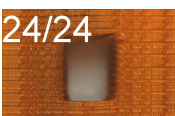

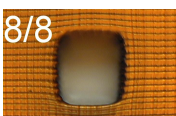
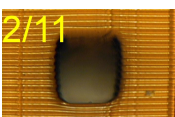
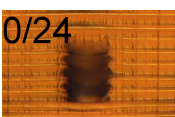

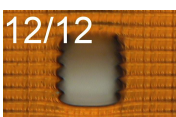
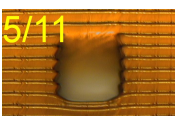
Channel	Layer	Sudan I concentration			
		0.4%	0.2%	0.15%	0.1%
100 $\mu$ m	10 $\mu$ m	16/16 	0/24 	0/30 	0/12 
	25 $\mu$ m	17/17 	0/14 	0/24 	0/11 
	50 $\mu$ m	0/8 	0/32 	0/36 	0/11 
150 $\mu$ m	10 $\mu$ m	16/16 	0/14 	0/20 	0/12 
	25 $\mu$ m	20/20 	11/14 	5/8 	0/11 
	50 $\mu$ m	0/8 	2/14 	15/20 	0/11 
200 $\mu$ m	10 $\mu$ m	16/16 	14/14 	12/24 	0/12 
	25 $\mu$ m	17/17 	14/14 	14/14 	0/11 
	50 $\mu$ m	0/8 	10/14 	23/23 	0/11 
250 $\mu$ m	10 $\mu$ m	24/24 	24/24 	24/24 	5/11 
	25 $\mu$ m	24/24 	24/24 	8/8 	2/11 
	50 $\mu$ m	0/24 	24/24 	12/12 	5/11 

Table 3.4: Normalized layer thicknesses,  $\zeta_l$ , and exposure times,  $t_l$ , for the results in Table 3.3.

	Sudan I concentration											
	0.4%			0.2%			0.15%			0.1%		
	10	25	50	10	25	50	10	25	50	10	25	50
$z_l$ ( $\mu\text{m}$ )	10	25	50	10	25	50	10	25	50	10	25	50
$\zeta_l$	0.57	1.42	2.85	0.30	0.75	1.50	0.17	0.43	0.87	0.08	0.31	0.62
$t_l$ (s)	0.8	2	8.5	0.45	0.71	1.5	0.47	0.61	1		0.52	0.75

The minimum flow channel heights,  $H_{\min}$ , fabricated with 100% yield for the resins are 100, 200, 200, and 300  $\mu\text{m}$ , respectively, for the cases shown in Table 3.3.

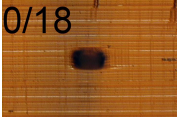
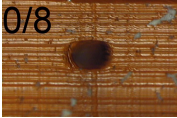
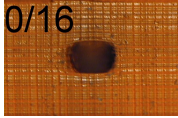
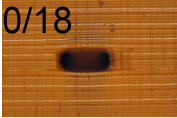
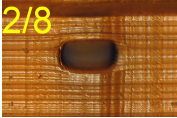

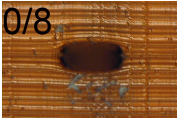
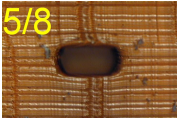
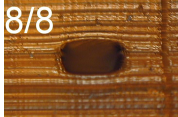
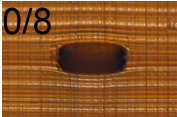
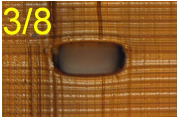
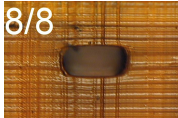
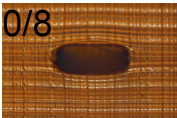
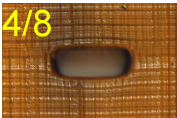

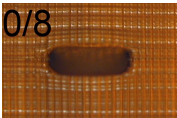
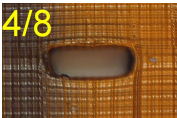
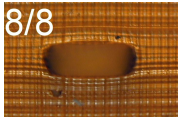
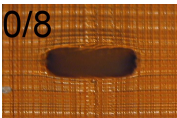
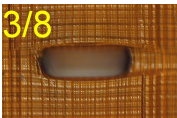

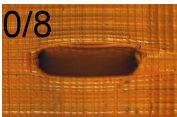
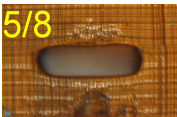
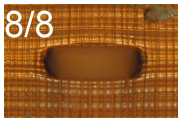
From Table 3.3, the resin with the smallest  $h_a$  clearly leads to the smallest channel height. To explore this further for 0.4% Sudan I resin, consider Table 3.5, which shows fabricated channels as a function of channel height and width. Channel width is given in pixels (i.e., number of micromirrors in the DLP micromirror array). A pixel in the plane of the build layer is 27  $\mu\text{m}$  square. Unsurprisingly, a width of 2 pixels never results in open flow channels, whereas a 3 pixel width is sometimes successful. We expect this is due to the fidelity of the image formed in the build plane by the projection optics. The minimum pixel width to guarantee 100% yield is 4 pixels (108  $\mu\text{m}$ ). We find this to be true for all Sudan I PEGDA resins that were tested except those with larger  $h_a$ , in which case a width of 5 pixels is needed. From Table 3.5 the minimum flow channel height for 100% yield for 0.4% Sudan I is 90  $\mu\text{m}$ .

To decrease the flow channel height still further we created a 0.6% Sudan I PEGDA resin. Since the absorption is very high we found it problematic to accurately measure  $h_a$  using the method described in Sect. 3.2.2. Instead, we used the curve fit in Fig. 3.7b to estimate  $h_a$  as 11  $\mu\text{m}$ . Results are shown in Table 3.6. As with 0.4% resin, the minimum channel width is 4 pixels. For 100% yield the minimum channel height is 60  $\mu\text{m}$ . The corresponding cross sectional area is 20 times smaller than the results for commercial 3D printing service bureaus.

From the trends observed in our flow channel results, there is a clear path to fabricate even smaller flow channels. To reduce flow channel height, the resin absorbance must be increased to obtain smaller  $h_a$ . The build layer thickness also needs to be reduced accordingly. To decrease the channel width, the x-y pixel size must be smaller so that a 4 pixel feature is commensurately reduced in size while maintaining high image fidelity. This means the DLP micromirror array



Table 3.5: Channels in 0.4% Sudan I resin as a function of width and height for  $t_l = 0.8$  s and  $z_l = 10$   $\mu\text{m}$  ( $\zeta_l = 0.57$ ).

Width	Channel height		
	70 $\mu\text{m}$	80 $\mu\text{m}$	90 $\mu\text{m}$
2 pixels	0/18 	0/8 	0/16 
3 pixels	0/18 	2/8 	13/16 
4 pixels	0/8 	5/8 	8/8 
5 pixels	0/8 	3/8 	8/8 
6 pixels	0/8 	4/8 	8/8 
7 pixels	0/8 	4/8 	8/8 
8 pixels	0/8 	3/8 	8/8 
9 pixels	0/8 	5/8 	8/8 

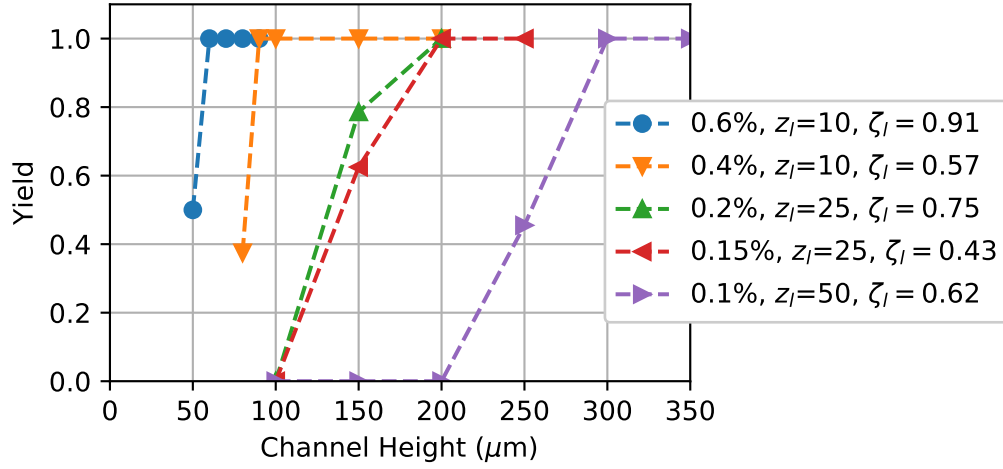
must be imaged with smaller magnification optics, which in turn reduces the x-y build area. To compensate, larger pixel count DLPs need to be used such as the  $1920 \times 1080$  pixel DLP6500 or  $2560 \times 1600$  pixel DLP9000.

The yield as a function of flow channel height is plotted in Fig. 3.14a for the various Sudan I PEGDA resins used in this study, and for the build layer thicknesses that gave the smallest flow channels results. Note that the normalized layer thickness,  $\zeta_l$ , for each case is between  $\sim 0.4$

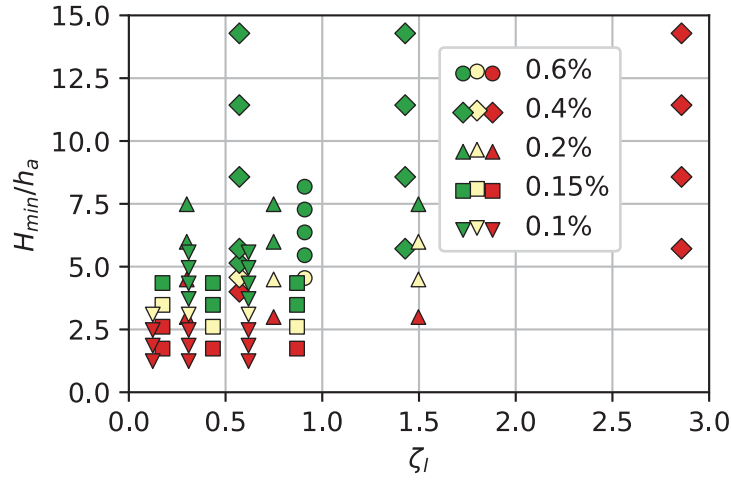
Table 3.6: Channels in 0.6% Sudan I resin as a function of width and height for  $t_l = 1.55$  s and  $z_l = 10 \mu\text{m}$  ( $\zeta_l = 0.91$ ).

Width	Channel height				
	50 $\mu\text{m}$	60 $\mu\text{m}$	70 $\mu\text{m}$	80 $\mu\text{m}$	90 $\mu\text{m}$
3 pixels		4/12	1/6	2/6	1/6
4 pixels	6/8	8/8	8/8	8/8	8/8
5 pixels	4/8	8/8	8/8	8/8	8/8
6 pixels	5/8	8/8	8/8	8/8	8/8
7 pixels	6/8	8/8	8/8	8/8	8/8
8 pixels	1/8	8/8	8/8	8/8	6/6
9 pixels	1/8	8/8	8/8	8/8	4/4

and  $\sim 0.9$ . Other than the 0.15% and 0.2% Sudan I resins, increasing absorber concentration (decreasing  $h_a$ ) leads to smaller flow channel heights, with the smallest being 60  $\mu\text{m}$ . Alternatively, yield data from all of the Sudan I PEGDA resins can be plotted as a function of the normalized channel height,  $H_{min}/h_a$ , and normalized layer thickness as shown in Fig. 3.14b. The data can be summarized with the following observations. Minimum flow channel heights occur for  $0.3 \leq \zeta_l \leq 1$ . In resins with  $h_a \gtrsim 50 \mu\text{m}$  the minimum flow channel height is  $\sim 3.5h_a$ , while for resins with  $h_a \lesssim 40 \mu\text{m}$  it is  $\sim 5.5h_a$ . At this point it is unclear why these are different and further investigation is warranted.



(a)

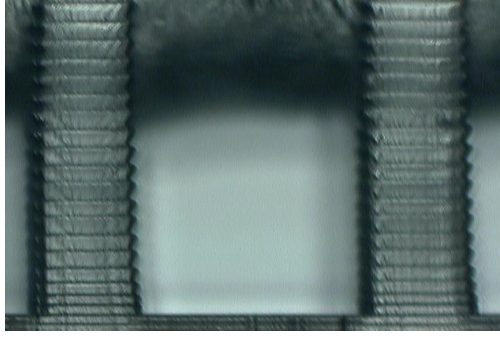


(b)

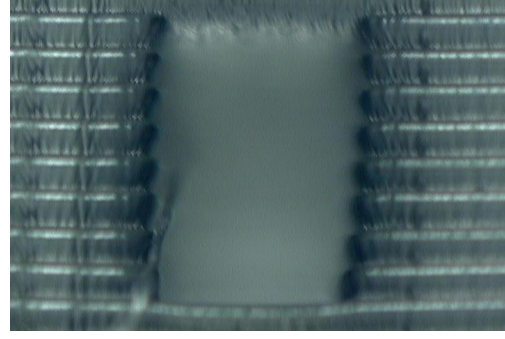
Figure 3.14: (a) Minimum flow channel height with 100% yield for PEGDA resins with different Sudan I concentrations. (b) Experimental results of yield (green: 100%, yellow: partial, red: none) for normalized channel height and normalized layer thickness.

Results for commercial and open source resins are shown in Fig. 3.15. The minimum flow channel height for PlasClear is  $8.1h_a$ . The reason it is so large is that PlasClear's high viscosity (Table 3.1) prevents uncured resin from being fully flushed from smaller flow channels. This is an example of something other than a resin's optical properties being the limiting factor in determining the minimum flow channel height. The designed minimum flow channel height for FSL Clear that was reliably open is  $\sim 3.4h_a$ . However, since much of the channel is blocked by polymerized resin, the actual size of the opening is substantially less than the design height. For this resin we

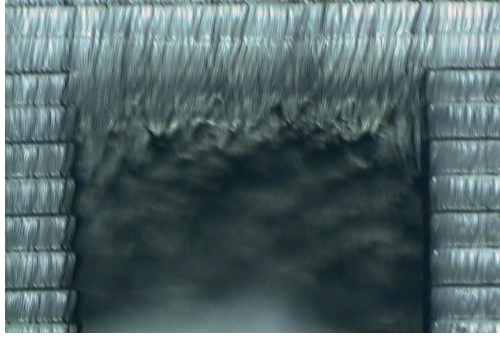




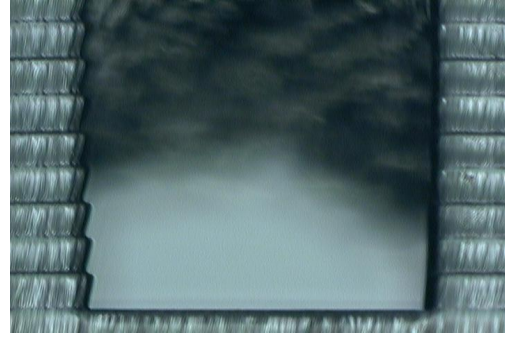
(a) PlasClear,  $1000\ \mu\text{m} \times 20\ \text{pixels}$ .  $\zeta_l = 0.41$



(b) PR48,  $400\ \mu\text{m} \times 7\ \text{pixels}$ .  $\zeta_l = 0.62$



(c) FSL Clear,  $1100\ \mu\text{m} \times 30\ \text{pixels}$ .  $\zeta_l = 0.31$ , top of channel



(d) FSL Clear, bottom of channel

Figure 3.15: Smallest consistently open channels printed with commercial and open source resins. Microscope photos (a), (c), and (d) are taken with a  $5\times$  objective while (b) uses a  $10\times$  objective. The build layer thickness for (a) and (b) is  $50\ \mu\text{m}$ , and  $100\ \mu\text{m}$  for (c) and (d).

found considerable variation in the fraction of the flow channel height that is blocked. For PR48 the minimum flow channel height is  $5.0h_a$ , which is similar to higher absorption Sudan I PEGDA resins.

### 3.5 Conclusions

In summary, we have investigated the effect of resin optical properties on the minimum flow channel size that can be fabricated with DLP-SLA 3D printing. We have developed a mathematical model of the optical dose delivered to a 3D printed part as a function of depth for multiple exposed layers in the presence of flow channels (voids). The model shows that there is a fundamental trade-off between the homogeneity of the dose within an individual layer and how far the polymerization front extends into an underlying flow channel during fabrication. We experimentally tested the



minimum flow channel size that can be fabricated by formulating custom PEGDA resins with 1% Irgacure 819 photoinitiator and a variety of Sudan I concentrations to vary the penetration depth,  $h_a$ , over an order of magnitude, 11  $\mu\text{m}$  to 119  $\mu\text{m}$  (which is dependent on the 3D printer source spectrum). We find that the minimum flow channel height for a particular resin is typically  $\sim 3.5\text{--}5.5h_a$ . The minimum channel width that can be fabricated with 100% yield is 4 pixels for our 3D printer, which is likely to be as good as or perhaps better than other DLP-SLA 3D printers. We experimentally determined  $h_a$  for an open source and two commercial resins and found that their minimum flow channel size is consistent with our findings for the custom resins as long as the resin is not too viscous such that flow channels can be adequately flushed after fabrication. Further reductions in flow channel size should be readily achievable by increasing resin absorbance (i.e., reducing  $h_a$ ) and increasing the x-y plane resolution of the projected image from the DLP micromirror array. These advances should facilitate broad usage of 3D printing methods for the construction of truly microfluidic (rather than millifluidic) devices.

## **CHAPTER 4. HIGH DENSITY 3D PRINTED MICROFLUIDIC VALVES, PUMPS, AND MULTIPLEXERS**

In this chapter we show significant miniaturization of 3D printed microfluidic devices with integrated valves and pumps based on the resin formulation work in Chapter 3 and our demonstration of the first reported 3D printed valves [24]. Specifically, we show how to use a DLP-SLA 3D printer with our inexpensive custom resin formulation to fabricate robust membrane valves 40 pixels in diameter (1.08 mm) with a minimum chamber height of 60  $\mu\text{m}$ . These valves are only 10% the volume of our previous 3D printed valves, [24] and we have improved their durability from 800 actuations to 1 million actuations. To achieve such durability, we modify the resin composition by adding a thermal initiator such that a post-printing 30 minute oven cure drives further polymerization of the material to create a greater degree of cross linking and mechanical toughness. We then demonstrate a simple pump structure consisting of two valves and one displacement chamber (DC), and experimentally characterize its maximum back pressure and maximum flow rate. Finally, we combine 5 valves and one DC into a compact 3-to-2 multiplexer with integrated pump, utilizing the flexibility of 3D printing to densely arrange device elements within the 3D volume of the device. We also show that the multiplexer can be used as a mixer and that its mixing efficiency can be improved by increasing the number of inlets in the DC. The work in this chapter is reported in Ref. 61.

### **4.1 Experimental**

#### **4.1.1 Materials**

Our resin formulations consist of monomer, photoinitiator, and absorber, which for this work are poly(ethylene glycol) diacrylate (PEGDA, MW 258), Sudan I, and Irgracure 819, respectively [24], [81], [86]. We also include a thermal initiator, azobisisobutyronitrile (AIBN), for post-print thermal curing, the details of which are discussed in Sect. 4.2.1. It is important to note that

use of a low molecular weight PEGDA results in excellent water stability for fabricated parts, [81] with no swelling or degradation in mechanical strength. PEGDA, Sudan I, and AIBN are obtained from Sigma-Aldrich (St. Louis, MO), and Irgacure 819 from BASF (Vandalia, Illinois). Each is used as received.

The specific resin formulation employed for the work reported in this chapter is the 0.4% Sudan I resin discussed in Chapter 3. It is prepared by mixing 0.4% (w/w) Sudan I, 1% (w/w) Irgacure 819, and 0.01% (w/w) AIBN with PEGDA, and sonicating for 30 minutes. The resin is stored in an amber glass bottle wrapped in aluminum foil to protect it from light exposure.

#### **4.1.2 3D Printer**

We use an Asiga Pico Plus 27 DLP-SLA 3D printer as described in Chapter 3, which has an LED peak wavelength of 412 nm and an in-plane resolution (pixel pitch) of 27  $\mu\text{m}$ . Microfluidic devices in an individual print run are fabricated on a glass slide (25 mm  $\times$  37.5 mm  $\times$  1.2 mm) which is attached to the printer build table with double-sided tape. We experienced no issues with the slide damaging the teflon film comprising the bottom of the resin tray as long as we followed the 3D printer manufacturer's build table alignment procedure. Each slide is prepared by cleaning with acetone and isopropyl alcohol (IPA), followed by immersion in 2% 3-(trimethoxysilyl) propyl methacrylate in toluene for 2 hours. After silane deposition slides are kept in toluene until use.

There are two reasons we use glass slides. The first is that they avoid the need to fabricate the first device layer on the rough (anodized Al) surface of the 3D printer build table, which, especially for resins with high optical absorbance, requires a significantly longer exposure time for the first layer to attach to the build table. Long exposure times deplete the available binding sites on the surface of the layer, making attachment of the next layer problematic. The second reason is that the smooth surfaces of the glass slide offer convenient optical access to observe the interior components of the microfluidic device.

### 4.1.3 Device Fabrication

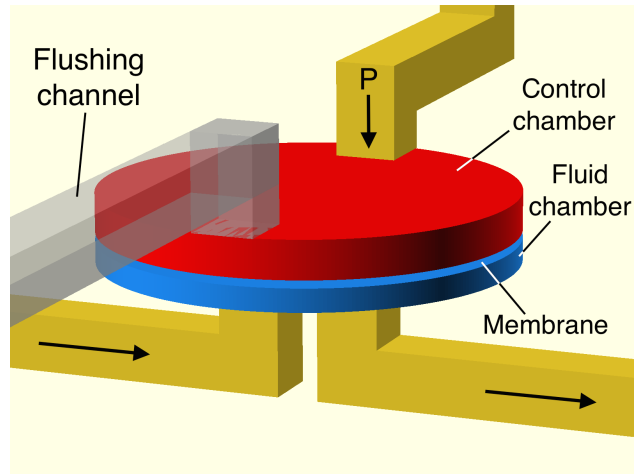
Our build layer thickness,  $l$ , is  $10\text{ }\mu\text{m}$ , which results in a normalized layer thickness,  $\zeta = l/h_d$ , of 0.57 for the 0.4% Sudan I resin. This is well within the optimal build thickness range we established in Chapter 3.

The key active component in our devices is a membrane valve, the structure of which is shown in Fig. 4.1a [24]. The valve consists of a  $20\text{ }\mu\text{m}$  thick membrane (i.e., 2 build layers) sandwiched between two cylindrical voids which comprise a control chamber ( $100\text{ }\mu\text{m}$  high) and a fluid chamber ( $60\text{ }\mu\text{m}$  high), each 40 pixels ( $1.08\text{ mm}$ ) in diameter. The corresponding dimensions of Rogers' 3D printed valves are  $50\text{ }\mu\text{m}$  membrane thickness, with  $250\text{ }\mu\text{m}$  control chamber and  $250\text{ }\mu\text{m}$  fluid chamber heights, both of which are  $2\text{ mm}$  in diameter [24]. The valves in this chapter are only 10% of the volume of the valves in Rogers' paper ( $0.165\text{ mm}^3$  compared to  $1.73\text{ mm}^3$ ). The valves in Rogers' paper were fabricated with a different DLP-SLA 3D printer (B9 Creator) prior to developing our quantitative approach to resin formulation.

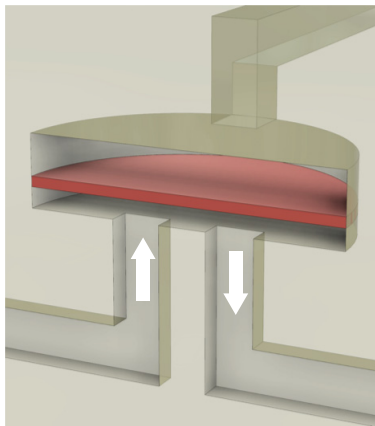
When no pressure is applied to the control chamber (as illustrated in Fig. 4.1b), the valve is open and fluid can flow between the two channels at the bottom of the fluid chamber. A photomicrograph of an open valve is shown in Fig. 4.1d. The lighting makes it easy to see the pixelation of the bottom surface of the fluid chamber. The measured surface roughness for horizontal surfaces fabricated with 0.4% Sudan I resin is  $0.5\text{ }\mu\text{m}$  with a length scale the size of the pixel pitch. As shown in Fig. 4.1c, when pressure is applied to the control chamber the membrane deflects downward and seals the fluid channels. The central circular region in which the membrane contacts the bottom of the fluid chamber can be clearly seen in Fig. 4.1e.

In our devices valves are connected with flow channels that are  $150\text{ }\mu\text{m}$  high and 6 pixels ( $162\text{ }\mu\text{m}$ ) wide. Although smaller channels can be fabricated with 0.4% Sudan I resin, we chose this somewhat larger size to ensure easy, high yield fabrication, even for flow channels as long as  $118\text{ mm}$ . Consequently, we never had a problem with flow channel fabrication for the devices discussed in subsequent sections.

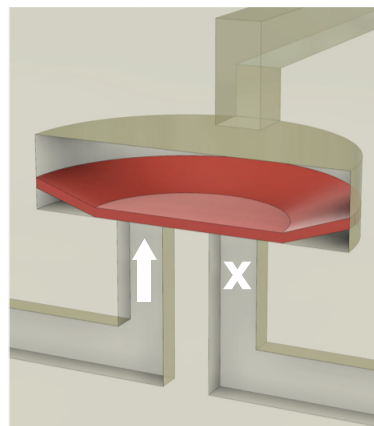
After 3D printing, unpolymerized resin must be flushed from the interiors of microfluidic structures. An advantage of our PEGDA resin formulations is that they are low viscosity ( $57\text{ cP}$ ), making flushing much easier than for many commercial resins that have significantly higher viscosity. As shown in Chapter 3, the difficulty of flushing unpolymerized resin can be the limiting



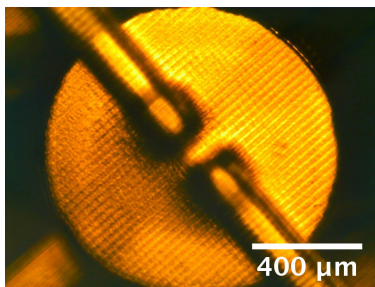
(a)



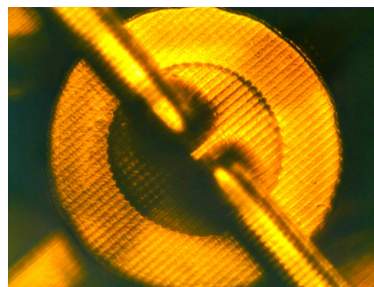
(b)



(c)



(d)



(e)

Figure 4.1: CAD design of (a) for a 3D printed membrane valve. Schematic illustration and microscope photos of (b), (d) open and (c), (e) closed valves. The microscope photos show the bottom of the valve. See text for details.

factor in determining the minimum achievable void size for commercial resins, rather than the actual optical properties of the resin.

Immediately after 3D printing is completed, the sample is removed from the build table and soaked in IPA for 2-3 minutes to dissolve much of the unpolymerized resin. The control and fluid chambers are then carefully flushed with IPA, following which vacuum is applied to extract residual IPA from microfluidic structures. Note that the control chamber design in Fig. 4.1a has a second channel specifically to permit flushing unpolymerized resin.

Next, we bake the device at 80°C for 30 minutes to activate the thermal initiator to drive further polymerization. It should be noted that a blanket UV exposure is completely ineffective at curing our 3D printed devices because the UV light only penetrates a small fraction of a millimeter even after many hours of exposure due to the high absorption of the resin.

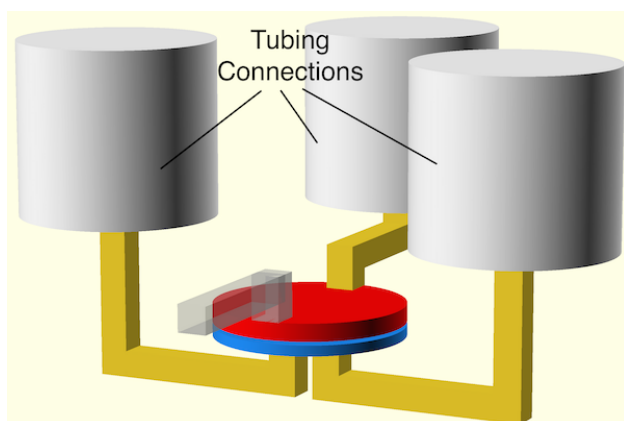


Figure 4.2: Complete 3D printed valve CAD design includes cylindrical holes in which to connect PTFE tubing.

After baking, a device is prepared for testing by inserting Microbore PTFE tubing (0.022"ID  $\times$  0.042"OD) into corresponding cylindrical holes in the device (Fig. 4.2), and gluing the tubing in place (Loctite Instant Mix 5 Minute Epoxy). The epoxy is also used to plug the flushing channels for all control chambers.

Total device build and preparation time is approximately 4 hours, and consists of (1) 3D printing (<1 hour), (2) flushing unpolymerized resin (5-7 minutes for all of the devices in a single print run), (3) oven bake (30 minutes), and (4) inserting tubing followed by mixing and applying epoxy to the junction between the tubing and device and letting the epoxy cure for 2 hours. Despite

being labelled as 5 minute epoxy, we found that a 2 hour cure time was needed for the epoxy to achieve a hardness that facilitated leak-tight seals and good tubing strain relief. The epoxy cure step is by far the most time-consuming aspect of our current device fabrication and preparation process. This time can be dramatically reduced to just a few minutes by substituting a UV curable adhesive for the 5 minute epoxy, thereby reducing the total device fabrication and preparation time to under 2 hours.

CAD and .stl design files for the valve, pump, and multiplexer reported in this chapter are freely available online [87].

## 4.2 Results and Discussion

### 4.2.1 3D Printed Valves

To evaluate the performance of 3D printed valves, we first measured the maximum fluid pressure,  $P_{\text{fluid}}$ , at which the valve stays closed for a given control pressure,  $P_{\text{control}}$ , applied to the membrane to close the valve. A schematic of the test setup is shown in the inset of Fig. 4.3a. The valve fluid inlet is connected to a syringe pump, the control chamber is pressurized to deflect the membrane and close the valve, and the syringe pump is set to inject deionized (DI) water into the valve at 20  $\mu\text{L}/\text{min}$ . Two pressure sensors, G1 and G2, (Honeywell 24CFFA6G) are used to continuously measure the fluid and control pressure, respectively. Fig. 4.3a shows the result of a typical valve pressure measurement. The fluid pressure initially rises monotonically, peaks, and then drops to a steady state which is lower than the control pressure. The pressure difference,  $\Delta P = P_{\text{control}} - P_{\text{fluid}}$ , is measured as the average pressure difference over a 2 second interval centered at 20 seconds after the peak fluid pressure occurs, which can be interpreted as the minimum pressure required to deflect the membrane enough to just barely close the valve. We therefore expect that  $\Delta P$  should increase as the fluid chamber height increases or the membrane thickness increases because either change makes it more difficult to deflect the membrane enough to close the valve. This is confirmed in Fig. 4.3b and 4.3c which show the corresponding experimental measurements. In Fig. 4.3b, an increase in  $\Delta P$  from a little over 2 psi to 4 psi is observed as the fluid chamber height increases from 50  $\mu\text{m}$  to 80  $\mu\text{m}$  because the membrane has to deflect more to close the valve. We experimentally determined that the fabrication yield for valves with a 50  $\mu\text{m}$  chamber height is

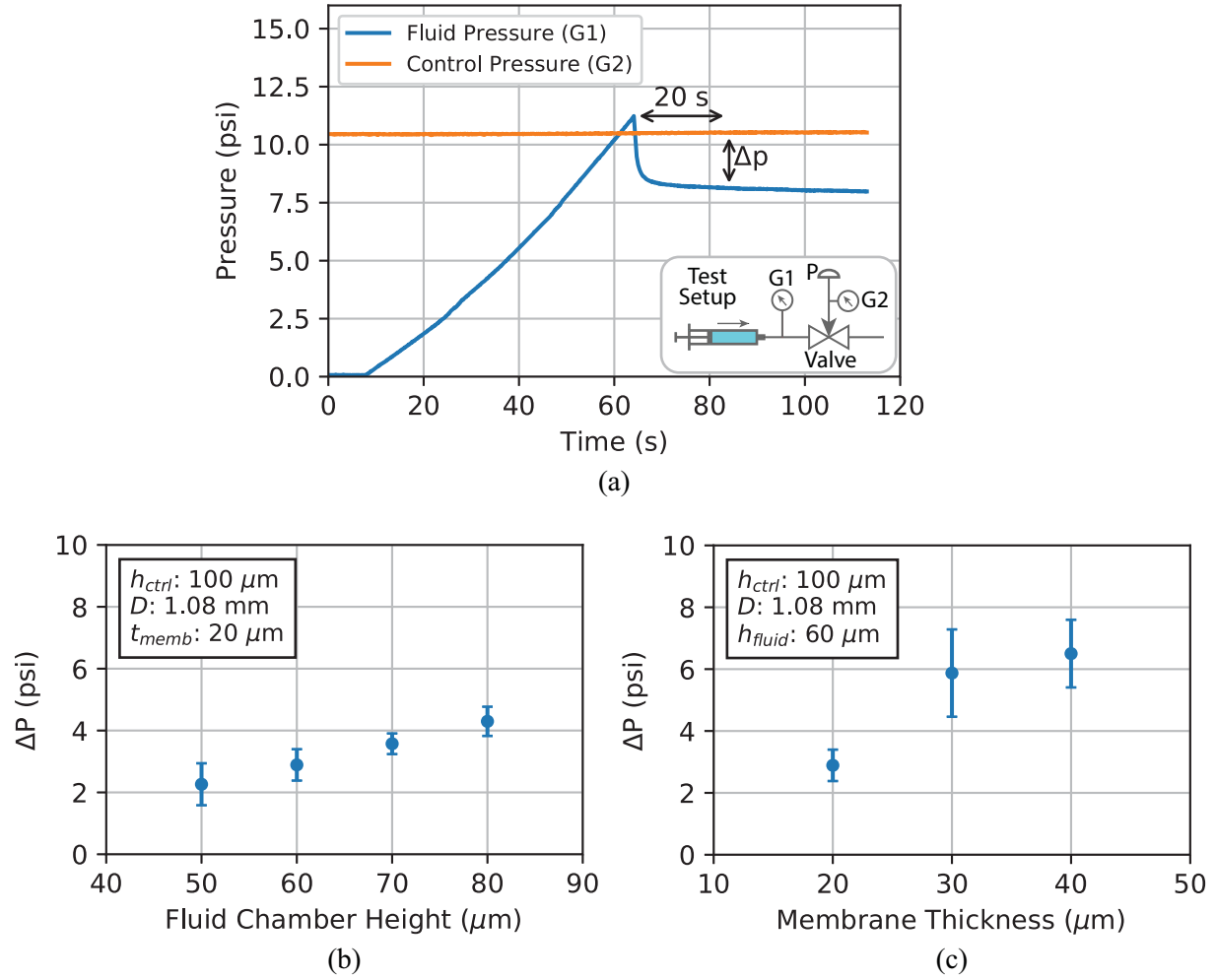


Figure 4.3: (a) Typical valve pressure measurement and (inset) schematic illustration of test setup. The fluid and control pressures are measured with pressure sensors G1 and G2. (b)  $\Delta P$  as a function of fluid chamber height and (c) membrane thickness. Each data point in (b) and (c) consists of an average of at least 10 valves, with most being an average of over 20 valves. Error bars indicate  $\pm 1$  standard deviation.  $h_{ctrl}$ : control chamber height;  $D$ : diameter;  $t_{memb}$ : membrane thickness;  $h_{fluid}$ : fluid chamber height.

substantially less than for a  $60 \mu\text{m}$  chamber height, which is nearly 100%. We therefore chose a  $60 \mu\text{m}$  fluid chamber height for the devices reported in this chapter. Similarly, as shown in Fig. 4.3c, the membrane becomes stiffer and requires more pressure to close as its thickness increases from 2 layers ( $20 \mu\text{m}$ ) to 4 layers ( $40 \mu\text{m}$ ).

An important criterion for an active fluidic device is its durability. In Rogers' demonstration of 3D printed valves, [24] the valves typically lasted 800 actuations before the membranes broke. However, he had previously tested similar cleanroom-fabricated valves to 115,000 actua-



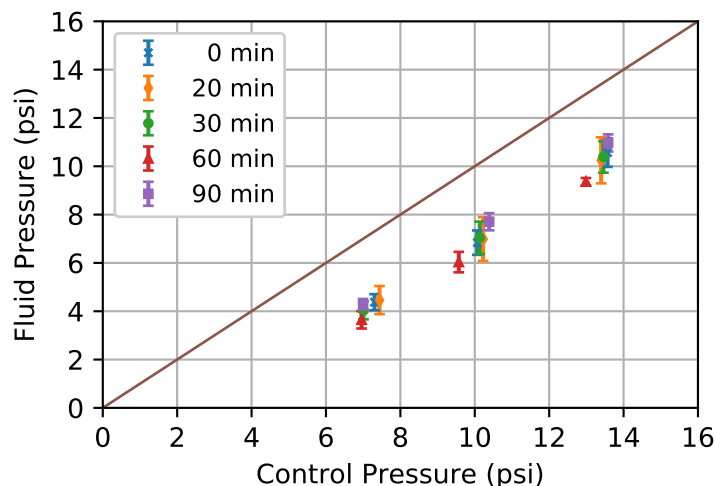


Figure 4.4: Valve maximum fluid pressure as a function of control pressure for different baking times. The number of valves tested for each baking time are 0 min: 3, 20 min: 8, 30 min: 9, 60 min: 8, 90 min: 7.

tions with no sign of breakage or degradation in their properties [86]. Following 3D printing and prior to thermal curing, valve membranes in the present study typically lasted only one or two actuations before breaking. We hypothesized that additional polymerization was needed to increase the mechanical robustness of the membranes. However, as detailed in Chapter 3, other constraints prevent trying to achieve this with longer layer exposure times during 3D printing. Hence we added a thermal initiator with a post-print oven bake to drive further polymerization. We tested a variety of bake times at 80°C, and found that they had no effect on pump properties as shown in Fig. 4.4. A bake time of 30 minutes seemed to offer the best trade-off between mechanically robust membranes, short bake time, and yield.

In our largest yield test, we began with 54 fabricated valves, one of which was found to leak between the flow channels during its first actuation. We later established that such as-built leaks can be avoided by simply increasing the separation between the channels in the bottom of the valve from 4 pixels to 6 pixels. Of the 53 remaining valves, all but one continued working after 10,000 actuations. The one that failed had its membrane break during the first 1,000 actuations. Of the 53 that survived, we tested one to 1 million actuations, after which it still worked. The flow channels and fluid chamber were filled with water during the entire 30 hours it took to run the test.

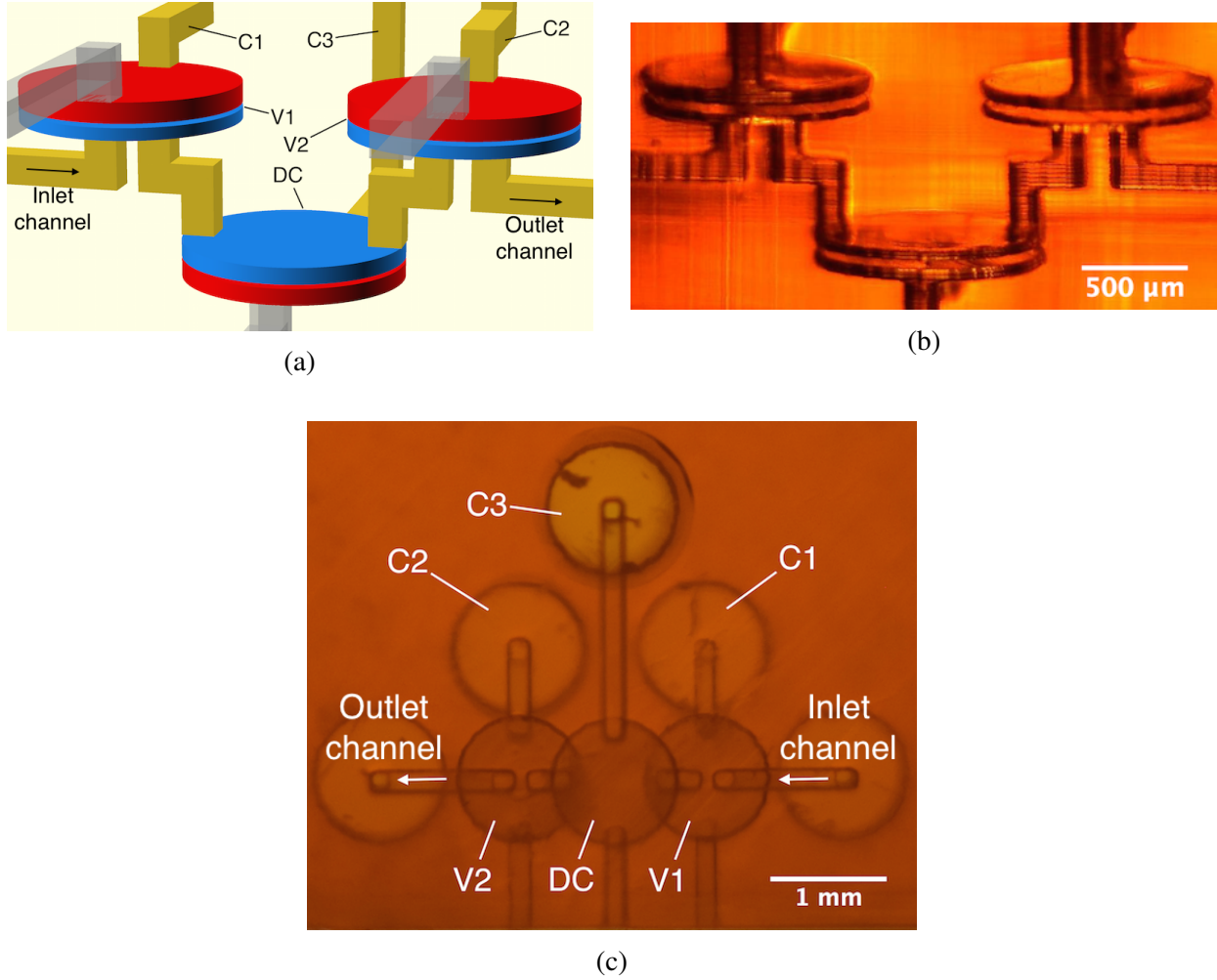


Figure 4.5: (a) CAD design of 3D printed pump. C1-C3 connect to external pressure sources. The partially transparent channels are flushing channels for the valve control chambers, which are later sealed with epoxy. (c) Side view of a 3D printed pump. See text for details. (c) Bottom view photograph of 3D printed pump in (b).

#### 4.2.2 3D Printed Pumps

As shown in Fig. 4.5a, a pump consists of two valves (V1 and V2) with a valve-like displacement chamber (DC) in between. The difference between a DC and a valve is that the inlet and outlet channels are placed on the edge of the fluid chamber for a DC rather than in the center as for a valve. This prevents the DC from being able to stop flow when actuated. Note also that the DC is oriented upside down compared to the valves. In a valve the fluid chamber is under the membrane whereas in the DC it is on top of the membrane.

Table 4.1: Pump timing logic. Red: actuated (pressure applied; valves closed); green: not actuated (valves open).

	$t_0$	$t_1$	$t_2$	$t_3$	$t_4$
V1	●	●	●	●	●
DC	●	●	●	●	●
V2	●	●	●	●	●

Valve actuation is controlled by applying pressure to C1 and C2, whereas DC actuation is controlled with C3. A photo of a pump looking from underneath is shown in Fig. 4.5c. The DC appears to partially overlap V1 and V2 since they are placed at different heights in the 3D build volume. The undersides of cylindrical holes are also visible for PTFE tubing to connect C1, C2, and C3 to pressure sources, and the inlet and outlet channels to an off-chip fluid source and sink. Fig. 4.5b is a side view photo of a pump showing the fabricated spatial arrangement of the DC and valves, along with their corresponding flow and control channels.

The pump uses a 5-phase cycle as shown in Table 4.1. At  $t_0$ , both valves are closed and pressure is applied to the DC. The DC fluid chamber is therefore in a state of minimum volume. At  $t_1$ , V1 opens and the DC pressure is released so the membrane returns to equilibrium thereby pulling fluid through V1 into the DC fluid chamber. At  $t_2$ , V1 closes to isolate fluid in the DC from the inlet flow channel, followed by V2 opening at  $t_3$  in preparation for expelling fluid from the DC into the outlet channel, which occurs by actuating the DC at  $t_4$ . The cycle then repeats by going back to  $t_0$  in which V1 is closed. The time difference between any two sequential phases is  $\Delta t = t_i - t_{i-1}$ , which we call the phase interval. Unless otherwise noted, the valve and DC actuation pressure is  $\sim 9$  psi.

A pump's maximum flow rate,  $Q_{max}$ , for a given set of operating parameters is defined as the flow rate when there is zero back pressure (such as when the fluid source, pump, and fluid outlet are all at the same height). We evaluated  $Q_{max}$  as a function of  $\Delta t$  under two conditions for the unactuated DC control chamber: (1) an applied vacuum of 10 psi (520 mmHg) and (2) vent to atmosphere. In the latter case the restoring force on the membrane is just the elastic strain of the stretched membrane. In the former, an applied vacuum at first assists the elastic strain until the membrane is undeflected and then pulls the membrane up into the control chamber.

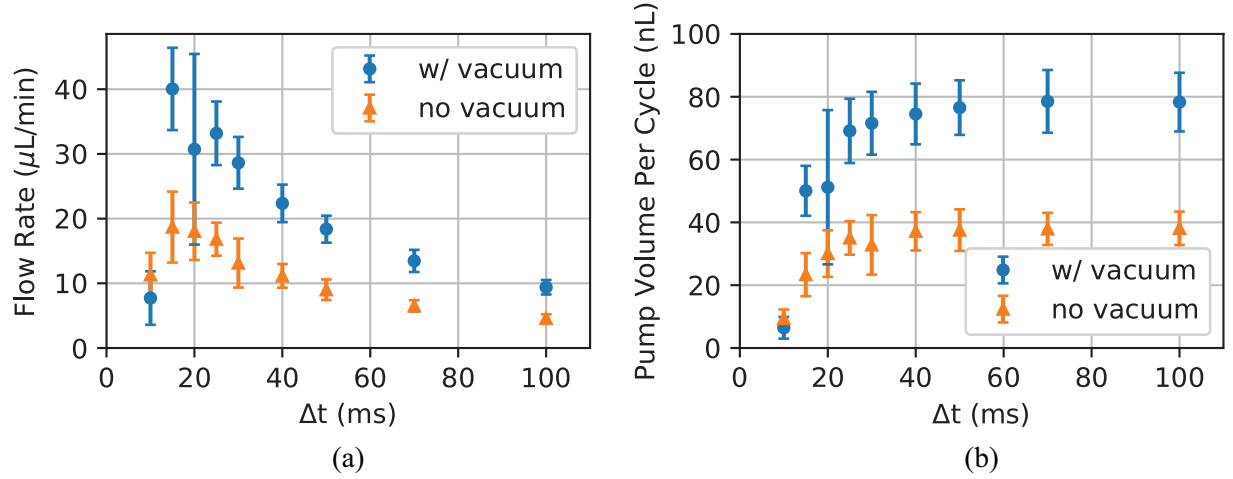


Figure 4.6: (a) Maximum flow rate (zero back pressure) as a function of the phase interval,  $\Delta t$ . (b) Fluid volume expelled by pump for a single pump cycle calculated from the data in (a). 9 pumps were tested with vacuum and 5 without. The large error bars for vacuum at 20 ms are due to 2 pumps having significantly smaller flow rates than the others.

The measured maximum flow rate,  $Q_{max}$ , is shown as a function of  $\Delta t$  in Fig. 4.6a. The maximum flow rate increases as  $\Delta t$  decreases, reaching a peak of 40  $\mu\text{L}/\text{min}$  for  $\Delta t = 15$  ms when vacuum is applied to the DC. The flow rate then drops rapidly as  $\Delta t$  continues to decrease. Note that for  $\Delta t \geq 15$  ms, the maximum flow rate with vacuum is approximately twice as large as without vacuum. Calculating the displaced fluid volume as a function of  $\Delta t$  (Fig. 4.6b), it is apparent that the vacuum pulls the membrane up into the control volume enough to essentially double the volume expelled by the DC for  $t_3 \rightarrow t_4$  as compared to the no vacuum case. We arbitrarily chose 50 ms (maximum expelled volume) as the phase interval for all subsequent measurements, and used vacuum with the DC.

A pump's maximum back pressure is defined as the maximum pressure the pump can work against such that the flow rate just goes to zero. The inset in Fig. 4.7a shows the experimental setup we used to measure the maximum back pressure of a 3D printed pump. The pump operates to push fluid into a closed channel in which the pressure is monitored with pressure sensor G1. The control pressure actuating the valves and DC is measured with G2. A typical measurement is shown in Fig. 4.7a. The back pressure is calculated by averaging data in the last 10 s. In Fig. 4.7b, we compare the measured maximum back pressure for control pressures of approximately 6, 9, and 11 psi. A linear curve fit shows an x-intercept of  $\sim 4.5$  psi, which is the minimum control

pressure needed for the pump to be able to push fluid into a zero back pressure outlet. According to Fig. 4.7b, a control pressure of 9 psi is sufficient to generate a back pressure of approximately 4 psi, whereas a control pressure of 11 psi generates a back pressure of  $\sim 8$  psi.

In Fig. 4.8 we measure the flow rate as a function of the height of the outlet above the fluid source and pump. As expected, the flow rate slowly decreases with outlet height. An outlet height of 120 cm corresponds to 1.7 psi of back pressure, in which case the average flow rate decreases from 19.3  $\mu\text{L}/\text{min}$  to 17.2  $\mu\text{L}/\text{min}$ .

### 4.2.3 3D Printed Multiplexers and Mixers

We now use the example of a 3-to-2 multiplexer to illustrate how 3D printing enables high density 3D layout of microfluidic components in a single device. The simplest function of a 3-to-2 multiplexer is to pump fluid from any of three inputs to any of 2 outputs. As discussed in Section 3.2, a pump can be constructed with a DC placed between two valves. Therefore, the smallest component count for a 3-to-2 multiplexer is shown in Fig. 4.9a where a DC is placed between three input valves (V1, V2, V3) and two outlet valves (V4, V5). Pumping, for example, from Buffer to Outlet 1 uses V1-DC-V4 with all other valves closed. Similarly, pumping from Red to Outlet 2 uses V2-DC-V5. Fluid can be pumped from any of the inlets to any of the outlets by using the associated inlet and outlet valves in conjunction with the DC while keeping all other valves

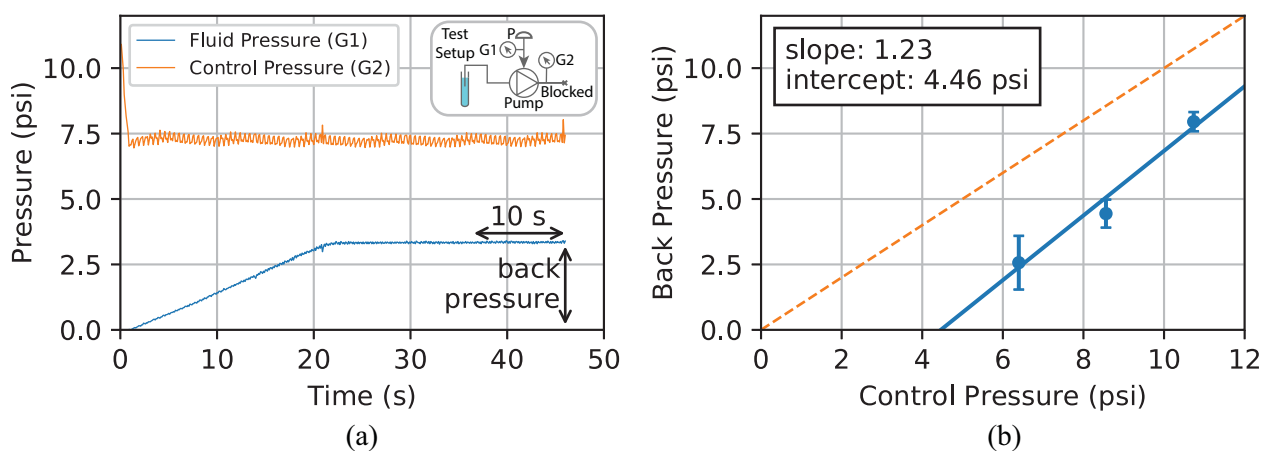


Figure 4.7: (a) Typical maximum back pressure measurement and (inset) experimental setup. (b) Maximum back pressure as a function of control pressure (average and standard deviation for 7 pumps).

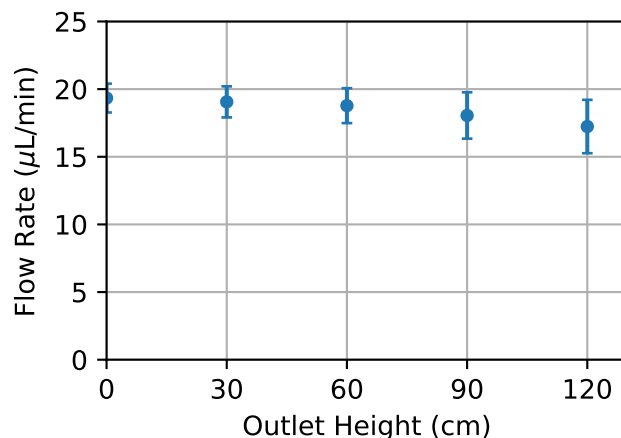


Figure 4.8: Flow rate as a function of the outlet height for a control pressure of 9 psi (average and standard deviation for 6 pumps). Different pumps were used in all tests.

closed. (As a side note, the configuration in Fig. 4.9a can actually pump fluid from any inlet or outlet to any other inlet or outlet by using the corresponding valves with the DC and appropriate phasing of their actuations.)

One possible 3D layout of the components in Fig. 4.9a is shown in Fig. 4.9b in which V1, V2, and V3 are located directly above V4, DC, and V5, respectively. Flow channels and control channels are easily routed through 3D space to form the connections indicated in the schematic diagram in Fig. 4.9a. The valve, DC, and flow channel dimensions are the same as discussed in previous sections.

A fabricated device is shown in Fig. 4.9c, looking from below through the glass slide substrate. The valves V1, V2, and V3 are occluded (indicated by dashed white lines) behind V4, DC, and V5 (indicated by solid white lines). PTFE tubing is epoxied in the inlets on the left, and the outlet flow channels are on the right. The three inlet tubes contain buffer (Buffer), diluted red dye in water (Red), and diluted black dye in water (Black), respectively. Both Red and Black have previously been pumped through the device, followed by Buffer. This is the reason the flow channels from the Red and Black inlets to the DC are filled with Red and Black, respectively.

Fig. 4.9d–i show an example set of operations conducted with the multiplexer that exercise the various combinations of inlets to outlets. It begins with Red being pumped to Outlet 1 (Fig. 4.9d), followed by Black to Outlet 2 (Fig. 4.9e), Buffer to Outlet 2 (Fig. 4.9f), Buffer to Outlet 1 (Fig. 4.9g), Red to Outlet 2 (Fig. 4.9h), and Black to Outlet 1 (Fig. 4.9i). Its dynamic op-

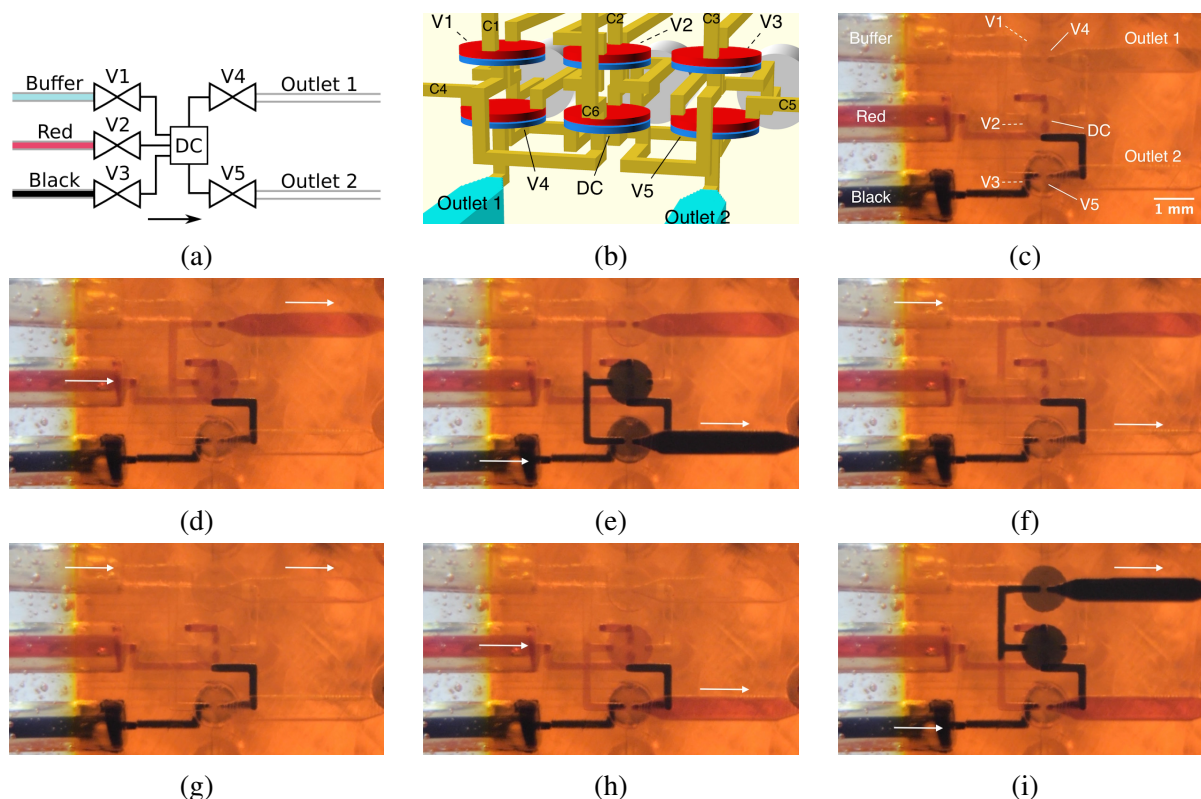


Figure 4.9: (a) Multiplexer schematic diagram. (b) CAD design taking advantage of stacked layout flexibility enabled by 3D printing. Valve labeling is the same as (a) with corresponding control lines labeled C1, C2, etc. (c) Bottom view of multiplexer fabricated according to the CAD design in (b). (d)-(i) Demonstration of arbitrary 3-to-2 multiplexing. See text for details. Arrows indicate active flow direction.

eration is shown in the ESI Movie S1 of Ref. 61. During each inlet/outlet combination, the pump is typically run for 50 periods to more than fully flush the previous fluid in the large ( $500 \mu\text{m} \times 500 \mu\text{m} \times 2.5 \text{ mm}$ ) outlet channels. The large outlet channel size is chosen solely to make it easy to see the colored fluids. As a further note, it takes approximately 3 pump periods to flush fluid from the DC when switching from one fluid to another.

The multiplexer can also be used as a mixer by, for example, operating two of the inlet valves simultaneously during pumping, in which case the fluids from the two inlets will be drawn together through the pump and expelled into an outlet. Prior to initiating pump action, we first opened V2, V3, DC, and V5 while raising the reservoirs from which red and black fluid are drawn about 15 cm above the microfluidic device. All of the other valves are closed. Fig. 4.10a illustrates the gravity-induced flow of Red and Black through the device. The upper right inset shows Black



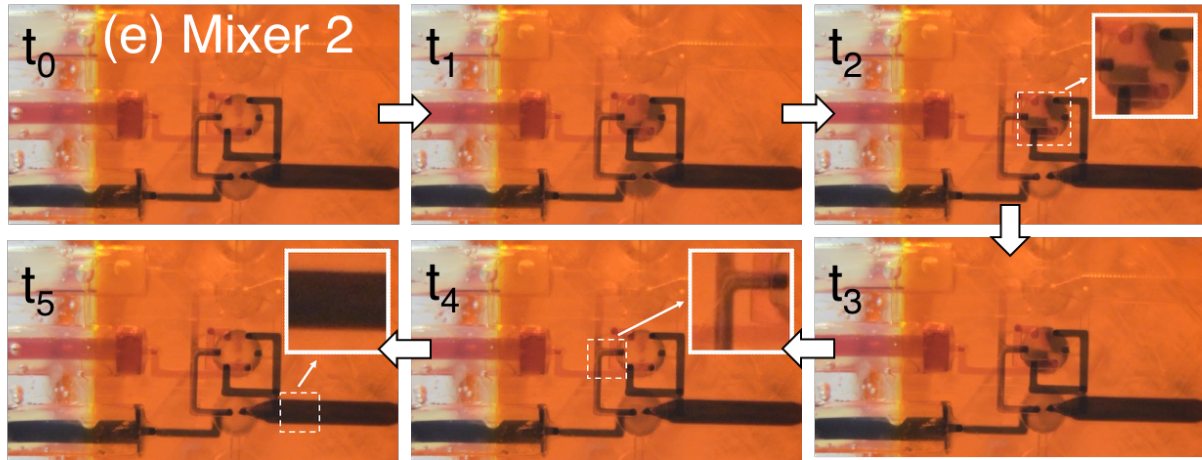
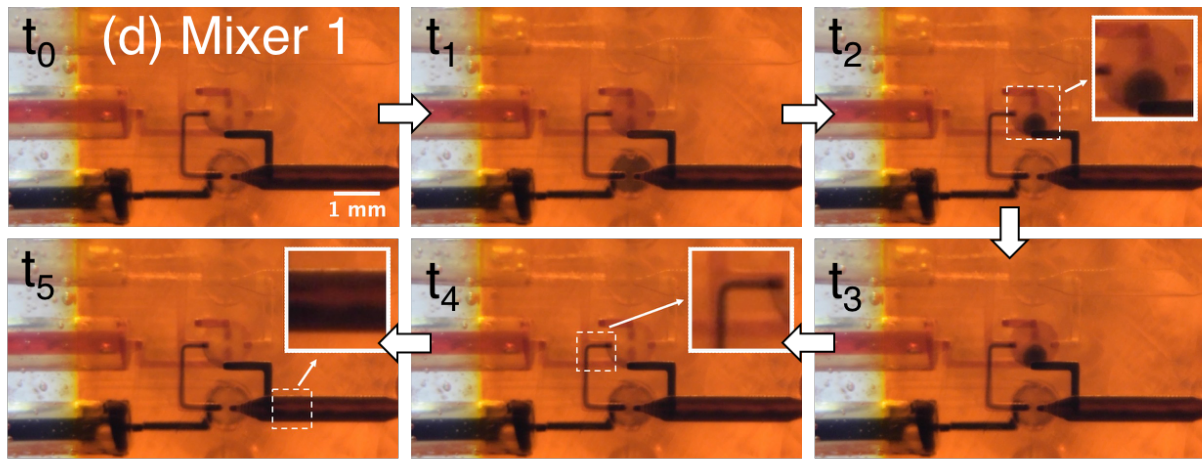
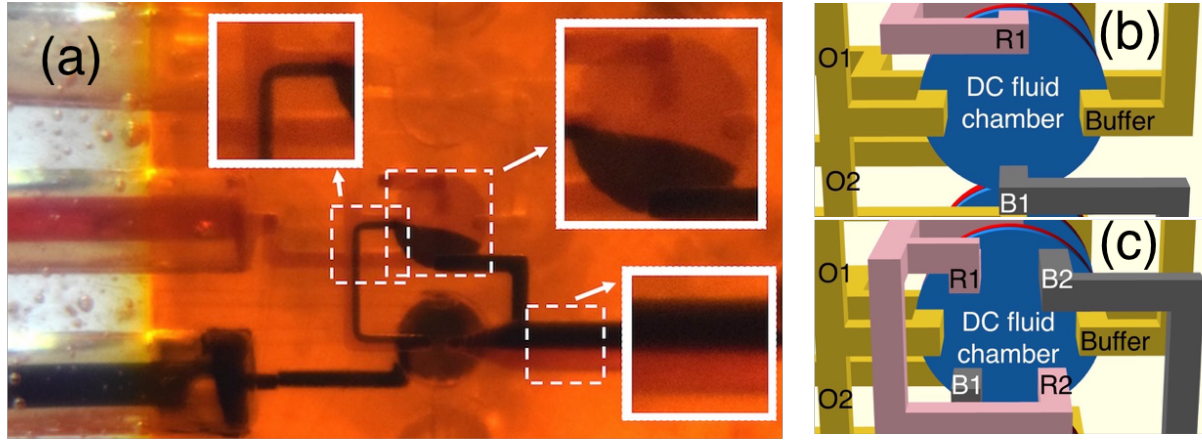


Figure 4.10: (a) Flow generated only by gravity. Note lack of Red/Black mixing. (b, c) Bottom view of DC channel layout in (b) Mixer 1 and (c) Mixer 2. Red channels, R1 in (b) and R1 and R2 in (c), connect the Red inlet valve (V2 in Fig. 4.9a) to the DC, while the black channels, B1 in (b) and B1 and B2 in (c), connect the Black inlet valve (V3) to the DC. Buffer is the channel that connects the Buffer inlet to the DC through valve V1. O1 and O2 connect the DC to Outlets 1 and 2, respectively, through valves V4 and V5. (d) and (e) compare the mixing performance of the designs in (b) and (c). See text for details.



Table 4.2: Mixer timing logic. Red: actuated (pressure applied; valves closed); green: not actuated (valves open). Valves not listed in the table are closed.

	$t_0$	$t_1$	$t_2$	$t_3$	$t_4$
V2	●	●	●	●	●
V3	●	●	●	●	●
DC	●	●	●	●	●
V5	●	●	●	●	●

entering the DC from below and Red from above, corresponding to the physical locations of their inlets into the DC. The upper left inset shows the segregated Red/Black flow stream through the DC outlet channel, which maintains its segregation through V5 and Outlet 2 (lower right inset image). Clearly, the only mixing that occurs is due to diffusion across the boundary between the two fluids.

Now consider simultaneous pumping from Red and Black into Outlet 2 according to the timing logic in Table 4.2. The results are shown in Fig. 4.10d in which each image shows the device state for the corresponding timing logic in Table 4.2 (note that  $t_5$  is the same state as  $t_0$ ). Prior to taking these images, the device was operated long enough such that it had reached a steady-state condition. At  $t_1$  fluid is draw into the DC through open valves V2 and V3, both of which are closed at  $t_2$ . The inset for  $t_2$  shows the spatial segregation of fresh Red and Black just drawn into the DC. At  $t_3$  the valve to Outlet 2, V5, is opened, following which fluid is expelled from the DC through V5 into Outlet 2 at  $t_4$ . The inset at  $t_4$  shows similar Red/Black segregation in the DC outlet channel, but by the time it makes it through V5 and into Outlet 2 there is much more mixing than in Fig. 4.10a. However, there is still a discernible red streak near the middle of Outlet 2 (see inset at  $t_5$ ).

As soon as we had this result we realized that mixing could be improved by increasing the degree to which Red and Black are interleaved in the DC, which is easily accomplished with a change in geometry. Consider for example the bottom view of the DC in Fig. 4.10b in which Red is introduced into the DC through flow channel R1, and Black through B1. By splitting each Red and Black inlet into two inlets and interleaving them as shown in Fig. 4.10c (labeled as R1, R2, B1, and B2), additional mixing can be created in the DC. The mixing properties of the resultant

device are shown in Fig. 4.10e using the same sequence of steps as Fig. 4.10d. The inset image for  $t_2$  shows red and black regions localized around their respective DC inlets, while the inset at  $t_4$  shows more Red/Black streams in the DC outlet channel, resulting in better mixing in Outlet 2 as seen in the inset at  $t_5$ . The rapid iteration time enabled by 3D printing allowed us to redesign, fabricate, and test this new DC inlet design within a day.

As a final comment, the 3-to-2 multiplexer in Fig. 4.9 can be readily scaled to larger numbers of inlets and outlets. At this point it is unclear what the practical scaling limit is, but it will likely be determined by the fabrication yield of the valves, in which case our fabrication techniques would need to be further refined to increase the valve yield.

### 4.3 Conclusions

In this chapter we have demonstrated the potential of 3D printing to enable both rapid fabrication iteration and high density integration of microfluidic components. We have reported the smallest yet 3D printed valves and characterized valve performance and durability. Incorporation of a thermal initiator in the resin together with a post-print bake dramatically improves durability. Fifty two out of 54 valves were successfully tested up to 10,000 actuations, at which point we stopped the tests because of how long they took. One valve was tested to 1 million actuations, after which it still performed well. We have used these valves to create compact pumps and characterized their maximum back pressure and maximum flow rate. Flow rates as high as  $40\ \mu\text{L}/\text{min}$  have been demonstrated. We have also demonstrated a 3-to-2 multiplexer with integrated pump, and shown that it can also be used as a mixer. Moreover, we have shown the ability to implement and test a new idea to improve mixing within only a day, thereby illustrating the power of 3D printing to enable a “fail fast and often” iterative device development strategy.

## **CHAPTER 5. CUSTOM 3D PRINTER AND RESIN FOR $18\ \mu\text{m} \times 20\ \mu\text{m}$ MICROFLUIDIC FLOW CHANNELS**

Previously in Chapter 3 we showed that custom resin formulation in conjunction with a relatively high resolution DLP-SLA 3D printer ( $27\ \mu\text{m}$  pixel pitch in the image plane) enabled us to 3D print microfluidic flow channels with cross sectional area ( $108\ \mu\text{m} \times 60\ \mu\text{m}$ ) near the boundary between the microfluidic and large microfluidic regimes. In this chapter, we show how 3D printing can be further extended to fabricate microfluidic flow channels with cross sectional area small enough to truly be in the microfluidic regime. Our approach is to construct our own high resolution 3D printer ( $7.56\ \mu\text{m}$  pixel pitch in the image plane) and develop a custom resin specifically tailored to take advantage of the 385 nm LED spectrum of the 3D printer. Moreover, we introduce a new channel narrowing technique that results in reliably printing flow channels as small as  $18\ \mu\text{m} \times 20\ \mu\text{m}$ , which is 18 times smaller than our previous results in Chapter 3. To demonstrate the efficacy of our approach, we fabricate 41 mm long 3D serpentine flow channels in a volume of only  $1.56\ \text{mm} \times 0.38\ \text{mm} \times 0.21\ \text{mm} = 0.12\ \text{mm}^3$ . We also demonstrate high aspect ratio channels  $<25\ \mu\text{m}$  wide and 3 mm tall. In short, we show that when appropriately applied, DLP-SLA is an effective method to 3D print truly microfluidic voids, which lays the foundation for 3D printing to challenge the dominance of conventional methods of microfluidic prototyping and development such as soft lithography and hot embossing. The work in this chapter is reported in Ref. 62.

### **5.1 Materials and Methods**

#### **5.1.1 Custom 3D Printer**

Our two most important design criteria for constructing a custom 3D printer for microfluidics are a high resolution light engine and a UV LED light source. The former is critical to achieve small in-plane ( $x$ - $y$ ) void size, while the latter enables a wider selection of materials for

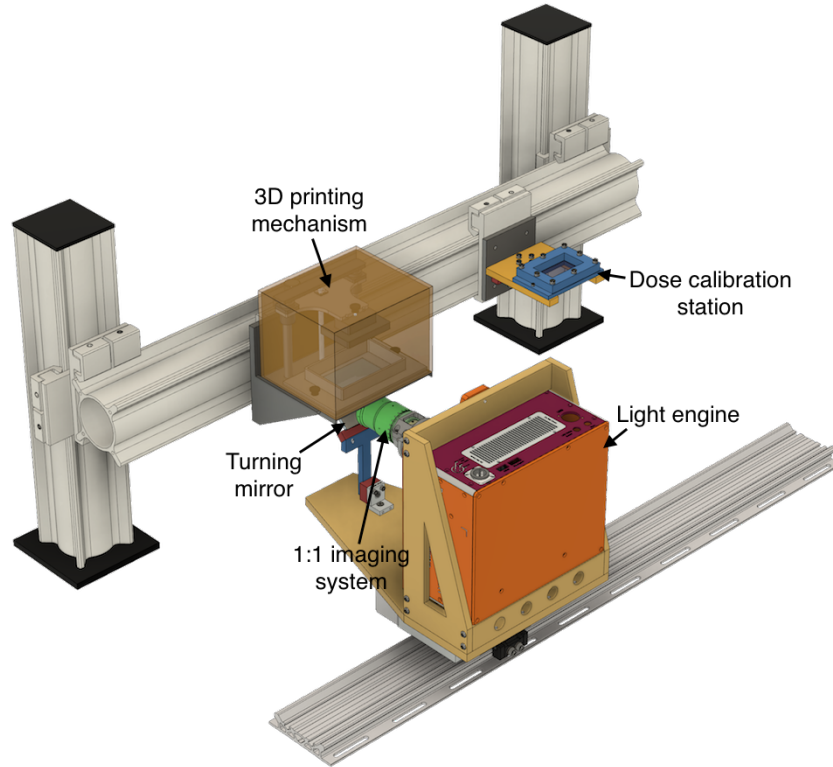


Figure 5.1: 3D CAD model of our custom 3D printer.

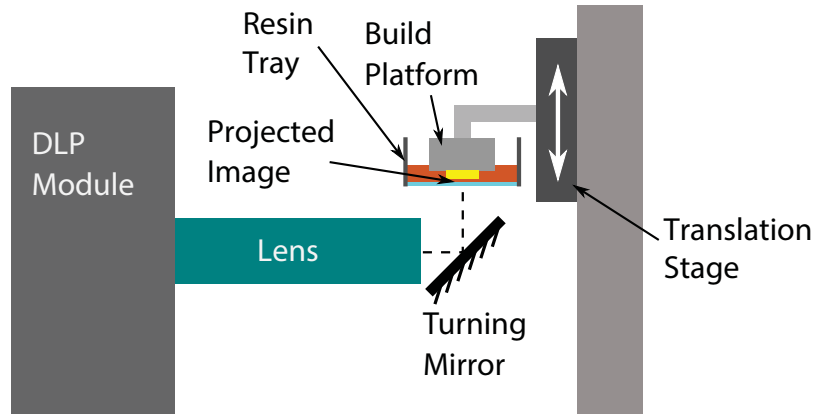


Figure 5.2: Schematic illustration of 3D printer.

custom resin formulation than the 405 nm sources we have previously worked with in Chapter 3. As we show in Sect. 5.2.1, creating a resin with the correct optical properties relative to the light source is critical to achieve small out-of-plane ( $z$  dimension) void size.

Our custom 3D printer design is shown in Fig. 5.1. A schematic illustration of its layout is included in Fig. 5.2. The custom 3D printer comprises a light engine, a  $45^\circ$  turning mirror

with 3 axes of adjustment, a 3D printing mechanism, and custom-made mounts. The light engine and turning mirror are attached to a common base, which in turn is mounted to a rail so that the assembly can be conveniently shifted between the 3D printing mechanism on the left and a resin dose calibration set up (detailed in Sect. 5.1.4) on the right.

The light engine (Visitech, Lier, Norway) is based on a TI DLP9000 (Texas Instruments) containing a  $2560 \times 1600$  micromirror array. With a 1:1 imaging system, the image plane resolution is  $7.56 \mu\text{m}$  and the projected area is  $19.35 \text{ mm} \times 12.10 \text{ mm}$ . The optical source in the light engine is a 385 nm LED. We measure the peak wavelength and full-width at half-maximum (FWHM) of the source to be 383.4 nm and 12.6 nm, respectively. The  $45^\circ$  turning mirror reflects light from the horizontally mounted light engine such that projected patterns can be focused through the transparent bottom of a resin tray. A Solus 3D printing mechanism (Junction3D, Santa Clarita, CA) is heavily modified to serve as a platform for the 3D printing process. The bottom of the resin tray is a replaceable teflon film that is tensioned on an underlying quartz window to guarantee flatness.

In its current configuration, the ultimate build size of our custom 3D printer is  $19.35 \text{ mm} \times 12.10 \text{ mm} \times 80 \text{ mm}$ , where the XY size and the Z size are determined by the projected image from the light engine and the Solus mechanism, respectively. Note that we have deliberately traded-off XY size in favor of higher XY resolution, which is required to obtain small in-plane void size. If desired, the XY build size can be increased without compromising resolution by exposing multiple images side-by-side for each layer. This can be accomplished, for example, by translating the light engine in XY. In this chapter we use a single image position for each layer, and defer translating the light engine to future work.

We have developed custom Python software to operate our custom 3D printer. The software controls the 3D printing mechanism over a serial channel using G-code and the light engine over I<sup>2</sup>C to a low-level hardware interface. Images are sent with a graphics card through HDMI. All synchronization of 3D printer functions is performed in the Python code. The code gives us absolute control over all aspects of the 3D printer, including arbitrary exposure times for arbitrary layers during a 3D print, multiple independent exposures per layer, variable layer thicknesses, and, most importantly, single pixel precision in the projected images.

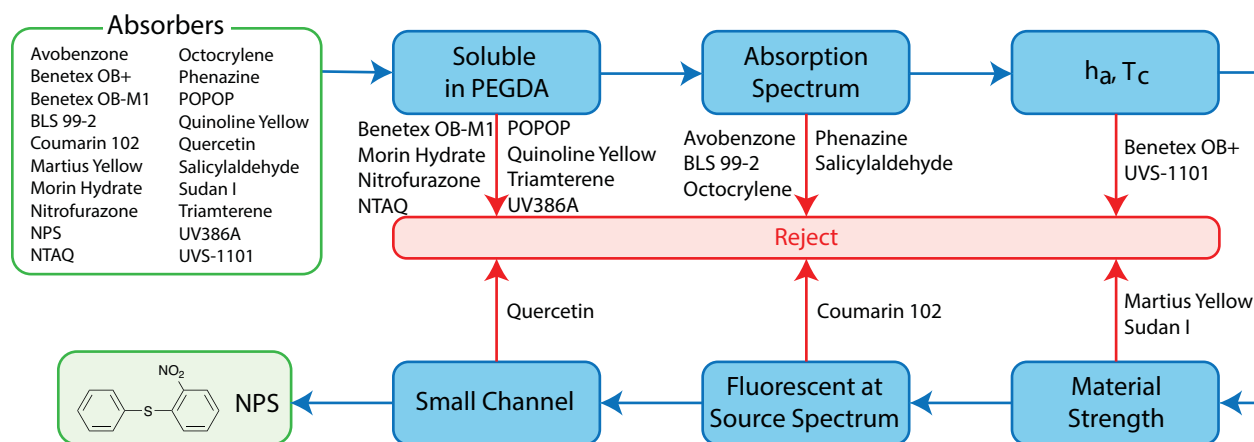


Figure 5.3: UV absorber evaluation criteria and process flow. 20 absorbers are initially considered. Rejected absorbers are indicated at each step in the process where they do not pass the evaluation criterion.

### 5.1.2 Materials

The focus of our resin formulation efforts is finding one or more UV absorbers that will give the optical properties needed to achieve small void size in the  $z$  dimension. Similar to our previous work in Ref. 24 and Chapter 3 and 4, we use poly(ethylene glycol) diacrylate (PEGDA, MW258) as the monomer and phenylbis(2,4,6-trimethylbenzoyl)phosphine oxide (Irgacure 819) as the photoinitiator. They are obtained from Sigma-Aldrich (St. Louis, MO) and BASF (Vandalia, Illinois), respectively.

Part of the motivation for use of a PEGDA-based resin is that it has low non-specific adsorption and is suitable for electrophoretic separations [81]. Moreover, Urrios *et al.* showed that their PEGDA resin formulation could be made biocompatible with a specific post-processing treatment [55]. Regarding solvent compatibility, we have found 3D printed PEGDA resins to be compatible with some solvents such as isopropyl alcohol and ethanol, but not others such as acetone and toluene.

As indicated in Fig. 5.3, we evaluate 20 potential UV absorbers. Their molecular structures are shown in Fig. 5.4. Nearly all are inexpensive and readily available. These absorbers are organized in Table 5.1 as well as their vendors. Each chemical is used as received.

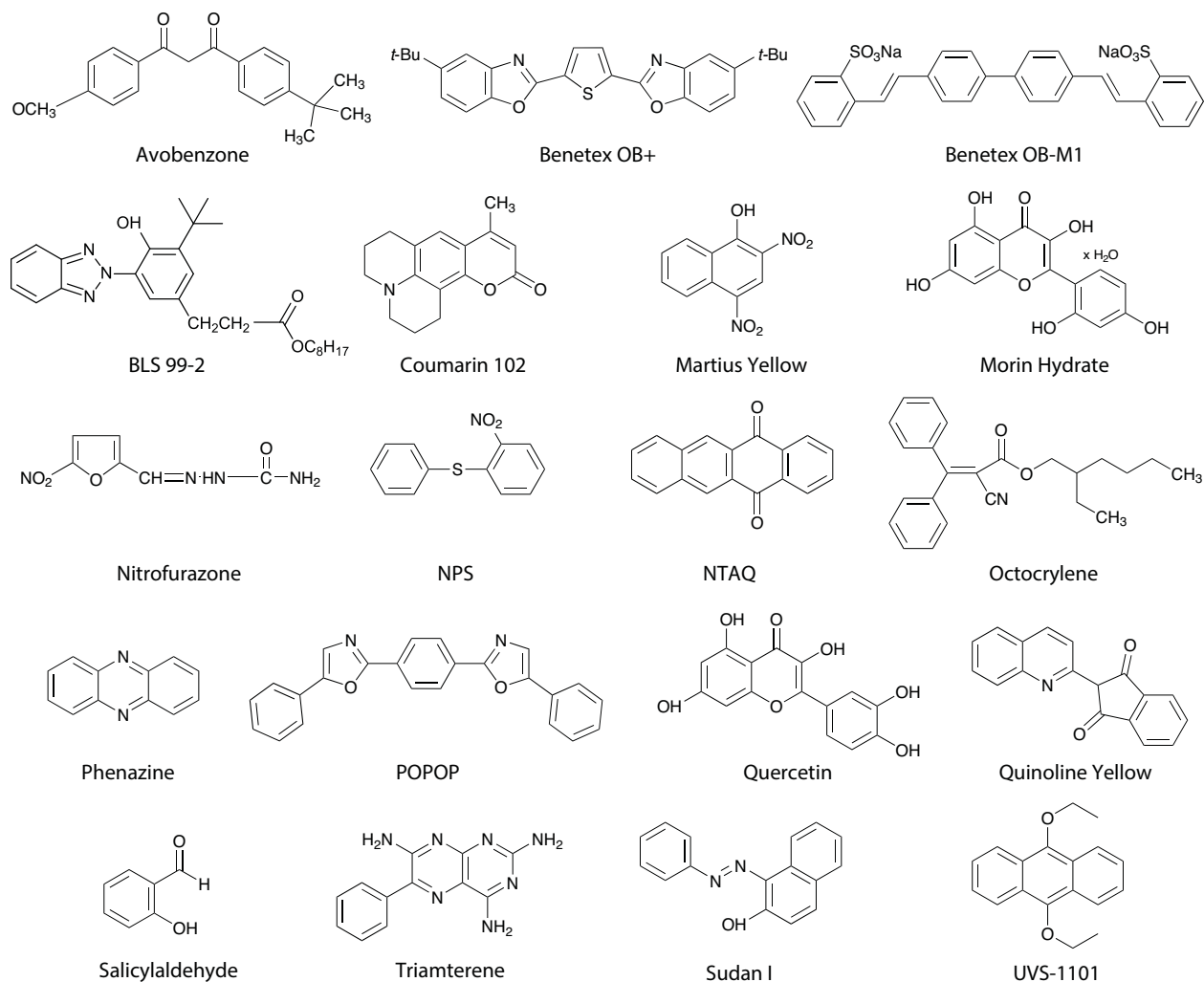


Figure 5.4: Molecular structures for monomer, photoinitiator, and UV absorbers used in this study (except for UV386A, which is proprietary).

Resins studied for 3D printing are prepared by mixing 1% (w/w) Irgacure 819 and the desired concentration of UV absorber with PEGDA, and sonicating for 30 min. All photoinitiator-containing resins are stored in amber glass bottles after mixing.

### 5.1.3 Molar Absorptivity Measurement

The absorption spectrum of each UV absorber is measured by mixing the absorber at a specific concentration with PEGDA and placing a drop of resin in the gap between a glass slide and a coverslip separated by 65  $\mu\text{m}$  spacers. The resin is illuminated through the glass slide with attenuated light from a broadband XCITE-120Q source (Lumen Dynamics, Ontario, Canada).

Table 5.1: UV absorbers

Absorber	Chemical Name	Vendor
Avobenzene	—	MakingCosmetics (Snoqualmie, WA)
Benetex OB+	2,5-bis(5-tert-butyl-benzoxazol-2-yl)thiophene	Sigma-Aldrich (St. Louis, MO)
Benetex OB-M1	disodium 4,4'-bis(2-sulfonatostyryl)biphenyl	TCI America (Portland, OR)
BLS 99-2	benzenepropanoic acid	Mayzo (Suwanee, GA)
Coumarin 102	2,3,6,7-tetrahydro-9-methyl-1H,5H-quinolizino (9,1-gh)coumarin	Alfa Aesar (Haverhill, MA)
Martius Yellow	—	Sigma-Aldrich (St. Louis, MO)
Morin Hydrate	—	Sigma-Aldrich (St. Louis, MO)
Nitrofurazone	—	TCI America (Portland, OR)
NPS	2-nitrophenyl phenyl sulfide	TCI America (Portland, OR)
NTAQ	5,12-naphthacenequinone	Santa Cruz Biotechnology (Dallas, TX)
octocrylene	—	MakingCosmetics (Snoqualmie, WA)
phenazine	—	Santa Cruz Biotechnology (Dallas, TX)
POPOP	1,4-bis-(2-(5-phenyloxazolyl))-benzene	Santa Cruz Biotechnology (Dallas, TX)
Quinoline Yellow	—	Sigma-Aldrich (St. Louis, MO)
Quercetin	3,3',4',5,6-pentahydroxyflavone	Sigma-Aldrich (St. Louis, MO)
salicylaldehyde	—	Thermo Fisher Scientific (Waltham, MA)
Sudan I	—	Sigma-Aldrich (St. Louis, MO)
triamterene	—	Alfa Aesar (Haverhill, MA)
UV386A	—	QCR Solutions (St. Lucie, FL)
UVS-1101	9,10-diethoxyanthracene	Alfa Aesar (Haverhill, MA)



The transmitted light is captured by a fiber with 100  $\mu\text{m}$  diameter core connected to a QE65000 spectrometer (Ocean Optics, Dunedin, FL). The molar absorptivity is calculated from the measured absorption spectra of resins with and without an absorber, and from the known resin thickness.

#### **5.1.4 Dose Calibration**

Polymerization thickness as a function of optical dose is measured with the set up on the right in Fig. 5.1, which consists of a custom resin container with a 75 mm  $\times$  50 mm glass window in the bottom. When the light engine is shifted on the rail to this calibration station, the height of the resin container is adjusted so that the projected image is focused on the top surface of the window. A layer of resin  $\sim$ 1 mm thick is applied to the window and exposed to a series of 1 mm<sup>2</sup> square patterns with different exposure times, which results in different polymerization depths. After rinsing unpolymerized resin with isopropyl alcohol (IPA), we measured the thickness of the polymerized regions using a Zeta-20 3D optical profilometer (Zeta Instruments, San Jose, CA).

#### **5.1.5 3D Printing**

3D prints are fabricated on diced and silanized glass slides. The silanization procedure is given in Chapter 4, except that here we use a silane concentration of 10% rather than 2%. All 3D prints are exposed with a measured optical irradiance of 21.2 mW/cm<sup>2</sup> in the image plane.

#### **5.1.6 Material Mechanical Properties**

As discussed in Sect. 5.2.2, we experimentally observe that some UV absorbers appear to hinder the photopolymerization process such that a given dose results in noticeably different material strengths for different absorbers. To illustrate this phenomenon, we measure the hardness and Young's modulus of two resins containing different UV absorbers. Measurements are made with 19.35 mm  $\times$  12.10 mm  $\times$  5 mm 3D printed blocks of polymerized resin printed with a 5  $\mu\text{m}$  layer thickness. Their Shore hardness is measured with a Rex Gauge Model 1600 durometer (Buffalo Grove, IL) for both ASTM D2240 Type A and Type D scales. The Young's Modulus is measured in compression with an Instron 3455 (Instron, Norwood, MA).

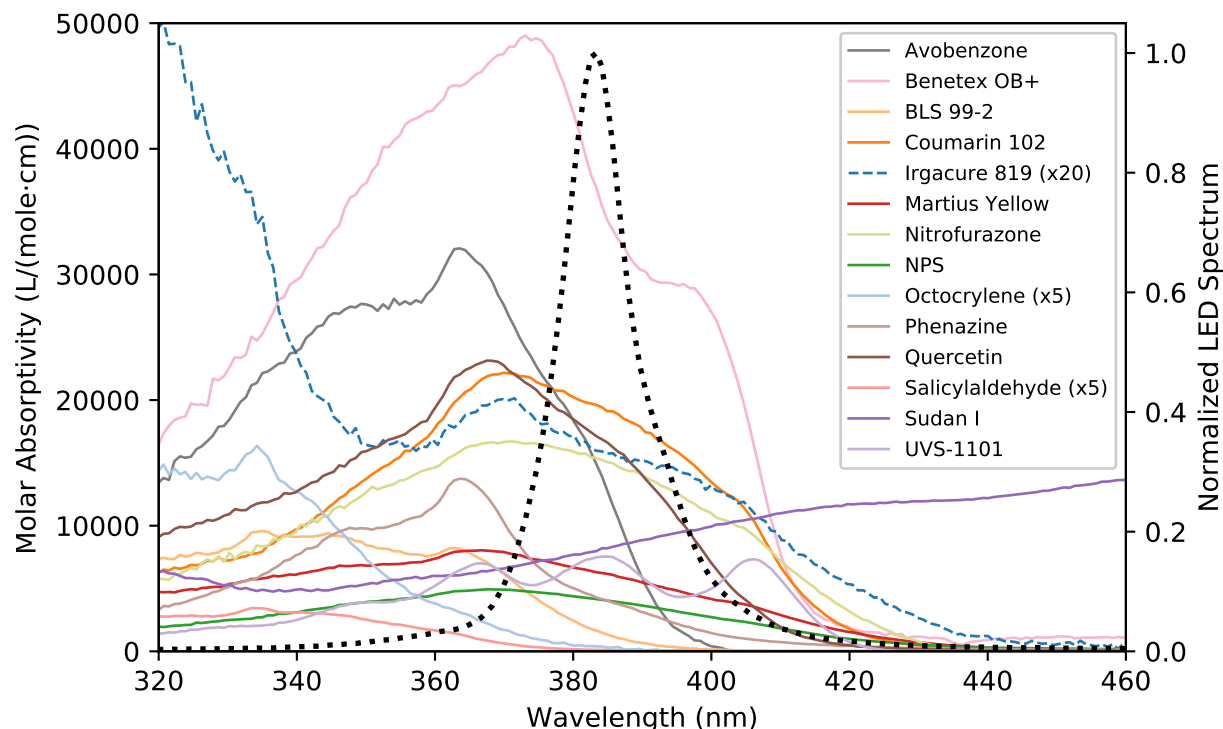


Figure 5.5: Measured molar absorptivity and LED source spectrum.

### 5.1.7 Post-Print Curing

In Chapter 4 0.01% w/w azobisisobutyronitrile (AIBN) was added to the resin to enable post-print thermal curing to drive further polymerization and obtain improved mechanical properties. However, we find that the 385 nm source of our new 3D printer activates AIBN such that it is consumed during 3D printing, and is therefore unavailable for post-print thermal curing. We tried an alternate thermal initiator, benzoyl peroxide, but found that it was likewise activated during 3D printing. Therefore, we employ an optical curing approach in this chapter. The key is to use a photoinitiator with absorbance that extends to longer wavelengths than the long wavelength cut off of the UV absorber such that light in this region penetrates through the device. For example, in Fig. 5.5, the Irgacure 819 absorption spectrum extends to  $\sim 460$  nm, while NPS and Martius Yellow drop off at  $\sim 440$  nm. For post-print optical curing we use an inexpensive consumer UV nail curer (54 Watt Professional UV Nail Dryer, Royal Nails) that emits a broad spectrum.

## 5.2 Results and Discussion

In this section we begin by stepping through the process of developing a custom resin to fabricate truly microfluidic void sizes based on our new 3D printer, taking into account the source and UV absorber spectra. A mathematical model is developed, from which the optical penetration depth for a resin,  $h_a$ , can be calculated directly from its measured molar absorptivity and desired absorber concentration, and also determine  $h_a$  and the critical exposure time,  $T_c$ , (see Chapter 3 for the model details) from experimental measurement of polymerization thickness as a function of exposure time. Our assessment leads to the selection of NPS as the UV absorber for our custom resins. Next, we evaluate the minimum achievable void size as a function of layer thickness and layer exposure time for 2% w/w NPS concentration. Using calculated dose as a function of  $z$ , we develop a model for the minimum achievable void size, and demonstrate that the model is predictive by applying it to 3% NPS resin to obtain flow channels with a design height of 18  $\mu\text{m}$ . We then introduce a new channel narrowing technique that reduces channel width from  $\sim 38 \mu\text{m}$  to  $\sim 20 \mu\text{m}$ . Finally, we demonstrate the utility of our methods by fabricating 41 mm long 3D serpentine flow channels and high aspect ratio flow channels.

### 5.2.1 Absorber Selection

#### Criteria

Our approach to evaluating UV absorber candidates is illustrated in Fig. 5.3, which we apply to 20 candidate absorbers. These candidates were primarily found by examining chemical manufacturer websites and manually assessing absorption spectra in the 20 volumes of Ref. 88.

Most UV absorbers are powders that must be mixed with PEGDA, a liquid. The first test criterion is therefore whether the absorber is soluble. Table 5.2 shows the results of our solubility measurements. Seven of the 20 candidate absorbers are found to be insoluble in PEGDA and an eighth, nitrofurazone, has such a low solubility (0.07%) that it is unusable.

The next criterion is whether the absorber's absorption spectrum fully overlaps the emission spectrum of the light engine optical source. Fig. 5.5 shows the measured molar absorptivity as a function of wavelength for the remaining absorber candidates. It also shows the molar absorptivity of the photoinitiator, Irgacure 819, and the light engine source spectrum. As is evident

Table 5.2: Solubility in PEGDA and fluorescence with 385 nm excitation. Dash indicates insolubility.

Material	Solubility (%)	Fluorescent
Avobenzone	>5	
Benetex OB+	0.25	Yes
Benetex OB-M1	—	Yes
BLS 99-2	>5	
Coumarin 102	0.8	Yes
Irgacure 819	>5	
Martius Yellow	3	
Morin Hydrate	—	
Nitrofurazone	0.07	
NPS	>5	
NTAQ	—	
Octocrylene	>5	
Phenazine	1.8	
POPOP	—	Yes
Quercetin	0.8	
Quinoline Yellow	—	
Salicylaldehyde	>5	
Sudan I	2.7	
Triamterene	—	Yes
UV386A	—	
UVS-1101	0.5	Yes

from the figure, 5 absorber candidates have poor spectral overlap with the source. In each case, the absorber's long wavelength tail is insufficient to cover the full source spectrum. The result is that some of the source spectrum will penetrate deeper into the device during 3D printing, causing unpolymerized resin in what should be voids to polymerize and thereby fill the voids. Such absorbers are therefore incapable of being used to fabricate small voids, as we show below.

## Mathematical Model

In Chapter 3 we noted that the polymerization depth,  $z_p$  for an exposure time of  $t_p$  is

$$z_p = h_a \ln \frac{t_p}{T_c}, \quad (5.1)$$

where  $h_a = 1/\alpha$  and  $\alpha$  is the resin's absorption coefficient. This result assumes monochromatic illumination, which is valid if the absorption coefficient is relatively constant over the source spectrum. However, in this chapter we consider wavelength-dependent absorption such that a more refined model needs to be developed.

Consider a photopolymerizable resin with absorption coefficient  $\alpha(\lambda)$  occupying the half space  $z \geq 0$  and illuminated by a polychromatic light source,  $I_0(\lambda)$ , from the  $-z$  direction. The dose ( $\text{J}/\text{cm}^2$ ) at  $z$  for exposure time  $t$  can be expressed as (see Table 5.3 for a comprehensive comparison of the monochromatic and polychromatic cases)

$$D(z, t) = t \int_0^\infty I_0(\lambda) e^{-\alpha(\lambda)z} d\lambda. \quad (5.2)$$

Normalizing by the dose at  $z = 0$  we obtain,

$$D_n(z) = \frac{D(z, t)}{D(0, t)} \quad (5.3)$$

$$= \frac{\int_0^\infty I_0(\lambda) e^{-\alpha(\lambda)z} d\lambda}{\int_0^\infty I_0(\lambda) d\lambda}. \quad (5.4)$$

The normalized dose,  $D_n(z)$ , indicates how rapidly the relative dose decreases as a function of  $z$ , and has the functional form of a weighted average of  $e^{-\alpha(\lambda)z}$  over  $\lambda$  with weighting function  $I_0(\lambda)$ . Based on calculations with measured spectra for numerous absorbers, we have found that this weighted average can be approximated as

$$D_n(z) \approx ae^{-z/b} + c \quad (5.5)$$

$$= 1 - a(1 - e^{-z/b}), \quad (5.6)$$

where we have used  $c = 1 - a$  in Eq. 5.6, which can be derived from  $D_n(0) = 1$ . When there is good spectral overlap between an absorber and the source spectrum,  $a = 1$  and the approximation for  $D_n(z)$  reduces to

$$D_n(z) \approx e^{-z/h_a}, \quad (5.7)$$

Table 5.3: Comparison of monochromatic and polychromatic resin exposures.

Line	Parameter	Units	Symbol	Monochromatic Case	Polychromatic Case
1	Irradiance at $z = 0$	$\text{W}/\text{cm}^2$	$I_0$	$I_0$	$\int_0^\infty I_0(\lambda) d\lambda$
2	Irradiance as a function of $z$	$\text{W}/\text{cm}^2$	$I(z)$	$I_0 e^{-\alpha z}$	$\int_0^\infty I_0(\lambda) e^{-\alpha(\lambda)z} d\lambda$
3	Dose as a function of $z, t$	$\text{J}/\text{cm}^2$	$D(z, t)$	$t I_0 e^{-\alpha z}$	$t \int_0^\infty I_0(\lambda) e^{-\alpha(\lambda)z} d\lambda$
4	Critical dose	$\text{J}/\text{cm}^2$	$D_c$	$t_p I_0 e^{-z_p/h_a}$	$t_p \int_0^\infty I_0(\lambda) e^{-\alpha(\lambda)z_p} d\lambda$
5	Time to reach critical dose at $z = 0$	s	$T_c$	$D_c / I_0$	$D_c / \int_0^\infty I_0(\lambda) d\lambda$
6	Polymerization depth	$\mu\text{m}$	$z_p$	$h_a \ln \frac{t_p}{T_c}$	see Eq. 5.15

where we have recognized that  $b = h_a$ . We refer to Eq. 5.7 as Model 1 and Eq. 5.6 as Model 2. Both depend solely on the spectral properties of the absorber and the source. Given the molar absorptivity,  $\epsilon(\lambda)$ , from Fig. 5.5, the absorption coefficient,  $\alpha(\lambda)$ , is

$$\alpha(\lambda) = \log(10)\epsilon(\lambda)C, \quad (5.8)$$

where the molar concentration,  $C$ , can be calculated from the w/w absorber concentration,  $C_{w/w}$ , in percent as

$$C = \frac{C_{w/w} \eta_P}{100 M_a} \quad (5.9)$$

in which  $\eta_P$  is the density of PEGDA and  $M_a$  is the absorber molar mass.

Fig. 5.6a and 5.6b show example calculations of  $D_n(z)$  using Eqs. 5.4 and 5.8 for three resins based on their measured absorption spectra and the light engine source spectrum. As seen in Fig. 5.5, both Irgacure 819 and NPS have good spectral overlap with the source spectrum, such that fitting Model 2 to the calculated  $D_n(z)$  yields  $a$  very close to 1, in which case  $b$  from Model 2 and  $h_a$  from Model 1 agree to within 5%. On the other hand, avobenzene does not have good spectral overlap with the source such that  $a < 0.9$ , and  $b$  and  $h_a$  differ by 60%. Note that for Irgacure 819 and NPS,  $D_n(z) \rightarrow 0$  as  $z \rightarrow \infty$ , whereas for avobenzene  $D_n(z) \rightarrow \sim 0.1$ . Hence at depths beyond

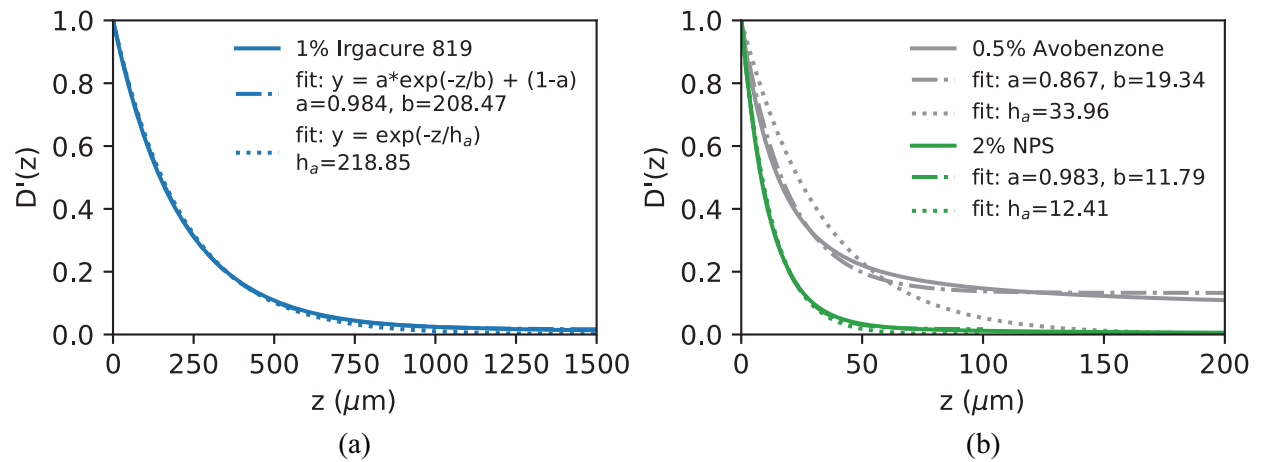


Figure 5.6: (a)  $D_n(z)$  calculated from molar absorptivity for 1% Irgacure 819 resin. (b) Same as (a) except for 1% Avobenzene and 2% NPS resins.

several  $h_a$ , NPS resin will remain largely unexposed, whereas avobenzene resin will continue to photopolymerize, making it unusable to fabricate small voids.

### Polymerization as a Function of Dose

The critical dose,  $D_c$ , on Line 4 in Table 5.3 is the dose required to just polymerize a resin for a given irradiance. This dose occurs at the leading edge of the polymerization thickness,  $z_p$ , which corresponds to a specific polymerization time,  $t_p$ . For the monochromatic case we can solve Line 4 for the polymerization time (using Line 5) as

$$\frac{t_p}{T_c} = e^{z_p/h_a}, \quad (5.10)$$

which leads to Eq. 5.1 for  $z_p$ , referred to as Model 3, which is also on Line 6.

For the polychromatic case we cannot obtain an analytic expression for the polymerization depth,  $z_p$ . Instead, we must solve for  $t_p$ . Beginning with Line 5,

$$T_c = \frac{D_c}{\int_0^\infty I_0(\lambda) d\lambda}, \quad (5.11)$$

and substituting for  $D_c$  (Line 4), we obtain

$$\frac{T_c}{t_p} = \frac{\int_0^\infty I_0(\lambda) e^{-\alpha(\lambda)z_p} d\lambda}{\int_0^\infty I_0(\lambda) d\lambda} \quad (5.12)$$

$$= D_n(z_p) \quad (5.13)$$

$$\approx (1 - a) + a \exp(-z_p/b), \quad (5.14)$$

where  $D_n(z)$  is the normalized dose defined in Eq. 5.3 and Eq. 5.14 is from Eq. 5.6. Solving for  $t_p$  we obtain

$$t_p = \frac{T_c}{(1 - a) + a \exp(-z_p/b)}. \quad (5.15)$$

In Chapter 3 we utilized a resin characterization method in which the polymerization thickness is measured for a series of exposure times, followed by fitting the data to Eq. 5.1 to determine



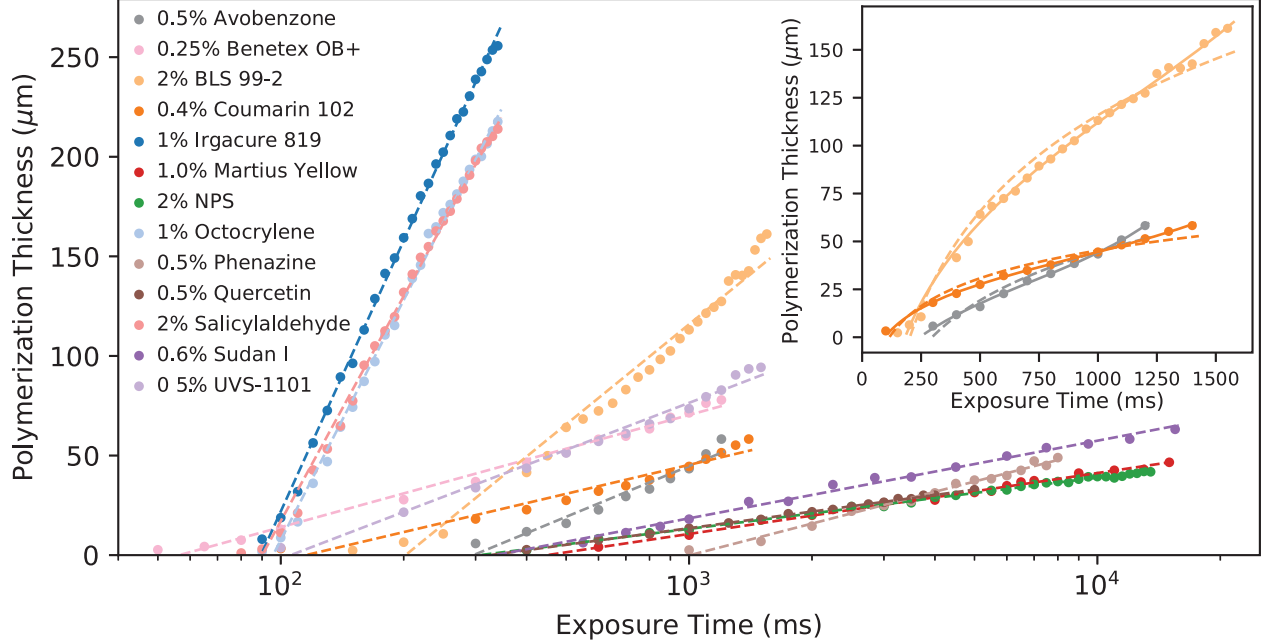


Figure 5.7: Measured polymerization thickness as a function of exposure time for 13 resins. Each resin contains 1% Irgacure 819 in addition to the specified UV absorber. Dashed lines indicate fit to Model 3. Inset shows that Model 4 (solid lines) is a better fit for some resins.

$h_a$  and  $T_c$ . We employ a similar method in this chapter, except that when there is poor spectral overlap between the absorber and the source spectrum, the polymerization behavior is better modeled by Eq. 5.15. We refer to Eq. 5.15 as Model 4. The fit parameters of Model 3 and 4 are based solely on measured polymerization thickness as a function of optical exposure time.

Fig. 5.7 shows the measured polymerization thickness as a function of exposure time for a wide selection of custom resins. In each case, the corresponding dashed line shows the fit to Model 3. The inset graph also shows the fit to Model 4 as solid lines for the three resins that have the poorest fit to Model 3 (1.0% avobenzone, 2% BLS 99-2, and 0.5% Coumarin 102).

The fits to Models 1 – 4 for all of the resins are shown in Table 5.4. When the fit for  $a$  in Models 2 or 4 is  $\sim 1$ , the absorber has good spectral overlap with the source. In this case Models 1 and 3 are valid and typically show good agreement with each other even though they are generated from completely different measurements, thereby indicating the consistency of our analysis methods.

In addition to good spectral overlap, we also require that  $h_a$  be suitably small in order to realize 3D printed channels with small vertical void size. We therefore restrict our choice of

Table 5.4: Summary of fit parameters based on measured spectra and on measured thickness vs. exposure time data. All resins are formulated with 1% Irgacure 819 in addition to the specified absorber.

Material	Solubility	Concentration	Fit from measured spectrum				Fit from measured thickness vs. exposure time					
			Model 1		Model 2		Model 3		Model 4			
			$h_a$ ( $\mu\text{m}$ )	$a$	$b$ ( $\mu\text{m}$ )	$h_a$ ( $\mu\text{m}$ )	$T_c$ (ms)	$a$	$b$ ( $\mu\text{m}$ )	$T_c$ (ms)		
<b>Photoinitiator</b>												
Irgacure 819	>5%	1%	218.85	0.98	208.47	196.13	89.42	1.00	193.40	88.21		
<b>UV Absorbers</b>												
Avobenzene	>5%	1%	15.10	0.92	10.70	20.00	283.23	0.84	10.49	258.93		
Benetex OB+	0.25%	0.25%	19.15	0.97	17.50	24.47	56.37	0.98	21.65	55.95		
BLS 99-2	>5%	2%	57.28	0.97	50.65	72.49	202.13	0.92	51.30	181.92		
Coumarin 102	0.8%	0.5%	11.98	0.97	11.03	19.55	123.59	0.95	12.00	90.90		
Martius Yellow	3%	1%	15.26	0.98	14.34	13.28	448.69	1.00	13.03	423.74		
NPS	>5%	2%	11.74	0.98	11.17	11.18	307.33	1.00	10.88	280.44		
NPS		3%	8.28	0.99	7.94	8.05	413.72	1.00	8.16	427.58		
Octocrylene	>5%	1%	194.96	0.98	184.13	173.84	95.75	1.00	173.00	95.27		
Phenazine	1.8%	0.5%	33.47	0.97	30.30	23.03	1005.38	0.96	19.51	936.94		
Quercetin	0.8%	0.5%	16.16	0.96	14.12	12.03	324.96	1.00	12.18	333.04		
Salicylaldehyde	>5%	2%	175.21	0.98	166.75	162.94	90.05	1.00	164.19	90.58		
Sudan I	2.7%	0.6%	18.08	1.00	17.99	16.92	335.62	1.00	14.95	227.14		
UVS-1101	0.5%	0.5%	31.20	0.98	28.92	34.03	105.75	0.96	24.11	78.80		

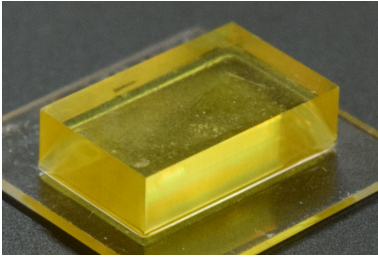
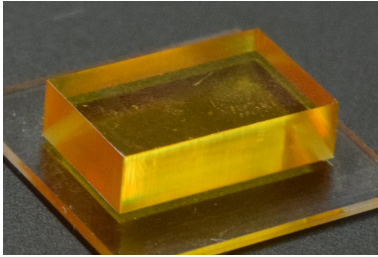
absorbers to those that can achieve the smallest  $h_a$ , which, in conjunction with previous criteria, limits the possible absorbers to Coumarin 102, Martius Yellow, NPS, Quercetin, and Sudan I.

### 5.2.2 Material Properties and Layer Dose

For a given irradiance and build layer thickness, the layer exposure time determines the dose and hence the degree of crosslinking in a layer. Smaller layer exposure times result in less crosslinking and hence less overall hardness and smaller Young's modulus. On the other hand, longer exposure time yields greater hardness and Young's modulus, but increases the exposure of resin in regions intended to be voids, thereby limiting the minimum vertical void size that can be achieved. There is thus a layer exposure time trade-off between material properties and minimum vertical void size. A resin that achieves adequate material properties with a smaller layer exposure time will yield a smaller vertical void size than a resin that requires a longer layer exposure time to obtain the same material properties.

As an example of the effect of two absorbers on material properties as a function of layer exposure time, consider 2% NPS and 1.2% Martius Yellow resins, which have  $h_a$  values of 11.2 and 9.8  $\mu\text{m}$ , respectively. Table 5.5 shows the results of Young's Modulus and Type A and D Shore durometer measurements. For 2% NPS, a layer exposure time of 280 ms yields a somewhat

Table 5.5: Comparison of Young's modulus and durometer measurements for NPS and Martius Yellow resins. Durometer measurements are unitless and Young's Modulus, E, is in MPa.

2% NPS				1.2% Martius Yellow			
							
$t_{exp}$ (ms)	A	D	E	$t_{exp}$ (ms)	A	D	E
280	86	21	3.5	500	84	—	2.7
400	94	52	6.6	1000	93	70	6.7
280 cured	97	75	7.7	500 cured	94	47	5.5

harder and stiffer material than a 500 ms layer exposure time for 1.2% Martius Yellow. When the materials undergo the same length post-print cure, the NPS resin still has greater hardness and Young's modulus. We therefore expect to achieve significantly smaller vertical void size with the NPS resin, which is consistent with my experimental observations.

In my experience making 3D printed valves and pumps in Chapter 4, post-print curing is necessary for long valve and pump operational lifetime. Since optical curing is necessary for the reasons discussed in Sect. 5.1.7, Sudan I is eliminated from consideration because its absorption spectrum extends far beyond the long wavelength limit of Irgacure 819 such that it cannot be optically cured to achieve good material properties.

### 5.2.3 Small Cross Section Channels

Our ultimate criterion for absorber selection is which absorber(s) result in the smallest cross section channels. Experimentally we find that Coumarin 102 can yield small channels only when they are close to the last exposed layer; deeper channels are always closed. We ascribe this to the fact that Coumarin 102 is fluorescent at 385 nm. Since fluorescent light is emitted at longer wavelengths than the excitation light, and much of it is beyond the long wavelength cutoff of Coumarin 102 absorption, the fluorescent light can penetrate deeper during printing such that resin in underlying channels is exposed and polymerized. Resin in channels near the surface do not receive enough dose from fluorescence in subsequent layers to become polymerized.

In the case of Quercetin, we found that small channel sizes could be fabricated, but they exhibited internal delamination. While it may be possible to find conditions in which this does not occur, we chose to focus our efforts on the remaining absorber, NPS.

### Channel Height

Extensive testing with 2% NPS reveals a set of conditions that repeatably result in the smallest possible channel height with essentially 100% yield. This can be illustrated with Fig. 5.8, in which scanning electron microscope (SEM) images of channel cross sections are shown for the smallest achievable channel height (30  $\mu\text{m}$ ) for layer thicknesses,  $z_l$ , of 5, 7.5, and 10  $\mu\text{m}$ . For 8.3  $\mu\text{m}$  layers, the smallest channel height is 25  $\mu\text{m}$ . A plot of normalized dose as defined

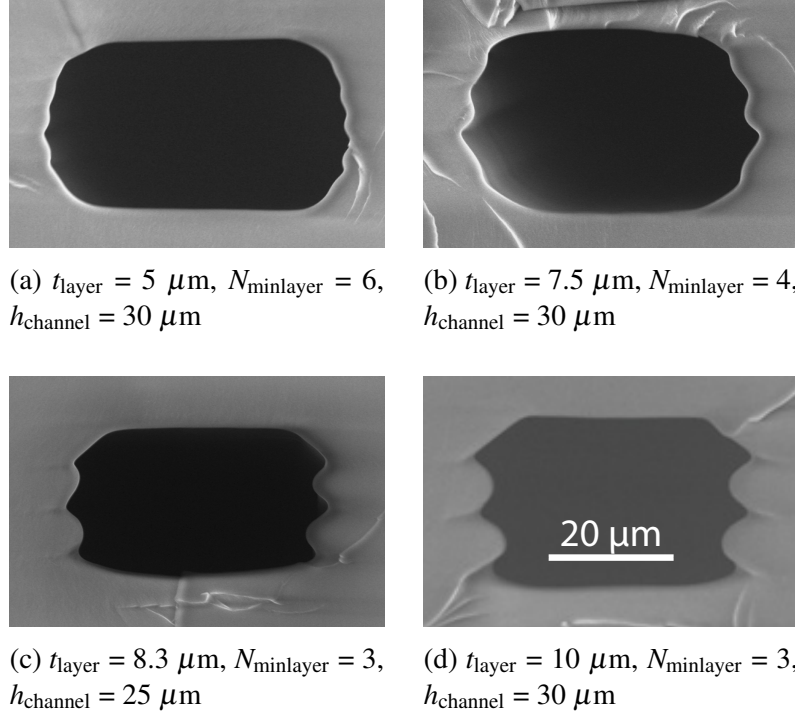


Figure 5.8: SEM images of flow channel cross sections for 2% NPS. See text for details. All channels are designed to be 4 pixels wide. Larger layer thickness results in larger vertical wall surface relief.  $t_{\text{layer}}$  is layer thickness,  $N_{\text{minlayer}}$  is the minimum number of layers for open channel, and  $h_{\text{channel}}$  is channel height.

in Chapter 3 ( $\Omega = D(z)/D_c$ )) is shown as a function of  $z/z_l$  for a generic case in Fig. 5.9 for the layers surrounding a flow channel intended to occupy layers 8-10. The normalized dose at the top of the channel is  $\Omega_{\text{tot},b}$ , which exponentially decays through the thickness of the channel. Successful channel formation requires that this exponential tail is small enough to avoid significant polymerization of resin in the channel.

Fig. 5.10 shows the calculated normalized dose for the actual experimental conditions of Fig. 5.8. An additional example case is shown for a  $25 \mu\text{m}$  channel made with  $5 \mu\text{m}$  layers, which never successfully forms clear channels. It is representative of many other parameter combinations that also fail. Experimentally, I find that the minimum height channel for a given layer thickness fulfills the following conditions: (1) the normalized dose at the back of the channel,  $\Omega_{c,b}$  is less than or equal to  $\sim 0.1$  and (2) the dose at the front of the channel,  $\Omega_{\text{tot},b}$  is such that it decays to less than or equal to  $\sim 1$  at a distance of  $L_{\text{min}}$  above the bottom of the channel, where  $L_{\text{min}}$  is given

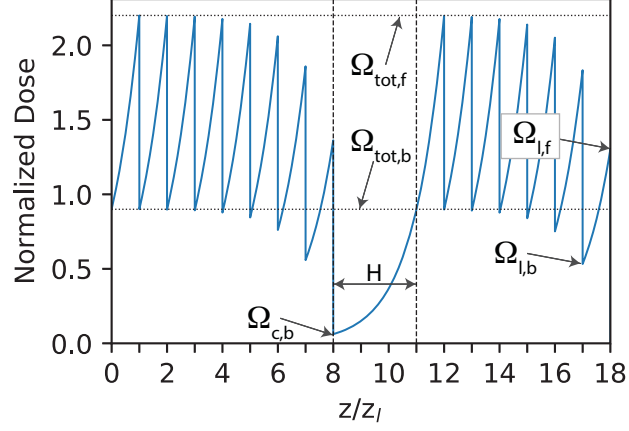


Figure 5.9: Normalized dose as a function of normalized depth.

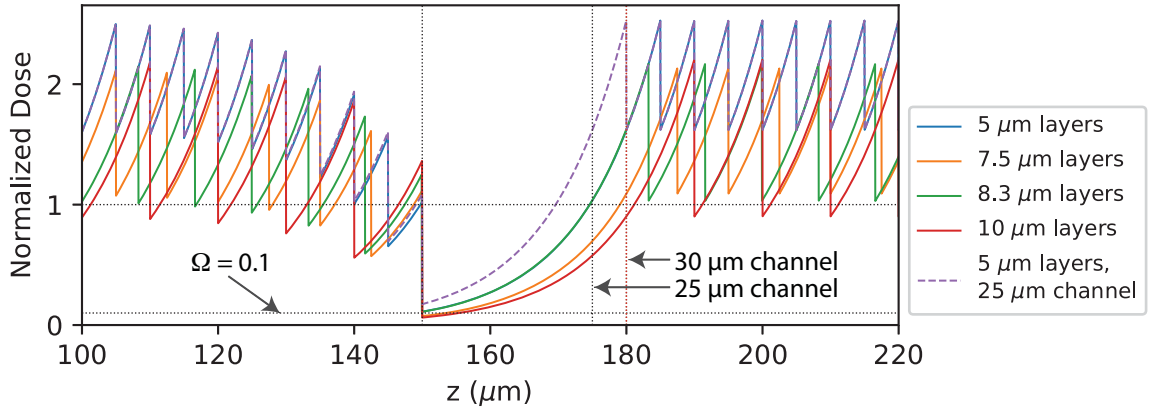


Figure 5.10: Calculated dose as a function of depth for the cases in Fig. 5.8.

by

$$L_{min} \approx -h_a \log(0.1) \quad (5.16)$$

$$= 2.3h_a. \quad (5.17)$$

Careful examination of the first 4 cases shown in Fig. 5.10 shows that these condition are fulfilled ( $2.3h_a = 25 \mu\text{m}$  for 2% NPS), whereas for the last case the second condition is not fulfilled ( $\Omega$  is  $\sim 1.7$  at  $25 \mu\text{m}$ ).

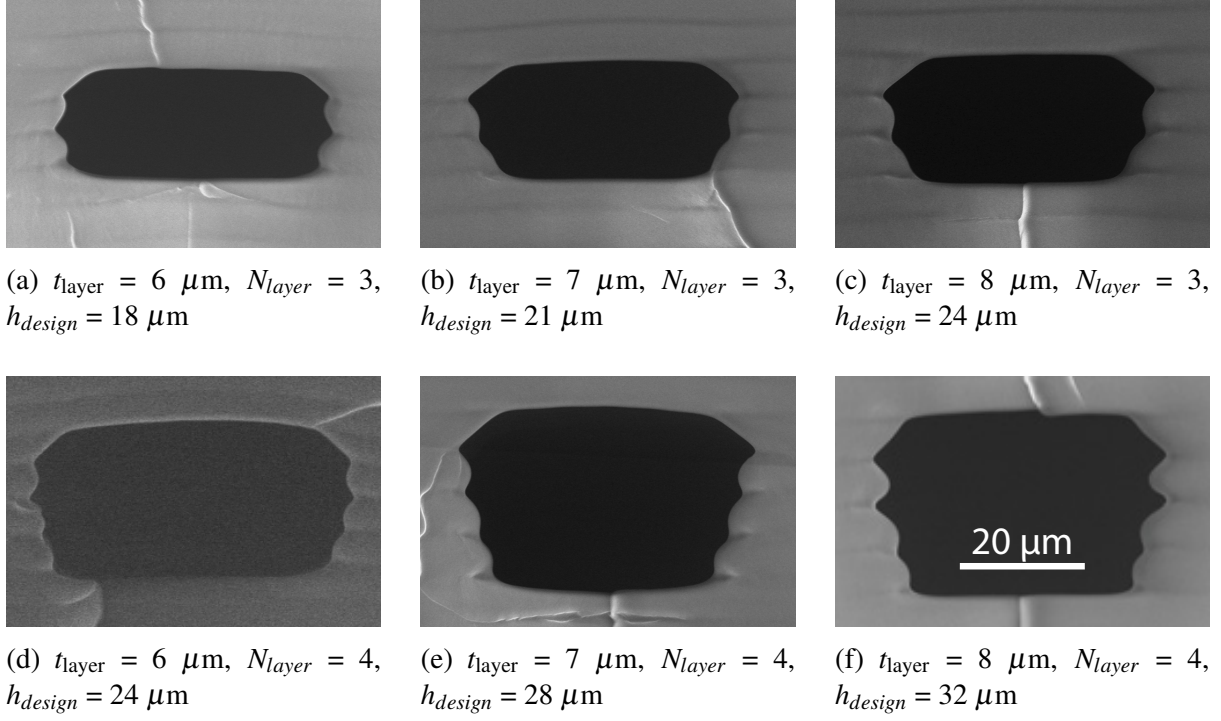


Figure 5.11: Same as Fig. 5.8 except for 3% NPS.  $t_{\text{layer}}$  is layer thickness,  $N_{\text{layer}}$  is number of layers, and  $h_{\text{design}}$  is the designed channel height.

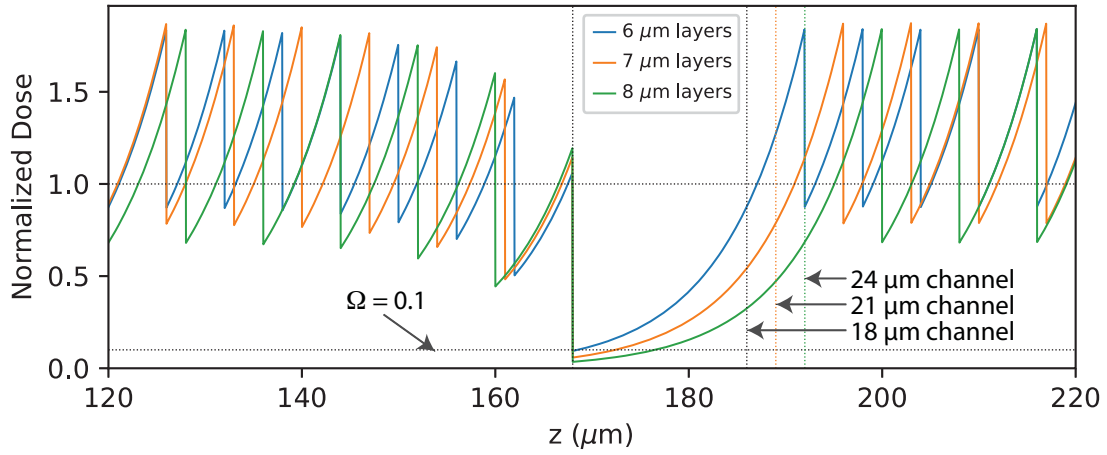


Figure 5.12: Calculated normalized dose as a function of depth for the 3 layer cases in Fig. 5.11

The smallest possible channel height is realized when the designed channel is 3 layers thick with a height  $L_{\text{min}}$ , in which case the normalized layer thickness,  $\zeta_l$ , is

$$\zeta_l = z_l / h_a \quad (5.18)$$

$$\approx 0.77. \quad (5.19)$$

Channels larger than this are possible with other layer thicknesses as long as conditions (1) and (2) are fulfilled.

To test whether this model is predictive, consider 3% NPS resin for which  $h_a = 8 \mu\text{m}$ , in which case

$$L_{min} = 2.3h_a = 18 \mu\text{m} \quad (5.20)$$

$$z_l = L_{min}/3 = 6 \mu\text{m} \quad (5.21)$$

$$\zeta_l = z_l/h_a = 0.75. \quad (5.22)$$

Fig. 5.11 shows the corresponding results where the 3 layer  $18 \mu\text{m}$  channel is clearly open, as are 3 layer channels with 7 and  $8 \mu\text{m}$  layers. The calculated normalized dose as a function of  $z$  in Fig. 5.12 clearly fulfills the model's conditions for all cases. As seen in the second row of SEM images in Fig. 5.11, increasing the channel height by adding more layers always results in open channels.

### Channel Width

The designed channel width for all of the cases presented so far is 4 pixels ( $30 \mu\text{m}$ ). Consistent with our results in Chapter 3, we found this to be the minimum channel width that gives 100% yield. However, the physical width of the channels in Figs. 5.8 and 5.11 is wider than the designed width by the equivalent of 1 to 2 pixels. This can be explained by noting that the teflon film at the bottom of the resin tray is slightly cloudy. It therefore causes scattering of the light imaged through it, which broadens the effective exposure region of each pixel that is turned on. Lack of exposure for the pixels in the channel reduces the dose received at the edges of the channels to below the polymerization threshold.

We have developed a channel narrowing method that compensates for this lack of sufficient dose at channel edges. The left image in Fig. 5.13a shows a typical primary exposure pattern for a single layer containing a flow channel where white and black regions correspond to full exposure and no exposure, respectively. The right image is a second exposure of the same layer where only the 1 or 2 pixels adjacent to the channel are exposed. Fig. 5.13b and 5.13c show the effect of 1 and 2 pixel edge exposures for different exposure times for 2% and 3% NPS resin, respectively.



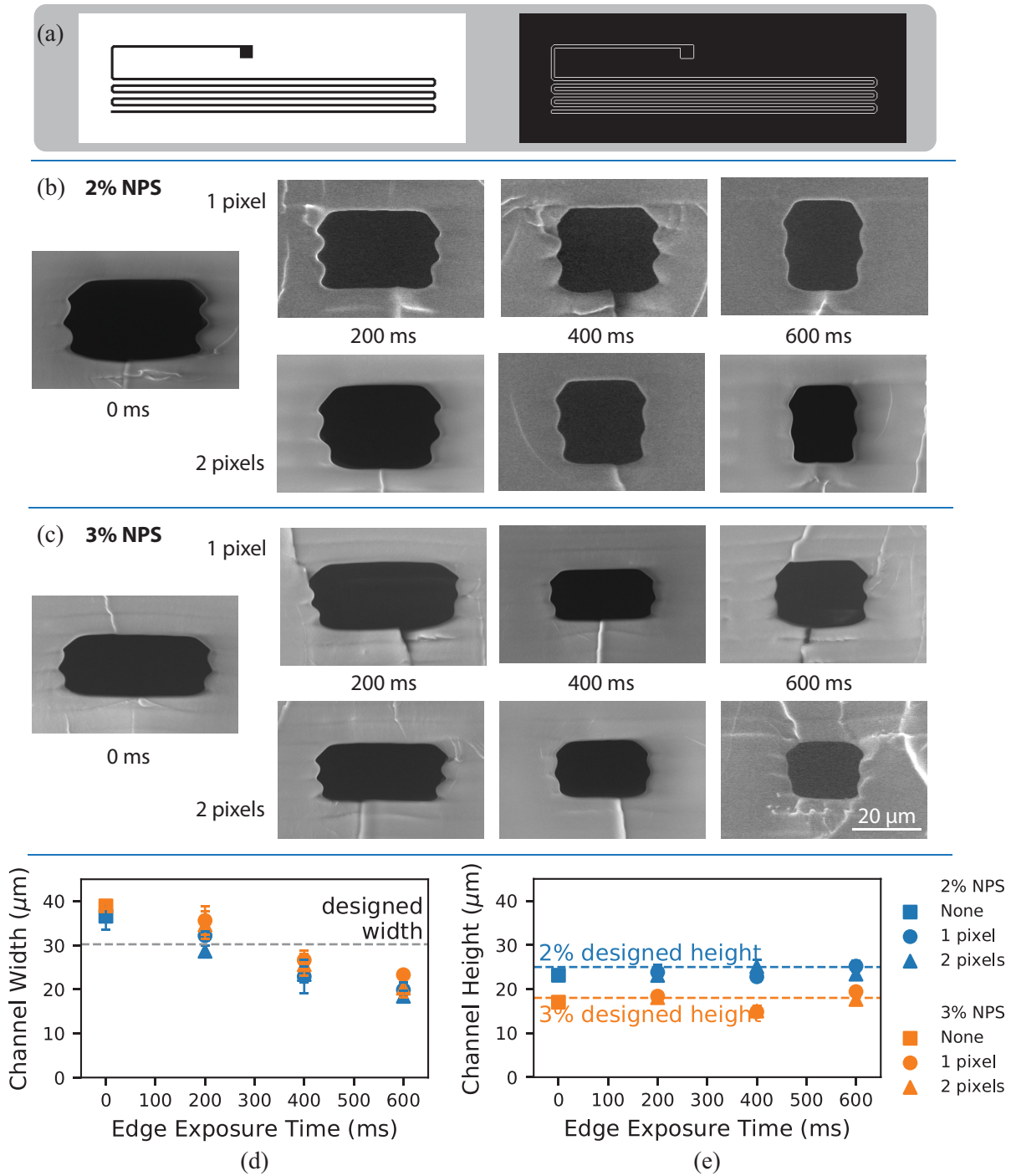


Figure 5.13: (a) Primary and additional edge exposure patterns for a single layer containing a flow channel. (b) Channel narrowing for 2% NPS resin for additional edge exposure. The build layer size is  $8.3 \mu\text{m}$  layers and the designed flow channel height is  $25 \mu\text{m}$ . (c) Same as (b) except for 3% NPS resin with  $6 \mu\text{m}$  layers and a designed flow channel height of  $18 \mu\text{m}$ . (d), (e) Measured channel width and height, respectively, as a function of edge exposure time.

This strategy is clearly very effective in narrowing the channel width, which is further illustrated in Fig. 5.13d where the measured channel width is plotted as a function of the edge exposure time. The width can be reduced from nearly  $40\text{ }\mu\text{m}$  to  $20\text{ }\mu\text{m}$ . As shown in Fig. 5.13e, the edge dose has no effect on the channel height (as expected). The final result is that  $18\text{ }\mu\text{m} \times 20\text{ }\mu\text{m}$  channels can be consistently fabricated with 3% NPS resin.

#### 5.2.4 Long Channels

As an illustration of the efficacy of our approach, consider the fabrication of serpentine channels in Fig. 5.14 in 3% NPS resin with a 1 pixel 400 ms edge exposure. A microscope image of a single layer serpentine channel is shown in Fig. 5.14a. Note the excellent optical clarity of imaging through the microscope slide substrate into the interior of the 3D printed device. A 3D

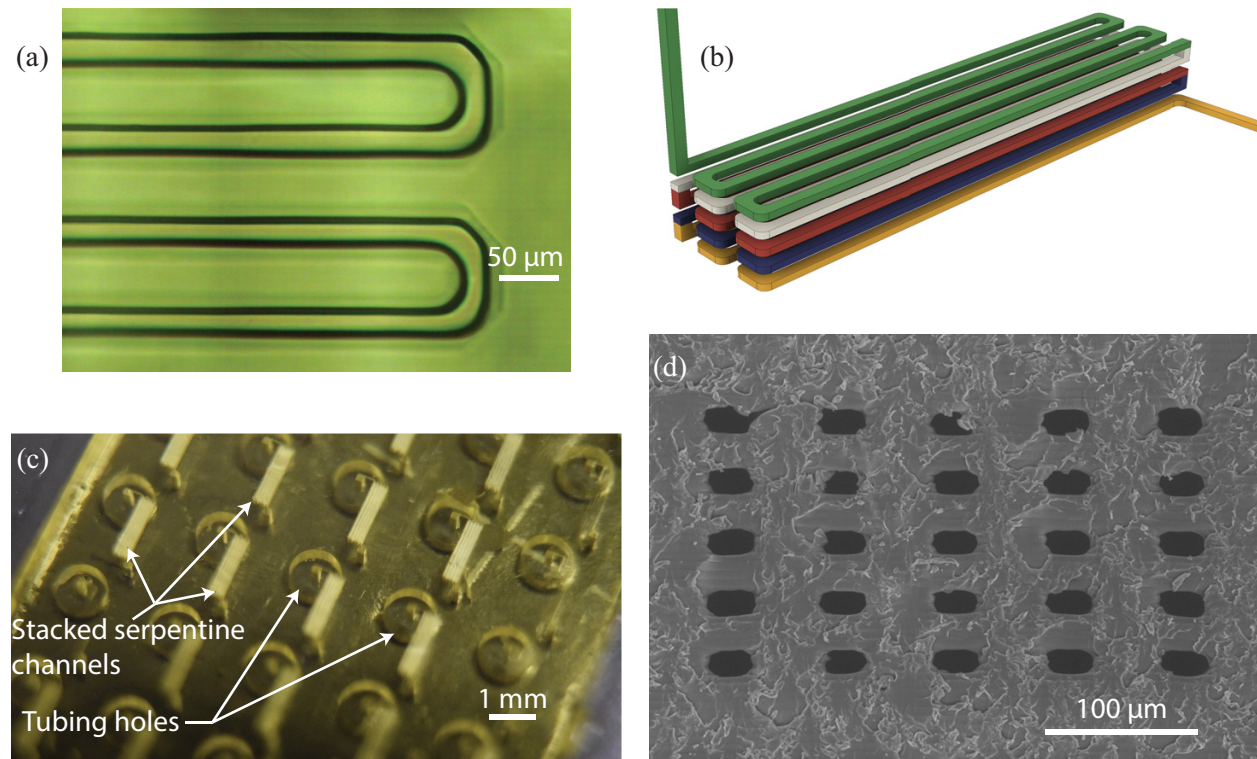


Figure 5.14: (a) Microscope photograph of single layer serpentine channel. (b) Schematic illustration of 3D stacked serpentine channel design. Each layer is shown as a different color. (c) Photograph of 3D printed device with 24 3D serpentine channels. The photo is taken through the glass slide on which the device is 3D printed. (d) SEM image of 3D serpentine channel cross section.

serpentine channel design is shown in Fig. 5.14b, with a photograph of a device containing 24 3D channels in Fig. 5.14c. An SEM cross section is shown in Fig. 5.14d. The channel is 41 mm long and occupies a volume of only  $1.56 \text{ mm} \times 0.38 \text{ mm} \times 0.21 \text{ mm} = 0.12 \text{ mm}^3$ .

### 5.2.5 Tall High Aspect Ratio Channel

As a further demonstration, consider the high aspect ratio channel shown in Fig. 5.15, fabricated with  $5 \mu\text{m}$  layers, 4 pixels wide in 2% NPS with 2 pixel 400 ms edge exposure. Since we are not going for the minimum channel height, we can use a smaller layer thickness to decrease the sidewall surface relief that naturally occurs due to the layered nature of the 3D printing process.

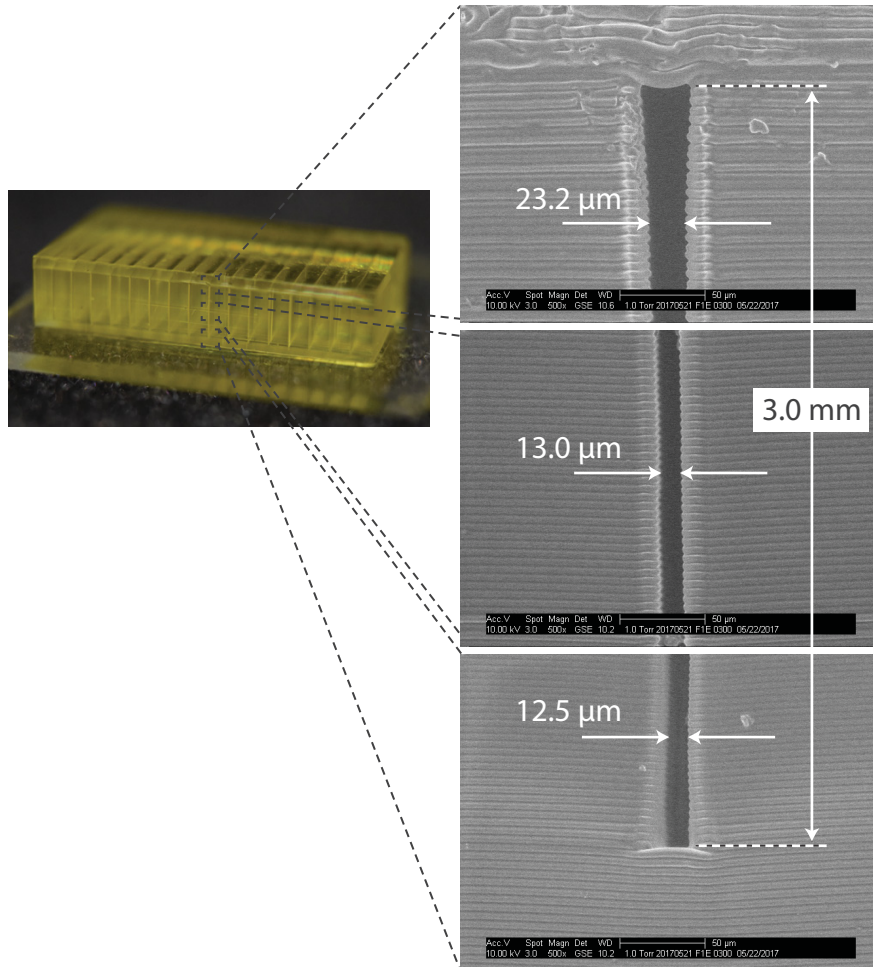


Figure 5.15: Photograph and SEM images of 3D printed high aspect ratio flow channel.

The channel width is  $<25\text{ }\mu\text{m}$  and its height is 3 mm (its length is 12 mm). Such channels are useful in nanoscale liposome synthesis for drug delivery as discussed in Ref. 89.

### 5.3 Conclusions

In summary, we have shown that DLP-SLA is fully capable of 3D printing truly microfluidic flow channels with designed cross sectional areas as small as  $18\text{ }\mu\text{m} \times 20\text{ }\mu\text{m}$ . The out-of-plane void size is dependent on formulating a resin that adequately limits optical penetration during each layer exposure, which requires that the absorber's absorption spectrum fully cover the source spectrum. Small in-plane (x-y) void size is a function of the projected image resolution with a minimum width of 4 pixels. We have also shown that an additional edge dose for each layer containing a flow channel is an effective method of narrowing flow channel width. Taken together, these advances open the door for 3D printing to displace conventional microfluidic fabrication methods such as soft lithography.

## CHAPTER 6. 3D PRINTED HIGH DENSITY, REVERSIBLE, CHIP-TO-CHIP MICROFLUIDIC INTERCONNECTS

Previously in Chapter 3 and 4, we demonstrated that our earlier custom resin and commercial 3D printer work ( $60\text{ }\mu\text{m} \times 108\text{ }\mu\text{m}$  cross section flow channels) enabled dense 3D layout of devices that included integrated valves and pumps. We are now applying our custom 3D printer and resin from Chapter 5 to realize even smaller valves and pumps, in which we see a  $30\times$  reduction in valve volume compared to the work in Chapter 4. Our expectation is that fully using all 3 spatial dimensions for component layout in conjunction with our new materials and methods will routinely result in 3D printed microfluidic devices with volumes on the order of  $10\text{ mm}^3$  or less. With such small size (only a few mm on a side), we anticipate that many devices (tens to  $\sim 100$ ) can be simultaneously printed in a single one hour 3D print run, thereby launching the possibility of using 3D printing for not only device prototyping, but also device manufacturing. This would have a profound impact on the microfluidics development process by eliminating the current separation between prototyping and manufacturing, which typically rely on entirely different processes and materials resulting in two independent and expensive development cycles, and instead consolidate them to use the same tools and materials.

A critical aspect of realizing this vision is being able to make tens to possibly hundreds of interconnections to such small chips in order to provide the necessary fluid and pneumatic i/o's. However, current world-to-chip interconnect methods achieve an areal density of at best  $1/\text{mm}^2$ , [90]–[100] and are therefore unsuitable for this purpose. In this chapter we propose that the world-to-chip interface be delegated to a separate, larger interface chip that in turn is connected through a new high density chip-to-chip interconnect to a much smaller device chip. This chip-to-chip interconnect method is designed to meet the following criteria: (1) support large numbers of interconnects at (2) high density ( $10\text{'s}/\text{mm}^2$ ) while (3) withstanding pneumatic and fluid pressures typical for 3D printed microfluidic valves and pumps (at least 20 psi) and that are (4) reusable and (5) easy to align and connect. We show that these objectives can be achieved with a Simple

Integrated Microgasket (SIM) that is directly 3D printed as part of a device chip. Moreover, we show that a more refined Controlled-Compression Integrated Microgasket (CCIM) can be directly integrated with no increase in fabrication time or complexity because of the ease of 3D printing. In both cases we demonstrate  $11 \times 11$  arrays of interconnects in an area of  $1.5 \text{ mm} \times 1.5 \text{ mm}$  ( $53 \text{ interconnects/mm}^2$ ) that withstand 100 separations and re-connections with no degradation in performance for an applied pressure up to 50 psi. We then investigate the scaling properties of CCIMs by demonstrating a  $20 \times 20$  array of interconnects in an area of  $3.0 \text{ mm} \times 3.0 \text{ mm}$ , and by showing that the areal density can be increased to  $88 \text{ interconnects/mm}^2$ . In short, using our approach, large numbers of high density chip-to-chip interconnects can be readily formed as part of a 3D printed microfluidic device (including alignment structures) with no requirement for additional materials or separately fabricated parts, thereby facilitating the vision outlined above [101].

Finally, to illustrate the utility of CCIM interconnects to accommodate a large number of world-to-chip connections, we use a spatially distributed set of discrete CCIMs as part of testing our new, miniaturized 3D printed pneumatic membrane valves that are only  $300 \text{ }\mu\text{m}$  in diameter. We demonstrate 28 world-to-chip connections in an interface chip with 28 chip-to-chip CCIMs to do lifetime testing of 45 valves arranged in a  $9 \times 5$  array in a device chip.

The work in this chapter is reported in Ref. 102.

## 6.1 Materials and Methods

### 6.1.1 3D Printer and Materials

The 3D printer used in this work is the custom 3D printer we describe in Chapter 5 with a 385 nm LED light source and a pixel pitch of  $7.56 \text{ }\mu\text{m}$  in the plane of the projected image. The photopolymerizable resin is poly(ethylene glycol) diacrylate (PEGDA, MW258) resin with 1% (w/w) phenylbis(2,4,6-trimethylbenzoyl)phosphine oxide (Irgacure 819) photoinitiator and 2% (w/w) 2-nitrophenyl phenyl sulfide (NPS) UV absorber described in the same chapter, which also details the suppliers we use for these materials.

### 6.1.2 3D Printing

3D prints are fabricated on diced and silanized glass slides, as detailed in Chapter 5. Each slide is prepared by cleaning with acetone and isopropyl alcohol (IPA), followed by immersion in 10% 3-(trimethoxysilyl) propyl methacrylate in toluene for 2 hours. After silane deposition slides are kept in toluene until use. The build layer thickness is 10  $\mu\text{m}$ , and each build layer is exposed with a measured optical irradiance of 21.2  $\text{mW cm}^{-2}$  in the image plane. Unless otherwise noted, the layer exposure time is 600 ms. After printing, unpolymerized resin in interior regions is gently flushed with IPA, followed by device UV curing in an inexpensive consumer UV nail curer (54 Watt Professional UV Nail Dryer, Royal Nails) that emits a broad spectrum [62].

### 6.1.3 Surface Roughness Measurement

Surface roughness measurements are made with a 3D printed rectangular block comprised of 4 adjacent equal-area regions, each of which has a different layer exposure time (600, 800, 1000, and 1200 ms). After fabrication, the surface roughness is measured in three different  $\sim 0.1 \text{ mm}^2$  areas in each exposure region and the average root-mean-square (RMS) roughness is calculated based on these measurements. Measurements are made with a Zeta-20 3D optical profiler (Zeta Instruments, San Jose, California) using a 10 $\times$  objective lens.

### 6.1.4 Pressure and Reusability Measurements

For pressure testing, an interface chip and test chip are aligned and clamped together with a custom aluminum clamp as shown in Figs. 6.1a and 6.1b. The test chip and interface chip are first fitted together using the matching 3D printed alignment features on each chip. These are then placed between machined aluminum pieces that have central cut-outs to facilitate optical access to the test and interface chips. O-rings are used on the interior lips of the aluminum pieces to avoid direct contact between the metal and glass slides on which the chips are 3D printed. The only tool required is a hex key which is used to gently (using two fingers) torque the four screws that hold the aluminum pieces together.

To test the performance of a single microgasket, a syringe pump is used to pressurize a given interconnect through its specific chip-to-world interface as shown in Fig. 6.1c. Pressure



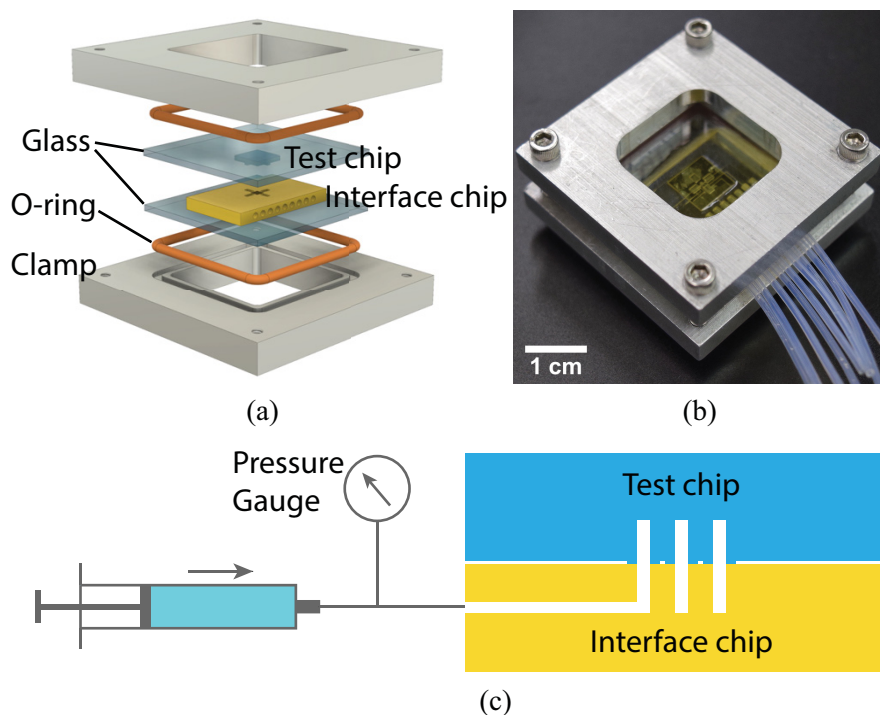


Figure 6.1: (a) Clamping mechanism for interface and test chips. (b) Photo of clamped interface and test chips ready for pressure testing. (c) Schematic illustration of pressure test set up. Syringe pump is connected sequentially to individual tubes to pressure test each associated interconnection port microgasket (see text for details).

is monitored with an electronic pressure transducer as the syringe pump pushes deionized (DI) water into the test chip at a flow rate of  $50 \mu\text{L}/\text{min}$ . Any compromise in the seal integrity of the microgasket manifests itself as a drop in pressure, which is readily measured with the pressure transducer.

The same basic process is used to test the  $11 \times 11$  interconnection arrays in Sections 6.2.2 and 6.2.3 except that a parallel technique is applied in which 120 (out of 121) interconnects on the interface chip are routed to a single PTFE tube such that they can all be pressurized simultaneously using a syringe pump. (See Chapter 4 for details on PTFE tubing and our attachment method.) If there is any leakage between the microgaskets and the interface chip, the pressure is released through the 121<sup>st</sup> interconnect which is deliberately fabricated with an incomplete microgasket, and which is connected to a second PTFE tube. Microgasket leakage therefore manifests itself as not only a drop in pressure, but also the appearance of DI water in the second PTFE tube. To test the reusability of the interconnections between the interface and test chips, the clamp mechanism



and interface and test chips for the  $11 \times 11$  interconnection arrays in Sections 6.2.2 and 6.2.3 are disassembled after a pressure test, followed by re-assembly and another pressure test. This is repeated 100 times.

## 6.2 Results and Discussion

### 6.2.1 Concept

The basic idea of using an interface chip to act as a chip-to-world intermediary for a small device chip is shown in Fig. 6.2a, where, as an example, 9 cylindrical recesses for PTFE tubing are

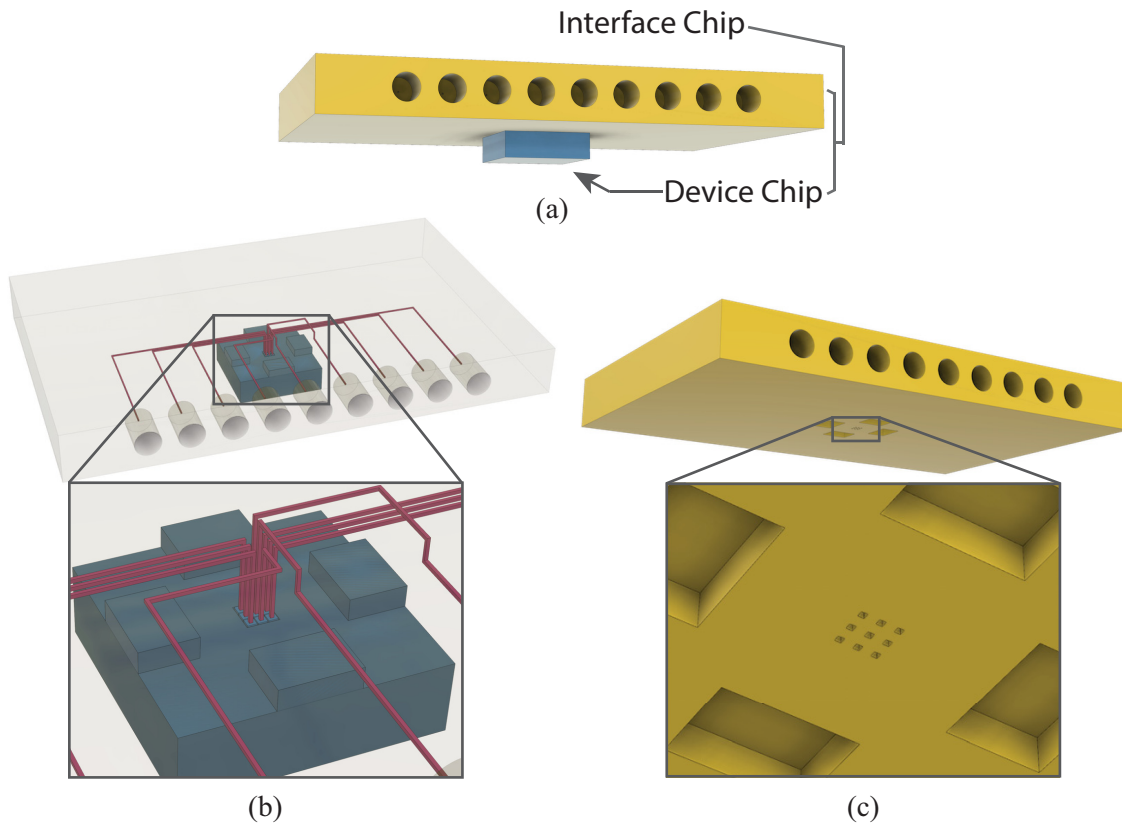


Figure 6.2: (a) Schematic illustration of a  $3.4 \text{ mm} \times 3.4 \text{ mm} \times 1 \text{ mm}$  device chip connected to an interface chip (clamping mechanism not shown). The interface chip supplies a world-to-chip interface with an array of cylindrical recesses into which PTFE tubing is epoxied. (b) Schematic illustration of the interior of the interface chip showing how channels are routed from the cylindrical recesses to an array of interconnects on the device chip. Alignment blocks on the top of the device chip are also visible. (c) Underside of interface chip. Close-up shows that interconnects consist of an array of flow channels that terminate on the flat bottom surface of the chip, and that the device chip alignment blocks fit into recesses on the interface chip.

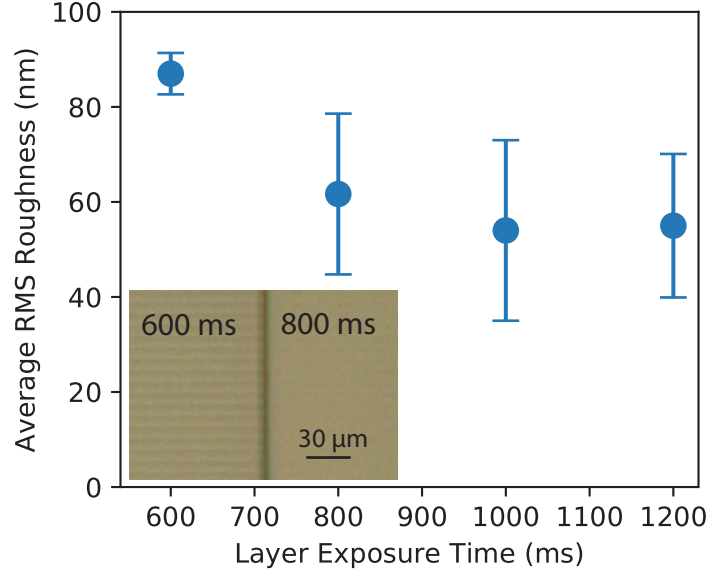


Figure 6.3: Measured average surface roughness as a function of layer exposure time. The error bars indicate the standard deviation of the three measurements for each exposure time that are described in Sect. 6.1.3. Inset: microscope photo of device with adjacent regions having 600 and 800 ms layer exposure times. Faint pixelation is more observable for the former than the latter.

shown as the world interface on one edge of the chip, and on the bottom of the chip is a small  $3 \times 3$  array of vertical channels (Figs. 6.2b and 6.2c) that interface with a matching set of channels on the device chip.

Alignment of the two chips is achieved with four rectangular recesses in the bottom of the interface chip (Fig. 6.2c) into which fit matching rectangular blocks on the device chip (Fig. 6.2b). We typically design the width of the rectangular blocks to be 2 pixels wider than the recesses to account for slight material shrinkage and to ensure a snug fit. With this approach we generally see an alignment accuracy of approximately one pixel between the vertical channels on the interface and device chips. Also, the recesses are designed to be deeper than the height of the blocks so that the lower surface of the interface chip contacts the upper surface of the device chip when they are clamped together as in Fig. 6.1.

Fortunately, horizontal surfaces as fabricated in our custom 3D printer are exceptionally smooth. As seen in Fig. 6.3, the average RMS surface roughness is 87 nm for a layer exposure time of 600 ms. The roughness is primarily due to slightly depressed pixel edges as seen in the inset Zeta-20 microscope image as a barely visible square pattern of lines. This in turn is presumably

due to the slightly lower optical dose along the projected pixel edges compared to the interior of each pixel region. Lower dose means less crosslinking in the polymer matrix such that some of the material may be marginally soluble in the isopropyl alcohol rinse that follows 3D printing. Note that as the layer dose increases, the average RMS roughness decreases until it asymptotes to  $\sim 55$  nm. Compared to the 600 ms layer exposure time, an increase of 33% to 800 ms results in a noticeably decreased square pattern in the inset image, indicating that more of the photopolymerized material at the pixel edges remains as part of the final print after rinsing. Since the RMS roughness is already very small at 600 ms exposure time, we choose to use this exposure in our tests since longer exposure times involve a tradeoff with the minimum achievable channel height [46], [61], [62]. We believe that the smooth as-printed horizontal surfaces in conjunction with the modest flexibility of our 3D printed material (Young's modulus  $\sim 7$ -8 MPa) [62] are the fundamental reasons that our high density interconnects work so well.

### 6.2.2 Simple Integrated Microgasket (SIM) Approach

A simple approach to forming leak-free interconnects is shown in Fig. 6.4a in which a square microgasket is printed around each vertical channel on the device chip. We find that tall microgaskets ( $D = 100 \mu\text{m}$ ) typically do not survive more than one clamping event in that many

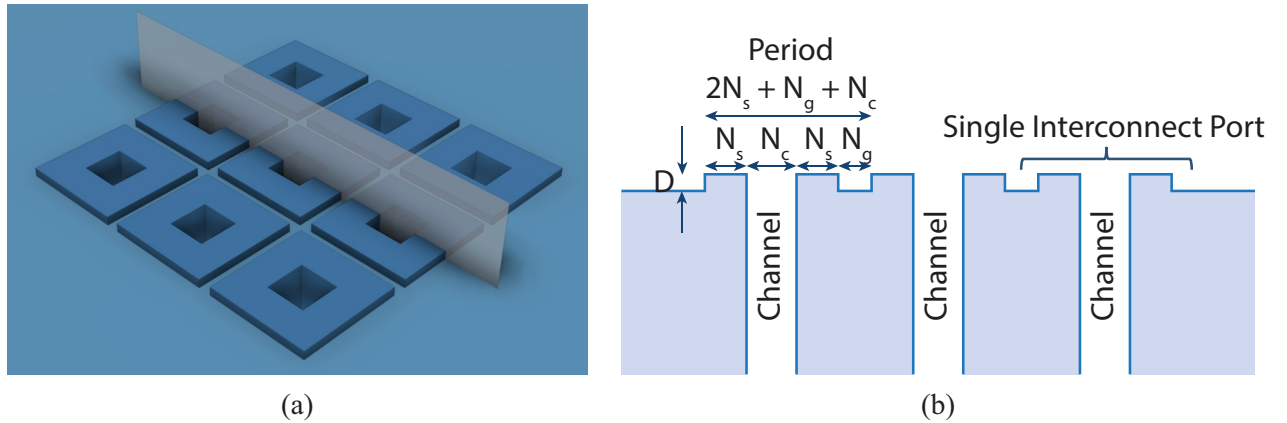


Figure 6.4: SIM design. (a) Integrated square microgaskets printed around each vertical channel on the top surface of a device chip. The top surface is in the XY plane with the Z direction being out of the plane. (b) Schematic illustration of the cross section of the vertical plane indicated in (a). The microgaskets have height  $D$  above the surrounding planar surface of the chip.

of the microgaskets become crushed. However, if the microgasket is only  $10\text{ }\mu\text{m}$  thick (i.e., one build layer), it survives a clamping event without noticeable damage.

A schematic cross sectional profile of the microgaskets and channels is shown in Fig. 6.4b. A channel is  $N_c$  pixels wide surrounded by a microgasket with a  $N_s$  pixel wide sealing surface and a gap of  $N_g$  pixels with the next microgasket. The period is

$$N_{per} = 2N_s + N_c + N_g \quad (6.1)$$

pixels, with a physical period of  $7.56\text{ }\mu\text{m}$  times  $N_{per}$ .

Table 6.1: Experimentally tested interconnect array sizes and periods.

Leak-free?	Array	$N_c$	$N_s$	$N_g$	Period (pixels)	Period ( $\mu\text{m}$ )	Density ( $\text{mm}^2$ )
Y	$3 \times 3$	6	6	6	24	182.4	30.0
Y	$11 \times 11$	6	5	4	20	152	43.3
Y	$11 \times 11$ $20 \times 20$	6	5	2	18	136.8	53.4
Y	$11 \times 11$	6	4	1	15	114	76.9
Y	$11 \times 11$	6	3	2	14	106.4	88.3
N	$11 \times 11$	6	3	1	13	98.8	102.4
N	$11 \times 11$	6	2	2	12	91.2	120.2
N	$11 \times 11$	6	2	1	11	83.6	143.1

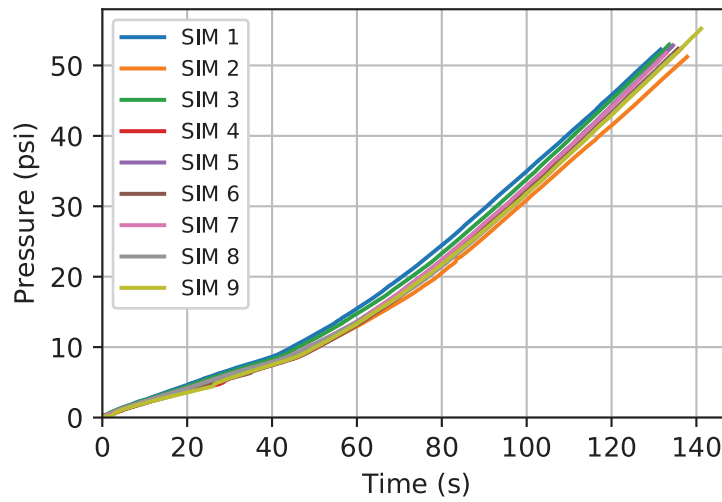


Figure 6.5: Using the device and interface chips in Fig. 6.2 for each of the 9 SIM in Fig. 6.4.

We fabricated the interface and device chips shown in Fig. 6.2 (the latter with SIM microgaskets having a microgasket height of  $D = 10\ \mu\text{m}$ ) with an interconnection period of 24 pixels ( $182.4\ \mu\text{m}$ ) in both X and Y for an areal density of 30 interconnects/ $\text{mm}^2$  (see Table 6.1 for geometry details). Pressure test results for each of the 9 interconnects are shown in Fig. 6.5, in which the pressure that builds up during syringe pump operation is shown as a function of time for each of the tests. In all cases, the pressure rises monotonically to  $\sim 50$  psi, at which point the test is terminated because leaks develop in the testing setup itself (i.e., the syringe gasket and various PTFE tube-to-tube connections). For each test, there is no evidence of leakage in the corresponding interconnect port, indicating that the ports maintain their integrity to at least 50 psi.

To test a larger number of interconnects at higher density, we designed an  $11 \times 11$  array of interconnects as shown in Fig. 6.6 with a period of 18 pixels ( $136.8\ \mu\text{m}$ ) in both X and Y for an areal density of 53 interconnects/ $\text{mm}^2$  (third row in Table 6.1), and a microgasket height of  $D = 10\ \mu\text{m}$ . Note that the fidelity and uniformity of the microgasket and vertical channel features is

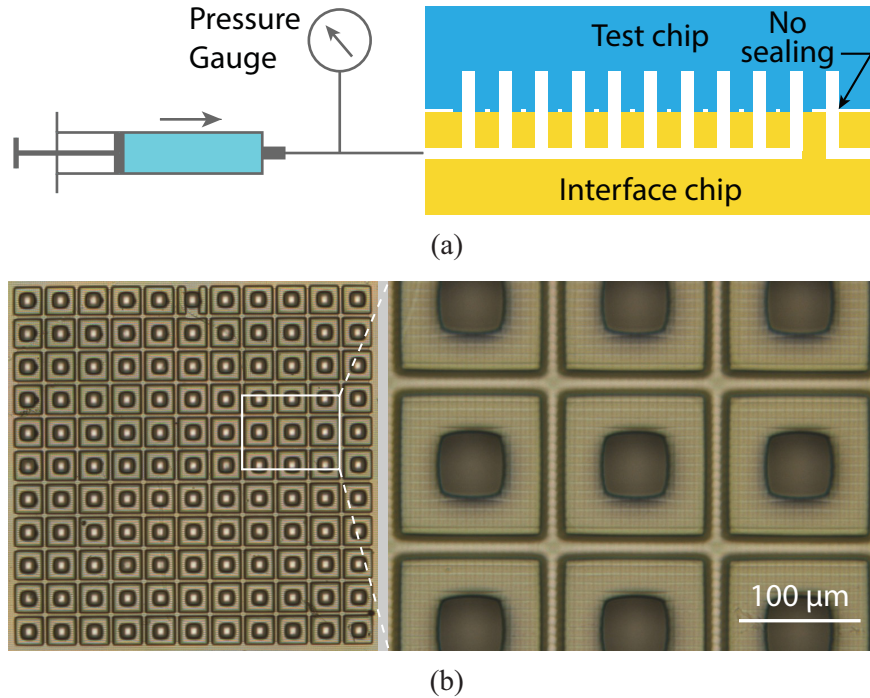


Figure 6.6: (a)  $11 \times 11$  interconnect array test set up. (b) Composite image from four Zeta-20 microscope images of fabricated  $11 \times 11$  array of SIMs. Close up shows details of SIMs, including slight pixelation of the sealing surface.

excellent, which is typical for the many SIM and CCIM devices we have 3D printed over several months.

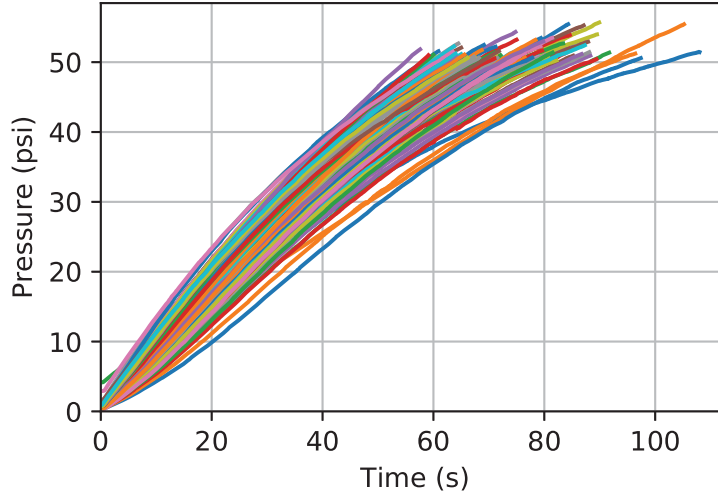


Figure 6.7: Pressure as a function of time for the test set up in Fig. 6.6a repeated 100 times.

The results of pressure testing for 100 repeated tests are shown in Fig. 6.7. The pressure that builds up during syringe pump operation is shown as a function of time for each of the runs. In all cases, there is no evidence of leakage in the interconnect ports, indicating that the ports maintain their integrity to at least 50 psi. As before, testing is terminated at 50 psi due to leaks in the testing apparatus.

### 6.2.3 Controlled-Compression Integrated Microgasket (CCIM) Approach

After 100 pressure tests, the planar surface of the interface chip for the SIM case begins to show slight signs of wear when observed in the Zeta-20. We therefore investigated an alternate microgasket design in which the compression of the microgasket is controlled by the geometry of the design (CCIM), as shown in Figs. 6.8a and 6.8b. The design features square microgaskets in a recessed region. The microgasket height,  $L$ , is  $100\text{ }\mu\text{m}$  and the recess is  $90\text{ }\mu\text{m}$  such that  $D = 10\text{ }\mu\text{m}$  as for the SIM case. When the CCIMs on a device chip are clamped to an interface chip, the microgaskets compress  $10\text{ }\mu\text{m}$  (i.e., 10% of their height) because the planar surface of the interface chip lands on the surrounding planar surface of the device chip, preventing further

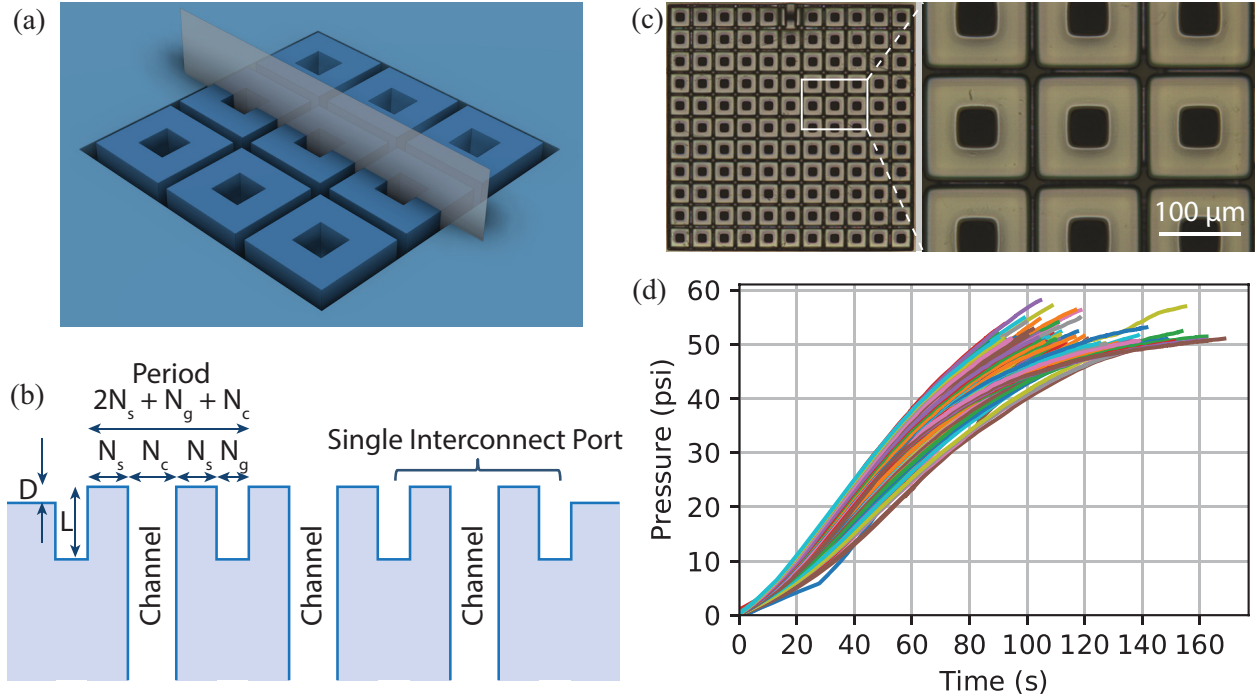


Figure 6.8: CCIM design. (a) Integrated microgaskets printed around each vertical channel in a square recess. (b) Schematic illustration of the cross section of the vertical plane in (a). The microgaskets have height  $D$  above the surrounding planar surface of the chip. (c) Composite image from four Zeta-20 microscope images of fabricated  $11 \times 11$  array of CCIMs. Close up shows details of CCIMs. (d) Pressure as a function of time for the test set up in Fig. 6.6a repeated 100 times.

compression of the microgaskets. This therefore limits the amount of force the microgaskets exert on the corresponding planar surface of the interface chip.

A fabricated  $11 \times 11$  CCIM device chip is shown in Fig. 6.8c with the same XY dimensions as the SIM device chip in Fig. 6.5 (i.e., third row in Table 6.1). Corresponding pressure tests are shown in Fig. 6.8d. Similar to the SIM device results, the CCIM tests show no evidence of leakage in the interconnect ports. Microscope observation of the interface chip interconnect surface shows less evidence of wear than for the SIM interconnect case. We have therefore focused on the CCIM design as our standard high density interconnect method. Note that with 3D printing there is no additional time, cost, or process complexity to fabricate the more complicated CCIM design compared to the SIM design. Nonetheless, the SIM design appears to be suitable for situations in which relatively few repeated sealings are required.



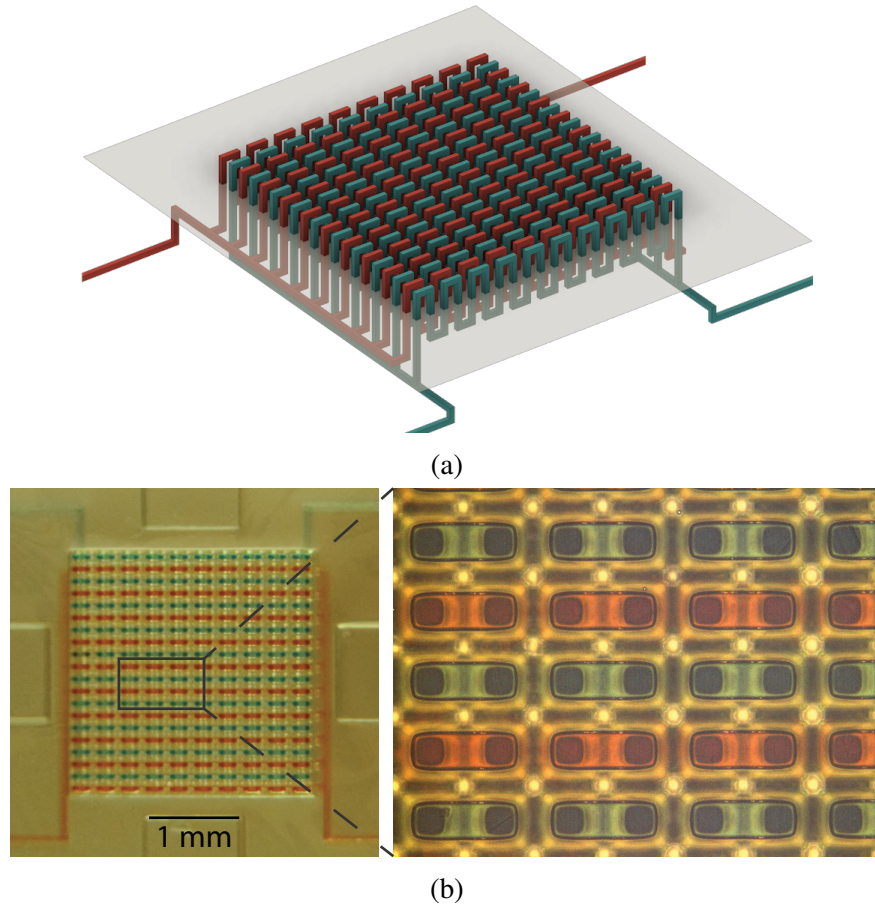


Figure 6.9: (a) Schematic illustration of geometry to test 400 CCIM interconnects in a  $20 \times 20$  array using two independent sets of flow channels (red and blue) that cross up and down between the chips. The plane shows the separation between device (upper) and interface (lower) chips. (b) Photograph of assembled device and interface chips. The two separate flow channels are filled with water containing red and blue food coloring. (Close-up) Microscope image of flow channels.

#### 6.2.4 Scaling

We investigated the potential to scale the CCIM design of Sect. 6.2.3 to larger numbers of interconnects. Keeping the same XY dimensions, we find that arrays of  $20 \times 20$  interconnects are easily achieved. An example is shown in Fig. 6.9 in which two independent microfluidic channels are vertically routed up and down across the chip-to-chip interface in an area of only  $3 \text{ mm} \times 3 \text{ mm}$ . One channel is filled with red food coloring and the other with blue food coloring. The close-up microscope image in Fig. 6.9b is focused on the highest horizontal channels in the device chip, and shows the very good fidelity and uniformity of the channels and interconnects.



Continuing to scale up the array size with the same CCIM XY dimensions, we found limitations when we reached 1,024 interconnects ( $32 \times 32$  array). A small amount of differential shrinkage between the interface and device chips caused the outer interconnection ports to have enough misalignment that they would not seal. This can be overcome by increasing the size of the microgaskets and therefore the period of the interconnects. However, we chose not to pursue this approach because of the concomitant decrease in interconnection density.

Instead, we evaluated whether the interconnect density can be increased for  $11 \times 11$  arrays, the results of which are summarized in Table 6.1. For a vertical channel width,  $N_c$ , of 6 pixels, we found that the seal width,  $N_s$ , could be decreased from 5 pixels to 3 pixels, such that, keeping the gap width,  $N_g$ , the same at 2 pixels, the period is reduced to 14 pixels ( $106.4 \mu\text{m}$ ) for an areal density of 88 interconnects/ $\text{mm}^2$ . With these dimensions, the interconnects still withstand an internal fluid pressure of 50 psi.

Decreasing the period any further results in interconnect arrays that do not fully seal. This appears to be due to shrinkage of the interface chip port geometry which is exacerbated by the relatively small volume of polymerized material that results from the high vertical channel density.

### 6.3 Demonstration: Valve Testing

In our group we now use CCIM interconnects for nearly all of our 3D printed microfluidic device development efforts because of how convenient it is to separate the chip-to-world interface from the actual device chip. As an example, consider the miniaturization of pneumatic membrane valves enabled by our custom 3D printer and NPS resin. Rogers originally demonstrated membrane valves with a PEGDA material in 2014 using a conventional cleanroom fabrication process [86]. These valves had a diameter of  $700 \mu\text{m}$ . He reported the first 3D printed membrane valves in 2015 using a B9 Creator 3D printer with a custom PEGDA resin [24]. Because of the limited resolution ( $50 \mu\text{m}$  pixel pitch) of the B9 Creator, the minimum demonstrated valve diameter was 2 mm. In Chapter 4 we showed 1.08 mm diameter valves with a similar custom resin and an Asiga Pico Plus 3D printer having a  $27 \mu\text{m}$  pixel pitch. Since our custom 3D printer has a  $7.56 \mu\text{m}$  pixel pitch, this suggests that it should be able to fabricate  $300 \mu\text{m}$  diameter valves (i.e.,  $1.08 \text{ mm} \times (7.56 \mu\text{m}/27 \mu\text{m})$ ), which we demonstrate in this section.

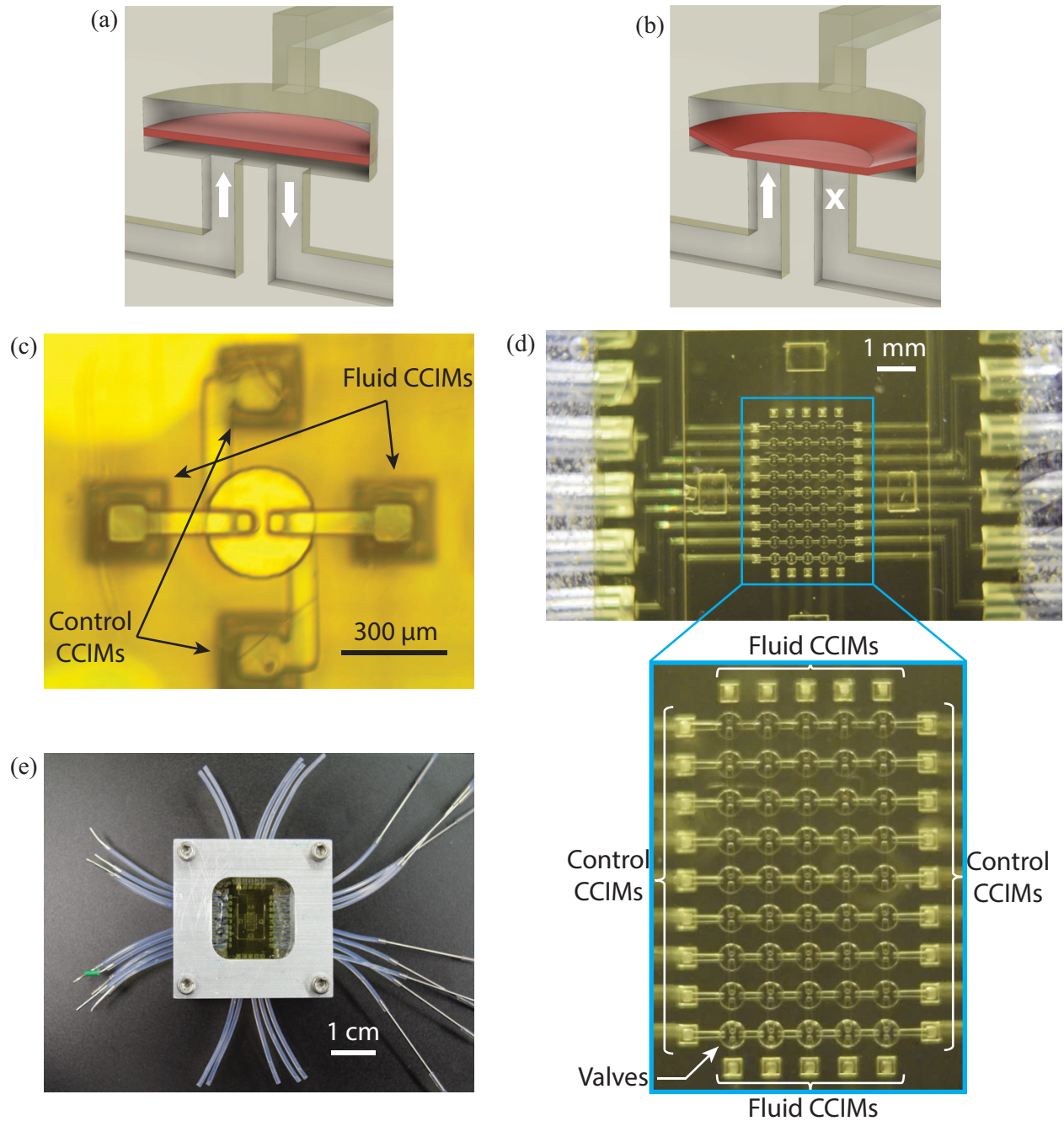


Figure 6.10: Schematic diagrams of 3D printed pneumatically actuated membrane valve in (a) open and (b) closed states. (c) Single  $300\ \mu\text{m}$  diameter valve with fluid and control channels connected to individual CCIMs. (d) (upper) Microscope image of 45-valve array chip assembled with corresponding interface chip in clamping fixture as shown in (e). (d) (lower) Close-up of 45-valve array with each row of valves having their control ports connected in series to a pair of CCIMs, and each column of valves having their fluid ports connected in series to a pair of CCIMs. Each valve is  $300\ \mu\text{m}$  in diameter.

Fig. 6.10a and 6.10b show the geometry of a 3D printed membrane valve. Fig. 6.10c shows a 300  $\mu\text{m}$  diameter 3D printed valve with its two fluid channels and two control channels connected to CCIMs such that the PTFE tubing chip-to-world connections are made with a separate interface chip. The valve membrane consists of two stacked 5  $\mu\text{m}$  layers, each exposed for 300 ms, and fluid and control chambers (i.e., the regions below and above the membrane in Fig. 6.10a) that are 20  $\mu\text{m}$  and 30  $\mu\text{m}$  tall, respectively. A control pressure of 9 psi works well to close such valves.

To test the valves we constructed an array of 45 valves arranged in 9 rows and 5 columns as shown in Fig. 6.10d. The control chambers of each row of valves are connected in series to a pair of CCIMs, and the fluid chambers of each column of valves are likewise connected in series to a pair of CCIMs such that there are a total of 28 CCIMs. The CCIMs are arranged around the periphery of the valve array, rather than concentrated in a small area as in Sect. 6.2. An interface chip connects these CCIMs through fluid channels to a set of 28 PTFE tubes as shown in Fig. 6.10e, in which the interface and valve array chips are clamped together. The photograph in Fig. 6.10d is taken through the glass substrate of the valve array chip and focused on the valve array, which means the CCIMs and channels in the interface chip are somewhat out of focus since they are outside the depth of focus of the camera's imaging system.

After 3D printing, unpolymerized resin is flushed from the channels and the fluid and control chambers of the valves by first clamping together the valve array and interface chips, after which vacuum and IPA is applied to a pair of tubes connected to one of the rows or columns of valves. This is repeated for each row and each column of valves until all of the unpolymerized resin is flushed. (Note that flushing unpolymerized resin from a valve's control chamber necessitates two connections to the control chamber.) After thorough flushing, the valve array chip is separated from the interface chip and optically cured.

To test the valves, the valve array and interface chips are again clamped with the aluminum fixture. One set of PTFE tubes connected to the control chambers is blocked by inserting small pieces of wire into their ends (the left set of tubes in Fig. 6.10e), while the other control chamber PTFE tubes are connected to their own solenoid valves and a pressure source. This allows each row of valves to be actuated with a single solenoid valve connected to a manifold pressurized at 9 psi. A water source suspended  $\sim 30$  cm above the valve chip (and therefore pressurized by gravity) is connected to each column of valves through the top PTFE tubes, and flow is observed through

the bottom PTFE tubes as a function of whether any row of valves is actuated or not. The top 8 rows of valves were actuated 10,000 times and the bottom row was actuated 1,000,000 times, after which all of the valves still function normally. A video of valve operation after this lifetime testing is shown in the ESI Video S1 of Ref. 102, where they are actuated with a 50 ms scrolling cycle.

Finally, we note that we have re-used the interface chip and its 28 world-to-chip connections to test a variety of 3D printed test chips containing different sized valves, displacement chambers, [61] and pumps. Interconnect chip re-use has proven to be an extremely convenient laboratory benefit of CCIMs.

## 6.4 Conclusions

We have shown that high density chip-to-chip interconnections are feasible between two 3D printed chips using only 3D printed structures on the chips themselves, i.e., no additional materials or parts are needed to effect a seal between the chips other than a mechanism to press the chips together. We have also shown that passive integrated alignment structures are sufficient to attain the necessary alignment accuracy between the two chips. We have introduced both SIM and CCIM geometries for integrated microgaskets, and have shown that both approaches withstand internal fluid pressures up to at least 50 psi in  $11 \times 11$  arrays of interconnections with an areal density of 53 interconnects/mm<sup>2</sup>, and can do so with no degradation in performance for 100 repeated tests. CCIM interconnections have been demonstrated for up to 400 interconnects ( $20 \times 20$ ), and up to an areal density of 88 interconnects/mm<sup>2</sup>. SIM and CCIM interconnections therefore fulfill the 5 chip-to-chip interconnect criteria set forth at the beginning of this Chapter, namely, (1) support large numbers of interconnects at (2) high density while (3) withstanding pneumatic and fluid pressures typical for 3D printed microfluidic valves and pumps and that are (4) reusable and (5) easy to align and connect.

In addition, we have shown an application of spatially distributed CCIMs in which they are used to simplify testing a 45 valve array with 28 world-to-chip interconnects, in the course of which we have demonstrated the smallest 3D printed valves to date (300  $\mu$ m diameter).

In this chapter we have focused on connecting a single device chip to an interface chip. We should note that it is also possible to connect multiple device chips to the same interface chip and either drive them all in parallel, or create some combination of parallel and independent fluid and

pneumatic connections. As a further observation, device chips could also be stacked vertically, one underneath another, with high density interconnections on both their top and bottom surfaces to chain them together. Finally, the 3D printed interface chip need not be only a passive device to route world connections to device chips; it could also incorporate active functions.

## CHAPTER 7. 3D PRINTED SELECTABLE DILUTION MIXER PUMPS

Microfluidic mixing is a critical operation in many chemical and biological applications [103] such as chemical synthesis, [104]–[109] polymerization, [110]–[112] extraction, [113]–[117] DNA analysis, [118]–[122] enzyme assays, [121], [123]–[125] and protein folding [126]–[129]. However, mixing is a challenge at the low Reynolds numbers typical of microfluidic device operation since fluid flow is laminar [130], [131]. Over several decades, a wide variety of both passive and active mixing strategies have been demonstrated. Comprehensive reviews of such strategies can be found in Refs. [130]–[132]. While demonstrating a 3-to-2 3D printed multiplexer with an earlier, larger version of our technology in Chapter 4, we show that a 3D printed valve and displacement chamber (DC) has the potential to achieve mixing in a compact device volume. Our purpose here is to use our current capabilities to explore the implementation of an active mixer with a selectable mixing ratio in the minimum possible volume that accomplishes mixing in minimum time for small ( $\sim 20$  nL) fluid volumes. We call such devices selectable dilution mixer pumps (SDMPs).

In this chapter, we first establish a low-cost video approach for absorption-based measurement of the local dye concentration in an outlet channel to determine mixing effectiveness. This simplifies data acquisition for SDMP characterization such that the only tools needed beyond pneumatic valve and pump controls are a smartphone for slow motion video capture and a microscope operating in transmission mode. We also test 3D printed pumps with varying DC dimensions to measure fluid volume expelled per pumping period, which increases with larger pump DCs. Then, having established pump operational parameters and a direct relative concentration measurement method, we implement and characterize two possible SDMP configurations: (1) a linear dilution mixer pump (LDMP) and (2) a parallelized dilution mixer pump (PDMP). Each configuration contains a number of pumps to inject variable amounts of fluid from two sources into their active mixing units to realize selectable mixing ratios. The volume occupied by the LDMP is only 1.5

mm<sup>3</sup>, and its mixing effectiveness is compared to diffusion-driven mixing and optimized by experimenting with different mixing operation sequences. In contrast to a LDMP, a PDMP (2.6 mm<sup>3</sup>) is designed to obtain a denser set of dilution ratios and shorten the overall mixing process. The shorter mixing process is achieved by minimizing pump idle time and synchronizing all pump operations. It also contains a 4-to-1 valve that controls 4 valve inlet channels to reduce the total number of required valves.

The work in this chapter is reported in Ref. 133.

## 7.1 Materials and Methods

### 7.1.1 3D Printer and Materials

The 3D printer used in this chapter is described in Chapter 5. It has a 385 nm LED light source and a pixel pitch of 7.56  $\mu\text{m}$  in the projected image plane. We use a custom photopolymerizable resin which consists of poly(ethylene glycol) diacrylate (PEGDA, MW258) with a 1% (w/w) phenylbis(2,4,6-trimethylbenzoyl)phosphine oxide (Irgacure 819) photoinitiator and a 2% (w/w) 2-nitrophenyl phenyl sulfide (NPS) UV absorber, details of which are provided in the Chapter 5.

### 7.1.2 3D Printing and Sample Preparation

We use 25 mm square silanized glass slides as 3D printing substrates. Slides are first rinsed with acetone and isopropyl alcohol (IPA), and then immersed in toluene mixed with 10% 3-(trimethoxysilyl)propyl methacrylate for 2 hours. After silanization, we store the glass slides in fresh toluene inside a closed container until use, which ranges from under an hour to several weeks. All 3D prints reported in this chapter are fabricated with a layer thickness of 10  $\mu\text{m}$ . Except where otherwise noted, each layer has an exposure time of 550 ms. The image plane irradiance is 21.2 mW·cm<sup>-2</sup> with an LED source spectrum as included in Chapter 5 with a peak at 383 nm.

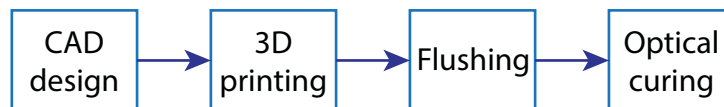


Figure 7.1: Microfluidic 3D printing fabrication process flow.

The fabrication process steps are illustrated in Fig. 7.1. After printing, unpolymerized resin must be flushed from all interior voids with IPA prior to optical curing. The flushing process requires that all voids have two means of access so the IPA can flow through each void region (channel, valve chamber, etc.), i.e., there must not be any dead ends in the printed structure since they generally cannot be flushed of unpolymerized resin, which would then become polymerized during optical curing. After flushing, a device is optically cured for 30 minutes in a custom curing station using a 430 nm LED (Thorlabs, Newton, New Jersey) having a measured irradiance of  $11.3 \text{ mW}\cdot\text{cm}^{-2}$  in the curing plane.

Unless otherwise noted for the DCs used in pumps, the fluid and control chamber heights are both  $50 \text{ }\mu\text{m}$ , and the membrane thickness is  $20 \text{ }\mu\text{m}$  (2 layers). Also, the actuation pressure and the vacuum pressure used to deflect valve and DC membranes are 20 psi and approximately -10 psi, respectively.

### **7.1.3 Concentration Measurement**

There are two commonly used approaches in the literature to measure concentration at the outlet of a mixer, fluorescence-based [134]–[150] and absorption-based [151]–[157]. Both take advantage of the fact that the pixel gray level for any pixel in a digital image of the fluid in an outlet channel is a function of the local concentration of the fluorescent or absorbent species in the small fluid region imaged to that pixel. In a fluorescence-based system, pixel gray level is linearly proportional to the concentration of fluorescent material, making data processing to directly obtain local concentration straightforward and intuitive. The downside is that working with a fluorescent material demands a relatively complicated and expensive setup which includes an excitation source and an optical filter in addition to a microscope and digital imager. In contrast, an absorption-based method requires only a digital imager with a microscope operated in transmission mode, and is therefore simpler and less expensive. However, in the literature numerous papers do not directly measure the local concentration based on pixel gray level using the absorption-based approach. Instead, the variance of the pixel gray level is calculated and interpreted as an indirect indicator of the degree of mixing, [151]–[155] rather than connecting measurements directly to local absorber concentration as in Refs. 158 and 159.



In this chapter, we develop a low-cost video approach to directly measure relative concentration as a function of time for the absorption-based method. For data collection, we mount an iPhone 8 Plus on a microscope (Olympus BX60) eyepiece to record slow motion ( $1920 \times 1080$  @ 240fps) video as raw output. The two different fluids are DI water (Water) and red-dyed water (Red) consisting of a few drops of Red 40 food coloring in DI water. The outlet of each type of mixer pump is a wide ( $\sim 210 \mu\text{m}$ ), shallow ( $50 \mu\text{m}$  unless otherwise noted) 3D printed outlet channel in which the spatially-varying fluid concentration is observed with the iPhone video.

According to Beer's law the transmitted light irradiance as a function of pixel location,  $(x, y)$ , is

$$I(x, y) = I_0(x, y) \exp^{-\alpha(x, y)z_c}, \quad (7.1)$$

where  $I_0(x, y)$  is the incident light irradiance,  $\alpha(x, y)$  is the spatially-dependent absorption coefficient based on local concentration, and  $z_c$  is the thickness of the material the light travels through (in our case, the height of the channel). We can solve for the absorbance,  $A(x, y) = \alpha(x, y)z_c$  in terms of the irradiance as

$$A(x, y) = -\log \left( \frac{I(x, y)}{I_0(x, y)} \right), \quad (7.2)$$

where  $I_0(x, y)$  is the irradiance when there is no red dye in a channel (i.e., only water in a channel). We therefore re-label  $I_0(x, y)$  as  $I_{\text{water}}(x, y)$ .  $I(x, y)$  is an individual video frame (i.e., image) from any point in the experiment video, typically during operation when dye is introduced to the outlet channel by the mixer pump. Likewise,  $I_{\text{water}}(x, y)$  is an individual video frame near the start of a video when all channels are filled with water and Red has not yet been introduced into the mixer.

Note that in general the absorbance can be written in terms of dye concentration,  $C(x, y)$ , as

$$A(x, y) = z_c(x, y) \log(10) \varepsilon C(x, y), \quad (7.3)$$

where  $\varepsilon$  is the absorptivity (in suitable units given the units of the concentration,  $C$ ) and  $z_c(x, y)$  is the channel thickness at pixel position  $(x, y)$ . Clearly, the absorbance,  $A$ , is linearly dependent on the concentration,  $C$ . This concentration can be thought of as the integrated concentration through the height of the outlet channel at a given pixel position. As long as the channel height is relatively small, we expect it to be a reasonable approximation of the local concentration.

The condition of maximum absorbance,  $A_{max}(x, y)$ , is when the full red dye concentration is in the outlet channel such that the irradiance is  $I_{red}(x, y)$ :

$$A_{max}(x, y) = -\log \left( \frac{I_{red}(x, y)}{I_{water}(x, y)} \right). \quad (7.4)$$

In each experiment video we fill the outlet channel with Red near the end of the video, while at the beginning of each experiment video the outlet channel is filled with Water. Each video therefore contains the calibration frames needed to determine  $I_{red}(x, y)$  and  $I_{water}(x, y)$ , and hence  $A_{max}(x, y)$ . The frames in the middle of the video track the progress of the mixer pump in creating the desired mixing ratio of the output fluid.

We can define the relative absorbance,  $A_{rel}(x, y)$  in reference to  $A_{max}(x, y)$  as

$$A_{rel}(x, y) = \frac{A(x, y)}{A_{max}(x, y)} \quad (7.5)$$

$$= \frac{z_c(x, y) \log(10) \epsilon C(x, y)}{z_c(x, y) \log(10) \epsilon C_{max}(x, y)} \quad (7.6)$$

$$= \frac{C(x, y)}{C_{max}(x, y)} \quad (7.7)$$

$$= C_{rel}(x, y). \quad (7.8)$$

$C_{rel}(x, y)$  is therefore the relative concentration at pixel position  $(x, y)$ . The mean of  $C_{rel}(x, y)$  over some region  $R$ ,  $\bar{C}_{rel}$ , is the average relative concentration and the standard deviation of  $C_{rel}(x, y)$ ,  $\sigma$ , over the same region is a direct measure of how well the solution is mixed, with, in the ideal case,  $\sigma = 0$  being fully mixed. As we show in Sect. 7.2, noise in the measurement process results in the fully mixed condition being manifested instead by a small  $\sigma$  value that does not change systematically in time.

## 7.2 Results and Discussion

### 7.2.1 Pumps

As shown schematically in Fig. 7.2(a), a 3D printed pump comprises an inlet valve, a DC, and an outlet valve [61]. The valves and the DC each have 2 vertically stacked circular chambers,

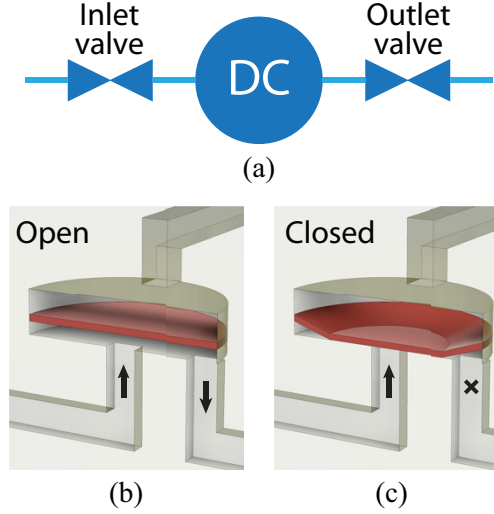


Figure 7.2: (a) Functional illustration of a 3D printed pump. (b) and (c) 3D printed valve in open and closed states. See text for details.

a control chamber and a fluid chamber, separated by a membrane which can be deflected according to the control chamber pressure [24]. For valves, fluid channels are located at the center and edge of the fluid chamber, respectively. As shown in Fig. 7.2(c) lower right, when the control chamber is pressurized the membrane (denoted by a reddish color even though it is the same material as the rest of the 3D print) deflects into the fluid chamber and blocks the central fluid channel, thereby closing the valve. When the control chamber pressure is released (Fig. 7.2(b)), the membrane returns to its equilibrium position, opening the valve. Alternatively, vacuum can be applied to open the valve, which pulls the membrane up into the control chamber.

A DC has both fluid channels located at the edges of the fluid chamber such that neither is blocked when the membrane deflects. Instead, the DC membrane movement pulls in or pushes out fluid depending on whether the control chamber is exposed to atmosphere or pressure. Alternatively, vacuum can be applied instead of atmosphere, in which case the volume of fluid pumped per pumping period increases to the degree that the membrane is pulled up into the control chamber by the vacuum. The pump fluid direction is determined by which of the inlet and outlet valves are open and closed during DC pressurization and de-pressurization.

The pump operates using a 5-phase cycle as detailed in Chapter 4. We call each phase time a clock cycle,  $\tau_{clock}$ , and one 5-phase pump cycle a pumping period,  $\tau_{pump}$ , which equals  $5\tau_{clock}$ . In this chapter,  $\tau_{clock}$  is 100 ms.

We typically fabricate valve and DC membranes that are only 10-20  $\mu\text{m}$  thick. We find that without enough polymer cross-linking during 3D printing, the membrane may not be tough enough to avoid tearing during operation, limiting valve durability. In the past when we used commercial 3D printers (and therefore created larger structures), we were forced to use the same exposure time for every layer in a 3D print, and for every pixel within each layer. This lack of flexibility exposes a fundamental trade-off with such printers when trying to print both valves and small channels in the same 3D print. The trade-off is that higher doses are required to improve the mechanical toughness of valve membranes, but higher doses preclude fabricating small channels, for which a smaller dose is required [62]. Since we have full control over all aspects of our custom 3D printer, in this chapter we increase the membrane exposure independent of other build layers, and other regions within the same build layer, such that we can achieve both strong membranes and small minimum channel size. Our approach is that for build layers that contain membranes, after the normal layer exposure and before moving the build platform to get ready for the next layer, we expose a secondary image which only illuminates the membrane areas, thereby giving them a greater dose than the rest of the layer and selectively toughening the membranes while maintaining a lower dose everywhere else in the layer, consistent with reliably fabricating small channels. In this manner we are able to achieve excellent membrane durability without sacrificing minimum channel size. Membrane exposure times are given in Table 7.1.

Table 7.1: Details on the thickness and exposure of different fluidic component membranes.

Device	Membrane Layer	Thickness ( $\mu\text{m}$ )	Exposure Time (ms)	Secondary Exposure (ms)
Valve	1	5	350	—
	2	5	350	—
4-to-1 Valve	1	10	550	250
	2	10	550	250
Pump DC	1	10	550	—
	2	10	550	—
Mixer DC	1	10	550	800
	2	10	550	800

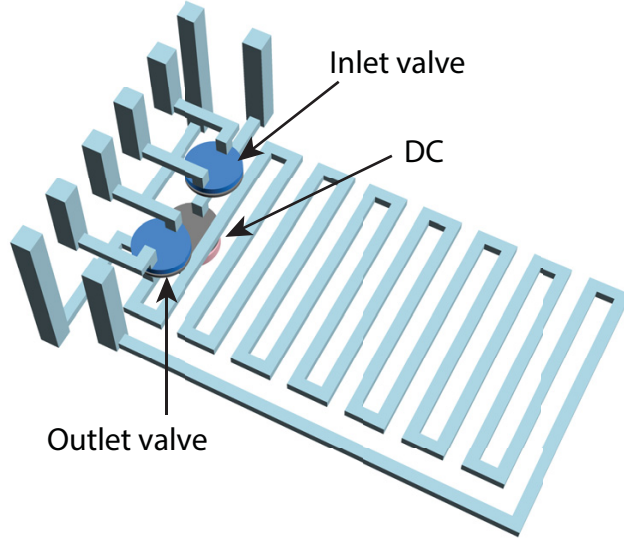


Figure 7.3: CAD drawing of a pump with a serpentine outlet channel.

To determine the expelled volume per pumping period,  $V_{pump}$ , we connect the pump outlet to a 3D printed serpentine channel as shown in Fig. 7.3. This serpentine channel has a well-defined cross-section area, and is integrated with the pump, which makes measuring the fluid volume pumped as a function of time as convenient as simply measuring the length of channel the fluid has traveled as captured in a video of pump operation. Specifically, we observe the progress of the fluid-air meniscus of black-dyed water during pump operation.

An example set of video frames are shown in Fig. 7.4a-7.4d. During pump operation, the outlet valve must be opened before the DC expels fluid, which results in the meniscus initially moving backward as fluid is drawn into the outlet valve fluid chamber. This can be seen by comparing Fig. 7.4a with Fig. 7.4b. The volume drawn into the valve is  $V_{valve}$ . Next, the meniscus moves forward according to how much fluid volume is expelled by the DC,  $V_{DC}$  (Fig. 7.4b  $\rightarrow$  7.4c). Finally, the outlet valve is closed, which pushes fluid into the outlet channel and further moves the meniscus forward by  $V_{valve}$  (Fig. 7.4c  $\rightarrow$  7.4d). This process generates a pulsatile flow with one step back ( $V_{valve}$ ) and two steps forward ( $V_{DC}$  and  $V_{valve}$ ). This is clearly seen in ESI Videos 1a and 1b of our recently submitted paper [133] for pumps with 40-pixel ( $304\ \mu\text{m}$ ) diameter valves and 40-pixel and 60-pixel ( $456\ \mu\text{m}$ ) diameter DCs, respectively. Note that the net forward motion of the meniscus for one pumping period corresponds to the displaced volume,  $V_{DC}$ , since the volume drawn in and expelled by the outlet valve during a pumping period is the same. Therefore the pump

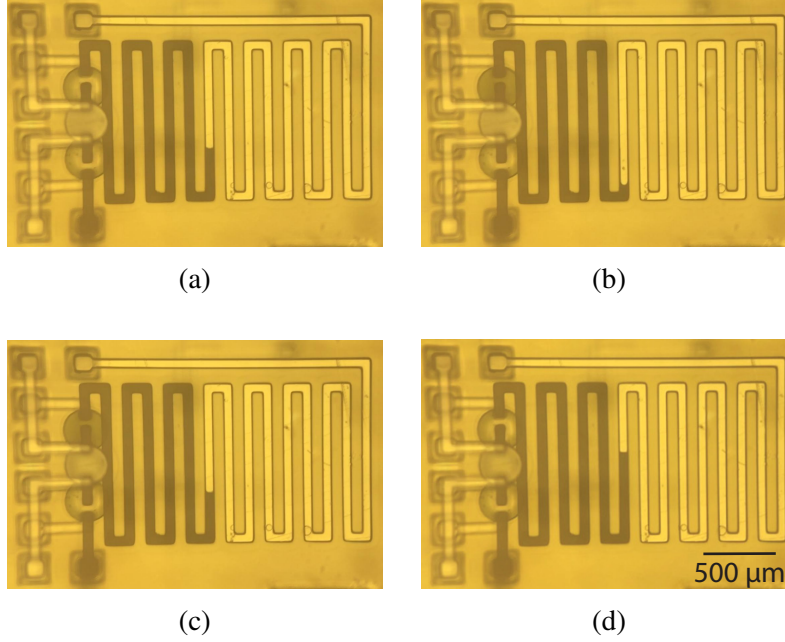


Figure 7.4: (a)-(d) Microscope photos of a pump at various stages in its operation. The DC has the same diameter as the valves, which is 40 pixels. (a)→(b): Outlet valve opens, and the meniscus moves back by the volume of the valve upward membrane displacement,  $V_{valve}$ ; (b)→(c): DC is actuated, and the meniscus moves forward by the volume of the DC downward membrane displacement,  $V_{DC}$ ; (c)→(d): outlet valve is actuated, and the meniscus moves further forward by the volume of the valve downward membrane displacement, which is the same as its upward membrane displacement,  $V_{valve}$ .

volume per pumping period,  $V_{pump}$  is just

$$V_{pump} = V_{DC}. \quad (7.9)$$

The specific approach we use to measure  $V_{pump}$  is counting dark pixels over the region of the serpentine channel, which is directly proportional to the area filled by the fluid. Based on our previous work in Chapter 5, the channel height is very consistent in our 3D prints. We can therefore calculate

$$V_{pump} = k(N_{n+1} - N_n)z_c, \quad (7.10)$$

where  $k$  is outlet channel area per image pixel, and  $N_{n+1}$  and  $N_n$  are the dark pixel counts after pump periods  $n + 1$  and  $n$ , respectively, and  $z_c$  is the channel height. Fig. 7.5 shows measured  $V_{pump}$  as a function of DC diameter. We would normally expect  $V_{pump}$  to increase as the square of

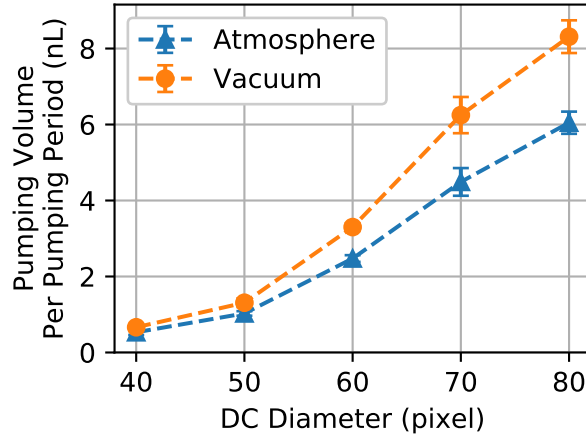


Figure 7.5: Measured pumping volume for DCs with different diameters and  $50\ \mu\text{m}$  height for both the fluid and control chambers. The unit of the x-axis dimension, pixel, is the DLP image plane pixel pitch,  $7.56\ \mu\text{m}$ .

the diameter, which is clearly not the case in the data. The reason is that the actual volume that is pumped is not just a function of the physical DC fluid chamber volume, but it is also affected by the membrane diameter in relation to its thickness and stiffness. Error bars in the figure refer to the standard deviation over numerous pumping periods. We also apply vacuum to the DC such that when it is not pressurized, the membrane is pulled up into the control chamber, creating more space for fluid, and therefore resulting in larger  $V_{pump}$  compared to just using atmospheric pressure.

## 7.2.2 Linear Dilution Mixer Pump (LDMP)

### Concept and Design

Fig. 7.6a depicts the basic idea of a linear dilution mixer pump (LDMP). It utilizes two pumps, Pump 1 (top) and Pump 2 (bottom), to inject fluids A and B, respectively, from their individual inlets into the mixer. These two pumps are designed to be identical so that the mixer receives an equal amount of fluid from either pump for one pumping period. We also design the mixer fluid capacity,  $V_{mixer}$ , to be  $NV_{pump}$  where  $N$  is an integer, so Pumps 1 and 2 need to operate a total of  $N$  pumping periods to fill the mixer. In our case,  $N = 6$ . We design the pumps with DCs that are 60 pixels in diameter with  $50\ \mu\text{m}$  tall fluid and control chambers, and operate the pumps with vacuum. From Fig. 7.5,  $V_{pump} = 3.3\ \text{nL}$  such that  $V_{mixer}$  is  $19.8\ \text{nL}$ .

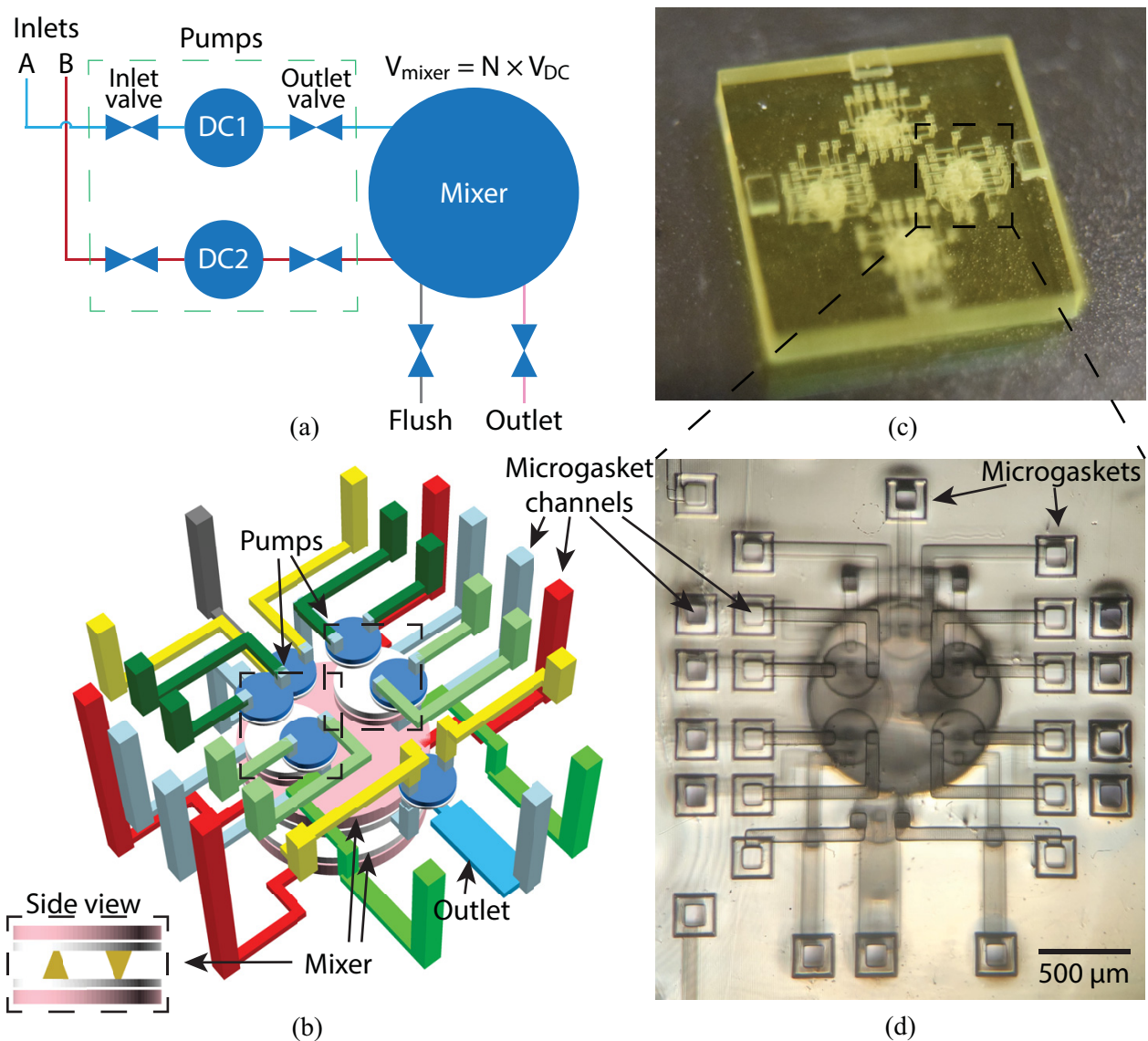


Figure 7.6: (a) Schematic of LDMP. It contains 2 pumps which are connected to a fluid reservoir. They can selectively pump fluid to the mixer which performs mixing. (b) 3D layout of (a). Pumps are stacked on top of the mixer, and the mixer has 2 large DCs connected to each other via cone-shaped channels. (c) Photograph of a 3D printed device designed for characterization of 4 LDMPs on a single chip. (d) Microscope photo of an LDMP which uses microgaskets developed in Chapter 6.

A CAD design of an LDMP is shown in Fig. 7.6b, in which the two pumps and the flush and outlet valves are located on top of a coupled pair of larger DCs that function as an active mixer. Note the tight 3D layout of valves, pumps, channels, and active mixer, which illustrates a key advantage of 3D printing, namely, arbitrary component placement and channel routing for efficient volume utilization. The LDMP volume is only  $1.5 \text{ mm}^3$ , not including the connections through the



microgasket channels since these are specific to this particular implementation for testing a single LDMP. In general, an LDMP would be connected to other microfluidic components in the same 3D print to comprise a functional device for a particular application.

The mixer side view in Fig. 7.6b shows that the two vertically stacked mixer DCs are connected with 2 oppositely-oriented cone-shaped channels. When the top DC is activated (pressurized) and the bottom DC is deactivated (switched to atmosphere or vacuum), most of the fluid in the mixer is forced from the top DC through these channels into the bottom DC, and vice versa. The mixing effect is achieved by repeatedly activating one mixer DC and releasing the other, and then reversing the process, thereby causing fluid to move back and forth between the mixer DCs. The opposite cone shapes of the connecting channels are intended to provide spatial asymmetry as fluid flows back and forth to aid in the mixing effect. Here, we define actuating each mixer DC once as a mixing period, denoted as  $\tau_{mix}$ , such that

$$\tau_{mix} = 2\tau_{clock}. \quad (7.11)$$

Fluid mixing is accomplished by actuating the mixer some number of mixing periods,  $N_{mix}$ , which requires a time  $N_{mix}\tau_{mix}$ . The value of  $N_{mix}$  needed to achieve good mixing is experimentally determined later in this section.

### Mixer Pump Cycle

A complete mixer pump cycle is illustrated in Fig. 7.7 consisting first of two clock cycles,  $\tau_{clock}$ , one to close the outlet valve and one to deactivate both mixer DCs, followed by  $N_{pump}$  sequential pumping periods and  $N_{mix}$  mixing periods, and, finally, two additional clock cycles, one to open the outlet valve and the other to activate both mixer DCs to expel the mixed fluid through the outlet valve. At this point the mixer pump cycle repeats. The time for a complete mixer pump cycle,  $\tau_{MP}$ , can be written as

$$\tau_{MP} = 2\tau_{clock} + N_{pump}\tau_{pump} + N_{mix}\tau_{mix} + 2\tau_{clock} \quad (7.12)$$

$$= (4 + 5N_{pump} + 2N_{mix})\tau_{clock}. \quad (7.13)$$

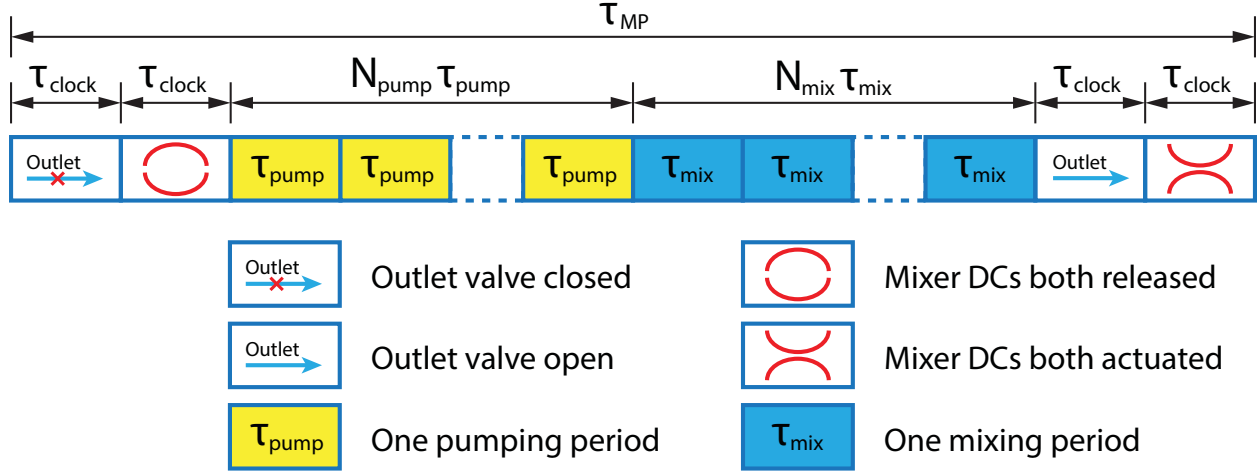


Figure 7.7: A complete mixer-pump cycle, denoted as  $\tau_{MP}$ . At the beginning, the outlet valve is closed. Then, both mixer DCs are released to be prepared for the fluid injected by pumps during the subsequent  $N_{pump}$  pumping periods,  $N_{pump}\tau_{pump}$ . After the mixer is filled, it mixes fluid for  $N_{mix}$  mixing periods for a time of  $N_{mix}\tau_{mix}$ . Finally, the outlet valve opens, and both mixer DCs are actuated to expel the mixture.

## Interface Chips

As discussed in Chapter 6, we use PTFE tubing as world-to-chip connections in 3D printed interface chips. With this approach, individual tubes are epoxied in cylindrical receptacles fabricated as part of the 3D printed interface chip, and the interface chip has internal channels that route each tube to a specific chip-to-chip interconnect.

Two such interface chips are required for an LDMP, one to facilitate flushing the device immediately after 3D printing and before optical curing, and the other for actual LDMP operation. As explained in Sect. 7.1.2, during flushing there must be a path to flow IPA into and out of every channel and fluid and control chamber to remove unpolymerized resin. For an LDMP, this requires a total of 24 chip-to-chip interconnects and corresponding PTFE tubes. A fabricated interface chip with attached PTFE tubes is shown in Fig. 7.8a, and clamped to an LDMP device chip in Fig. 7.8c.

During operation, valve and DC control chambers only need one connection to control the pressure in these chambers (and therefore the associated membrane deflection), rather than two as for flushing. Hence, only 14 connections are needed, 10 pneumatic and 4 fluidic. However, there are still 24 chip-to-chip interconnects on the device chip. We use a simple approach to block

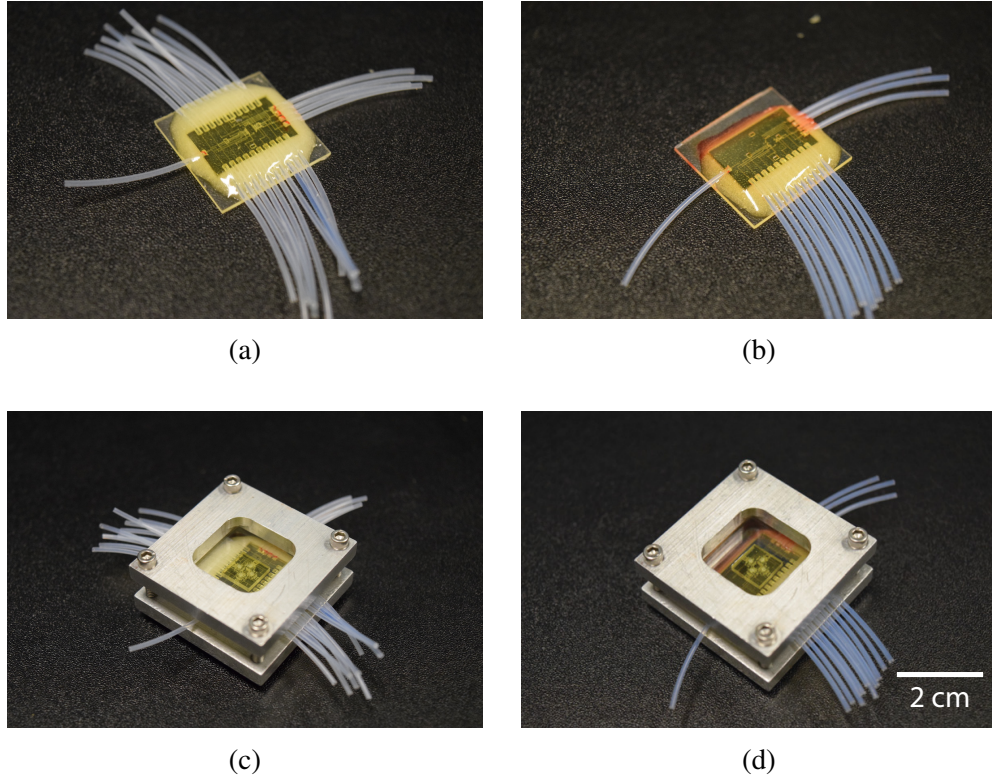


Figure 7.8: (a) LDMP flushing chip. (b) LDMP operation chip. (c) LDMP device chip assembled with flushing chip. (d) LDMP device chip assembled with operation chip.

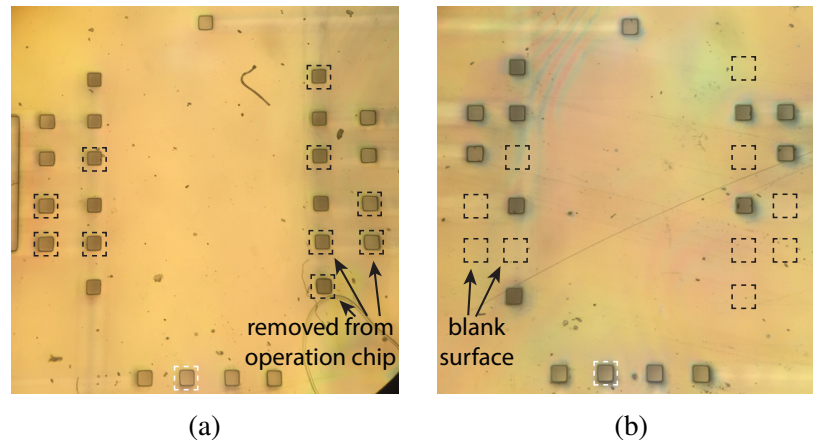


Figure 7.9: (a) Chip-to-chip interconnect surface of the LDMP flushing chip. Each channel matches to a microgasket interconnect on the LDMP device chip. (b) Chip-to-chip interconnect surface of the LDMP operation chip. The channels in black dashed boxes in (a) are removed, leaving a blank surface to seal the corresponding device chip microgasket channel. Because these chips are used for numerous designs, there is an extra channel which is not used in the LDMP, shown in the white dashed box.

the 2nd access channel to each valve and DC control chamber, illustrated in Fig. 7.9 and which consists of replacing an unneeded interface chip channel with a blank surface to seal that particular interconnect channel on the device chip. An operational interface chip is shown in Fig. 7.8b, and clamped to a device chip in Fig. 7.8d.

### Diffusion-driven Mixing

Next, we determine a baseline for LDMP mixing performance by using gravity to freely flow Water and Red through the device while observing the degree of mixing in the output channel. The fluid reservoirs for Water and Red are placed at the same height,  $\sim 30$  cm higher than the LDMP device, while all of the valves except the flushing valve are opened so Water and Red can flow through the device, i.e., in through their respective inlet ports and out through the outlet port. After the flow stabilizes, the segregation between Water and Red in the region of interest (ROI) in the outlet channel in Fig. 7.10a indicates an unsurprising lack of mixing. Next, we close the outlet valve, and observe the mixing process in the outlet channel driven only by diffusion. Using the method developed in Sect. 7.1.3, we calculate  $\sigma$  in the ROI for each individual frame for the entire process, which is shown in Fig. 7.10b. After starting gravity-driven flow around Frame 800 to 900, it stabilizes near Frame 1000, and the flow is allowed to proceed uninterrupted until near Frame 5000, over which time  $\sigma$  is relatively constant at  $\sim 0.175$ . Near Frame 5000 the outlet valve is closed, after which  $\sigma$  starts to drop exponentially as diffusion mixes the fluid that is now static

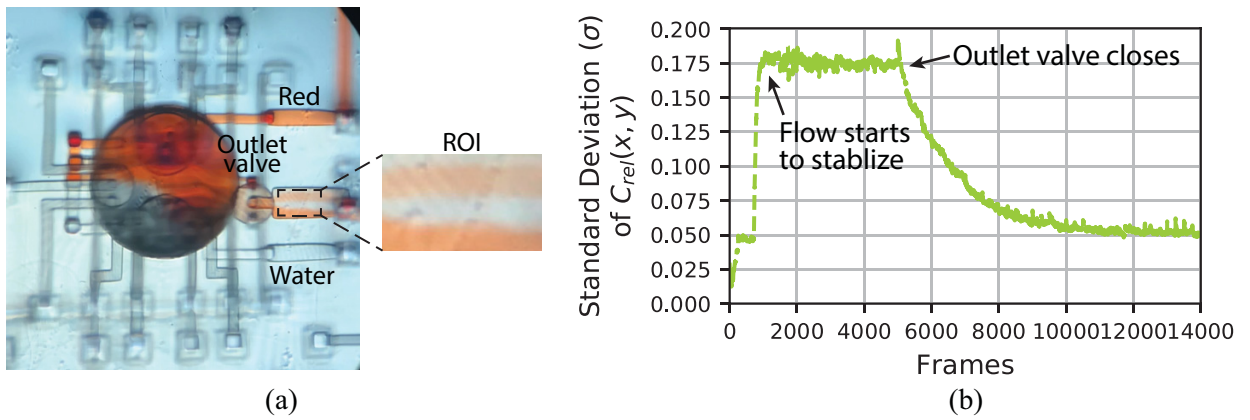


Figure 7.10: (a) Water and Red flow induced only by gravity. The fluid in the ROI encompassed by the dashed box is segregated, as expected. (b) Standard deviation,  $\sigma$ , of relative concentration,  $C_{rel}(x,y)$ , in the ROI as a function of frames in recorded video.

(no flow) in the outlet channel. It takes approximately 7,000 frames ( $\sim 29$  s) for  $\sigma$  to asymptote to the noise floor of  $\sim 0.05$ . This experiment confirms the expected problem with diffusion-driven passive mixing of a confined volume of fluid (in this case the 6 nL in the outlet channel), i.e., slow mixing. For a diffusion coefficient of  $D \approx 4 \times 10^{-10} \text{ m}^2/\text{s}$  [158], [159] for Red 40 dye and 1D diffusion over the width of the outlet channel,  $w$  (since the concentration is relatively constant over the length of the channel), the estimated diffusion time is  $w^2/(2D) = 28$  s, which agrees well with the measured value.

As noted in Sect. 7.2.2, the pumps inject  $\sim 20$  nL of fluid into the mixer during LDMP operation. The mixer is  $\sim 1$  mm in diameter so if the fluid was to sit in the mixer until it was mixed solely by diffusion, the diffusion time would be approximately  $(10^{-3}\text{m})^2/(4D) = 700$  s. Alternatively, if the 20 nL was injected into a cubic volume, it would take  $(20\text{nL} \times 10^{-12} \text{ m}^3/\text{nL})^{2/3}/(6D) \approx 30$  s to mix by diffusion. One figure of merit for a mixer is how much faster it mixes a given volume of fluid compared to diffusion-only mixing.

## Active Mixing

Using our new concentration-based analysis method from Sect. 7.1.3, we first investigate how many mixing periods,  $N_{mix}$ , guarantee thorough mixing. In a full mixer pump cycle (Sect. 7.2.2), we sequentially operate Pumps 1 and 2, each for three pumping periods, to achieve 1-to-2 dilution, and examine the degree of mixing as a function of  $N_{mix}$ . The results are shown in Fig. 7.11a-d for  $N_{mix}$  values of 1, 2, 6, and 8, respectively.

In each plot, the mean relative concentration,  $\bar{C}_{rel}$  (blue curve), in the ROI of the outlet channel is plotted on the left vertical axis as a function of the video frame number. For the first 1,000 frames, only Water is in the outlet channel so  $\bar{C}_{rel} \approx 0$ . For the last 10,000 frames, only Red is in the channel so  $\bar{C}_{rel} \approx 1$ . In between, the LDMP executes a series of mixer pump cycles. Each cycle can be tracked by the red curve, which indicates the state of the outlet valve as shown in Fig. 7.12. An upward pulse of the red curve shows when the outlet valve is open, which happens during one  $\tau_{cycle}$  per mixer pump cycle. It can therefore be used to visualize each mixer pump cycle on a plot. As expected, the period between peaks in the red curves increases as  $N_{mix}$  increases since  $\tau_{MP}$  becomes correspondingly longer. Also note that during the first few mixer pump cycles,  $\bar{C}_{rel}$  jumps up when the outlet valve opens, indicating that fluid containing an increasing amount of

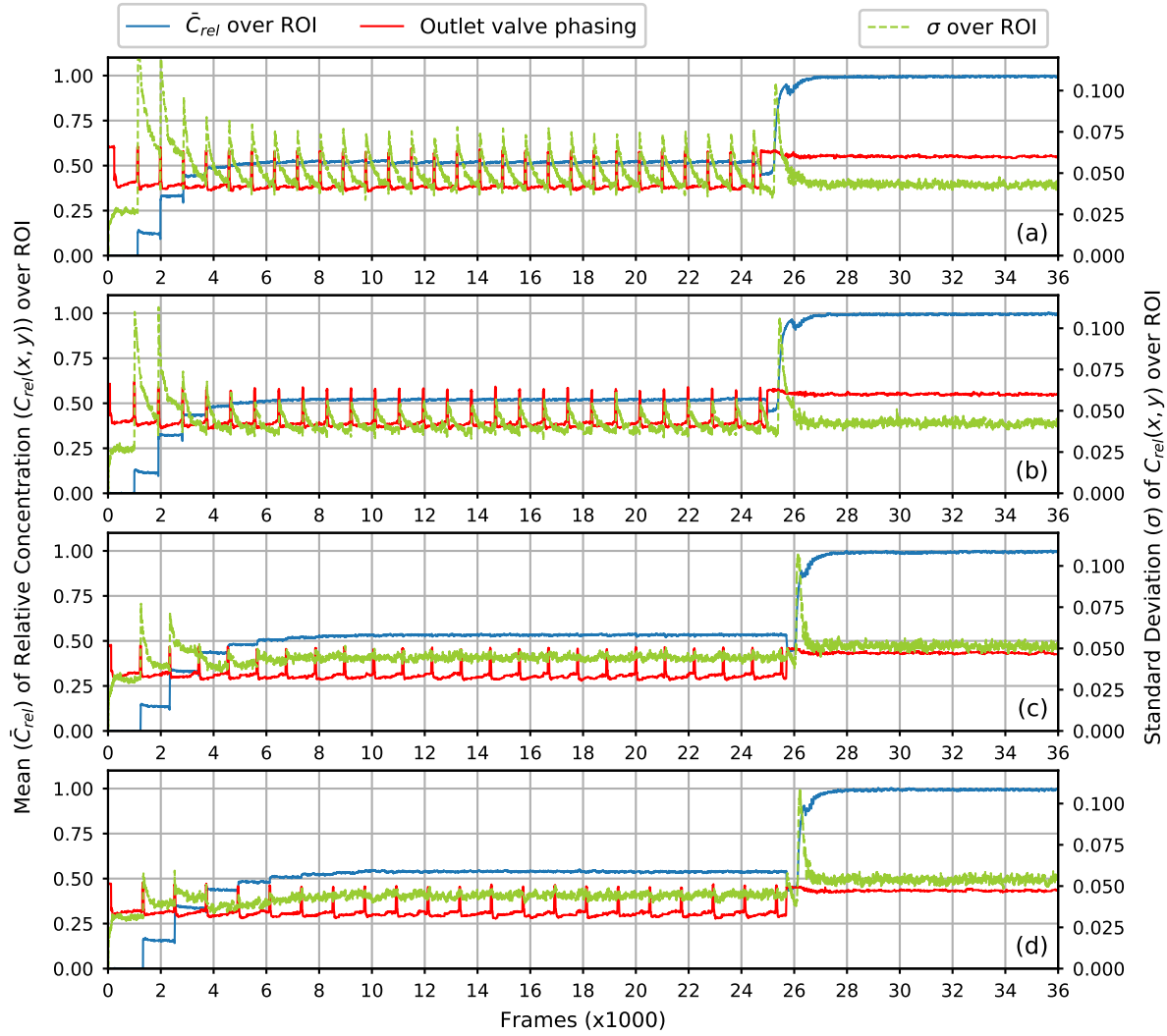


Figure 7.11: The mean and standard deviation of relative concentration  $C_{rel}(x,y)$  in the ROI as a function of the frame number. The state (open/closed) of the outlet valve is plotted as the red curve where a pulse corresponds to open. The outlet is initially filled with Water. Near Frame 26,000 ( $\sim 108$  s) the outlet channel is flushed with Red. (a)  $N_{mix} = 1$ . (b)  $N_{mix} = 2$ . (c)  $N_{mix} = 6$ . (d)  $N_{mix} = 8$ . See text for mixing details.

Red is injected into the outlet channel during that cycle. After  $\sim 6$  mixer pump cycles  $\bar{C}_{rel}$  stabilizes at a value of just over 0.5, the desired relative concentration, which indicates that  $\sim 6$  mixer pump cycles are required to flush the dead volume from the mixer and outlet channels to reach a stable relative concentration.

The standard deviation of  $C_{rel}(x,y)$ ,  $\sigma$ , over the ROI is shown as a green curve (right vertical axis) in each plot in Fig. 7.11. It gives a direct measure of the homogeneity (mixing) of

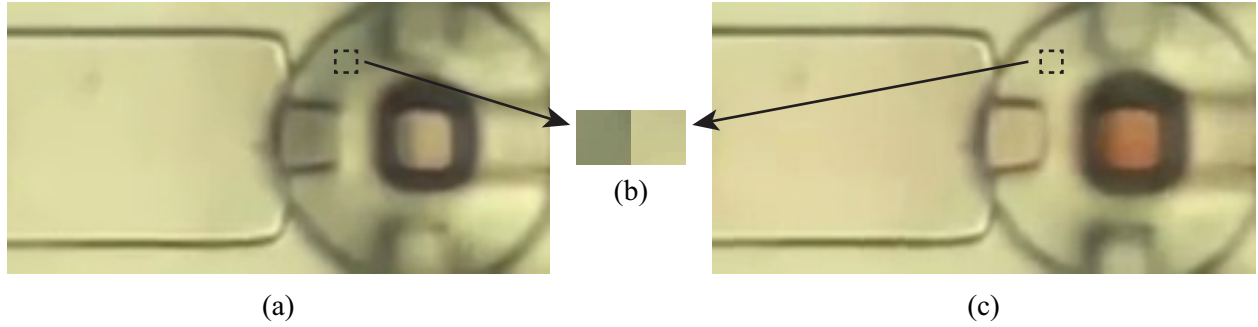


Figure 7.12: Microscope photos of the outlet valve in a mixer-pump in closed state (a) and open state (c). We average the pixel gray level inside the dashed box, and compare the results between closed and open state. (b) Direct comparison of the boxed region in closed and open state. The boxed region is darker in closed state.

the fluid for each frame in the video. For example, consider Fig. 7.11a ( $N_{mix} = 1$ ) after Frame 6,000. Every time the outlet valve opens (red curve pulse) the green curve jumps up to about the same level for each mixer pump cycle and then exponentially decays until the outlet valve opens for the next cycle. This indicates that the fluid that enters the outlet channel when the valve opens is not well mixed, and that as it sits statically in the outlet channel after the valve closes, diffusion continues the mixing process until the next time the outlet valve opens and new, not-well-mixed fluid is injected by the mixer. Nonetheless, the peak value of  $\sigma$  ( $\sim 0.07$ ) is significantly less than 0.175 in Fig. 7.10b for gravity-induced continuous flow, which demonstrates that even  $N_{mix} = 1$  gives better mixing than diffusion in continuous flow. For mixer pump cycles prior to Frame 6,000,  $\sigma$  is more a measure of poorly mixed fluid due to flushing the dead volume of the mixer.

Note that in Fig. 7.11b ( $N_{mix} = 2$ )  $\sigma$  jumps to a lower value when the outlet valve opens than in Fig. 7.11a. This means that the fluid entering the outlet channel is better mixed, but still not thoroughly mixed. Examining  $\sigma$  in Figs. 7.11c ( $N_{mix} = 6$ ) and (d) ( $N_{mix} = 8$ ) shows no evidence of a rapid increase in  $\sigma$  when the outlet valve opens, meaning that the fluid entering the outlet channel from the mixer is well mixed. For the case of  $N_{mix} = 5$  (not shown) there is still a noticeable increase in  $\sigma$  when new fluid is expelled from the mixer into the outlet channel. We therefore choose  $N_{mix} = 6$  for normal LDMP operation to ensure good mixing, and avoid larger values of



$N_{mix}$  so as to minimize the time it takes to execute a mixer pump cycle, which is

$$\tau_{MP} = (34 + 2N_{mix})\tau_{clock} \quad (7.14)$$

$$= (3.4 + 0.2N_{mix}) \text{ seconds.} \quad (7.15)$$

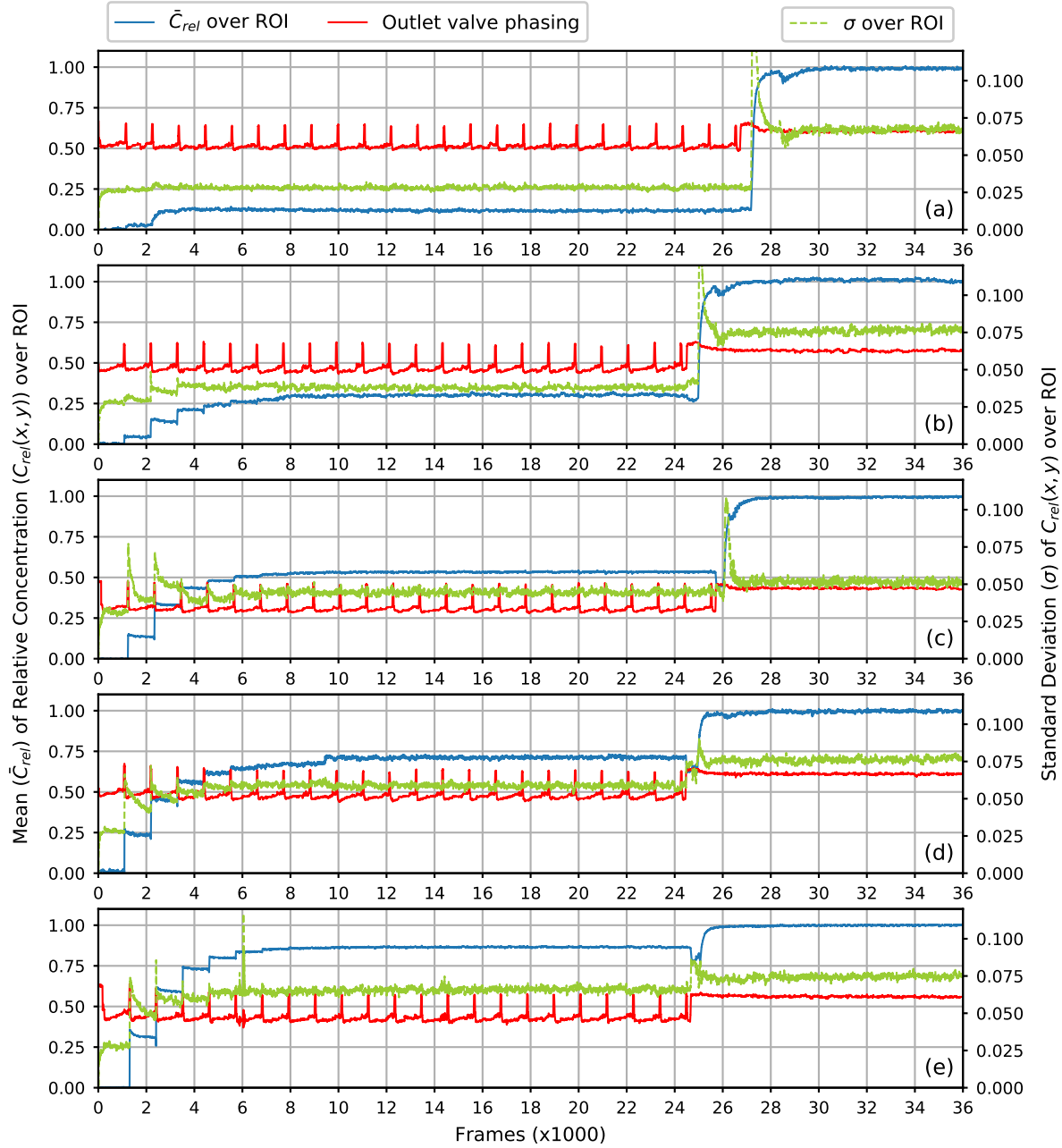


Figure 7.13: Experimental data for  $\bar{C}_{rel}$  and  $\sigma$  for different Red concentrations using  $N_{mix} = 6$  mixing periods. The Red concentration for (a)-(e) are  $i/6$  where  $i \in [1, 2, 3, 4, 5]$ .



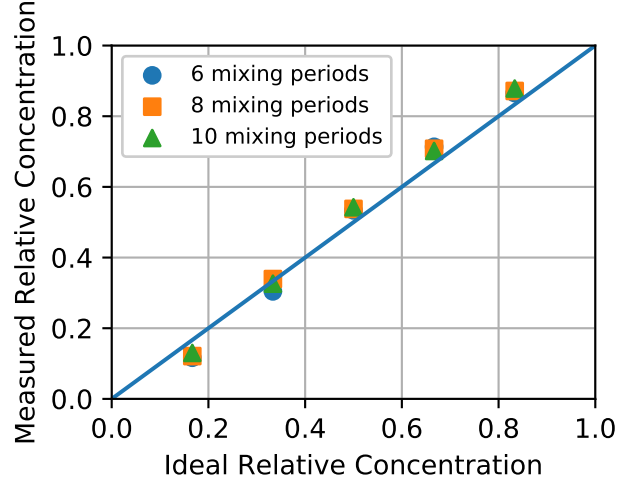


Figure 7.14: Plot of measured relative concentration vs. ideal relative concentration with 6, 8, and 10 mixing periods. The measured relative concentration is averaged over frames in 3 full consecutive mixer pump cycles starting from frame 20,000.

Therefore a mixer pump cycle with 6 mixing cycles takes  $\tau_{MP} = 4.6$  s, which is 6.5 times faster than diffusion alone for a 20 nL cubic volume, and 150 times faster than if the fluid just sat in the mixer.

Having determined how many mixing periods are needed to ensure good mixing, we now examine the fidelity of obtaining desired dilution ratios with an LDMP. Since the volume,  $V_{mixer}$ , is  $6V_{pump}$ , the possible Red dilution ratios are  $i/6$  where  $i \in [1, 2, 3, 4, 5]$ . Fig. 7.13a-e, contains experimental data for each of these cases with  $N_{mix} = 6$ . From these, the average relative concentration is calculated and plotted in Fig. 7.14. We find that the dilution fidelity is reasonably good, with the variation from ideal concentration for individual dilutions ranging from 4% to 15%. We also plot the same results for 8 and 10 mixing periods, which shows the same results as for 6 mixing periods and further demonstrates that increasing  $N_{mix}$  beyond 6 does not provide a noticeably greater degree of mixing.

### 7.2.3 4-to-1 Valve

The 3D printed valves we have discussed so far possess only 1 inlet channel. To simultaneously control 4 inlet channels, 4 such valves would be needed. Alternatively, we can create a 4-to-1 valve that performs the same function. In Fig. 7.15a, we show a CAD design of a 4-to-1 valve,

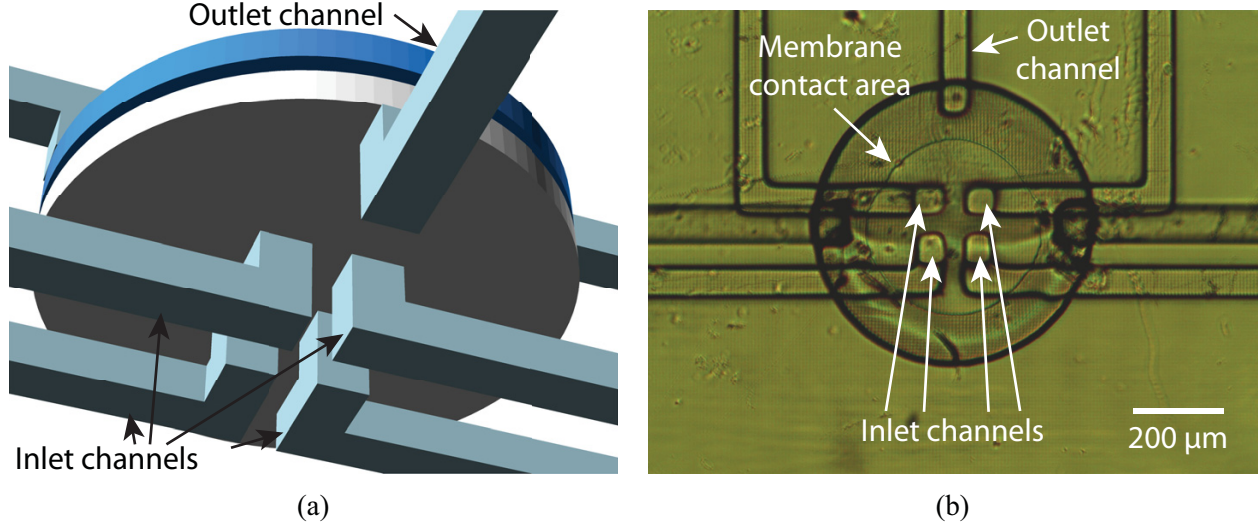


Figure 7.15: (a) CAD design of a 3D printed 4-to-1 valve that contains 4 inlet channels and 1 outlet channel. (b) Microscope photo of a fabricated 4-to-1 valve under pressure. The membrane is deflected such that it is in contact with the central area of the bottom of the valve, covering all 4 inlet channels and therefore closing the valve.

which we use in Sect. 7.2.4. By placing 4 inlets at the center of the valve, the deflected membrane is designed to seal all of them, simultaneously closing the fluidic pathway between these inlets and the outlet, as shown in Fig. 7.15b. To enable the membrane to seal over all four inlet channels, we have increased the valve diameter to 80 pixels ( $608 \mu\text{m}$ ). This 4-to-1 valve is not only smaller than four 40-pixel-diameter valves, but also notably reduces the structural complexity resulting from channel routing. Additionally, combining 4 valves into 1 means only 1 control chamber must be flushed after 3D printing, which simplifies the flushing operation.

#### 7.2.4 Parallelized Dilution Mixer Pump (PDMP)

In an LDMP, inlets A and B are each connected to their own pump. During routine operation if only one pump runs at a time, it takes  $6\tau_{\text{pump}}$  to fill the mixer. If we operate the 2 pumps simultaneously as much as possible, in the best case for a concentration of  $3/6$ ,  $3\tau_{\text{pump}}$  are needed to fill the mixer. In the worst case, (for example, a concentration of  $1/6$ ) the Red pump is idle for  $4\tau_{\text{pump}}$  out of  $5\tau_{\text{pump}}$  in every mixer pump cycle. To solve this problem, we consider a parallelized dilution mixer pump (PDMP) that exploits its pumps as much as possible to shorten the mixer pump cycle.

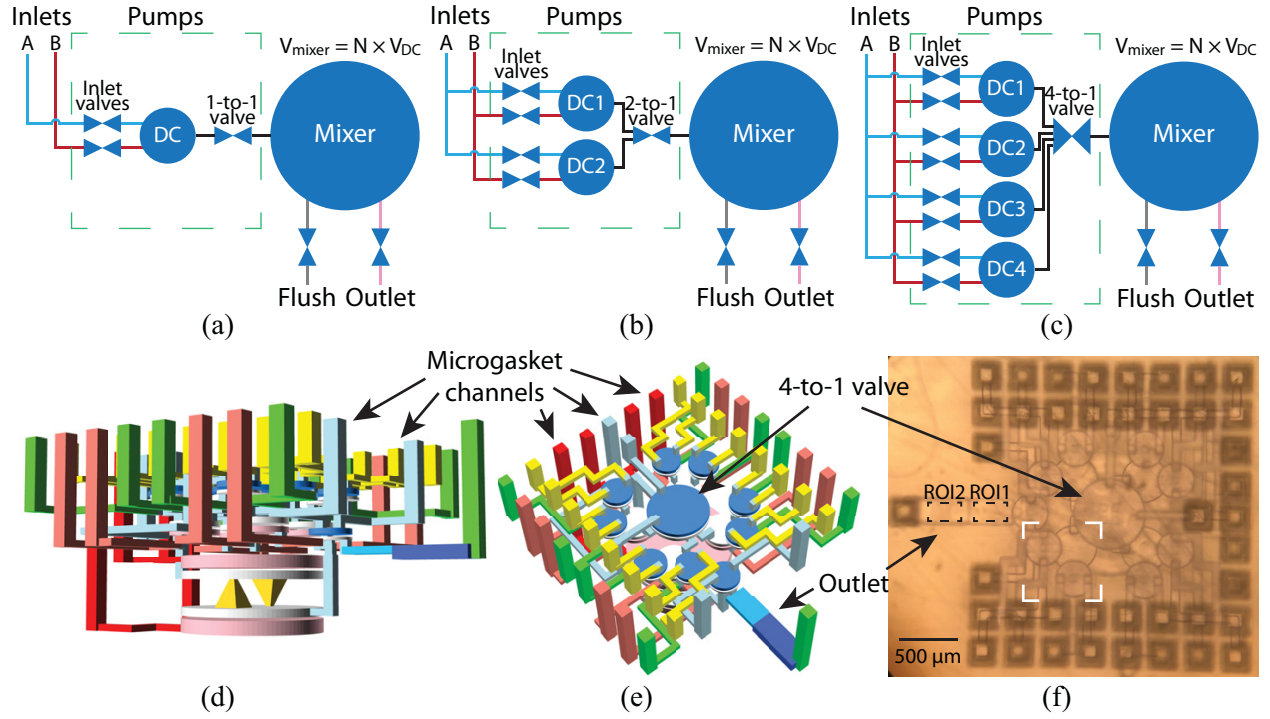


Figure 7.16: (a)-(c) Schematic of PDMPs with 1, 2, and 4 DIPs, respectively. A DIP has 2 inlet valves to enable pumping from either fluid source. The 1-to-1 valve is a normal valve, but a  $n$ -to-1 valve controls connecting  $n$  inlets to 1 outlet. (d, e) Different perspectives of a PDMP CAD design with 4 pumps and a 4-to-1 valve. The green vertical channels are fluidic channels, and the rest are control (pneumatic) channels. The outlet channel consists of two sections with heights of 50  $\mu\text{m}$  (ROI1) and 100  $\mu\text{m}$  (ROI2), respectively. (f) Microscope photo of a 3D printed device based on (d, e). Inside the white dashed box are 2 inlet valves and a DC.

In Fig. 7.16a-c, we consider several possible configurations for a PDMP. In the extreme case (Fig. 7.16a), there is only 1 pump in the PDMP. However, the pump has a pair of inlet valves, each connected to an individual fluid source such that the pump can be used to pump either fluid. We call this type of pump a dual inlet pump (DIP). If we want its DC to draw fluid from inlet A, we ensure that the inlet B valve is closed. Then the inlet A valve, DC, and 1-to-1 outlet valve together form a regular pump. Since there is only 1 pump, and because  $V_{\text{mixer}} = NV_{\text{pump}}$ , the single DIP must operate  $N$  mixing periods to fill the mixer.

In Fig. 7.16b, we double the number of DIPs and consolidate two 1-to-1 outlet valves into one 2-to-1 outlet valve. Because all of the DIPs in a PDMP are operated in parallel, the time to fill the mixer is cut in half, assuming that  $N$  is even. The same principle applies to the PDMP in Fig. 7.16c in which 4 DIPs and one 4-to-1 outlet valve are used.

Table 7.2: Comparison of LDMP and PDMPs with different DIP count. Here, we assume the pump DC dimensions are the same for LDMP and PDMPs, and that  $V_{mixer} = N \times V_{pump}$ .

	Inlet valves	DCs	Outlet valves	Pneumatic Lines	Shortest time to fill up mixer
LDMP	2	2	2	10	$N/2 \times \tau_{pump}$
PDMP (1 DIP)	2	1	1	8	$N \times \tau_{pump}$
PDMP (2 DIPs)	4	2	1	10	$N/2 \times \tau_{pump}$
PDMP (4 DIPs)	8	4	1	14	$N/4 \times \tau_{pump}$

Table 7.3: Available serial dilution ratios with various dilution factors for the fabricated PDMP design. A dilution factor of 4 is a subset of a dilution factor of 2.

Dilution factor	Concentration (actual pumped fluid volume ratios)			
2	1/2 (8/16)	1/4 (4/16)	1/8 (2/16)	1/16 (1/16)
3	1/3 (5/15)	1/9 (2/18)	—	—
4	1/4 (4/16)	1/16 (1/16)	—	—
5	1/5 (3/15)	—	—	—

In Table 7.2 we compare the number of valves, DCs, pneumatic lines, and time to fill the mixer for the best case LDMP with PDMPs having various DIP counts. As more DIPs are added to a PDMP, it takes less time to fill the mixer to its maximum capacity  $V_{mixer} = NV_{pump}$  if  $N$  is evenly divisible by the number of DIPs. However, more DIPs increases the complexity of the PDMP 3D layout (for both the PDMP and the interface chips), occupies more volume, and can increase the difficulty of flushing. Therefore, we implement the 4 DIP configuration in Fig. 7.16c as a compromise between faster filling of the mixer and increasing complexity. Our CAD design is shown from two different perspectives in Fig. 7.16d and e, and Fig. 7.16f shows a fabricated device, which occupies a volume of only  $2.6 \text{ mm}^3$  not counting the various external channels. In the flushing interface chip, we use 41 PTFE tubes, 32 to flush control chambers and 9 to flush fluid chambers and channels. In the operating interface chip, there are 16 tubes, 13 pneumatic and 3 fluidic.

To evaluate this PDMP design, we conduct serial dilutions for the dilution factors listed in Table. 7.3. The mixer in the PDMP is the same as in the LDMP, but we shrink the pump DC diameter from 60 pixels to 50 pixels and the fluid and control chamber heights from 50  $\mu\text{m}$  to 40  $\mu\text{m}$  to achieve a smaller pump volume, which we can estimate as 80% of  $V_{\text{pump}} = 1.31 \text{ nL}$  (vacuum) from Fig. 7.5c, or 1.05 nL. We reduce the pump volume so that more pump volumes can fit in the mixer, which gives us a wider range of possible dilution ratios. We experimentally find that  $V_{\text{mixer}} \approx 20V_{\text{pump}} = 21 \text{ nL}$ . We choose the denominators in the actual pumped fluid volume ratios in Table 7.3 to be as close to 20 as possible for two reasons. First, it allows more fluid to be mixed per mixer pump cycle, and, second, if there is too little fluid in the mixer, the membrane cannot be fully restored to its undeflected state or fully pulled into the control chamber, which limits how much the membrane can move. Limited membrane movement tends to be less effective for active mixing.

An  $N_{\text{mix}}$  of 6 is used for testing all of the dilution concentrations in Table 7.3. For serial dilution with a dilution factor of 2, a PDMP with 4 DIPs requires 4 pumping periods such that  $V_{\text{mixer}} = 16V_{\text{pump}}$ , leading to

$$\tau_{MP} = 2\tau_{\text{clock}} + 4\tau_{\text{pump}} + 6\tau_{\text{mix}} + 2\tau_{\text{clock}} \quad (7.16)$$

$$= 3.6 \text{ seconds}, \quad (7.17)$$

which is 8.3 times faster than diffusion alone for a 20 nL cubic volume, and 190 times faster than if the fluid sat statically in the mixer.

In contrast, an LDMP with the same DC size for the pumps would require 8 pumping periods at minimum for the best case 1/2 dilution ratio, making its  $\tau_{MP}$  5.6 s, which is over 50% longer than for the PDMP, and 15 pumping periods in the worst case for 1/16 dilution ( $\tau_{MP} = 9.1 \text{ s}$ ). Another noteworthy aspect of the PDMP design is that the outlet channel in Fig. 7.16e and f is divided into 2 sections, the first of which is 50  $\mu\text{m}$  tall, followed by a 100  $\mu\text{m}$  tall section. The taller section increases the measurement dynamic range for lower concentration ratios. As shown in Fig. 7.17, the measured relative concentrations are close to the designed values. For a dilution factor of 2, we test 3 different PDMPs, the results of which are plotted in red in Fig. 7.17. The

error bars for these points represent the standard deviation of the measurements for the 3 different PDMPs, which indicates good repeatability between different fabricated PDMPs.

### 7.3 Conclusions

We have taken advantage of our custom 3D printer and resin to demonstrate highly compact active microfluidic components with tight 3D layouts in only a few cubic millimeters. We have further shown that offloading world-to-chip connections to a separate 3D printed interface chip is an important facilitator of such miniaturization. We first examined 3D printed pumps, which can be realized with two valves and a displacement chamber, and demonstrated the relationship between displacement chamber size and the volume pumped per pumping cycle using a simple video-based analysis method in conjunction with a serpentine channel 3D printed as the pump outlet.

We then integrated 2 pumps with an active mixer to realize a selectable ratio linear dilution mixer pump (LDMP) in only  $1.5 \text{ mm}^3$ . It is designed to mix 20 nL of fluid in each mixer pump cycle. We have shown that 6 mixer periods are sufficient to fully mix the fluid as evidenced by our new video absorption-based measurement method that uses only a smartphone with a microscope operating in transmission mode. Using this new method, we are able to process the recorded slow motion videos and obtain the relative dye concentration and its spatial variation in the outlet

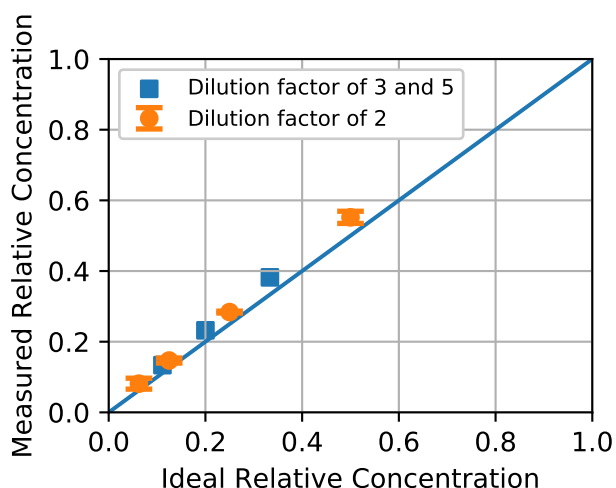


Figure 7.17: Measured relative concentration vs ideal for different dilution factors using PDMPs. Three PDMPs are tested for a dilution factor of 2 to obtain the error bars.

channel observation region. The measured linear set of concentrations the device can produce are close to the designed dilutions that range from  $1/6$  to  $5/6$ . Each mixer pump cycle takes 4.6 s.

To speed up the mixing process and achieve a denser set of dilution ratios, we created a parallelized dilution mixer pump (PDMP) which utilizes a new 4-to-1 valve that controls 4 inlets with only 1 pneumatic line. The PDMP shows that we can sacrifice structural simplicity to a gain shorter mixer pump cycle of 3.6 s using 4 dual input pumps. By reducing the pump DC size we also gain a greater range of dilution possibilities, and demonstrate serial dilutions with dilution factors of 2, 3, and 4, with the highest dilution ratio being  $1/16$ . All measured concentrations are close to the designed values.

## CHAPTER 8. CONCLUSIONS

### 8.1 Summary

#### 8.1.1 Optical Approach to Resin Formulation for 3D Printed Microfluidics

In Chapter 3, we formulated custom resins for a commercial Digital Light Processor stereolithographic (DLP-SLA) 3D printer based on an optical approach to minimize the void sizes it can fabricate. A mathematical model was developed for optical dose delivered through the thickness of a 3D printed part, including the effect of voids. There was a fundamental trade-off between the homogeneity of the optical dose within individual layers and how far the critical dose penetrated into a flow channel during fabrication. We presented an experimental investigation of the practical limits of flow channel miniaturization given the optical properties of a resin and found that the minimum flow channel height is  $\sim 3.5\text{--}5.5h_a$  where  $h_a$  was the optical penetration depth of the resin, and that the minimum width was 4 pixels in the build plane. We also showed that the ratio of the build layer thickness to  $h_a$  should be in the range 0.3–1.0 to obtain the minimum flow channel height for a given resin. The minimum flow channel size that we demonstrated for a custom resin is  $60\text{ }\mu\text{m} \times 108\text{ }\mu\text{m}$  for a  $10\text{ }\mu\text{m}$  build layer thickness.

#### 8.1.2 High Density 3D Printed Microfluidic Valves, Pumps, and Multiplexers

In Chapter 4, we demonstrated that 3D printing with a DLP-SLA 3D printer can be used to create high density microfluidic devices with active components such as valves and pumps. Based on the work in Chapter 3 on optical formulation of inexpensive resins, we demonstrated valves with only 10% of the volume of Rogers' original 3D printed valves [24], which were already the smallest that had been reported. Moreover, incorporation of a thermal initiator in the resin formulation along with a post-print bake could dramatically improve the durability of 3D printed valves up to 1 million actuations. Using two valves and a valve-like displacement chamber (DC),



we also created compact 3D printed pumps. With 5-phase actuation and a 15 ms phase interval, we obtained pump flow rates as high as 40  $\mu\text{L}/\text{min}$ . We also characterized maximum pump back pressure (i.e., maximum pressure the pump can work against), maximum flow rate (flow rate when there was zero back pressure), and flow rate as a function of the height of the pump outlet. We further demonstrated combining 5 valves and one DC to create a 3-to-2 multiplexer with integrated pump. In addition to serial multiplexing, the device could operate as a mixer. Importantly, we illustrated the rapid fabrication and test cycles that 3D printing made possible by implementing a new multiplexer design to improve mixing, and fabricate and test it within one day.

### **8.1.3 Custom 3D Printer and Resin for $18\ \mu\text{m} \times 20\ \mu\text{m}$ Microfluidic Flow Channels**

In Chapter 5, a custom DLP-SLA 3D printer was constructed and a specifically-designed, low cost, custom resin was formulated to readily achieve flow channel cross sections as small as  $18\ \mu\text{m} \times 20\ \mu\text{m}$ . This custom 3D printer had a projected image plane resolution of  $7.56\ \mu\text{m}$  and used a 385 nm LED, which significantly increased the available selection of UV absorbers for resin formulation compared to 3D printers with 405 nm LEDs. Beginning with 20 candidate absorbers, we stepped through evaluation criteria and process flow required to develop a high-resolution resin. In doing so, we discussed a new mathematical model for characterizing the resin optical penetration depth based only on measurement of the absorber's molar absorptivity. The final resin formulation used 2-nitrophenyl phenyl sulfide (NPS) as the UV absorber. A novel channel narrowing technique was developed so that, together with the new resin and 3D printer resolution, it enabled small flow channel fabrication. The efficacy of this technique was demonstrated by fabricating 3D serpentine flow channels 41 mm long in a volume of only  $0.12\ \text{mm}^3$ , and by printing high aspect ratio flow channels  $<25\ \mu\text{m}$  wide and 3 mm tall. These results indicated that 3D printing was finally positioned to challenge the pre-eminence of methods such as soft lithography for microfluidic device prototyping and fabrication.

### **8.1.4 3D Printed High Density, Reversible, Chip-to-chip Microfluidic Interconnects**

The development in miniaturizing 3D printed microfluidics in Chapter 4 and 5 offered the opportunity to fabricate highly integrated chips that measure only a few mm on a side. For such

small chips, an interconnection method was needed to provide the necessary world-to-chip reagent and pneumatic connections.

In Chapter 6, two types of connection mechanisms, Simple Integrated Microgaskets (SIMs) and Controlled-Compression Integrated Microgaskets (CCIMs), were introduced to connect a small device chip to a larger interface chip that implemented world-to-chip connections. SIMs or CCIMs were directly 3D printed as part of the device chip, and therefore no additional materials or components were required to make the connection to the larger 3D printed interface chip. We demonstrated 121 chip-to-chip interconnections in an  $11 \times 11$  array for both SIMs and CCIMs with an areal density of 53 interconnections/ $\text{mm}^2$ , and showed that they withstood fluid pressures of 50 psi. We further demonstrated their reusability by testing devices 100 times without seal failure. Scaling experiments showed that  $20 \times 20$  interconnection arrays were feasible, and that CCIM areal density could be increased to 88 interconnections/ $\text{mm}^2$ . We then showed the utility of spatially distributed discrete CCIMs by using an interconnection chip with 28 chip-to-world interconnects to test 45 3D printed valves in a  $9 \times 5$  array. Each valve was only  $300 \mu\text{m}$  in diameter (the smallest yet reported for 3D printed valves). Every row of 5 valves was tested to at least 10,000 actuations, with one row tested to 1,000,000 actuations. In all case there was no sign of valve failure, and the CCIM interconnections proved an effective means of using a single interface chip to test a series of valve array chips.

### **8.1.5 3D Printed Selectable Dilution Mixer Pumps**

In Chapter 7, We demonstrated the ability to 3D print tightly integrated structures with active valves, pumps, and mixers, and we used the compact chip-to-chip interconnects developed in Chapter 5 to move bulky world-to-chip connections to separate interface chips for both post-print flushing and post-cure device operation. As example devices, we first examined 3D printed pumps, followed by two types of selectable ratio mixer pumps, a linear dilution mixer pump (LDMP) and a parallelized dilution mixer pump (PDMP), which occupied volumes of only  $1.5 \text{ mm}^3$  and  $2.6 \text{ mm}^3$ , respectively. The LDMP generated a selectable dilution ratio from a linear set of possibilities, while the PDMP generated a denser set of possible dilutions with a maximum dilution ratio of 1/16. The PDMP also incorporated a new 4-to-1 valve to simultaneously control 4 inlet channels. To characterize LDMP and PDMP operation and performance, we presented a new, low-cost video

method to directly measure the relative concentration of an absorptive dye on a pixel-by-pixel basis for each video frame. Using this method, we found that 6 periods of the active mixer that formed the core of the LDMP and PDMP were sufficient to fully mix the fluid, and that the generated concentrations tracked the designed dilution ratios as expected. The LDMP mixed 20 nL per 4.6 s mixer pump period, while the PDMP used parallelized mixer input pumps to process the same fluid volume with greater choice of dilution ratios in a 3.6 s period.

## **8.2 Future Research**

While truly microfluidic channels and active components have been successfully demonstrated, there is much work to make 3D printing widely used in microfluidics.

### **8.2.1 3D Printer**

Despite the fact the custom 3D printer in Chapter 5 contained a pixel count of  $2560 \times 1600$ , its small pixel pitch in the focal plane,  $7.56 \mu\text{m}$ , led to an entire print area of  $19.35 \text{ mm} \times 12.10 \text{ mm}$ . In order to gain a large print area while still maintaining high resolution, one can mount the light engine on a XY translation stage, and stitch multiple exposed regions to form a larger build area.

### **8.2.2 Resin**

The current resin formulation, consisting of NPS, proves to be toxic to living cells without post-print treatment, so it would be beneficial to formulate a biocompatible resin. This process can be facilitated by using a 365 nm LED as DLP light source to widen the range of choices for both absorbers and photoinitiators. Moreover, if the photoinitiator has a wider absorption spectrum than absorber, it enables more effective optical curing. Also, more work can be done to investigate thermal initiators that are durable under UV. Once a biocompatible resin is in place, cell-related biomedical applications can be studied, which would hopefully speed up the adoption rate of 3D printing for microfluidics.

### **8.2.3 Other Possibilities**

As this dissertation progressed, the 3D printed devices become increasingly complex, so it takes longer and longer to design them. Similar to smart layout generation tools in many circuit design softwares, an automated microfluidic CAD design program would greatly assist the creation of new devices, shorten iterations, and encourage trying new ideas. Another aspect worth exploring is to use patterned silicon as substrate, which offers possibilities of bridging electrical/optical circuits with fluidic system.

## REFERENCES

- [1] <http://www.custompartnet.com/wu/3d-printing>, Accessed September, 2018. ix, 6, 8, 10
- [2] T. Billiet, M. Vandenhaute, J. Schelfhout, S. Van Vlierberghe, and P. Dubruel, “A review of trends and limitations in hydrogel-rapid prototyping for tissue engineering,” *Biomaterials*, vol. 33, no. 26, pp. 6020–6041, 2012. ix, 11
- [3] P. N. Nge, C. I. Rogers, and A. T. Woolley, “Advances in microfluidic materials, functions, integration, and applications,” *Chemical reviews*, vol. 113, no. 4, pp. 2550–2583, 2013. 1, 12
- [4] P. Neužil, S. Giselsbrecht, K. Länge, T. J. Huang, and A. Manz, “Revisiting lab-on-a-chip technology for drug discovery,” *Nature reviews Drug discovery*, vol. 11, no. 8, p. 620, 2012. 1
- [5] A. Khademhosseini, R. Langer, J. Borenstein, and J. P. Vacanti, “Microscale technologies for tissue engineering and biology,” *Proceedings of the National Academy of Sciences*, vol. 103, no. 8, pp. 2480–2487, 2006. 1
- [6] C. Xia and N. X. Fang, “3D microfabricated bioreactor with capillaries,” *Biomedical microdevices*, vol. 11, no. 6, pp. 1309–1315, 2009. 1
- [7] C. D. Chin, T. Laksanasopin, Y. K. Cheung, D. Steinmiller, V. Linder, H. Parsa, J. Wang, H. Moore, R. Rouse, G. Umvilighozo *et al.*, “Microfluidics-based diagnostics of infectious diseases in the developing world,” *Nature medicine*, vol. 17, no. 8, p. 1015, 2011. 1
- [8] A. M. Foudeh, T. F. Didar, T. Veres, and M. Tabrizian, “Microfluidic designs and techniques using lab-on-a-chip devices for pathogen detection for point-of-care diagnostics,” *Lab on a Chip*, vol. 12, no. 18, pp. 3249–3266, 2012. 1
- [9] S. Mulvaney, K. Myers, P. Sheehan, and L. Whitman, “Attomolar protein detection in complex sample matrices with semi-homogeneous fluidic force discrimination assays,” *Biosensors and Bioelectronics*, vol. 24, no. 5, pp. 1109–1115, 2009. 1
- [10] M. L. Sin, K. E. Mach, P. K. Wong, and J. C. Liao, “Advances and challenges in biosensor-based diagnosis of infectious diseases,” *Expert review of molecular diagnostics*, vol. 14, no. 2, pp. 225–244, 2014. 1
- [11] A. E. Saliba, L. Saias, E. Psychari, N. Minc, D. Simon, F. C. Bidard, C. Mathiot, J. Y. Pierga, V. Fraisier, J. Salamero *et al.*, “Microfluidic sorting and multimodal typing of cancer cells in self-assembled magnetic arrays,” *Proceedings of the National Academy of Sciences*, vol. 107, no. 33, pp. 14 524–14 529, 2010. 1

- [12] B. V. Chikkaveeraiah, V. Mani, V. Patel, J. S. Gutkind, and J. F. Rusling, "Microfluidic electrochemical immunoarray for ultrasensitive detection of two cancer biomarker proteins in serum," *Biosensors and Bioelectronics*, vol. 26, no. 11, pp. 4477–4483, 2011. 1
- [13] M. Hu, J. Yan, Y. He, H. Lu, L. Weng, S. Song, C. Fan, and L. Wang, "Ultrasensitive, multiplexed detection of cancer biomarkers directly in serum by using a quantum dot-based microfluidic protein chip," *ACS nano*, vol. 4, no. 1, pp. 488–494, 2009. 1
- [14] R. Malhotra, V. Patel, B. V. Chikkaveeraiah, B. S. Munge, S. C. Cheong, R. B. Zain, M. T. Abraham, D. K. Dey, J. S. Gutkind, and J. F. Rusling, "Ultrasensitive detection of cancer biomarkers in the clinic by use of a nanostructured microfluidic array," *Analytical chemistry*, vol. 84, no. 14, pp. 6249–6255, 2012. 1
- [15] B. L. Ziober, M. G. Mauk, E. M. Falls, Z. Chen, A. F. Ziober, and H. H. Bau, "Lab-on-a-chip for oral cancer screening and diagnosis," *Head & Neck: Journal for the Sciences and Specialties of the Head and Neck*, vol. 30, no. 1, pp. 111–121, 2008. 1
- [16] S. Mulvaney, C. Cole, M. Kniller, M. Malito, C. Tamanaha, J. Rife, M. Stanton, and L. Whiteman, "Rapid, femtomolar bioassays in complex matrices combining microfluidics and magnetoelectronics," *Biosensors and Bioelectronics*, vol. 23, no. 2, pp. 191–200, 2007. 1
- [17] F. Moltzahn, A. B. Olshen, L. Baehner, A. Peek, L. Fong, H. Stöppler, J. Simko, J. F. Hilton, P. Carroll, and R. Blelloch, "Microfluidic-based multiplex qRT-PCR identifies diagnostic and prognostic microRNA signatures in the sera of prostate cancer patients," *Cancer research*, 2011. 1
- [18] S. Vorwerk, K. Ganter, Y. Cheng, J. Hoheisel, P. F. Stähler, and M. Beier, "Microfluidic-based enzymatic on-chip labeling of mirnas," *New biotechnology*, vol. 25, no. 2-3, pp. 142–149, 2008. 1
- [19] A. Manz, D. J. Harrison, E. M. Verpoorte, J. C. Fetting, A. Paulus, H. Lüdi, and H. M. Widmer, "Planar chips technology for miniaturization and integration of separation techniques into monitoring systems: capillary electrophoresis on a chip," *Journal of Chromatography A*, vol. 593, no. 1-2, pp. 253–258, 1992. 1
- [20] D. R. Reyes, D. Iossifidis, P.-A. Auroux, and A. Manz, "Micro total analysis systems. 1. introduction, theory, and technology," *Analytical chemistry*, vol. 74, no. 12, pp. 2623–2636, 2002. 1
- [21] Q. Mei, Z. Xia, F. Xu, S. A. Soper, and Z. H. Fan, "Fabrication of microfluidic reactors and mixing studies for luciferase detection," *Analytical chemistry*, vol. 80, no. 15, pp. 6045–6050, 2008. 1
- [22] J. Friend and L. Yeo, "Fabrication of microfluidic devices using polydimethylsiloxane," *Biomicrofluidics*, vol. 4, no. 2, p. 026502, 2010. 1
- [23] S. K. Sia and G. M. Whitesides, "Microfluidic devices fabricated in poly (dimethylsiloxane) for biological studies," *Electrophoresis*, vol. 24, no. 21, pp. 3563–3576, 2003. 1

- [24] C. I. Rogers, K. Qaderi, A. T. Woolley, and G. P. Nordin, "3D printed microfluidic devices with integrated valves," *Biomicrofluidics*, vol. 9, no. 1, p. 016501, 2015. 1, 2, 38, 40, 44, 58, 93, 103, 124
- [25] A. K. Au, W. Huynh, L. F. Horowitz, and A. Folch, "3D-printed microfluidics," *Angewandte Chemie International Edition*, vol. 55, no. 12, pp. 3862–3881, 2016. 2
- [26] Y. He, Y. Wu, J. Z. Fu, Q. Gao, and J. J. Qiu, "Developments of 3D printing microfluidics and applications in chemistry and biology: a review," *Electroanalysis*, vol. 28, no. 8, pp. 1658–1678, 2016. 2
- [27] R. Amin, S. Knowlton, A. Hart, B. Yenilmez, F. Ghaderinezhad, S. Katebifar, M. Messina, A. Khademhosseini, and S. Tasoglu, "3D-printed microfluidic devices," *Biofabrication*, vol. 8, no. 2, p. 022001, 2016. 2
- [28] N. Bhattacharjee, A. Urrios, S. Kang, and A. Folch, "The upcoming 3D-printing revolution in microfluidics," *Lab on a Chip*, vol. 16, no. 10, pp. 1720–1742, 2016. 2
- [29] S. Waheed, J. M. Cabot, N. P. Macdonald, T. Lewis, R. M. Guijt, B. Paull, and M. C. Breadmore, "3D printed microfluidic devices: enablers and barriers," *Lab on a Chip*, vol. 16, no. 11, pp. 1993–2013, 2016. 2, 7
- [30] C. Chen, B. T. Mehl, A. S. Munshi, A. D. Townsend, D. M. Spence, and R. S. Martin, "3D-printed microfluidic devices: fabrication, advantages and limitationsa mini review," *Analytical Methods*, vol. 8, no. 31, pp. 6005–6012, 2016. 2
- [31] A. A. Yazdi, A. Popma, W. Wong, T. Nguyen, Y. Pan, and J. Xu, "3D printing: an emerging tool for novel microfluidics and lab-on-a-chip applications," *Microfluidics and Nanofluidics*, vol. 20, no. 3, pp. 1–18, 2016. 2
- [32] C. M. B. Ho, S. H. Ng, K. H. H. Li, and Y. J. Yoon, "3D printed microfluidics for biological applications," *Lab on a Chip*, vol. 15, no. 18, pp. 3627–3637, 2015. 2
- [33] Y. Huang, M. C. Leu, J. Mazumder, and A. Donmez, "Additive manufacturing: current state, future potential, gaps and needs, and recommendations," *Journal of Manufacturing Science and Engineering*, vol. 137, no. 1, p. 014001, 2015. 2
- [34] B. C. Gross, J. L. Erkal, S. Y. Lockwood, C. Chen, and D. M. Spence, "Evaluation of 3D printing and its potential impact on biotechnology and the chemical sciences," *Analytical Chemistry*, vol. 86, no. 7, pp. 3240–3253, 2014. 2
- [35] T. Femmer, I. Flack, and M. Wessling, "Additive manufacturing in fluid process engineering," *Chemie Ingenieur Technik*, vol. 88, no. 5, pp. 535–552, 2016. 2
- [36] Y. Lu, G. Mapili, G. Suhali, S. Chen, and K. Roy, "A digital micro-mirror device-based system for the microfabrication of complex, spatially patterned tissue engineering scaffolds," *Journal of Biomedical Materials Research Part A*, vol. 77A, no. 2, pp. 396–405, 2006. 2
- [37] F. P. Melchels, J. Feijen, and D. W. Grijpma, "A review on stereolithography and its applications in biomedical engineering," *Biomaterials*, vol. 31, no. 24, pp. 6121–6130, 2010. 2

- [38] K. C. Bhargava, B. Thompson, and N. Malmstadt, "Discrete elements for 3D microfluidics," *Proceedings of the National Academy of Sciences*, vol. 111, no. 42, pp. 15 013–15 018, 2014. 2, 12
- [39] A. I. Shallan, P. Smejkal, M. Corban, R. M. Guijt, and M. C. Breadmore, "Cost-effective three-dimensional printing of visibly transparent microchips within minutes," *Analytical chemistry*, vol. 86, no. 6, pp. 3124–3130, 2014. 2, 12
- [40] A. K. Au, W. Lee, and A. Folch, "Mail-order microfluidics: evaluation of stereolithography for the production of microfluidic devices," *Lab on a Chip*, vol. 14, no. 7, pp. 1294–1301, 2014. 2, 12
- [41] A. K. Au, N. Bhattacharjee, L. F. Horowitz, T. C. Chang, and A. Folch, "3D-printed microfluidic automation," *Lab on a chip*, vol. 15, no. 8, pp. 1934–1941, 2015. 2
- [42] C. Schubert, M. C. Van Langeveld, and L. A. Donoso, "Innovations in 3D printing: a 3D overview from optics to organs," *British Journal of Ophthalmology*, vol. 98, no. 2, pp. 159–161, 2013. 2
- [43] T. L. Gerstle, A. M. Ibrahim, P. S. Kim, B. T. Lee, and S. J. Lin, "A plastic surgery application in evolution: three-dimensional printing," *Plastic and reconstructive surgery*, vol. 133, no. 2, pp. 446–451, 2014. 2
- [44] R. Sochol, E. Sweet, C. Glick, S. Venkatesh, A. Avetisyan, K. Ekman, A. Raulinaitis, A. Tsai, A. Wienkers, K. Korner *et al.*, "3D printed microfluidic circuitry via multijet-based additive manufacturing," *Lab on a Chip*, vol. 16, no. 4, pp. 668–678, 2016. 2, 8
- [45] R. Walczak and K. Adamski, "Inkjet 3D printing of microfluidic structures on the selection of the printer towards printing your own microfluidic chips," *Journal of Micromechanics and Microengineering*, vol. 25, no. 8, p. 085013, 2015. 2
- [46] H. Gong, M. Beauchamp, S. Perry, A. T. Woolley, and G. P. Nordin, "Optical approach to resin formulation for 3D printed microfluidics," *RSC advances*, vol. 5, no. 129, pp. 106 621–106 632, 2015. 2, 3, 12, 87
- [47] Y. Ukita, Y. Takamura, and Y. Utsumi, "Direct digital manufacturing of autonomous centrifugal microfluidic device," *Japanese Journal of Applied Physics*, vol. 55, no. 6S1, p. 06GN02, 2016. 2
- [48] J. M. Lee, M. Zhang, and W. Y. Yeong, "Characterization and evaluation of 3D printed microfluidic chip for cell processing," *Microfluidics and Nanofluidics*, vol. 20, no. 1, p. 5, 2016. 2
- [49] L. Donvito, L. Galluccio, A. Lombardo, G. Morabito, A. Nicolosi, and M. Reno, "Experimental validation of a simple, low-cost, t-junction droplet generator fabricated through 3D printing," *Journal of Micromechanics and Microengineering*, vol. 25, no. 3, p. 035013, 2015. 2



- [50] N. P. Macdonald, J. M. Cabot, P. Smejkal, R. M. Guijt, B. Paull, and M. C. Breadmore, "Comparing microfluidic performance of three-dimensional (3D) printing platforms," *Analytical Chemistry*, vol. 89, no. 7, pp. 3858–3866, 2017. 2
- [51] K. G. Lee, K. J. Park, S. Seok, S. Shin, J. Y. Park, Y. S. Heo, S. J. Lee, T. J. Lee *et al.*, "3D printed modules for integrated microfluidic devices," *RSC Advances*, vol. 4, no. 62, pp. 32 876–32 880, 2014. 2, 8
- [52] K. B. Anderson, S. Y. Lockwood, R. S. Martin, and D. M. Spence, "A 3D printed fluidic device that enables integrated features," *Analytical chemistry*, vol. 85, no. 12, pp. 5622–5626, 2013. 2, 8
- [53] P. S. Venkateswaran, A. Sharma, S. Dubey, A. Agarwal, and S. Goel, "Rapid and automated measurement of milk adulteration using a 3D printed optofluidic microviscometer (omv)," *IEEE Sensors Journal*, vol. 16, no. 9, pp. 3000–3007, 2016. 2
- [54] H. N. Chan, Y. Shu, B. Xiong, Y. Chen, Y. Chen, Q. Tian, S. A. Michael, B. Shen, and H. Wu, "Simple, cost-effective 3D printed microfluidic components for disposable, point-of-care colorimetric analysis," *ACS Sensors*, vol. 1, no. 3, pp. 227–234, 2015. 2
- [55] A. Urrios, C. Parra-Cabrera, N. Bhattacharjee, A. M. Gonzalez-Suarez, L. G. Rigat-Brugarolas, U. Nallapatti, J. Samitier, C. A. DeForest, F. Posas, J. L. Garcia-Cordero *et al.*, "3D-printing of transparent bio-microfluidic devices in peg-da," *Lab on a Chip*, vol. 16, no. 12, pp. 2287–2294, 2016. 2, 58
- [56] G. W. Bishop, J. E. Satterwhite-Warden, I. Bist, E. Chen, and J. F. Rusling, "Electrochemiluminescence at bare and DNA-coated graphite electrodes in 3D-printed fluidic devices," *ACS sensors*, vol. 1, no. 2, pp. 197–202, 2015. 2
- [57] W. G. Patrick, A. A. Nielsen, S. J. Keating, T. J. Levy, C. W. Wang, J. J. Rivera, O. Mondragón-Palomino, P. A. Carr, C. A. Voigt, N. Oxman *et al.*, "DNA assembly in 3D printed fluidics," *PloS one*, vol. 10, no. 12, p. e0143636, 2015. 2
- [58] J. M. Zhang, E. Q. Li, A. A. Aguirre-Pablo, and S. T. Thoroddsen, "A simple and low-cost fully 3D-printed non-planar emulsion generator," *RSC Advances*, vol. 6, no. 4, pp. 2793–2799, 2016. 2
- [59] A. J. Morgan, L. H. San Jose, W. D. Jamieson, J. M. Wymant, B. Song, P. Stephens, D. A. Barrow, and O. K. Castell, "Simple and versatile 3D printed microfluidics using fused filament fabrication," *PloS one*, vol. 11, no. 4, p. e0152023, 2016. 2
- [60] M. J. Beauchamp, G. P. Nordin, and A. T. Woolley, "Moving from millifluidic to truly microfluidic sub-100- $\mu\text{m}$  cross-section 3D printed devices," *Analytical and bioanalytical chemistry*, vol. 409, no. 18, pp. 4311–4319, 2017. 2, 3, 7
- [61] H. Gong, A. T. Woolley, and G. P. Nordin, "High density 3D printed microfluidic valves, pumps, and multiplexers," *Lab on a Chip*, vol. 16, no. 13, pp. 2450–2458, 2016. 3, 38, 51, 87, 96, 102

- [62] H. Gong, B. P. Bickham, A. T. Woolley, and G. P. Nordin, "Custom 3D printer and resin for  $18\text{ }\mu\text{m} \times 20\text{ }\mu\text{m}$  microfluidic flow channels," *Lab on a Chip*, vol. 17, no. 17, pp. 2899–2909, 2017. 3, 55, 83, 87, 104
- [63] K. V. Wong and A. Hernandez, "A review of additive manufacturing," *ISRN Mechanical Engineering*, vol. 2012, 2012. 6
- [64] R. Noorani, *Rapid prototyping – principles and applications*. New Jersey: John Wiley & Sons, 2006. 6
- [65] K. G. Cooper, *Rapid prototyping technology*. New York, NY: Marcel Dekker, 2001, vol. 200. 6
- [66] A. Gebhardt, *Understanding additive manufacturing: rapid prototyping - rapid tooling - rapid manufacturing*. München: Hanser, 2012. 6
- [67] X. Yan and P. Gu, "A review of rapid prototyping technologies and systems," *Computer-Aided Design*, vol. 28, no. 4, pp. 307–318, 1996. 6
- [68] M. D. Symes, P. J. Kitson, J. Yan, C. J. Richmond, G. J. Cooper, R. W. Bowman, T. Vilbrandt, and L. Cronin, "Integrated 3D-printed reactionware for chemical synthesis and analysis," *Nature chemistry*, vol. 4, no. 5, p. 349, 2012. 6
- [69] J. L. Moore, A. McCuiston, I. Mittendorf, R. Ottway, and R. D. Johnson, "Behavior of capillary valves in centrifugal microfluidic devices prepared by three-dimensional printing," *Microfluidics and Nanofluidics*, vol. 10, no. 4, pp. 877–888, 2011. 6
- [70] Y. He, J. Qiu, J. Fu, J. Zhang, Y. Ren, and A. Liu, "Printing 3D microfluidic chips with a 3D sugar printer," *Microfluidics and Nanofluidics*, vol. 19, no. 2, pp. 447–456, 2015. 6
- [71] P. K. Yuen, "Embedding objects during 3D printing to add new functionalities," *Biomicrofluidics*, vol. 10, no. 4, p. 044104, 2016. 7
- [72] F. Li, N. P. Macdonald, R. M. Guijt, and M. C. Breadmore, "Using printing orientation for tuning fluidic behavior in microfluidic chips made by fused deposition modeling 3D printing," *Analytical chemistry*, vol. 89, no. 23, pp. 12 805–12 811, 2017. 7
- [73] A. L. Rutz, K. E. Hyland, A. E. Jakus, W. R. Burghardt, and R. N. Shah, "A multimaterial bioink method for 3D printing tunable, cell-compatible hydrogels," *Advanced Materials*, vol. 27, no. 9, pp. 1607–1614, 2015. 7
- [74] B. R. Ringeisen, R. K. Pirlo, P. K. Wu, T. Boland, Y. Huang, W. Sun, Q. Hamid, and D. B. Chrisey, "Cell and organ printing turns 15: diverse research to commercial transitions," *MRS bulletin*, vol. 38, no. 10, pp. 834–843, 2013. 7
- [75] B. Valantan, D. Pogacar, T. Brajliah, T. Z. Hartner, A. Pilipovic, and I. Drstvensek, "Development of a 3D printer for thermoplastic modelling," *Mater Technol*, vol. 46, no. 6, pp. 589–94, 2012. 7
- [76] R. Singh, "Process capability study of polyjet printing for plastic components," *Journal of mechanical science and technology*, vol. 25, no. 4, pp. 1011–1015, 2011. 7

- [77] V. Petrovic, J. Vicente Haro Gonzalez, O. Jordá Ferrando, J. Delgado Gordillo, J. Ramón Blasco Puchades, and L. Portolés Griñan, “Additive layered manufacturing: sectors of industrial application shown through case studies,” *International Journal of Production Research*, vol. 49, no. 4, pp. 1061–1079, 2011. 7
- [78] J. C. McDonald, M. L. Chabinyk, S. J. Metallo, J. R. Anderson, A. D. Stroock, and G. M. Whitesides, “Prototyping of microfluidic devices in poly (dimethylsiloxane) using solid-object printing,” *Analytical chemistry*, vol. 74, no. 7, pp. 1537–1545, 2002. 7
- [79] A. Bonyár, H. Sántha, B. Ring, M. Varga, J. G. Kovács, and G. Harsányi, “3D rapid prototyping technology (RPT) as a powerful tool in microfluidic development,” *Procedia Engineering*, vol. 5, pp. 291–294, 2010. 7
- [80] D. Mark, S. Haeberle, G. Roth, F. Von Stetten, and R. Zengerle, “Microfluidic lab-on-a-chip platforms: requirements, characteristics and applications,” in *Microfluidics Based Microsystems*. Springer, 2010, pp. 305–376. 12
- [81] C. I. Rogers, J. V. Pagaduan, G. P. Nordin, and A. T. Woolley, “Single-monomer formulation of polymerized polyethylene glycol diacrylate as a nonadsorptive material for microfluidics,” *Analytical chemistry*, vol. 83, no. 16, pp. 6418–6425, 2011. 13, 38, 39, 58
- [82] B. Adzima, “The ember printer: An open platform for software, hardware, and materials development,” uv.eb WEST Conference, Redondo Beach, CA, uv.eb WEST, March 10-11 2015. 13, 14
- [83] measured in the Nordin lab, 2015. 14
- [84] private communication from manufacturer, 2015. 14
- [85] P. F. Jacobs, *Rapid Prototyping and Manufacturing: Fundamentals of StereoLithography*. New York, NY: McGraw-Hill, Inc., 1992. 16
- [86] C. I. Rogers, J. B. Oxborrow, R. R. Anderson, L. F. Tsai, G. P. Nordin, and A. T. Woolley, “Microfluidic valves made from polymerized polyethylene glycol diacrylate,” *Sensors and Actuators B: Chemical*, vol. 191, pp. 438–444, 2014. 38, 45, 93
- [87] G. Nordin, “Design files for 3D printed microfluidic valve, pump, and multiplexer on figshare, cc-by license,” 2016. [Online]. Available: <https://dx.doi.org/10.6084/m9.figshare.3219661.v1> 43
- [88] L. Láng, *Absorption Spectra in the Ultraviolet and Visible Region*, ser. Absorption Spectra in the Ultraviolet and Visible Region. Academic Press, 1961. 63
- [89] R. R. Hood and D. L. DeVoe, “High-throughput continuous flow production of nanoscale liposomes by microfluidic vertical flow focusing,” *small*, vol. 11, no. 43, pp. 5790–5799, 2015. 80
- [90] A. A. S. Bhagat, P. Jothimuthu, A. Pais, and I. Papautsky, “Re-usable quick-release interconnect for characterization of microfluidic systems,” *Journal of Micromechanics and Microengineering*, vol. 17, no. 1, p. 42, 2006. 81

- [91] S. Miserendino and Y.-C. Tai, "Modular microfluidic interconnects using photodefinable silicone microgaskets and mems o-rings," *Sensors and Actuators A: Physical*, vol. 143, no. 1, pp. 7–13, 2008. 81
- [92] G. A. Cooksey, A. L. Plant, and J. Atencia, "A vacuum manifold for rapid world-to-chip connectivity of complex pdms microdevices," *Lab on a Chip*, vol. 9, no. 9, pp. 1298–1300, 2009. 81
- [93] D. Sabourin, D. Snakenborg, and M. Dufva, "Interconnection blocks: a method for providing reusable, rapid, multiple, aligned and planar microfluidic interconnections," *Journal of Micromechanics and Microengineering*, vol. 19, no. 3, p. 035021, 2009. 81
- [94] R. Lo and E. Meng, "Reusable, adhesiveless and arrayed in-plane microfluidic interconnects," *Journal of Micromechanics and Microengineering*, vol. 21, no. 5, p. 054021, 2011. 81
- [95] A. Chen and T. Pan, "Fit-to-flow (f2f) interconnects: Universal reversible adhesive-free microfluidic adaptors for lab-on-a-chip systems," *Lab on a Chip*, vol. 11, no. 4, pp. 727–732, 2011. 81
- [96] P. Skafte-Pedersen, C. G. Sip, A. Folch, and M. Dufva, "Modular microfluidic systems using reversibly attached pdms fluid control modules," *Journal of Micromechanics and Microengineering*, vol. 23, no. 5, p. 055011, 2013. 81
- [97] E. Wilhelm, C. Neumann, T. Dутtenhofer, L. Pires, and B. E. Rapp, "Connecting microfluidic chips using a chemically inert, reversible, multichannel chip-to-world-interface," *Lab on a Chip*, vol. 13, no. 22, pp. 4343–4351, 2013. 81
- [98] A. Pfreundt, K. B. Andersen, M. Dimaki, and W. E. Svendsen, "An easy-to-use microfluidic interconnection system to create quick and reversibly interfaced simple microfluidic devices," *Journal of Micromechanics and Microengineering*, vol. 25, no. 11, p. 115010, 2015. 81
- [99] S. Zhao, R. Chen, Y. Yu, L. He, J. Liu, X. Chen, and S. Qin, "A multifunctional, plug-and-play and low-cost microfluidic connector system based on electronics standard," *RSC Advances*, vol. 5, no. 118, pp. 97 422–97 426, 2015. 81
- [100] P. F. Wagler, U. Tangen, J. Ott, and J. S. McCaskill, "General-purpose, parallel and reversible microfluidic interconnects," *IEEE Transactions on Components, Packaging and Manufacturing Technology*, vol. 5, no. 3, pp. 291–300, 2015. 81
- [101] G. P. Nordin, H. Gong, and A. T. Woolley, "Miniaturizing 3D printed microfluidics," MicroTAS 2017 keynote address, slides available at DOI: 10.5281/zenodo.1133980, Oct. 82
- [102] H. Gong, A. T. Woolley, and G. P. Nordin, "3D printed high density, reversible, chip-to-chip microfluidic interconnects," *Lab on a Chip*, vol. 18, no. 4, pp. 639–647, 2018. 82, 96
- [103] G. S. Jeong, S. Chung, C. B. Kim, and S. H. Lee, "Applications of micromixing technology," *Analyst*, vol. 135, no. 3, pp. 460–473, 2010. 98

- [104] J. I. Yoshida, H. Kim, and A. Nagaki, "Green and sustainable chemical synthesis using flow microreactors," *ChemSusChem*, vol. 4, no. 3, pp. 331–340, 2011. 98
- [105] W. Ehrfeld, K. Golbig, V. Hessel, H. Löwe, and T. Richter, "Characterization of mixing in micromixers by a test reaction: single mixing units and mixer arrays," *Industrial & Engineering Chemistry Research*, vol. 38, no. 3, pp. 1075–1082, 1999. 98
- [106] M. C. Mitchell, V. Spikmans, and A. J. de Mello, "Microchip-based synthesis and analysis: control of multicomponent reaction products and intermediates," *Analyst*, vol. 126, no. 1, pp. 24–27, 2001. 98
- [107] S. Suga, A. Nagaki, and J. I. Yoshida, "Highly selective friedel–crafts monoalkylation using micromixing," *Chemical Communications*, no. 3, pp. 354–355, 2003. 98
- [108] H. Kim, K. I. Min, K. Inoue, D. P. Kim, J. I. Yoshida *et al.*, "Submillisecond organic synthesis: Outpacing fries rearrangement through microfluidic rapid mixing," *Science*, vol. 352, no. 6286, pp. 691–694, 2016. 98
- [109] I. Lignos, S. Stavrakis, G. Nedelcu, L. Protesescu, A. J. deMello, and M. V. Kovalenko, "Synthesis of cesium lead halide perovskite nanocrystals in a droplet-based microfluidic platform: fast parametric space mapping," *Nano letters*, vol. 16, no. 3, pp. 1869–1877, 2016. 98
- [110] A. Nagaki, K. Kawamura, S. Suga, T. Ando, M. Sawamoto, and J.-i. Yoshida, "Cation pool-initiated controlled/living polymerization using microsystems," *Journal of the American Chemical Society*, vol. 126, no. 45, pp. 14 702–14 703, 2004. 98
- [111] F. Bally, C. A. Serra, V. Hessel, and G. Hadziioannou, "Micromixer-assisted polymerization processes," *Chemical Engineering Science*, vol. 66, no. 7, pp. 1449–1462, 2011. 98
- [112] J. Peng, C. Tian, L. Zhang, Z. Cheng, and X. Zhu, "The in situ formation of nanoparticles via raft polymerization-induced self-assembly in a continuous tubular reactor," *Polymer Chemistry*, vol. 8, no. 9, pp. 1495–1506, 2017. 98
- [113] N. Assmann, A. Ładosz, and P. Rudolf von Rohr, "Continuous micro liquid-liquid extraction," *Chemical Engineering & Technology*, vol. 36, no. 6, pp. 921–936, 2013. 98
- [114] V. Haverkamp, W. Ehrfeld, K. Gebauer, V. Hessel, H. Löwe, T. Richter, and C. Wille, "The potential of micromixers for contacting of disperse liquid phases," *Fresenius' journal of analytical chemistry*, vol. 364, no. 7, pp. 617–624, 1999. 98
- [115] S. Freitas, H. P. Merkle, and B. Gander, "Microencapsulation by solvent extraction/evaporation: reviewing the state of the art of microsphere preparation process technology," *Journal of controlled release*, vol. 102, no. 2, pp. 313–332, 2005. 98
- [116] M. E. Leblebici, S. Kuhn, G. D. Stefanidis, and T. Van Gerven, "Milli-channel mixer and phase separator for solvent extraction of rare earth elements," *Chemical Engineering Journal*, vol. 293, pp. 273–280, 2016. 98

- [117] O. Jafari, M. Rahimi, and F. H. Kakavandi, "Liquid-liquid extraction in twisted micromixers," *Chemical Engineering and Processing: Process Intensification*, vol. 101, pp. 33–40, 2016. 98
- [118] R. H. Liu, J. Yang, R. Lenigk, J. Bonanno, and P. Grodzinski, "Self-contained, fully integrated biochip for sample preparation, polymerase chain reaction amplification, and DNA microarray detection," *Analytical chemistry*, vol. 76, no. 7, pp. 1824–1831, 2004. 98
- [119] C. Y. Lee, G. B. Lee, J. L. Lin, F. C. Huang, and C. S. Liao, "Integrated microfluidic systems for cell lysis, mixing/pumping and DNA amplification," *Journal of Micromechanics and Microengineering*, vol. 15, no. 6, p. 1215, 2005. 98
- [120] Y. H. Chang, G. B. Lee, F. C. Huang, Y. Y. Chen, and J. L. Lin, "Integrated polymerase chain reaction chips utilizing digital microfluidics," *Biomedical microdevices*, vol. 8, no. 3, pp. 215–225, 2006. 98
- [121] I. N. Kefala, V. E. Papadopoulos, G. Karpou, G. Kokkoris, G. Papadakis, and A. Tserepi, "A labyrinth split and merge micromixer for bioanalytical applications," *Microfluidics and Nanofluidics*, vol. 19, no. 5, pp. 1047–1059, 2015. 98
- [122] R. Kurita and O. Niwa, "Microfluidic platforms for DNA methylation analysis," *Lab on a Chip*, vol. 16, no. 19, pp. 3631–3644, 2016. 98
- [123] A. G. Hadd, D. E. Raymond, J. W. Halliwell, S. C. Jacobson, and J. M. Ramsey, "Microchip device for performing enzyme assays," *Analytical chemistry*, vol. 69, no. 17, pp. 3407–3412, 1997. 98
- [124] B. J. Burke and F. E. Regnier, "Stopped-flow enzyme assays on a chip using a microfabricated mixer," *Analytical chemistry*, vol. 75, no. 8, pp. 1786–1791, 2003. 98
- [125] Y. Ukita, T. Asano, K. Fujiwara, K. Matsui, M. Takeo, S. Negoro, T. Kanie, M. Katayama, and Y. Utsumi, "Application of vertical microreactor stack with polystyrene microbeads to immunoassay," *Sensors and Actuators A: Physical*, vol. 145, pp. 449–455, 2008. 98
- [126] H. Roder and K. Wüthrich, "Protein folding kinetics by combined use of rapid mixing techniques and nmr observation of individual amide protons," in *Nmr In Structural Biology: A Collection of Papers by Kurt Wüthrich*. World Scientific, 1995, pp. 691–699. 98
- [127] O. Bilsel, C. Kayatekin, L. A. Wallace, and C. R. Matthews, "A microchannel solution mixer for studying microsecond protein folding reactions," *Review of scientific instruments*, vol. 76, no. 1, p. 014302, 2005. 98
- [128] A. Borgia, K. R. Kemplen, M. B. Borgia, A. Soranno, S. Shammash, B. Wunderlich, D. Nettels, R. B. Best, J. Clarke, and B. Schuler, "Transient misfolding dominates multidomain protein folding," *Nature communications*, vol. 6, p. 8861, 2015. 98
- [129] L. Jiang, Y. Zeng, Q. Sun, Y. Sun, Z. Guo, J. Y. Qu, and S. Yao, "Microsecond protein folding events revealed by time-resolved fluorescence resonance energy transfer in a microfluidic mixer," *Analytical chemistry*, vol. 87, no. 11, pp. 5589–5595, 2015. 98

- [130] C. Y. Lee, C. L. Chang, Y. N. Wang, and L. M. Fu, "Microfluidic mixing: a review," *International journal of molecular sciences*, vol. 12, no. 5, pp. 3263–3287, 2011. 98
- [131] G. Cai, L. Xue, H. Zhang, and J. Lin, "A review on micromixers," *Micromachines*, vol. 8, no. 9, p. 274, 2017. 98
- [132] Y. K. Suh and S. Kang, "A review on mixing in microfluidics," *Micromachines*, vol. 1, no. 3, pp. 82–111, 2010. 98
- [133] H. Gong, A. T. Woolley, and G. P. Nordin, "3D printed selectable dilution mixer pumps," *Biomicrofluidics*, 2018 (submitted). 99, 105
- [134] A. D. Stroock, S. K. Dertinger, A. Ajdari, I. Mezić, H. A. Stone, and G. M. Whitesides, "Chaotic mixer for microchannels," *Science*, vol. 295, no. 5555, pp. 647–651, 2002. 100
- [135] T. D. Luong, V. N. Phan, and N. T. Nguyen, "High-throughput micromixers based on acoustic streaming induced by surface acoustic wave," *Microfluidics and nanofluidics*, vol. 10, no. 3, pp. 619–625, 2011. 100
- [136] S. Wang, X. Huang, and C. Yang, "Mixing enhancement for high viscous fluids in a microfluidic chamber," *Lab on a chip*, vol. 11, no. 12, pp. 2081–2087, 2011. 100
- [137] D. Ahmed, X. Mao, B. K. Juluri, and T. J. Huang, "A fast microfluidic mixer based on acoustically driven sidewall-trapped microbubbles," *Microfluidics and nanofluidics*, vol. 7, no. 5, p. 727, 2009. 100
- [138] C. Y. Lim, Y. C. Lam, and C. Yang, "Mixing enhancement in microfluidic channel with a constriction under periodic electro-osmotic flow," *Biomicrofluidics*, vol. 4, no. 1, p. 014101, 2010. 100
- [139] Y. Du, Z. Zhang, C. Yim, M. Lin, and X. Cao, "A simplified design of the staggered heringbone micromixer for practical applications," *Biomicrofluidics*, vol. 4, no. 2, p. 024105, 2010. 100
- [140] Y. Wang, J. Zhe, B. T. Chung, and P. Dutta, "A rapid magnetic particle driven micromixer," *Microfluidics and Nanofluidics*, vol. 4, no. 5, pp. 375–389, 2008. 100
- [141] Y. Lam, H. Gan, N. T. Nguyen, and H. Lie, "Micromixer based on viscoelastic flow instability at low reynolds number," *Biomicrofluidics*, vol. 3, no. 1, p. 014106, 2009. 100
- [142] M. Z. Huang, R. J. Yang, C. H. Tai, C. H. Tsai, and L. M. Fu, "Application of electrokinetic instability flow for enhanced micromixing in cross-shaped microchannel," *Biomedical microdevices*, vol. 8, no. 4, pp. 309–315, 2006. 100
- [143] T. Tofteberg, M. Skolimowski, E. Andreassen, and O. Geschke, "A novel passive micromixer: lamination in a planar channel system," *Microfluidics and Nanofluidics*, vol. 8, no. 2, pp. 209–215, 2010. 100
- [144] Z. Chen, M. Bown, B. OSullivan, J. MacInnes, R. Allen, M. Mulder, M. Blom, and R. vant Oever, "Performance analysis of a folding flow micromixer," *Microfluidics and nanofluidics*, vol. 6, no. 6, pp. 763–774, 2009. 100

- [145] R. T. Tsai and C. Y. Wu, "An efficient micromixer based on multidirectional vortices due to baffles and channel curvature," *Biomicrofluidics*, vol. 5, no. 1, p. 014103, 2011. 100
- [146] K. Ward and Z. H. Fan, "Mixing in microfluidic devices and enhancement methods," *Journal of Micromechanics and Microengineering*, vol. 25, no. 9, p. 094001, 2015. 100
- [147] Q. Lang, Y. Ren, D. Hobson, Y. Tao, L. Hou, Y. Jia, Q. Hu, J. Liu, X. Zhao, and H. Jiang, "In-plane microvortices micromixer-based AC electrothermal for testing drug induced death of tumor cells," *Biomicrofluidics*, vol. 10, no. 6, p. 064102, 2016. 100
- [148] Y. Wu, Y. Ren, Y. Tao, L. Hou, Q. Hu, and H. Jiang, "A novel micromixer based on the alternating current-flow field effect transistor," *Lab on a Chip*, vol. 17, no. 1, pp. 186–197, 2017. 100
- [149] Y. Li, C. Liu, X. Feng, Y. Xu, and B. F. Liu, "Ultrafast microfluidic mixer for tracking the early folding kinetics of human telomere g-quadruplex," *Analytical chemistry*, vol. 86, no. 9, pp. 4333–4339, 2014. 100
- [150] A. S. Yang, F. C. Chuang, C. K. Chen, M. H. Lee, S. W. Chen, T. L. Su, and Y. C. Yang, "A high-performance micromixer using three-dimensional tesla structures for bio-applications," *Chemical Engineering Journal*, vol. 263, pp. 444–451, 2015. 100
- [151] W. Buchegger, C. Wagner, B. Lendl, M. Kraft, and M. J. Vellekoop, "A highly uniform lamination micromixer with wedge shaped inlet channels for time resolved infrared spectroscopy," *Microfluidics and Nanofluidics*, vol. 10, no. 4, pp. 889–897, 2011. 100
- [152] C. H. Lin, C. H. Tsai, and L. M. Fu, "A rapid three-dimensional vortex micromixer utilizing self-rotation effects under low reynolds number conditions," *Journal of Micromechanics and Microengineering*, vol. 15, no. 5, p. 935, 2005. 100
- [153] M. Du, Z. Ma, X. Ye, and Z. Zhou, "On-chip fast mixing by a rotary peristaltic micropump with a single structural layer," *Science China Technological Sciences*, vol. 56, no. 4, pp. 1047–1054, 2013. 100
- [154] S. Hardt, H. Pennemann, and F. Schönfeld, "Theoretical and experimental characterization of a low-reynolds number split-and-recombine mixer," *Microfluidics and Nanofluidics*, vol. 2, no. 3, pp. 237–248, 2006. 100
- [155] Y. Abbas, J. Miwa, R. Zengerle, and F. von Stetten, "Active continuous-flow micromixer using an external braille pin actuator array," *Micromachines*, vol. 4, no. 1, pp. 80–89, 2013. 100
- [156] J. B. You, K. Kang, T. T. Tran, H. Park, W. R. Hwang, J. M. Kim, and S. G. Im, "Pdms-based turbulent microfluidic mixer," *Lab on a Chip*, vol. 15, no. 7, pp. 1727–1735, 2015. 100
- [157] K. Chen, H. Lu, M. Sun, L. Zhu, and Y. Cui, "Mixing enhancement of a novel c-sar microfluidic mixer," *Chemical Engineering Research and Design*, vol. 132, pp. 338–345, 2018. 100
- [158] C. P. Coelho, S. Desai, D. Freeman, and J. White, "A robust approach for estimating diffusion constants from concentration data in microchannel mixers," in *Proceedings of 2005*



*NSTI nanotechnology conference and trade show (Nanotech 2004), Anaheim, CA, 2005, pp. 549–552. 100, 113*

- [159] M. H. Werts, V. Raimbault, R. Texier-Picard, R. Poizat, O. Français, L. Griscom, and J. R. Navarro, “Quantitative full-colour transmitted light microscopy and dyes for concentration mapping and measurement of diffusion coefficients in microfluidic architectures,” *Lab on a Chip*, vol. 12, no. 4, pp. 808–820, 2012. 100, 113